The Origins and Properties of Giant Planets on Extreme Orbits

Thesis by
Julie Alanna Inglis

In Partial Fulfillment of the Requirements for the
Degree of
Ph.D. in Planetary Sciences

CALIFORNIA INSTITUTE OF TECHNOLOGY
1200 E California Blvd. Pasadena, California, 91125

2026
Defended September 5, 2025

Julie Alanna Inglis
ORCID: 0000-0001-9164-7966

ACKNOWLEDGEMENTS

I am truly grateful for the many people who have been a part of my journey until now, from grade school teachers, basketball coaches, mentors, and friends. Thank you all for the part you played in helping me to this point. I will be forever grateful.

To my friends and cohort, who survived starting graduate school during a global pandemic, thank you for all the fun adventures, midnight meteor showers, art nights, DnD sessions, weekend pickle ball games, and endless support along the way. To all the other planetary science grad students, postdocs, and alumni—especially Nicole Wallack, Mike Greklek-McKeon, Shreyas Vissapragada, Jess Spake, Tess Marlin, Maria Carmarca, Morgan Saidal, Yu Yu Phua, Zac Milby, Jonathan Gomez, Kim Paragas, Matt Belyakov, and Ryleigh Davis, thank you for making my days in South Mudd bright. Thank you to my housemates, both human—Kali, Jocelyn, Sujeeka, and Melissa—and not—Lilly, Petie, Timbit, Goose, and Butter Tart—for being there for all the highs and lows. And a special thanks to the friends and colleagues who helped work alongside me to make the GPS division better for everyone, especially Hemani Kalucha, Lily Dove, and Clare Singer, for their kindness and determination that everyone feel welcome, safe, and supported through their academic career.

I am grateful to all of my amazing collaborators and academic mentors over the years, especially my wonderful PhD advisor, Heather Knutson, for being a supportive, encouraging, and brilliant mentor these last five years. I could not have wished for a better PhD advisor. Thank you to Nikole Lewis and Tiffany Kataria, who gave me the opportunity to work on an amazing JWST project as a second-year graduate student, which was my dream when I started my PhD. To the rest of my thesis committee, Konstantin Batygin, Geoffrey Blake, and Andrew Howard, thank you for your advice and guidance. Thank you to Luke Finnerty and Jerry Xuan and the members of the KPIC and KPF instrument teams for all the help with observing and data reduction over the years. I am thankful for the members of Heather Knutson's research group, for being friends, collaborators, and conference companions. Thank you to my undergraduate advisor, Ralph Pudritz, who cheered me on endlessly and gave me my first exoplanet project. A special thanks to Nicole Wallack, for being a steadfast friend, mentor, and unparalleled collaborator, for listening to all my hair-brained ideas and being my brown dwarf friend in a group of small planet folks.

Thank you to the GPS Division administrators, especially Julie Lee and Jen Shechet,

those in the Planetary Sciences offices, and Ruth Loisel, for all their assistance, friendship, and support, and to the GPS division, for providing a supportive and welcoming environment, and for the amazing opportunity to explore the world and learn about new places and geology.

Thank you to my family, especially my big brother, David, his wife, Emily, and my adorable nieces and nephew, for making winter holidays so full of fun, love, and joy. Thank you Mom for all the love and support over the years, especially during undergrad where I didn't think I would make it through my physics degree. I wouldn't be here without you. Thank you to my big sister, Sally, for being an absolute powerhouse of confidence, kindness, and determination—you inspire me every day—and thank you to my younger brother Ian, for being a model of courage, strength, and finding your own path. Thank you, Dad, for the adventures, and for always being excited to hear about my research.

Lastly, I want to thank two important friends who did not get to see me finish my PhD. Firstly, Dave Heffler, who was always so excited to talk about physics and math with a young girl, thank you for all your faith and excitement over my accomplishments, for always wanting to teach me something new, and for the sailing lessons on the lake. I miss you every day. And Petie, the kitten I adopted after passing my qualifying exams, for always being there after a hard day to greet me at the door. I couldn't have made it this far without you. I will never forget either of you.

ABSTRACT

Over the past three decades we have discovered thousands of exoplanets orbiting nearby stars, greatly expanding our understanding of the galactic planet population. Most of these exoplanetary systems have properties that are markedly different from those of our own solar system. Some systems contain gas giant planets with masses comparable to or even larger than that of Jupiter orbiting only a few stellar radii from the surfaces of their host stars. In other systems, gas giants have been discovered with orbital separations more than 100 times the Earth-Sun distance. Both of these populations challenge our understanding of gas giant planet formation, and it has been suggested that they might have initially formed at intermediate orbital separations and then migrated to their present-day locations.

In this thesis, I combine multiple observational techniques to characterize the properties of giant planets on extreme orbits in order to constrain their formation and migration histories. In Chapter 1, I fit both low- and high-resolution infrared spectra of the massive, widely separated, planetary-mass companion ROXs 42B b in order to measure the elemental abundances of carbon and oxygen in its atmosphere. In Chapter 2, I use two decades of astrometric monitoring to measure the mutual inclination between the orbital plane of ROXs 42B b and that of its host binary. In Chapter 3, I demonstrate how mid-infrared emission spectroscopy with JWST/MIRI LRS can be used to characterize the properties of both clouds and gas-phase absorbers in the atmosphere of HD 189733 b, a hot gas giant on a close-in orbit. In Chapter 4, I present a preliminary analysis of new high-resolution optical spectroscopy of the second hottest transiting planet currently known, TOI-2109 b. I use these optical high-resolution spectra to detect the presence of Fe, Mg, and Ti in this planet's atmosphere, and discuss how the relative abundances of refractory and volatile species can be used to constrain the solid-to-gas ratio of materials incorporated into the planet's envelope. In the conclusion, I discuss how the complementary techniques utilized in this thesis can be combined to develop a holistic view of the properties of gas giant planets on extreme orbits, which in turn allows us to test competing models for their origin.

PUBLISHED CONTENT AND CONTRIBUTIONS

Inglis, Julie et al. (May 2024a). "Atmospheric Retrievals of the Young Giant Planet ROXs 42B b from Low- and High-resolution Spectroscopy". In: *The Astronomical Journal* 167, p. 218. ISSN: 0004-6256. DOI: 10.3847/1538-3881/ad2771.
J.A.I analyzed the data and wrote the manuscript.

Inglis, Julie et al. (Oct. 2024b). "Quartz Clouds in the Dayside Atmosphere of the Quintessential Hot Jupiter HD 189733 b". In: *The Astrophysical Journal* 973, p. L41. ISSN: 0004-637X. DOI: 10.3847/2041-8213/ad725e.
J.A.I reduced and analyzed the data and wrote the manuscript.

TABLE OF CONTENTS

LIST OF ILLUSTRATIONS

LIST OF TABLES

Chapter 1

INTRODUCTION

In the three decades since the first discovery of an exoplanet around a main sequence star (51 Peg b; Mayor et al., 1995), our understanding of the exoplanetary population has exploded. To date, there are over 5,000 confirmed exoplanets (shown in Fig 1.1), with many more expected to be discovered by current and future missions. Already, these discoveries have revealed a diverse array of planetary systems that are markedly different from our own solar system. Hot Jupiters, gas giant planets on close-in orbits with masses similar to Jupiter, are found around $0.5 - 1.5\%$ of sun-like stars (e.g. Cumming et al., 2008; Fressin et al., 2013; Wright et al., 2012). On the other extreme, direct imaging surveys have revealed the presence of giant planets with masses many times that of Jupiter at orbital separations much greater than the orbit of Neptune. These distant giants have an occurrence rate of only 1% (Bowler et al., 2018).

Despite their relatively low occurrence rates, the existence of both hot Jupiters and directly-imaged giant planets challenges our understanding of gas giant formation and migration processes. In the solar system, gas giants are located external to the location of the water ice line, where water is expected to condense out of the gas phase in the protoplanetary disk. The water ice line is thought to correspond to the region where gas giants form most efficiently (Okuzumi et al., 2012; Drążkowska et al., 2017; Chachan et al., 2023). This is supported by the measured occurrence rates from radial velocity surveys, which indicate that giant planets are most likely to be found at moderate distances from their host stars. These surveys find that the occurrence rates for gas giant planets substantially increases outside of 1 au, and peaks between 2-10 au (Fernandes et al., 2019; Fulton et al., 2021). Formation in situ is thought to be challenging for hot Jupiters, as the high disk mid-plane temperatures prevent the condensation of sufficient solid mass, and a large critical core mass is required to initiate runaway gas accretion (Lin et al., 1996; Rafikov, 2006). However, in situ accretion of gas envelopes may be possible under certain conditions (Batygin et al., 2016). This raises the question of whether the observed populations of hot Jupiters and distant directly-imaged gas giants could have formed in-situ, or if they instead formed at intermediate orbital separations and then migrated to their current location.

High eccentricity migration, through processes such as planet-planet scattering (Rasio et al., 1996; Chatterjee et al., 2008) or Lidov-Kozai oscillations (Lidov, 1962; Kozai, 1962), is often proposed as a pathway for planets to migrate inward from moderate orbital separations. Systems with hot Jupiters commonly have more massive external companions, and these external companions have a larger median eccentricity than the broader population of gas giants at similar orbital separations, suggesting a past history of dynamical interactions(**zink_hot_-2023**). As we discuss in more detail below, the accretion and migration histories of giant planets may leave observable signatures in the atmospheric compositions and orbital properties of these populations of planets.

There are similar challenges involved in forming massive super Jupiters at distances of 100s of au from their host star. These planetary mass companions are thought to be distinct from the population of widely-separated brown dwarf companions ($\gtrsim$ 13 M_{Jup}) due to their higher occurrence rate and lower orbital eccentricities (Nielsen et al., 2019; Wagner et al., 2019; Bowler et al., 2020; Nagpal et al., 2023). They may also exhibit stellar spin-orbit orientations that are distinct from those of the brown dwarf population, which could points to a distinct formation mechanism, though the current population with measured spin-orbit orientations is small (Bowler et al., 2023). Surveys of young sun-like stars indicate that the typical size of protoplanetary disks is $\lesssim$60 au (Maury et al., 2019; Tobin et al., 2020). While there are a handful of anomalously large disks that extend out beyond 100 au (e.g. GG Tau; Guilloteau et al., 1999), it is still thought to be difficult to form an object many times the mass of Jupiter in the outer regions of these disks where the surface density of material is low and dynamical timescales are long. Like hot Jupiters, these companions may have formed at smaller orbital separations and subsequently been delivered to their current location through planet-planet scattering, capture from another star, or other dynamical processes. These processes may have left observable signatures in the present-day atmospheres and orbital configurations of these systems. Fortunately, both of these populations of planets are uniquely favorable for atmospheric characterization due to their temperatures and sizes.

1.1 Formation of Giant Planets

The final composition of a gas giant planet's envelope is a complex function of both its host disk properties and its formation and migration history. In the simplest picture of giant planet formation (e.g. Pollack et al., 1996; Lambrechts et al., 2012), a massive core is assembled from solid materials in the local region of the

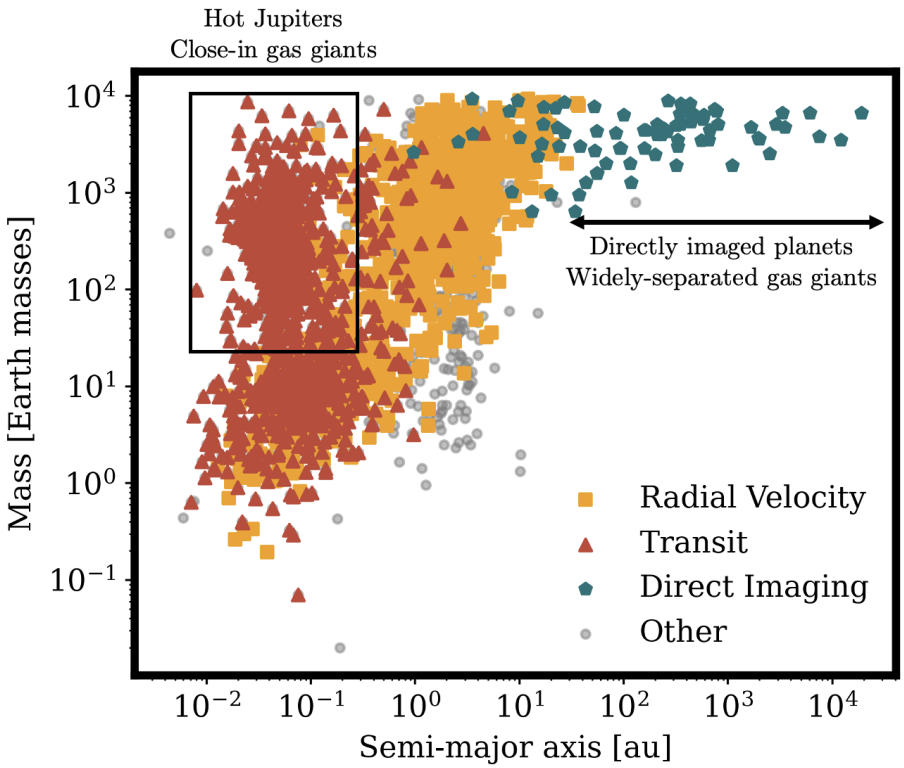

Figure 1.1 The current population of known exoplanets. Data retrieved from Exoplanet Archive on June 24, 2025.

protoplanetary disk. Once this core reaches a sufficient mass, it begins to accrete a mixture of gas and solids from the disk until gas pressure can no longer balance gravity and the planet moves into a runaway gas accretion phase. The planet then quickly grows to about the mass of Jupiter.

The composition of the gas and solids incorporated into the planet's envelope depends on its location within the protoplanetary disk. The mid-plane temperature of a protoplanetary disk decreases steeply with increasing radius. For a sun-like star, water condenses from the vapor phase into solids at approximately 2 au, CO_2 around 10 au, and CO beyond 40 au (Oberg et al., 2011; Madhusudhan, 2012; Öberg et al., 2021). These icelines alter the C/O ratio of both the gas and solids that are accreted by the growing gas giant such that the final composition of its upper atmosphere depends on the exact ratio of gas and solids incorporated into this region. This picture is additionally complicated by the radial migration of small solids, which can transport volatile-rich materials from the outer disk, and also the possible migration of the growing gas giant while still embedded in the protoplanetary disk (Öberg

et al., 2021; Shibata et al., 2022; Chachan et al., 2023). Although it is difficult to definitively associate particular atmospheric compositions with specific formation locations, the sum of these processes means that the planet's observed atmospheric composition can be significantly different in both bulk metals and elemental ratios than that of its host star. This is consistent with the large compositional diversity of transiting giant planet atmospheres observed by JWST (Kempton et al., 2024).

Alternatively, gas giant planets may also form via disk instability, wherein an overdense region of the disk collapses and forms a massive gas-dominated object. This instability occurs more easily in more massive and/or cooler disks (Toomre, 1964; Boss, 1997; Boley, 2009). It is expected to preferentially occur in the outer regions of the disk, and typically produces brown dwarf companions with a size of 10s of Jupiter masses (Boley, 2009). This mechanism is more likely to produce planets with atmospheric compositions similar to those of their host stars than core accretion. Although composition gradients within the protoplanetary disk, as well as the transport and trapping of dust, could potentially result in non-stellar atmospheric compositions (Boley et al., 2011), surveys of the atmospheric compositions of widely separated companions with masses between $10 - 30$ M_{Jup} indicate that their atmospheric compositions are consistent with those of their host stars (Xuan et al., 2024). This suggests that the default expectation of stellar atmospheric compositions is a reasonable first-order approximation for companions formed via gravitational instability. In Chapter 1 of this thesis, I utilize atmospheric observations of the widely-separated directly-imaged companion, ROXs-42B b, to measure the atmospheric C/O and metallicity. I then compare it with its host star in order to test whether it formed via core accretion or disk instability.

Along with atmospheric composition, orbital parameters such as eccentricity and spin-orbit alignment contain clues to the formation history of giant planets. The collapse of a cloud to form a protoplanetary disk is expected to be axisymmetric, forming a protoplanetary disk that is well-aligned with the stellar spin axis. Subsequent dynamical processes, such as a stellar flyby (Batygin et al., 2020) or planet-planet scattering (Rasio et al., 1996), can then act to introduce a misalignment between the planetary orbital axis and stellar spin. This phenomenon has been observed in the hot Jupiter population, where a subset of hot Jupiters have been shown to possess high sky-projected stellar obliquities (Rice et al., 2022), measured through the Rossiter-McLaughlin effect (Rossiter, 1924; McLaughlin, 1924). These obliquity measurements have typically been interpreted as evidence of high

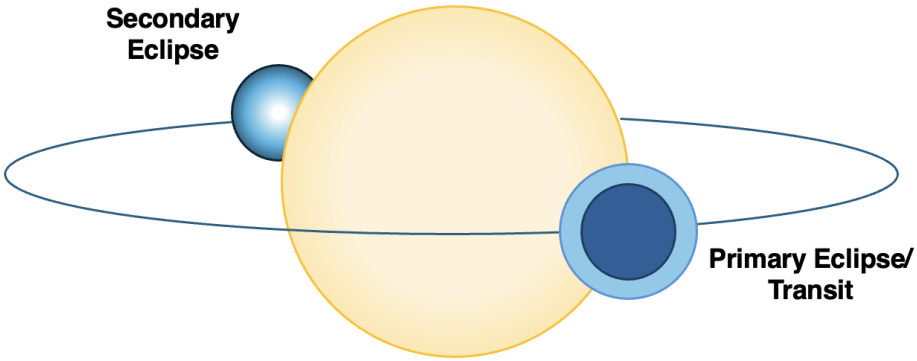

Figure 1.2 A schematic showing the orbital phases and planet-star configuration during primary eclipse (transit) and secondary eclipse.

eccentricity migration (Rice et al., 2022).

Widely-separated directly-imaged planetary mass companions also appear to have different distributions of spin-orbit alignments and orbital eccentricities than brown-dwarf companions, although there are only a small number of such systems with published measurements to date (Bowler et al., 2023; Bowler et al., 2020). Together with the observed differences in their occurrence rates and semi-major axis distributions (Nielsen et al., 2019), this suggests that the planetary mass companions formed within the protoplanetary disk, rather than through a star-like process such as core fragmentation. A subset of these planetary-mass companions have been found orbiting binaries. For these systems, a measurement of the mutual inclination between the binary orbit and companion orbit can provide additional clues to the system's formation and dynamical history. Binary stars with exterior transiting planets, for example, typically have small mutual inclinations, suggesting formation in an aligned circumbinary disk (Dupuy et al., 2022). The distribution of mutual inclinations for widely-separated circumbinary planets is relatively unknown, with only a handful of measurements. In Chapter 2 of this thesis, I use 20 years of astrometric monitoring of the ROXs 42B b system to measure the mutual inclination between the host binary and planet orbits in order to provide additional constraints on the formation of this system that are complementary to the atmospheric measurements presented in Chapter 1.

1.2 Atmospheric Characterization of Giant Planets

The atmospheres of giant planets are readily observable at visible and infrared wavelengths using a variety of techniques. Observations of exoplanet atmospheres

rely on the identification of atomic or molecular features in the planet's emission or transmission spectrum. Molecules such as H_2O, CO, and CO_2 typically have features at infrared wavelengths, corresponding to transitions in rotational or vibrational states, while atoms such as Fe and Mg have strong features at visible wavelengths due to electronic transitions.

Transmission spectroscopy is the classic technique for observing the atmospheres of transiting exoplanets (Seager et al., 2000; Charbonneau et al., 2002). This approach measures the wavelength-dependent transit depth when the planet passes in front of its host star. Published studies with HST and JWST have uncovered many molecules in the atmospheres of transiting hot Jupiters to date, including H_2O, CO, H_2S, CO_2, and CH_4, as well as evidence for silicate clouds and photochemical hazes in the form of muted absorption features and/or optical scattering slopes (see review by Kempton et al., 2024).

Emission spectroscopy can also provide a complimentary view of the atmospheric properties of gas giants. While the flux from the host star is typically many orders of magnitude (100-1,000) times brighter than the emission from the planet, it is still possible to detect the planet's emission using one of several techniques. High-precision broadband photometric or spectroscopic observations can be used to observe the planet's secondary eclipse, when the planet disappears behind its host star. The magnitude of the drop in flux during the eclipse is equivalent to the planet's emission at that wavelength. For isolated or widely-separated giant planets, advanced imaging techniques are able to spatially separate the light of the planet from that of its host star, allowing us to directly measure the planet's emission spectrum. For space-based observations, the resolution is typically lower than $\sim 2,000$, which can make it challenging to differentiate between molecules with overlapping features, such as water and methane, with limited wavelength coverage (Welbanks et al., 2025).

Exoplanetary atmospheres can also be observed at high spectral resolution. High-resolution spectroscopy has some distinct advantages over low resolution spectroscopy or broadband photometry. high-resolution spectrographs are capable of resolving individual emission or absorption lines, allowing for precise measurements of abundance ratios of molecules and atoms through their line depth ratios, and measurements of wind speeds and atmospheric dynamics using line broadening and velocity shifts. high-resolution observations of ultra-hot transiting gas giants in the optical have yielded detections of many atomic and ionic species in the atmo-

Planet	Teq (K)	Atomic Species	Ionic Species
KELT-9 b	4050	H Na Mg Ca Ti V Cr Fe Ni O	Ca+ Sr+ Ba+ Sc+ Ti+ Cr+ Fe+ Y+
TOI-2109 b	3646	Mg Ti Fe	
WASP-33 b	2780	H Ti V Fe Si	Ca+
WASP-189 b	2640	H Na Mg Ca Sr Ti V Cr Fe Ni	Ca+ Sr+ Ba+ Ti+ Fe+
HAT-P-70 b	2550	H Na Mg Ca V Cr Fe	Ca+ Fe+
WASP-121 b	2450	H Li Na K Mg Ca V Cr Mn Fe Co Ni	Ca+ Sr+ Ba+ Sc+ Ti+ Fe+
MASCARA-4 b	2400	H Na Mg Ca Sr V Cr Mn Fe	Ca+ Bar+ Ti+ Fe+
MASCARA-2 b	2260	H Na Mg Ca Cr Mn Fe	Ca+ Cr+ Fe+
WASP-76 b	2180	H Li Na K Mg Ca V Cr Mn Fe Ni O	Ca+ Ba+ Fe+
HAT-P-67 b	1930	H Na He	Ca+

Figure 1.3 Summary of the detected atomics and ionic species in ultra-hot Jupiter atmospheres sorted in order of decreasing equilibrium temperature. This is an updated version of Figure 6 in Snellen (2025), including additional detections in WASP-33 b from Cont et al. (2022), and TOI-2109 b from Cont et al. (2025) and the work in this thesis. The detected species as color coded as non-metals (blue), alkali metals (green), alkaline earth metals (orange), and transition metals (yellow). New detections from this work are underlined.

spheres of giant planets (Fig. 1.3; see review by Snellen, 2025). In Chapter 4 of this thesis, I use Keck/KPF to observe the optical emission spectrum of the second hottest transiting planet, TOI-2109 b, at high-resolution. In this chapter, I showcase our preliminary atomic detections and discuss the next steps for this project.

Once either a transmission or emission spectrum has been obtained, it can be inverted to constrain the temperature profile and elemental abundances in the uppermost layers of the atmosphere using either self-consistent models (forward models) or Bayesian atmospheric retrievals. Forward model grids, such as the `Sonora` (Marley et al., 2021) or `Phoenix` (Allard et al., 1995; Husser et al., 2013) models, are self-consistent 1D atmospheric models calculated based on a handful of planetary parameters such as composition, surface gravity, and effective temperature. Grid models are useful for testing our ability to predict the observed atmospheric properties of exoplanets based on a small number of intrinsic variables. Alternatively, the major pitfall of forward models is their limited number of free parameters and simplified physics, such as the 3D atmospheric circulation, radiative feedback from clouds or other internal heating sources such as tides, that can affect the observed properties of planetary atmospheres (Roman et al., 2021; Welbanks et al., 2024; Batygin, 2025).

Conversely, atmospheric retrievals are a more flexible, data-driven method for characterizing planetary atmospheres. This technique relies on parameterizing the complicated physics of a planetary atmosphere, such as the pressure-temperature profile, surface gravity, and chemistry, into a dozen or so variables. A Bayesian sampling

technique such as MCMC or nested sampling is then used to compare thousands of model atmospheres generated over a wide range of possible parameters to the observed data in order to find the range of values that are consistent with the measured planetary spectrum. There are many existing open-source retrieval codes, each of which treats the radiative transfer, thermal structure parameterization, and opacities slightly differently, including `petitRADTRANS` (Mollière et al., 2019), `Poseidon` (MacDonald, 2023), `Platon` (Zhang et al., 2020), among others. As retrievals are fully driven by the data, this allows for more flexibility to capture unknown processes and chemistry in planetary atmospheres. However, this flexibility can lead to unphysical solutions for the atmosphere, so the prior range for the parameters must be chosen with care.

Aerosols, in the form of hazes and clouds, remain one of the largest challenges for interpreting observations of planetary atmospheres. Aerosols are ubiquitous in the solar system, from the hydrogen sulfide clouds on Venus to the hazes of Titan, and are expected to be found in the atmospheres of most exoplanets cooler than $\sim$ 2500 K. The currently predicted "aerosol sequence" in planetary atmospheres is as follows: for gas giants hotter than $\sim$ 1000 K, silicate and metal clouds are expected to dominate, while at lower temperatures this transitions to photochemically produced hazes, and at temperatures below $\sim$ 350 K, water clouds appear (for more information see review by Gao et al., 2020). In Fig. 2.9, we show an example atmospheric pressure-temperature profile for a few classical exoplanets compared to different condensation curves, showing the many species that might condense out in a planetary atmosphere with an abundance high enough to potentially affect the planet's observed spectrum. Although there are additional cloud species that could form in principle, such as sulfide clouds (e.g. MnS and Zns), they have not been directly detected yet (Wakeford et al., 2015). Mid-infrared features from silicate clouds, on the other hand, have been observed in the spectra of cool brown dwarfs by Spitzer (Burgasser et al., 2008; Suárez et al., 2022; Suárez et al., 2023), and more recently by JWST (Grant et al., 2023; Inglis et al., 2024).

Clouds have a significant effect on exoplanet spectra, muting or completely obscuring features (Wakeford et al., 2015). This can result in biased abundance measurements, particularly in the near infrared where no distinct cloud features exist to identify the type of aerosols present and constrain their properties (Inglis et al., 2024). Adding more wavelength coverage, or directly measuring the features of clouds in the mid infrared using instruments like JWST/MIRI LRS, is crucial to overcome

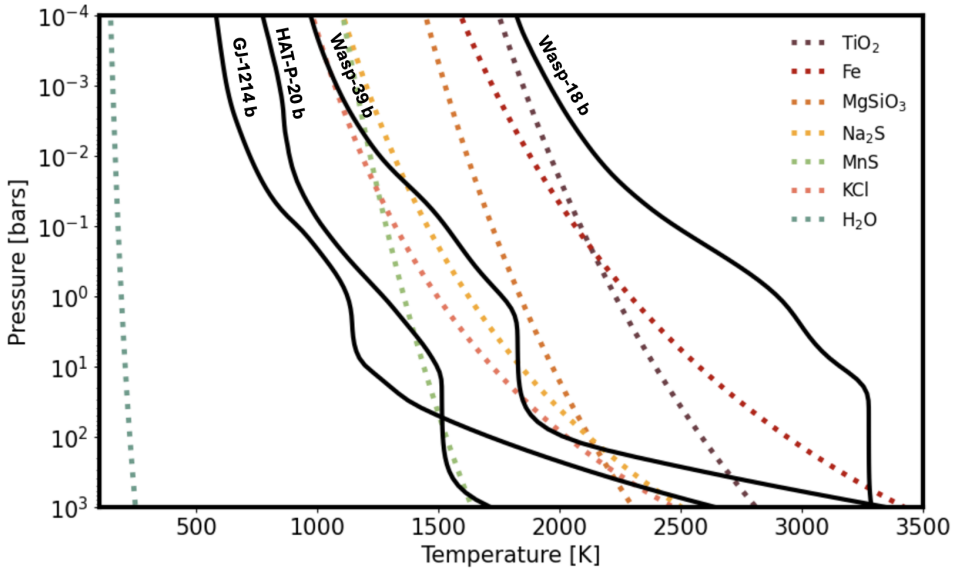

Figure 1.4 Example P-T profiles for four well-characterized exoplanets generated using `petitRADTRANS` (Mollière et al., 2020) compared to condensation curves for various potential condensate species that could be present in the atmospheres of exoplanets.

this limitation. In Chapter 3 of this thesis, I demonstrate how measurements with JWST/MIRI LRS can be used to directly measure the composition and properties of silicate clouds in the atmosphere of hot Jupiters, allowing us to quantify their effect on observed spectra. This work was the first to detect silicate clouds in the day-side atmosphere of a hot Jupiter.

References

Allard, France and Peter H. Hauschildt (May 1995). "Model Atmospheres for M (Sub)Dwarf Stars. I. The Base Model Grid". In: *The Astrophysical Journal* 445, p. 433. ISSN: 0004-637X. DOI: 10.1086/175708.

Batygin, Konstantin (May 2025). "From Tides to Currents: Unraveling the Mechanism that Powers WASP-107b's Internal Heat Flux". In: *The Astrophysical Journal* 985, p. 87. ISSN: 0004-637X. DOI: 10.3847/1538-4357/adccc4. (Visited on 09/16/2025).

Batygin, Konstantin, Peter H. Bodenheimer, and Gregory P. Laughlin (Oct. 2016). "In Situ Formation and Dynamical Evolution of Hot Jupiter Systems". In: *The Astrophysical Journal* 829, p. 114. ISSN: 0004-637X. DOI: 10.3847/0004-637X/829/2/114.

Batygin, Konstantin et al. (Mar. 2020). "Dynamics of Planetary Systems within Star Clusters: Aspects of the Solar System's Early Evolution". In: *The Astronomical Journal* 159, p. 101. ISSN: 0004-6256. DOI: 10.3847/1538-3881/ab665d.

Boley, Aaron C. (Mar. 2009). "The Two Modes of Gas Giant Planet Formation". In: *The Astrophysical Journal* 695.1, p. L53. ISSN: 0004-637X. DOI: 10.1088/0004-637X/695/1/L53.

Boley, Aaron C., Ravit Helled, and Matthew J. Payne (July 2011). "The Heavy-Element Composition of Disk Instability Planets can Range From Sub- to Super-Nebular". In: *The Astrophysical Journal* 735.1, p. 30. ISSN: 0004-637X, 1538-4357. DOI: 10.1088/0004-637X/735/1/30.

Boss, Alan P. (June 1997). "Giant Planet Formation by Gravitational Instability". In: *Science* 276.5320, pp. 1836–1839. DOI: 10.1126/science.276.5320.1836.

Bowler, Blunt, and Nielsen (Jan. 2020). "Population-level Eccentricity Distributions of Imaged Exoplanets and Brown Dwarf Companions: Dynamical Evidence for Distinct Formation Channels*". In: *The Astronomical Journal* 159.2, p. 63. ISSN: 1538-3881. DOI: 10.3847/1538-3881/ab5b11.

Bowler, Brendan P. and Eric L. Nielsen (Jan. 2018). *Occurrence Rates from Direct Imaging Surveys*. Springer International Publishing AG. DOI: 10.1007/978-3-319-55333-7_155. (Visited on 01/28/2025).

Bowler, Brendan P. et al. (Apr. 2023). "Rotation Periods, Inclinations, and Obliquities of Cool Stars Hosting Directly Imaged Substellar Companions: Spin-Orbit Misalignments Are Common". In: *The Astronomical Journal* 165, p. 164. ISSN: 0004-6256. DOI: 10.3847/1538-3881/acbd34.

Burgasser, Adam J. et al. (Feb. 2008). "Clouds, Gravity, and Metallicity in Blue L Dwarfs: The Case of 2MASS J11263991–5003550*". In: *The Astrophysical Journal* 674.1, p. 451. ISSN: 0004-637X. DOI: 10.1086/524726.

Chachan et al. (Jan. 2023). "Breaking Degeneracies in Formation Histories by Measuring Refractory Content in Gas Giants". en. In: *The Astrophysical Journal* 943.2, p. 112. ISSN: 0004-637X. DOI: 10.3847/1538-4357/aca614.

Charbonneau, David et al. (Mar. 2002). "Detection of an Extrasolar Planet Atmosphere". In: *The Astrophysical Journal* 568, pp. 377–384. ISSN: 0004-637X. DOI: 10.1086/338770.

Chatterjee, Sourav et al. (Oct. 2008). "Dynamical Outcomes of Planet-Planet Scattering". en. In: *The Astrophysical Journal* 686.1, p. 580. ISSN: 0004-637X. DOI: 10.1086/590227. (Visited on 08/22/2025).

Cont, D. et al. (Dec. 2022). "Atmospheric characterization of the ultra-hot Jupiter WASP-33b. Detection of Ti and V emission lines and retrieval of a broadened line profile". In: *Astronomy and Astrophysics* 668, A53. ISSN: 0004-6361. DOI: 10.1051/0004-6361/202244277. (Visited on 08/22/2025).

Cont, D. et al. (June 2025). “Retrieving day- and nightside atmospheric properties of the ultra-hot Jupiter TOI-2109b - Detection of Fe and CO emission lines and evidence for inefficient heat transport”. en. In: *Astronomy & Astrophysics* 698, A31. ISSN: 0004-6361, 1432-0746. DOI: 10.1051/0004-6361/202554572.

Cumming, Andrew et al. (May 2008). “The Keck Planet Search: Detectability and the Minimum Mass and Orbital Period Distribution of Extrasolar Planets”. In: *Publications of the Astronomical Society of the Pacific* 120, p. 531. ISSN: 0004-6280. DOI: 10.1086/588487.

Drążkowska, J. and Y. Alibert (Dec. 2017). “Planetesimal formation starts at the snow line”. In: *Astronomy and Astrophysics* 608, A92. ISSN: 0004-6361. DOI: 10.1051/0004-6361/201731491. (Visited on 09/16/2025).

Dupuy et al. (Mar. 2022). “Orbital Architectures of Planet-Hosting Binaries II. Low Mutual Inclinations Between Planetary and Stellar Orbits”. In: *Monthly Notices of the Royal Astronomical Society* 512.1, pp. 648–660. ISSN: 0035-8711, 1365-2966. DOI: 10.1093/mnras/stac306.

Fernandes, Rachel B. et al. (Mar. 2019). “Hints for a Turnover at the Snow Line in the Giant Planet Occurrence Rate”. In: *The Astrophysical Journal* 874, p. 81. ISSN: 0004-637X. DOI: 10.3847/1538-4357/ab0300.

Fressin, François et al. (Apr. 2013). “The False Positive Rate of Kepler and the Occurrence of Planets”. In: *The Astrophysical Journal* 766, p. 81. ISSN: 0004-637X. DOI: 10.1088/0004-637X/766/2/81.

Fulton, Benjamin J. et al. (July 2021). “California Legacy Survey. II. Occurrence of Giant Planets beyond the Ice Line”. In: *The Astrophysical Journal Supplement Series* 255, p. 14. ISSN: 0067-0049. DOI: 10.3847/1538-4365/abfcc1.

Gao, Peter et al. (Oct. 2020). “Aerosol composition of hot giant exoplanets dominated by silicates and hydrocarbon hazes”. In: *Nature Astronomy* 4.10, pp. 951–956. ISSN: 2397-3366. DOI: 10.1038/s41550-020-1114-3.

Grant, David et al. (Oct. 2023). “JWST-TST DREAMS: Quartz Clouds in the Atmosphere of WASP-17b”. In: 956.2, L29, p. L29. DOI: 10.3847/2041-8213/acfc3b. arXiv: 2310.08637 [astro-ph.EP].

Guilloteau, Dutrey, and Simon (Aug. 1999). “GG Tauri: the ring world”. In: *Astronomy and Astrophysics* 348, pp. 570–578. ISSN: 0004-6361.

Husser, T.-O. et al. (May 2013). “A new extensive library of PHOENIX stellar atmospheres and synthetic spectra”. en. In: *Astronomy & Astrophysics* 553, A6. ISSN: 0004-6361, 1432-0746. DOI: 10.1051/0004-6361/201219058.

Inglis, Julie et al. (May 2024). “Atmospheric Retrievals of the Young Giant Planet ROXs 42B b from Low- and High-resolution Spectroscopy”. In: *The Astronomical Journal* 167, p. 218. ISSN: 0004-6256. DOI: 10.3847/1538-3881/ad2771.

Kempton, Eliza M. -R. and Heather A. Knutson (July 2024). "Transiting Exoplanet Atmospheres in the Era of JWST". In: *Reviews in Mineralogy and Geochemistry* 90, pp. 411–464. DOI: 10.2138/rmg.2024.90.12.

Kozai, Yoshihide (Nov. 1962). "Secular perturbations of asteroids with high inclination and eccentricity". In: *The Astronomical Journal* 67, pp. 591–598. ISSN: 0004-6256. DOI: 10.1086/108790.

Lambrechts, M. and A. Johansen (Aug. 2012). "Rapid growth of gas-giant cores by pebble accretion". In: *Astronomy & Astrophysics* 544, A32. ISSN: 0004-6361, 1432-0746. DOI: 10.1051/0004-6361/201219127.

Lidov, M. L. (Oct. 1962). "The evolution of orbits of artificial satellites of planets under the action of gravitational perturbations of external bodies". In: *Planetary and Space Science* 9, pp. 719–759. ISSN: 0032-0633. DOI: 10.1016/0032-0633(62)90129-0.

Lin, D. N. C., P. Bodenheimer, and D. C. Richardson (Apr. 1996). "Orbital migration of the planetary companion of 51 Pegasi to its present location". en. In: *Nature* 380.6575, pp. 606–607. ISSN: 1476-4687. DOI: 10.1038/380606a0.

MacDonald, Ryan J. (Jan. 2023). "POSEIDON: A Multidimensional Atmospheric Retrieval Code for Exoplanet Spectra". In: *The Journal of Open Source Software* 8, p. 4873. DOI: 10.21105/joss.04873.

Madhusudhan, Nikku (Oct. 2012). "C/O Ratio as a Dimension for Characterizing Exoplanetary Atmospheres". In: *The Astrophysical Journal* 758.1, p. 36. ISSN: 0004-637X, 1538-4357. DOI: 10.1088/0004-637X/758/1/36.

Marley, Mark et al. (July 2021). *Sonora Bobcat: cloud-free, substellar atmosphere models, spectra, photometry, evolution, and chemistry*. DOI: 10.5281/zenodo.5063476.

Maury, A. J. et al. (Jan. 2019). "Characterizing young protostellar disks with the CALYPSO IRAM-PdBI survey: large Class 0 disks are rare". In: *Astronomy and Astrophysics* 621, A76. ISSN: 0004-6361. DOI: 10.1051/0004-6361/201833537.

Mayor, Michel and Didier Queloz (Nov. 1995). "A Jupiter-mass companion to a solar-type star". en. In: *Nature* 378.6555, pp. 355–359. ISSN: 1476-4687. DOI: 10.1038/378355a0.

McLaughlin, D. B. (July 1924). "Some results of a spectrographic study of the Algol system." In: *The Astrophysical Journal* 60, pp. 22–31. ISSN: 0004-637X. DOI: 10.1086/142826.

Mollière, P. et al. (July 2019). "petitRADTRANS: a Python radiative transfer package for exoplanet characterization and retrieval". In: *Astronomy & Astrophysics* 627, A67. ISSN: 0004-6361, 1432-0746. DOI: 10.1051/0004-6361/201935470.

Mollière, P. et al. (Aug. 2020). "Retrieving scattering clouds and disequilibrium chemistry in the atmosphere of HR 8799e". In: *Astronomy & Astrophysics* 640, A131. ISSN: 0004-6361, 1432-0746. DOI: 10.1051/0004-6361/202038325.

Nagpal, Vighnesh et al. (Feb. 2023). "The Impact of Bayesian Hyperpriors on the Population-level Eccentricity Distribution of Imaged Planets". In: *The Astronomical Journal* 165, p. 32. ISSN: 0004-6256. DOI: 10.3847/1538-3881/ac9fd2.

Nielsen, Eric L. et al. (July 2019). "The Gemini Planet Imager Exoplanet Survey: Giant Planet and Brown Dwarf Demographics from 10 to 100 au". In: *The Astronomical Journal* 158, p. 13. ISSN: 0004-6256. DOI: 10.3847/1538-3881/ab16e9.

Oberg, Karin I., Ruth Murray-Clay, and Edwin A. Bergin (Dec. 2011). "The effects of snowlines on C/O in planetary atmospheres". In: *The Astrophysical Journal* 743.1, p. L16. ISSN: 2041-8205, 2041-8213. DOI: 10.1088/2041-8205/743/1/L16.

Öberg, Karin I. and Edwin A. Bergin (Jan. 2021). "Astrochemistry and compositions of planetary systems". In: *Physics Reports* 893, pp. 1–48. ISSN: 0370-1573. DOI: 10.1016/j.physrep.2020.09.004.

Okuzumi, Satoshi et al. (June 2012). "Rapid Coagulation of Porous Dust Aggregates outside the Snow Line: A Pathway to Successful Icy Planetesimal Formation". In: *The Astrophysical Journal* 752, p. 106. ISSN: 0004-637X. DOI: 10.1088/0004-637X/752/2/106.

Pollack, James B. et al. (Nov. 1996). "Formation of the Giant Planets by Concurrent Accretion of Solids and Gas". In: *Icarus* 124, pp. 62–85. ISSN: 0019-1035. DOI: 10.1006/icar.1996.0190.

Rafikov, Roman R. (Sept. 2006). "Atmospheres of Protoplanetary Cores: Critical Mass for Nucleated Instability". In: *The Astrophysical Journal* 648, pp. 666–682. ISSN: 0004-637X. DOI: 10.1086/505695.

Rasio, Frederic A. and Eric B. Ford (Nov. 1996). "Dynamical Instabilities and the Formation of Extrasolar Planetary Systems". In: *Science* 274.5289, pp. 954–956. DOI: 10.1126/science.274.5289.954. (Visited on 08/22/2025).

Rice, Malena, Songhu Wang, and Gregory Laughlin (Feb. 2022). "Origins of Hot Jupiters from the Stellar Obliquity Distribution". In: *The Astrophysical Journal* 926, p. L17. ISSN: 0004-637X. DOI: 10.3847/2041-8213/ac502d.

Roman, Michael T. et al. (Feb. 2021). "Clouds in Three-dimensional Models of Hot Jupiters over a Wide Range of Temperatures. I. Thermal Structures and Broadband Phase-curve Predictions". en. In: *The Astrophysical Journal* 908.1, p. 101. ISSN: 0004-637X. DOI: 10.3847/1538-4357/abd549.

Rossiter, R. A. (July 1924). "On the detection of an effect of rotation during eclipse in the velocity of the brigher component of beta Lyrae, and on the constancy of velocity of this system." In: *The Astrophysical Journal* 60, pp. 15–21. ISSN: 0004-637X. DOI: 10.1086/142825.

Seager, S. and D. D. Sasselov (July 2000). "Theoretical Transmission Spectra During Extrasolar Giant Planet Transits". In: *The Astrophysical Journal* 537.2, pp. 916–921. ISSN: 0004-637X, 1538-4357. DOI: 10.1086/309088.

Shibata, Sho and Ravit Helled (Feb. 2022). "Enrichment of Jupiter's atmosphere by late planetesimal bombardment". In: *The Astrophysical Journal Letters* 926.2, p. L37. ISSN: 2041-8205, 2041-8213. DOI: 10.3847/2041-8213/ac54b1.

Snellen, Ignas (May 2025). *Exoplanet atmospheres at high spectral resolution*. DOI: 10.48550/arXiv.2505.08926.

Suárez, Genaro and Stanimir Metchev (May 2022). "Ultracool dwarfs observed with the *Spitzer* infrared spectrograph – II. Emergence and sedimentation of silicate clouds in L dwarfs, and analysis of the full M5–T9 field dwarf spectroscopic sample". In: *Monthly Notices of the Royal Astronomical Society* 513.4, pp. 5701–5726. ISSN: 0035-8711, 1365-2966. DOI: 10.1093/mnras/stac1205.

– (Aug. 2023). "Ultracool dwarfs observed with the Spitzer Infrared Spectrograph – III. Dust grains in young L dwarf atmospheres are heavier". In: *Monthly Notices of the Royal Astronomical Society* 523.3, pp. 4739–4747. ISSN: 0035-8711. DOI: 10.1093/mnras/stad1711.

Tobin, John J. et al. (Feb. 2020). "The VLA/ALMA Nascent Disk and Multiplicity (VANDAM) Survey of Orion Protostars. II. A Statistical Characterization of Class 0 and Class I Protostellar Disks". en. In: *The Astrophysical Journal* 890.2, p. 130. ISSN: 0004-637X. DOI: 10.3847/1538-4357/ab6f64.

Toomre, A. (May 1964). "On the gravitational stability of a disk of stars." In: *The Astrophysical Journal* 139, pp. 1217–1238. ISSN: 0004-637X. DOI: 10.1086/147861.

Wagner, Kevin, Dániel Apai, and Kaitlin M. Kratter (May 2019). "On the Mass Function, Multiplicity, and Origins of Wide-orbit Giant Planets". In: *The Astrophysical Journal* 877, p. 46. ISSN: 0004-637X. DOI: 10.3847/1538-4357/ab1904.

Wakeford, H. R. and D. K. Sing (Jan. 2015). "Transmission spectral properties of clouds for hot Jupiter exoplanets". en. In: *Astronomy & Astrophysics* 573, A122. ISSN: 0004-6361, 1432-0746. DOI: 10.1051/0004-6361/201424207.

Welbanks, Luis et al. (June 2024). "A high internal heat flux and large core in a warm Neptune exoplanet". en. In: *Nature* 630.8018. Publisher: Nature Publishing Group, pp. 836–840. ISSN: 1476-4687. DOI: 10.1038/s41586-024-07514-w.

Welbanks, Luis et al. (Apr. 2025). *The Challenges of Detecting Gases in Exoplanet Atmospheres*. ADS Bibcode: 2025arXiv250421788W. DOI: 10.48550/arXiv.2504.21788.

Wright, J. T. et al. (July 2012). "The Frequency of Hot Jupiters Orbiting nearby Solar-type Stars". In: *The Astrophysical Journal* 753, p. 160. ISSN: 0004-637X. DOI: 10.1088/0004-637X/753/2/160.

Xuan et al. (July 2024). “Are These Planets or Brown Dwarfs? Broadly Solar Compositions from High-resolution Atmospheric Retrievals of 10–30 MJup Companions”. en. In: *The Astrophysical Journal* 970.1, p. 71. ISSN: 0004-637X. DOI: 10.3847/1538-4357/ad4796.

Zhang, Michael et al. (Aug. 2020). “PLATON II: New Capabilities and a Comprehensive Retrieval on HD 189733b Transit and Eclipse Data”. In: *The Astrophysical Journal* 899.1, p. 27. ISSN: 0004-637X. DOI: 10.3847/1538-4357/aba1e6.

Chapter 2

ATMOSPHERIC RETRIEVALS OF THE YOUNG GIANT PLANET ROXS 42B B FROM LOW- AND HIGH-RESOLUTION SPECTROSCOPY

Inglis, Julie et al. (May 2024). "Atmospheric Retrievals of the Young Giant Planet ROXs 42B b from Low- and High-resolution Spectroscopy". In: *The Astronomical Journal* 167, p. 218. ISSN: 0004-6256. DOI: 10.3847/1538-3881/ad2771.

2.1 Abstract

Previous attempts have been made to characterize the atmospheres of directly-imaged planets at low-resolution (R∼10s-100s), but the presence of clouds has often led to degeneracies in the retrieved atmospheric abundances with cloud opacity and temperature structure that bias retrieved compositions. In this study, we perform retrievals on the ultra-young ($\lesssim$ 5 Myr) directly-imaged planet ROXs 42B b with both a downsampled low-resolution JHK-band spectrum from Gemini/NIFS and Keck/OSIRIS, and a high-resolution K-band spectrum from pre-upgrade Keck/NIRSPAO. Using the atmospheric retrieval framework of `petitRADTRANS`, we analyze both data sets individually and combined. We additionally fit for the stellar abundances and other physical properties of the host stars, a young M spectral type binary, using the SPHINX model grid. We find that the measured C/O, 0.50 ± 0.05, and metallicity, [Fe/H] = -0.67 ± 0.35, for ROXs 42B b from our high-resolution spectrum agree with that of its host stars within 1σ. The retrieved parameters from the high-resolution spectrum are also independent of our choice of cloud model. In contrast, the retrieved parameters from the low-resolution spectrum show strong degeneracies between the clouds and the retrieved metallicity and temperature structure. When we retrieve on both data sets together, we find that these degeneracies are reduced but not eliminated, and the final results remain highly sensitive to cloud modeling choices. We conclude that high-resolution spectroscopy offers the most promising path for reliably determining atmospheric compositions of directly-imaged companions independent of their cloud properties.

2.2 Introduction

Directly-imaged planets are a population of massive, self-luminous companions, typically observed from orbital separations comparable to that of Saturn, to well beyond the orbital distance of Neptune (10s-100s of au). These companions are typically young, with ages $\lesssim$ 100 Myr, and are often distinguished from brown dwarf companions ($\sim 13 - 80$ M_J) as having masses near or below the deuterium-burning limit at $\sim$13 M_J (Bowler, 2016; Currie et al., 2022). A more physically motivated distinction between directly-imaged planets and brown dwarfs would be based on formation process, as planets are expected to form bottom-up from core accretion, while brown dwarf companions form from gravitational collapse, however this is challenging to distinguish for individual objects (Pollack et al., 1996; Boss, 1997; Alibert et al., 2005).

Population studies indicate that these lower mass companions have properties that are distinct from those of massive brown dwarf companions. Planetary-mass companions appear to have a higher occurrence rate than brown dwarf companions to the same stellar population, and tend to have lower orbital eccentricities (Nielsen et al., 2019; Wagner et al., 2019; Bowler et al., 2020a; Nagpal et al., 2023), and distinct stellar spin-orbit orientations (Bowler et al., 2023). The differing properties of these two populations suggest that they likely have distinct formation channels, but the nature of these formation channels is currently debated. It has also been suggested that one or both populations might not have formed in situ, but instead migrated away from their initial formation locations (Scharf et al., 2009). However, Bryan et al. (2016) failed to find evidence for additional massive bodies in systems hosting wide-separation directly-imaged companions that could have acted as scatterers, suggesting this is not the dominant formation mechanism for these planets.

Numerous studies have explored how the elemental abundances of giant planet atmospheres, which are often parameterized as a carbon-to-oxygen ratio (C/O) and bulk metallicity (e.g. [Fe/H]), can encode information about their formation and migration histories (e.g. Madhusudhan, 2012; Oberg et al., 2011; Cridland et al., 2016; Mordasini et al., 2016; Turrini et al., 2021). Companions that form via gravitational instability, including cloud fragmentation and disk instability, are expected to have envelope compositions that are largely similar to those of their host stars (analogous to binary star formation), although it has been shown that disk structures can result in local enhancements of solid material that can be incorporated during collapse (Boley et al., 2010; Boley et al., 2011). Alternatively, core accretion (Pollack et al.,

1996; Lambrechts et al., 2012) is expected to produce giant planets with a wide range of C/O and bulk metallicity values. This is because the compositions of the solid and gaseous components of the disk vary as a function of time and location within the disk, and different planets are expected to accrete different quantities of solids versus gas (Oberg et al., 2011; Turrini et al., 2021; Chachan et al., 2023). However, since collapse from instability is more likely to occur early in the disk's lifetime (Boley, 2009), a newly formed planet could still have access to a substantial reservoir of material in the disk. If the planet is able to accrete additional material following initial collapse phase, a range of envelope compositions may be possible for planets formed via disk instability as well. Nonetheless, atmospheric composition could still probe the formation and migration histories of directly-imaged planets and help distinguish between different formation scenarios.

Atmospheric characterization analyses of directly-imaged planets have historically made use of photometric and low-resolution spectroscopic data sets (resolving power $R \sim 20 - 100$), which are compared to grids of self-consistent, one-dimensional radiative-convective equilibrium forward models (e.g. the early studies of the HR 8799 planets: Galicher et al., 2011; Barman et al., 2011; Currie et al., 2011; Marley et al., 2012). These models have relatively limited degrees of freedom, and often produce poor fits to these spectra. More recently, a number of studies have begun to utilize spectral inversion, or atmospheric retrieval, techniques to model the atmospheres of isolated brown dwarfs (Line et al., 2017; Burningham et al., 2017; Burningham et al., 2021; Lueber et al., 2022; Calamari et al., 2022; Hood et al., 2023), directly-imaged companions (Mollière et al., 2020; Ruffio et al., 2021; Wang et al., 2022; Zhang et al., 2023), and brown dwarf companions (Xuan et al., 2022). These atmospheric retrievals can be used to place constraints on the C/O ratios and metallicities of these objects, as well as other physical quantities such as their radii, surface gravities, and cloud properties.

Many of the directly-imaged planets and brown dwarfs examined in the literature lie in a temperature regime where silicates are expected to condense in their upper atmospheres (Marley et al., 2015). The presence of these clouds has a strong effect on the observed shapes of their low-resolution emission spectra (e.g. Burningham et al., 2017). Previous studies have explored a wide range of cloud models with varying degrees of physical motivation and success at reproducing the observed features. They also revealed that low-resolution retrievals often exhibit strong degeneracies between their retrieved cloud properties and other physical parameters,

such as effective temperature and metallicity. For example, a retrieval analysis by Burningham et al. (2017) found that their cloud-free models tended towards isothermal pressure-temperature (P-T) profiles and high metallicities in order to compensate for the effects of clouds. This degeneracy has been noted in many subsequent studies, with a variety of proposed solutions e.g. Piette et al., 2020; Zhang et al., 2023. Lueber et al. (2022) found that their treatment of cloud opacity also resulted in trade-offs with the retrieved surface gravity, and were unable to obtain good constraints on the C/O ratios of many of the brown dwarfs in their sample. On the other hand, Mollière et al. (2020) retrieved a C/O value consistent with solar in their paper on HR 8799 e. This value was independent of the cloud model used and did not correlate with other physical parameters such as the vertical temperature structure.

We can obtain a complementary perspective on the atmospheres of these cloudy objects using high-resolution spectroscopy. At high spectral resolution, the ratios of the line depths of different molecular species can be used to constrain their relative abundances in a way that is less biased by the presence of continuum opacity sources from clouds. Since the cores of absorption lines are emitted higher up in the atmosphere than the continuum flux, high-resolution spectroscopy also allows observers to probe a much broader range of pressures, including pressures that lie above the cloud tops. This can increase the signal-to-noise of molecular detections for cloudy objects (Gandhi et al., 2020; Hood et al., 2020). In their recent study of the brown dwarf companion HD 4747 B, Xuan et al. (2022) found their retrieved abundances from high-resolution spectroscopy were insensitive to their choice of cloud model. Similarly, Wang et al. (2022) performed joint retrievals on low and high-resolution spectroscopy of HR 8799 e and found that while clouds are likely present in this planet's atmosphere, they are located deeper in the atmosphere than where the majority of the flux was emitted, resulting in a minimal effect on their observed spectrum. They obtained good constraints on the C/O, C/H, and O/H ratios, retrieving values that were consistent with other studies of the HR 8799 planets (e.g. Ruffio et al., 2021) and AF Lep b (Zhang et al., 2023).

ROXs 42B b is an ultra-young directly-imaged planetary companion on a wide orbit around a low mass binary star. Its large separation ($\sim$1") from its host stars makes it a favorable target for atmospheric characterization. Its large orbital separation and low-mass binary host make it an interesting case study for formation. In this paper, we perform atmospheric retrievals on low- and high-resolution spectroscopy of the

young companion ROXs 42B b. Bowler et al. (2014) published a medium-resolution spectrum for this object spanning J-, H- and K-bands (1.1 - 2.4 μm), while Bryan et al. (2018) published a high-resolution K-band spectrum. However, neither of these studies sought to interpret these data using atmospheric retrieval modeling. We use the open-source radiative transfer code `petitRADTRANS` (Mollière et al., 2019; Mollière et al., 2020) in order to constrain the properties of ROXs 42B b's atmosphere, including its C/O ratio and metallicity. We compare our constraints from low-resolution only (§2.6), high-resolution only (§2.6), and joint high- and low-resolution retrievals (§2.6) to explore the advantages and disadvantages of each data type in the context of atmospheric characterization. We compare our retrieved abundances for ROXs 42B b to those of its primary, which is an unresolved binary, in §2.7 and discuss implications for the formation of this system.

2.3 System Properties

ROXs 42B is a close binary system[1] in the ρ Ophiuchus star-forming region (Bouvier et al., 1992). A candidate companion was first identified around the binary by Ratzka et al. (2005). The companion was later confirmed by Kraus et al. (2014) and Currie et al. (2014b). Kraus et al. (2014) measured a projected separation of 1.17", which corresponds to a separation of 175 au with the updated distance from Gaia Collaboration (2022). The primary binary, ROXs 42B AB, has a (unresolved) spectral type of M0 and has been identified as a young system based on weak Hα emission, X-ray emission, and possible lithium absorption in its optical spectrum (Bouvier et al., 1992). Isochronal fitting gives an approximate stellar age of $6.8^{+3.4}_{-2.3}$ Myr (Kraus et al., 2014). Models suggest individual component masses of 0.89 ± 0.08 and 0.36 ± 0.04 $M_{\odot}$ (Kraus et al., 2014). The absence of infrared excess in either $W3$ or $W4$ in WISE observations, or a radio emission at 1.3 mm, indicates that this system does not contain a significant protoplanetary disk (Kraus et al., 2014; Daemgen et al., 2017). However, Spitzer observations at 8 μm suggest that the companion, ROXs 42B b has excess infrared emission, and might therefore host a circumplanetary disk despite the lack of accretion signatures (Martinez et al., 2021). ROXs 42B b is closest to a spectral type of L0, but is also observed to have colors much redder than field objects of a similar spectral type, which could be due to

[1]ROXs 42A and ROXs 42C are two nearby stars located within the error circle of the Einstein Observatory which first identified the Rho Ophiuchus X-ray source, ROXs 42 (Montmerle et al., 1983). While ROXs 42C has a similar age to ROXs 42B, it has a very different mass and is widely separated from ROXs 42B, and so is unlikely to be affiliated, while ROXs 42A is likely a field star (Bouvier et al., 1992).

circumstellar dust (Kraus et al., 2014; Daemgen et al., 2017).

Evolutionary model fits to photometry of ROXs 42B b place approximate bounds on its mass of 10 ± 4 M_J for an assumed age between $1 - 5$ Myr (Kraus et al., 2014) using models from Chabrier et al. (2000). In a follow-on study, Bowler et al. (2014) obtained medium-resolution near infrared (NIR) JHK-band spectra of the companion and found that the shape of the H-band flux peak was best-matched by grid models with low surface gravities, consistent with its relatively young age. Published constraints on the effective temperature of this object vary. Values from the photometric study of Currie et al. (2014a) ranged from $1800-2200$ K depending on the models used and whether or not clouds were included. Currie et al. (2014b) fit a low-resolution K-band spectrum from VLT/SINFONI and found a significantly higher effective temperature range of 1800-2600 K, which also varied depending on their treatment of clouds in the grid models. There are currently no published constraints on ROXs 42B b's atmospheric metallicity or C/O ratio, due to the limitations of fits to publicly available grid models (Currie et al., 2014a; Daemgen et al., 2017). Bryan et al. (2018) obtained a high-resolution K-band spectrum for this object and used it to measure a projected rotational velocity of $9.5^{+2.1}_{-2.3}$ km s^{-1}, but this study assumed a solar composition atmosphere. To date, the only published composition constraint for this object is an upper limit on its CO_2 abundance from Daemgen et al. (2017).

There are currently no published composition constraints for the primary, ROXs 42B AB, either. Only a few directly-imaged planet hosts in the literature have measured abundances, e.g. HR 8799 (Wang et al., 2020). In most cases, the retrieved chemical abundances are compared to solar values instead of their stellar value. However, in order to make determinations about the formation mechanisms of the companion, it is necessary to have stellar properties to compare to our retrieved abundances for the companion. In Section 2.7, we fit the optical SNIFS spectrum of the (unresolved) primary ROXs 42B AB from Bowler et al. (2014) using the SPHINX M dwarf model grid from Iyer et al. (2023) to constrain the abundances of the host binary.

2.4 Archival Data Used in This Study

Low-resolution Spectroscopy of ROXs 42B b

Bowler et al. (2014) published a medium resolution (R$\sim$1000) spectrum of ROXs 42B b. The H-band data in this study were taken on UT May 9, 2012 and the J-band data were taken on UT May 14 and July 4, 2012 using ALTAIR, the facility AO

Table 2.1. Summary of the previously derived system parameters and data used in our analysis of ROXs 42B b along with new derived parameters for the host star from this work using the SPHINX model grid from Iyer et al. (2023).

Parameter	Value	Reference
	Primary (ROXs 42B AB)	
RA (J2000)	16 31 15.018	Gaia Collaboration (2022)
Dec (J2000)	-24 32 43.715	Gaia Collaboration (2022)
SpT	M0±1	Bowler et al. (2014)
m_J (mag)	9.91 ± 0.02	Bowler et al. (2014)
m_H (mag)	9.02 ± 0.02	Bowler et al. (2014)
m_{K_s} (mag)	8.67 ± 0.02	Bowler et al. (2014)
$m_{L'}$ (mag)	8.42 ± 0.05	Daemgen et al. (2017)
A_V	$1.7^{+0.9}_{-1.2}$	Bowler et al. (2014)
dist (pc)	$146.447^{+0.6627}_{-0.6627}$	Gaia Collaboration (2022)
Age (Myr)	$6.8^{+3.4}_{-2.3}$	Kraus et al. (2014)
M_1 ($M_\odot$)	0.89 ± 0.08	Kraus et al. (2014)
M_2 ($M_\odot$)	0.36 ± 0.04	Kraus et al. (2014)
T_{eff} (K)	3850 ± 80[a]	Kraus et al. (2014)
binary sep (mas)	≈ 83	Kraus et al. (2014)
flux ratio (ΔK)	≈ 1.1	Kraus et al. (2014)
R_1 ($R_\odot$)	1.51 ± 0.02	This work
R_2 ($R_\odot$)	1.39 ± 0.02	This work
$T_{eff,1}$ (K)	3650 ± 20	This work
$T_{eff,2}$ (K)	2600 ± 20	This work
log g_1 (cgs)	4.12 ± 0.1	This work
log g_2 (cgs)	4.26 ± 0.1	This work
M_1 ([$M_\odot$)	1.12 ± 0.13	This work
M_2 ($M_\odot$)	1.29 ± 0.26	This work
C/O	0.54 ± 0.01	This work
[Fe/H]	−0.30 ± 0.03	This work
A_V	2.1 ± 0.1	This work
	Companion (ROXs 42B b)	
SpT	L1±1	Bowler et al. (2014)
m_J (mag)	16.91 ± 0.11	Kraus et al. (2014)
m_H (mag)	15.88 ± 0.05	Kraus et al. (2014)
m_{K_s} (mag)	15.01 ± 0.06	Kraus et al. (2014)
$m_{L'}$ (mag)	13.97 ± 0.06	Daemgen et al. (2017)
$m_{Br\alpha}$ (mag)	13.90 ± 0.08	Daemgen et al. (2017)
m_{M_s} (mag)	14.01 ± 0.23	Daemgen et al. (2017)
sep (")	1.170	Kraus et al. (2014)
sep (au)	175	Kraus et al. (2014)[b]
M (M_J)	10 ± 4	Kraus et al. (2014)
Age (Myr)	3 ± 2	Bryan et al. (2018)
v sini	$9.5^{+2.1}_{-2.3}$	Bryan et al. (2018)
T_{eff}	1800–2600 K (K-band)	Currie et al. (2014b)
	1950-2000 (photometry)	Currie et al. (2014a)
	1600-2000 K (photometry)	Daemgen et al. (2017)

Note. — a) The reported T_{eff} corresponds to the primary, brighter component in the binary, calculated using the reported K-band flux ratio in Ratzka et al. (2005). b) Calculated using the separation measured by Kraus et al. (2014) and the updated distance from Gaia Collaboration (2022).

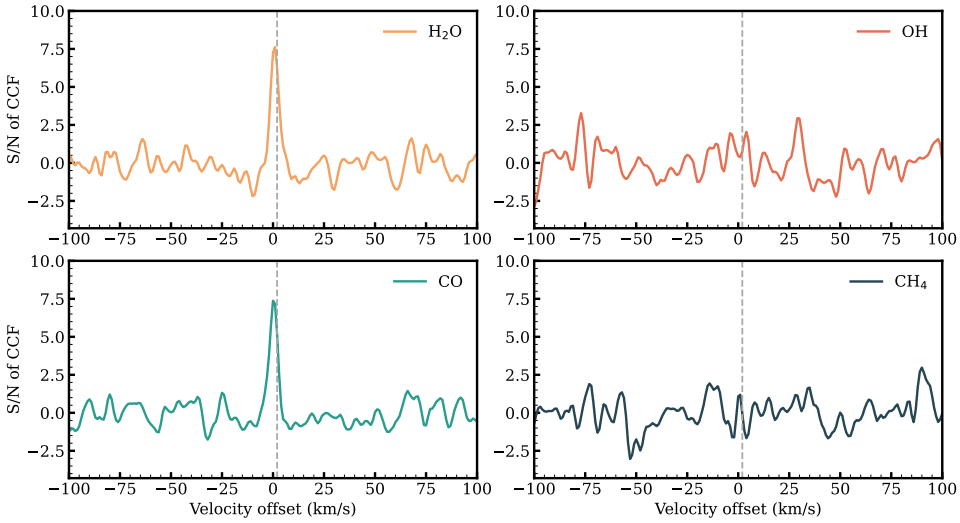

Figure 2.1 Cross-correlation functions (CCFs) showing detections of CO and H_2O using two orders (2.27 – 2.38 μm) from the high-resolution NIRSPEC K-band spectrum. The significance is computed by dividing the CCF by the standard deviation of the out-of-peak baseline.

system, and the Near-Infrared Integral Field Spectrometer (NIFS, McGregor et al., 2003), an image-slicer integral field spectrograph with a resolution of R~5000. The K-band data were taken with the OH-Suppressing Infrared Imaging Spectrograph (OSIRIS, Larkin et al., 2006) on Keck II on UT August 20 2011. The OSIRIS measurements used NGSAO, with an average seeing of $\sim 0.6''$. The data was them binned and smoothed from its original resolution to $R \sim 1000$ to increase signal-to-noise per resolution element. Details about the data reduction can be found in Bowler et al. (2014). In this study, we further binned the data to a resolution of R=300 for the retrievals. This allowed us to use the correlated-k opacities from `petitRADTRANS`, rather than substantially down-sampling the line-by-line opacities, which would result in inaccuracies, and reduce the run times for our retrievals. While medium resolution data has been suggested as a way to overcome the degeneracies of low-resolution data (e.g. Hood et al., 2023), we find that running our retrievals at R~1000 result in unphysical solutions due to low signal-to-noise and opacity sampling. These issues vanish when we bin to slightly lower resolution. We find no substantial differences to our retrieved parameters for a resolution of R~100-600, only a difference in run time. We opt for R~300 to optimize between resolution and run time.

High-resolution Spectroscopy of ROXs 42B b

Bryan et al. (2018) obtained a high-resolution K-band spectrum of ROXs 42B b on UT June 1 and 2, 2015, using the pre-upgrade NIRSPEC instrument (R∼25,000) on Keck II. The target was observed using a 0.041×2.26" slit in adaptive optics (AO) mode in order to minimize blending with the primary star. For ROXs 42B b, both the companion and primary (separation $\sim$ 1.2") were observed simultaneously in the slit, with their light spatially separated on the detector. The host star's spectrum was then used to derive a wavelength solution and telluric correction for the lower signal-to-noise ratio (SNR) planetary data. Details on the observations and data reduction can be found in Bryan et al. (2018). We used two spectral orders spanning $\lambda = 2.27 - 2.38$ μm in our retrieval because they contain absorption lines from both water and CO, including two strong CO bandheads. The other spectral orders had less accurate telluric corrections and wavelength solutions, and we therefore follow the example of Bryan et al. (2018) and exclude them from our analysis.

In Figure 2.1 we show the cross-correlation function for our continuum-normalized, radial velocity-corrected high-resolution spectrum compared to single molecular template spectra. We detect H_2O and CO, which are expected to be the dominant near-infrared absorbers in an atmosphere of this temperature, at greater than 8σ. We do not detect CH_4 or OH, which are predicted to have much lower abundances.

SNIFS Optical Spectrum of ROXs 42B AB

In order to derive an estimate for the abundances of the binary host stars, we use a low-resolution optical spectrum obtained on UT May 20 2012 by the SuperNova Integral Field Spectrograph (SNIFS) at the University of Hawai'i 2.2-m telescope and published in Bowler et al. (2014). SNIFS is an integral field unit with simultaneous coverage of the blue (3000-5200 Å) and red (5200-9500 Å) optical regions at a resolving power of R∼1300. Additional details about the data reduction can be found in Bowler et al. (2014). In this study, we binned the SNIFs optical spectrum to a resolution of R∼100 for comparison with the SPHINX model grid, which has a native resolution of R∼250 (Iyer et al., 2023).

2.5 Atmospheric retrieval setup

We use the retrieval framework implemented in `petitRADTRANS` (Mollière et al., 2019; Mollière et al., 2020) to model our low- and high-resolution spectra. We use a retrieval setup similar to the one described in Mollière et al. (2020), which we describe in more detail below.

Following previous studies (Mollière et al., 2020; Burningham et al., 2017; Xuan et al., 2022, etc.), we assume that the atmosphere of ROXs 42B b is in local chemical equilibrium, with the exception of potential quenched carbon chemistry. We use `petitRADTRANS` to calculate layer-dependent chemical abundances by interpolating tables generated by easyCHEM, a Gibbs Free Energy minimizer (Mollière et al., 2019). We parameterize the bulk chemistry using a C/O ratio and metallicity, [Fe/H], which together set the abundances for all of the individual species. We perform initial fits to test for the potential presence of disequilibrium chemistry by fitting for a carbon quench pressure, which fixes the abundances of carbon monoxide, water, and methane to a constant value at pressures lower than the quench pressure. We find that the quench pressure either tends to very low values or is completely unconstrained, and therefore exclude it from our final fits. This is not surprising, as methane is expected to have a very low abundance throughout ROXs 42B b's atmosphere and it is primarily the measured ratio of CH_4 to CO that constrains the quench pressure when the atmosphere is not in chemical equilibrium (Fortney et al., 2020; Xuan et al., 2022).

Opacities

We use the pre-tabulated correlated-k and line-by-line opacities from `petitRADTRANS` (Mollière et al., 2019) to model our low and high-resolution spectra, respectively. We include opacities from CO, H_2O, FeH, CO_2, OH, H_2S, PH_3, Na, and K in our models. For completeness, we included the opacities of CH_4, HCN, and NH_3 in our initial fits, but found that this had no effect on our retrieved posteriors for either the low- or high-resolution fits. This is not surprising, as these molecules are all predicted to have very low abundances in the relatively hot atmosphere of ROXs 42B b. We find similar results for tests including VO and TiO. We find that the alkali species, Na and K, are particularly important for fitting our low-resolution data, as their absorption wings can affect the continuum shape at the blue edge of J-band. We use the same base line list from the VALD opacity database (Piskunov et al., 1995), and try three different treatments of the wings, including the long wing treatment from Burrows et al. (2003a), custom pressure broadening (for details see Mollière et al., 2019) and a Lorentz profile (Schweitzer et al., 1996), to quantify the effect of this choice on our retrieved abundances. We found that the differences were negligible and used the custom pressure broadening in our final fits. To cut down on computation time for our high-resolution retrievals, we down-sampled our opacities by a factor of 4 (native resolution of 10^6, new resolution of R=250,000).

Table 2.2. A summary table of all fitted parameters in our high-resolution (HR) and low-resolution (LR) `petitRADTRANS` retrievals and our adopted priors. The parameters for each of our two cloud models are detailed in separate sections. In the third column we note whether each parameter is used for our high-resolution (HR) or low-resolution (LR) retrievals. All parameters are used in our joint retrievals.

Parameter	Prior	Description	Retrieval
R_P	$\mathcal{U}$(1, 3) R_J	planet radius in Jupiter radii	LR
log g	$\mathcal{U}$(2, 5.5)	log of the planet surface gravity	LR,HR
$v \sin i$	$\mathcal{U}$(0, 20) km s^{-1}	projected rotational velocity of the planet	HR
rv	$\mathcal{U}$(-10, 10) km s^{-1}	apparent radial velocity of the planet	HR
A_v	$\mathcal{U}$(0, 5)	optical extinction coefficient	LR
b	$\mathcal{U}$	error inflation term	LR,HR
scale K	$\mathcal{U}$(0.9, 1.1)	scale factor for K-band	LR
scale H	$\mathcal{U}$(0.9, 1.1)	scale factor for H-band	LR
		Temperature Model Parameters	
T_1, T_2, T_3	$\mathcal{U}$(0.1, 1)	anchor points for the spline pressure temperature profile (as fractions of adjacent points)	LR,HR
α	$\mathcal{U}$(1, 2)	power law for optical depth model	LR,HR
δ	$\mathcal{U}$(0, 1)	proportionality constant in optical depth model	LR,HR
T_{int}	$\mathcal{U}$(300, 2700) K	interior temperature of planet	LR,HR
		Chemistry Model Parameters	
C/O	$\mathcal{U}$(0.3, 1.5)	C/O ratio of planet atmosphere	LR,HR
[Fe/H]	$\mathcal{U}$(-1.5, 3)	log metallicity of planet atmosphere, relative to solar	LR,HR
$P_{\rm quench}$	$\mathcal{U}$(-6, 2) bars	carbon quench pressure for disequilibrium chemistry model	LR,HR
		Grey Cloud Model Parameters	
κ_0	log-$\mathcal{U}$(-6, 10)	cloud opacity at the cloud base	LR,HR
γ	$\mathcal{U}$(0, 15)	power law for scaling cloud opacity with pressure	LR,HR
P_0	log-$\mathcal{U}$(-6, 2) bars	log pressure of the cloud base in bars	LR,HR
		EddySed Cloud Model Parameters	
$\sigma_{\rm norm}$	$\mathcal{U}$(1.0, 3.0)	width of cloud particle size distribution	LR,HR
f_{sed}	$\mathcal{U}$(0,15)	sedimentation efficiency (for calculating cloud deck parameters)	LR,HR
K_{zz}	log-$\mathcal{U}$(5, 13)	vertical mixing efficiency (for calculating cloud deck parameters)	LR,HR
$X_{species}$	log-$\mathcal{U}$(-4.5,1)	enhancement factor of given cloud species at the cloud base relative to equilibrium abundance (species included: Fe, $MgSiO_3$, Al_2O_3.)	LR,HR

This new resolution is still 10× the resolution of our data. We confirm that this resolution is sufficient for our data by generating synthetic data using `petitRADTRANS` and retrieve at both native and down sampled resolutions. We find no significant differences in the retrieved posterior distributions.

Temperature Structure

We adopt the six-parameter spline pressure-temperature profile from Mollière et al. (2020). This spline profile splits the atmosphere into three layers. The lowest layer of the atmosphere is located beneath the radiative-convective boundary. In this region, the temperature profile is set equal to the moist adiabat corresponding to the assumed atmospheric temperature and composition. The middle layer, which extends from the radiative-convective boundary to the point where the optical depth $\tau = 0.1$, is a radiative photosphere where the temperature structure is set based on the optical depth and the classical Eddington approximation. The uppermost layer begins at $\tau = 0.1$ and extends to a pressure of 10^{-6} bars. In this layer, the temperature is set using a cubic spline anchored by four equidistant points in log(P). This allows for a more complicated temperature structure than is permitted by the Eddington approximation, which forces the temperature at pressures above the photosphere to be isothermal. In our fits we penalize combinations of parameters that result in temperature inversions, which we do not expect to be present given ROXs 42B b's wide orbital separation.

Clouds

Previous studies of isolated brown dwarfs and directly-imaged planets with effective temperatures similar to that of ROXs 42B b have consistently found that clouds are required in order to accurately model their low-resolution spectra (e.g. Burningham et al., 2017; Burningham et al., 2021; Mollière et al., 2020; Lueber et al., 2022). Both Bowler et al. (2014) and Currie et al. (2014a) found evidence for the presence of clouds in the atmosphere of ROXs 42B b when comparing to grid models. Spitzer mid-infrared spectroscopy of isolated brown dwarfs with spectral types similar to that of ROXs 42B b indicate that absorption from silicate grains is ubiquitous in these atmospheres (Suárez et al., 2023). There are many cloud models of varying complexity in the literature, ranging from one parameter opaque cloud decks, to multiple cloud decks of different scale heights, pressure bases, and scattering properties. We consider two different cloud models in our retrievals: a simple, three parameter gray cloud deck, and the more complicated, physically motivated

EddySed cloud model (Ackerman et al., 2001; Mollière et al., 2020).

For our gray cloud model, we consider a simple cloud deck with a wavelength-independent opacity, and parameterize the opacity by the cloud base pressure, P_{base}, the opacity at the cloud base, κ_0, and the pressure scaling power law, γ, as follows:

$$\kappa(P) = \kappa_0 \left(\frac{P}{P_{base}} \right)^{\gamma}. \tag{2.1}$$

In addition to this simple cloud prescription, we also carry out fits using the EddySed cloud model from Ackerman et al. (2001) as implemented in `petitRADTRANS` (Mollière et al., 2020). In this cloud model, the location of the cloud base is set by where the condensation curve of a given cloud species intersects with the atmospheric pressure temperature profile. The vertical extent and number density of the clouds is calculated using parameters representing the vertical mixing, K_{zz}, and the sedimentation efficiency f_{sed}. In addition, we fit for a multiplicative factor which scales the abundance of each cloud species relative to the equilibrium chemistry-predicted value at the cloud base, $X_{species}$.

We use a Mie scattering model to calculate the wavelength-dependent opacity from each cloud species in the EddySed model. We determine which cloud species to include in our model by comparing likely P-T profiles for ROXs 42B b to condensation curves for a wide range of potential cloud species. Based on this, we find that iron (Fe), enstatite ($MgSiO_3$), fosterite (Mg_2SiO_4), quartz (SiO_2), and corundum (Al_2O_3) are all possible cloud species that could condense in the atmosphere of ROXs 42B b. Signatures of silicates clouds have been observed in Spitzer IRS data of similar spectral type brown dwarfs (e.g. Cushing et al., 2006; Burgasser et al., 2008; Burningham et al., 2021). Visscher et al. (2010) predict that the formation of quartz clouds will be repressed in favour of enstatite due to the high abundance of Mg, though this has been shown to not always be true by Burningham et al. (2021), whose retrievals favored enstatite clouds over deeper quartz clouds. On the other hand, Gao et al. (2020) predict that fosterite should be the dominant silicate species to condense from equilibrium chemistry and cloud microphysics. However, the cross sections of quartz, fosterite, and enstatite clouds have a nearly identical slope at near-infrared wavelengths with no unique features to differentiate them (Wakeford et al., 2015), so we choose to focus on enstatite clouds for this study. We explore multiple combinations of cloud species including Al_2O_3, Fe, and $MgSiO_3$, as well as different cloud particle properties (amorphous vs. crystalline) for the solid species in our retrieval, which changes the refractive indices and resulting scattering

cross sections. We find that our choice of amorphous versus crystalline structure has a negligible impact on our retrieved posterior probability distributions, so we use amorphous Mie scattering particles for our final models. This is consistent with model fits to mid-infrared Spitzer IRS spectra of brown dwarfs, which are best reproduced by amorphous silicate cloud particles (Luna et al., 2021; Suárez et al., 2023).

Additional Fit Parameters

We also fit for the surface gravity, parameterized as $\log(g)$. In the low-resolution retrievals, we additionally fit for a flux scaling parameter in order to match the overall flux level. Our high-resolution spectrum is continuum normalized, and so is not sensitive to the absolute flux level. `petitRADTRANS` computes the flux density emitted at the surface of the planet. To obtain the observed flux, we must multiply this quantity by a scale factor:

$$f_{obs} = \left(\frac{R}{d}\right)^2 f_{emit}, \tag{2.2}$$

where R is the object's radius and d is the distance to the system.

We allow for flux offsets between each of our low-resolution spectral bands (two offsets in total with J-band fixed) to account for the fact that they were observed with different instruments at different observational epochs. As this planet is located in a young star forming region, we additionally fit for an optical extinction coefficient, A_V, and correspondingly redden our model spectra to compare with our data. Bowler et al. (2014) calculated a reddening value for the primary binary of $1.7^{+0.9}_{-1.2}$ by comparing the optical SNIFS spectrum to optical templates from Pickles (1998). However, the constraints on this value are asymmetric and wide, and this value was calcuated assuming a single star, so we opt for a wide uniform prior on this value for our fits.

It is possible that the error bars of our data may be under-estimated due to the presence of correlated noise sources. We therefore add a logarithmic error term, b, in quadrature to the reported measurement errors for each spectral bin, such that the effective standard deviation of each point, i, becomes:

$$s_i^2 = \sigma_i^2 + 10^b. \tag{2.3}$$

For retrievals including the high-resolution data, we also include two additional parameters: the radial velocity offset, and the projected rotational velocity, $v\sin i$.

We adopt wide uniform or log-uniform priors for all parameters in our models and impose no restrictions other than excluding combinations of parameters that result in temperature inversions. A summary table of all the parameters included in the retrieval and their priors is shown in Table 2.2.

Nested Sampling

We fit the data using nested sampling as implemented in PyMultiNest, a python wrapper for MultiNest (Feroz et al., 2009). We run our retrievals with 1000 live points, and perform multiple runs using the optimal sampling efficiency for PyMultiNest to compute our evidence and posterior separate. Our "best fit" model is taken to be the sample with the highest likelihood. We compare different models using the Bayes factor, B_{12}, which gives the evidence for model 1 relative to model 2. It is calculated as:

$$B_{12} = \frac{Z_1}{Z_2}, \tag{2.4}$$

where Z is the evidence for each given model as computed by PyMultiNest. The higher the Bayes factor, the stronger the evidence supporting one model over another. We evaluate the Bayes factor for each of our different models relative to our best fit model and list the results in Table 2.3.

2.6 Atmospheric Retrievals

Low-Resolution Retrievals

In this section we describe the results of our retrievals on our low-resolution spectra. We fit our low-resolution data using five different cloud models: a 'clear' model, where there are no clouds present in the visible portion of the atmosphere, a gray cloud model, and three variations of the EddySed cloud model to account for the unknown cloud properties. Our variations of the EddySed cloud model include an iron cloud deck, an enstatite cloud deck, and a combination of iron and silicate clouds, as well as a combination of enstatite and corundum clouds. In Figure 2.3 we show the best fit spectra and residuals for our clear model, the best fitting model. In Figure 2.5 we show the posteriors for a few select parameters from each retrieval, including $\log(g)$, T_{eff}, C/O ratio, and [Fe/H]. The best fit values and 1-sigma uncertainties for key parameters are reported in Table 2.3.

We find that our clear model is preferred at 2.4 sigma over our grey cloud model, and 6.2 sigma from our EddySed cloud model. We find a super-solar metallicity of 1.37 ± 0.13. We also find a super-solar C/O ratio of 0.798 ± 0.019. Our retrieved C/O ratio, [Fe/H], and P-T profile are consistent between our clear, grey, and EddySed

Table 2.3. Best-fit values and confidence intervals for key parameters from ROXs 42B b retrievals.

Cloud Model	C/O	[Fe/H]	Radius (R_{Jup})	$v\sin i$ (kms^{-1})	log(g) (cgs)	$T_{\rm eff}$ (K)	Bayes Factor (σ)
High-Resolution Retrievals							
Clear	0.504 ± 0.048	-0.67 ± 0.35	N/A	10.52 ± 0.92	3.49 ± 0.57	2720 ± 80	1.0
Grey Clouds	0.510 ± 0.047	-0.64 ± 0.31	N/A	10.57 ± 0.83	3.46 ± 0.48	2800 ± 100	0.18 (-2.4σ)
EddySed ($MgSiO_3$ + Fe)	0.510 ± 0.032	-0.69 ± 0.33	N/A	10.35 ± 0.65	3.40 ± 0.45	2750 ± 80	2.8×10^{-8} (-6.2σ)
Low-Resolution Retrievals							
Clear	0.723 ± 0.029	1.37 ± 0.13	2.74 ± 0.06	N/A	3.9 ± 0.2	1890 ± 35	1.0
Grey clouds	0.705 ± 0.031	1.33 ± 0.17	2.78 ± 0.06	N/A	3.70 ± 0.21	1886 ± 36	0.15 (-2.5σ)
Grey clouds + fixed P-T	0.724 ± 0.007	1.37 ± 0.08	2.72 ± 0.05	N/A	3.58 ± 0.11	1876 ± 27	0.37 (-2.0σ)
Grey clouds + fixed P-T, A_V	0.732 ± 0.007	1.11 ± 0.08	2.61 ± 0.03	N/A	3.31 ± 0.06	1834 ± 11	2.1×10^{-9} (-6.6σ)
EddySed ($MgSiO_3$)	0.704 ± 0.033	1.35 ± 0.14	2.77 ± 0.06	N/A	3.79 ± 0.19	1895 ± 39	0.37 (-2.0σ)
EddySed (Fe, am)	0.694 ± 0.035	1.33 ± 0.18	2.78 ± 0.06	N/A	3.78 ± 0.20	1894 ± 34	0.67 (-1.6σ)
EddySed ($MgSiO_3$ + Fe, am)	0.696 ± 0.038	1.34 ± 0.16	2.77 ± 0.06	N/A	3.81 ± 0.20	1898 ± 40	0.034 (-3.1σ)
EddySed ($MgSiO_3$ + AlO_2, am)	0.702 ± 0.032	1.34 ± 0.16	2.78 ± 0.05	N/A	3.74 ± 0.18	1893 ± 38	0.54 (-1.8σ)
Joint Retrievals							
Clear	0.778 ± 0.003	0.37 ± 0.03	2.84 ± 0.02	5.55 ± 0.74	2.76 ± 0.08	1843 ± 22	1.0
Grey clouds	0.734 ± 0.008	0.46 ± 0.04	2.83 ± 0.01	5.57 ± 0.35	2.94 ± 0.05	1935 ± 12	1808 (4.3σ)
EddySed ($MgSiO_3$ + Fe)	0.691 ± 0.004	0.67 ± 0.02	2.81 ± 0.01	10.30 ± 0.35	3.47 ± 0.017	1905 ± 17	44.7 (3.2σ)

Note. — The right most column lists the Bayes factor (B) for each retrieval relative to the clear model ($B = 1$). The uncertainties for each parameter quoted are determined using the 68% confidence interval from our posteriors assuming a Gaussian distribution. For our cloudy models, 'am' stands for amorphous cloud particles + Mie scattering. Our reported Bayes factor are calculated relative to the clear model and then converted to a minimum sigma value using the method described in Benneke et al. (2013).

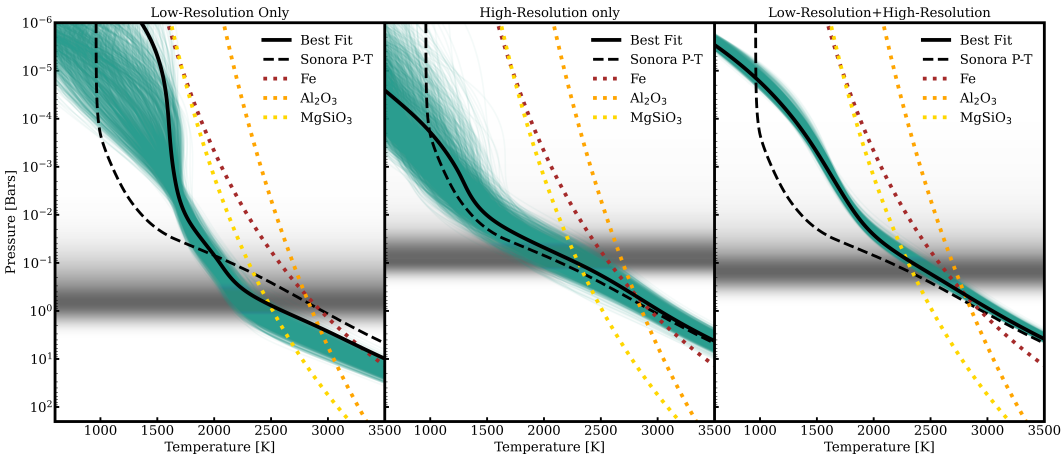

Figure 2.2 Retrieved pressure-temperature (P-T) profiles for our best-fit models (bold in Table 2.3) for our low-resolution data (left), high-resolution data (center), and both combined (right). Randomly sampled P-T curves are plotted in green. Condensation curves for important cloud species in young hot objects, Fe, Al_2O_3, TiO_2, and $MgSiO_3$ are shown for comparison (dotted lines). We overplot a Sonora Bobcat model (Marley et al., 2021a; Marley et al., 2021b) corresponding to the photometrically derived temperature and $\log(g)$. The grey gradient corresponds to the value of the wavelength-integrated flux contribution function.

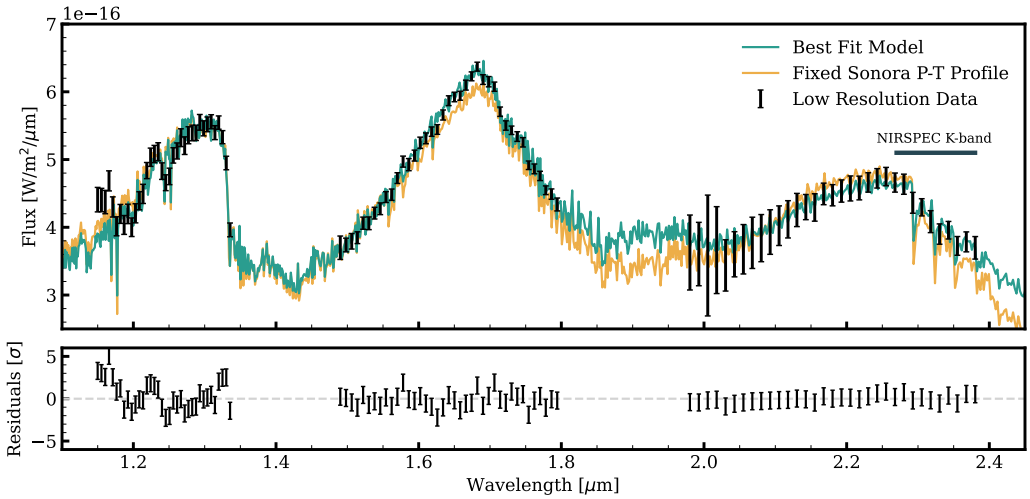

Figure 2.3 Retrieved best-fit model (green) compared to our low-resolution JHK-band spectrum from Bowler et al. (2014) (top panel) and error-weighted residuals (lower panel). Our full low-resolution retrievals are compared to the best fit model (yellow) from our retrievals where our P-T profile is fixed to a Sonora Bobcat P-T profile from (Marley et al., 2021b). The horizontal black line indicates the wavelength coverage of our Keck/NIRSPEC high-resolution K-band data for comparison.

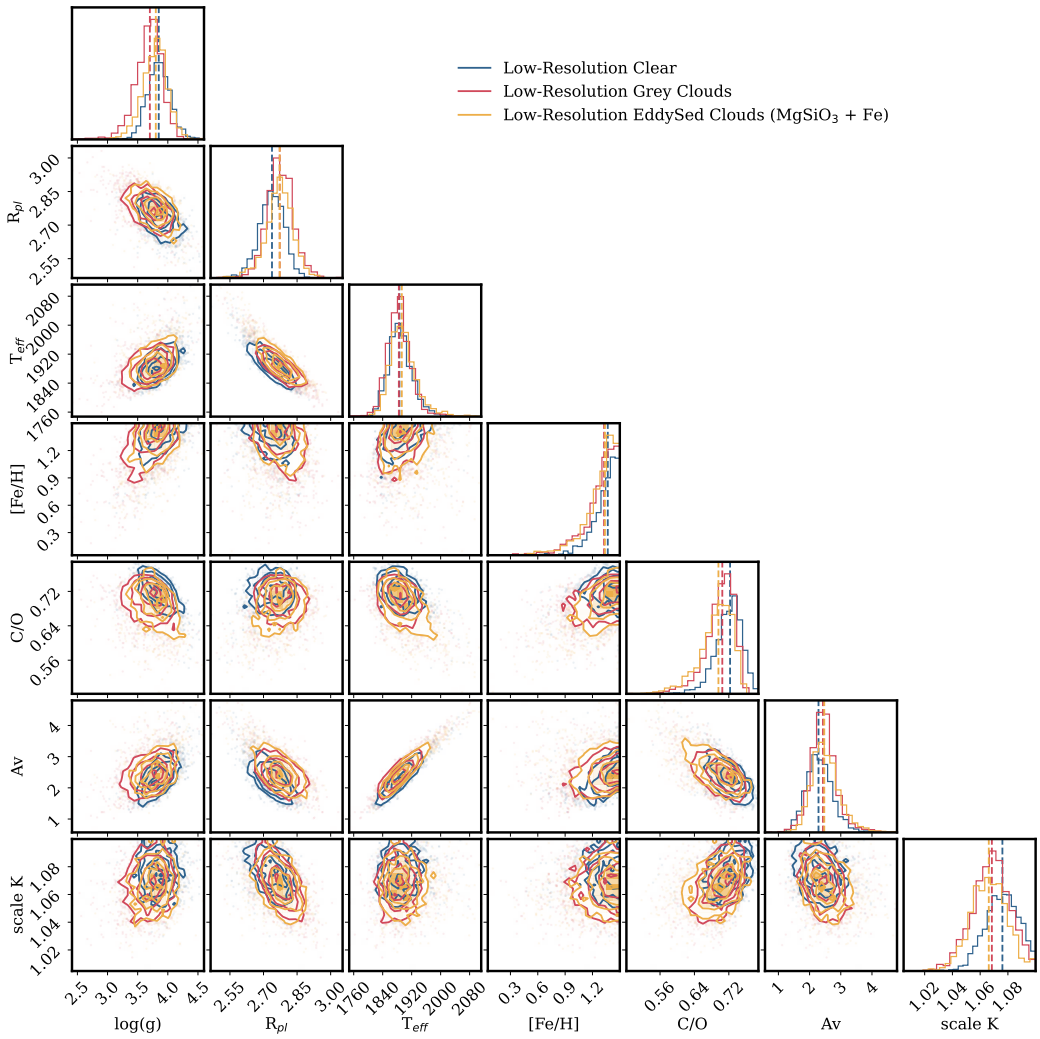

Figure 2.4 Corner plot comparing the posterior probability distributions of key parameters from retrievals on our low-resolution spectrum for our three considered cloud models: a clear sky, a simple gray cloud deck, and EddySed condensate clouds composed of Fe and $MgSiO_3$.

cloud models (Fig. 2.4). When cloud parameters are included in our fits, we find either clouds too deep in the atmosphere to affect the spectrum, or completely unconstrained values, which indicates that clouds are not necessary to reproduce our data, or there is insufficient information to constrain cloud properties.

Even with constraints on the anchor points of our spline P-T profile, our fits strongly prefer an isothermal temperature structure at pressures lower than 1 bar. These kinds of steep, isothermal P-T profiles have been seen in other studies (e.g. Burningham et al., 2017) and are thought to be an attempt to compensate for the effect of

cloud opacity using the flexibility of the P-T profile. While it has been suggested by Tremblin et al. (2017) that the atmospheres of these planets could in fact be isothermal and the observed reddening attributed to clouds could be explained by fingering convection, we find this is unlikely in the case of ROXs 42B b. Given that these objects are internally heated, it is very unlikely that their atmospheres would be isothermal; indeed, radiative equilibrium grid models predict a much steeper temperature profile for ROXs 42B b (e.g. the ATMO and Sonora Bobcat model grids. Phillips et al., 2020; Marley et al., 2021a; Marley et al., 2021b). The changing colors of brown dwarfs as a function of effective temperature, as well as the high frequency of rotational variability near the L-T transition, all provide strong evidence that clouds should be ubiquitous in the atmospheres of objects like ROXs 42B b (Bailer-Jones et al., 1999; Gelino et al., 2002; Marley et al., 2010; Apai et al., 2013; Radigan et al., 2014; Vos et al., 2019).

We also consider fits where we fix the P-T profile to a self-consistent Sonora model (Marley et al., 2021a; Marley et al., 2021b) with $\log(g) = 3.5$ and an effective temperature of 2100 K, matching the spectroscopically and photometrically derived parameters for ROXs 42B b (Currie et al., 2014b; Currie et al., 2014a). With this fixed P-T profile, we find that we are no longer able to adequately fit our low-resolution data using a cloud-free model, as there are no combination of parameters that can reproduce the data. With the P-T profile fixed, we find a smaller radius and T_{eff} than in our free P-T retrieval case, indicating that it is trading off with the radius in an attempt to conserve total luminosity. We additionally find a higher reddening coefficient, indicating the need for extra absorption to match our observed spectrum.

When we include gray clouds in our fixed P-T profile retrievals, we are able to match our low-resolution spectrum nearly as well as the retrievals with the free P-T profile, with the free P-T profile model preferred only slightly at 2σ. We find that the cloud base becomes constrained in the retrievals, but the optical depth of the clouds trades off with the reddening coefficient. We therefore try an additional fit where we fix the reddening value to the value calculated by Bowler et al. (2014) for the primary binary. In Figure 2.5 we compare the posteriors for our fixed P-T profile retrievals to our free P-T profile retrieval using the gray cloud model. We find that with the reddening and P-T profile fixed, cloud opacity becomes important to match our observed spectrum, and the metallicity, $\log(g)$ and planetary radius values all decrease substantially, while the C/O ratio increases only slightly. We conclude that there is a degeneracy between our retrieved chemistry and atmospheric temperature

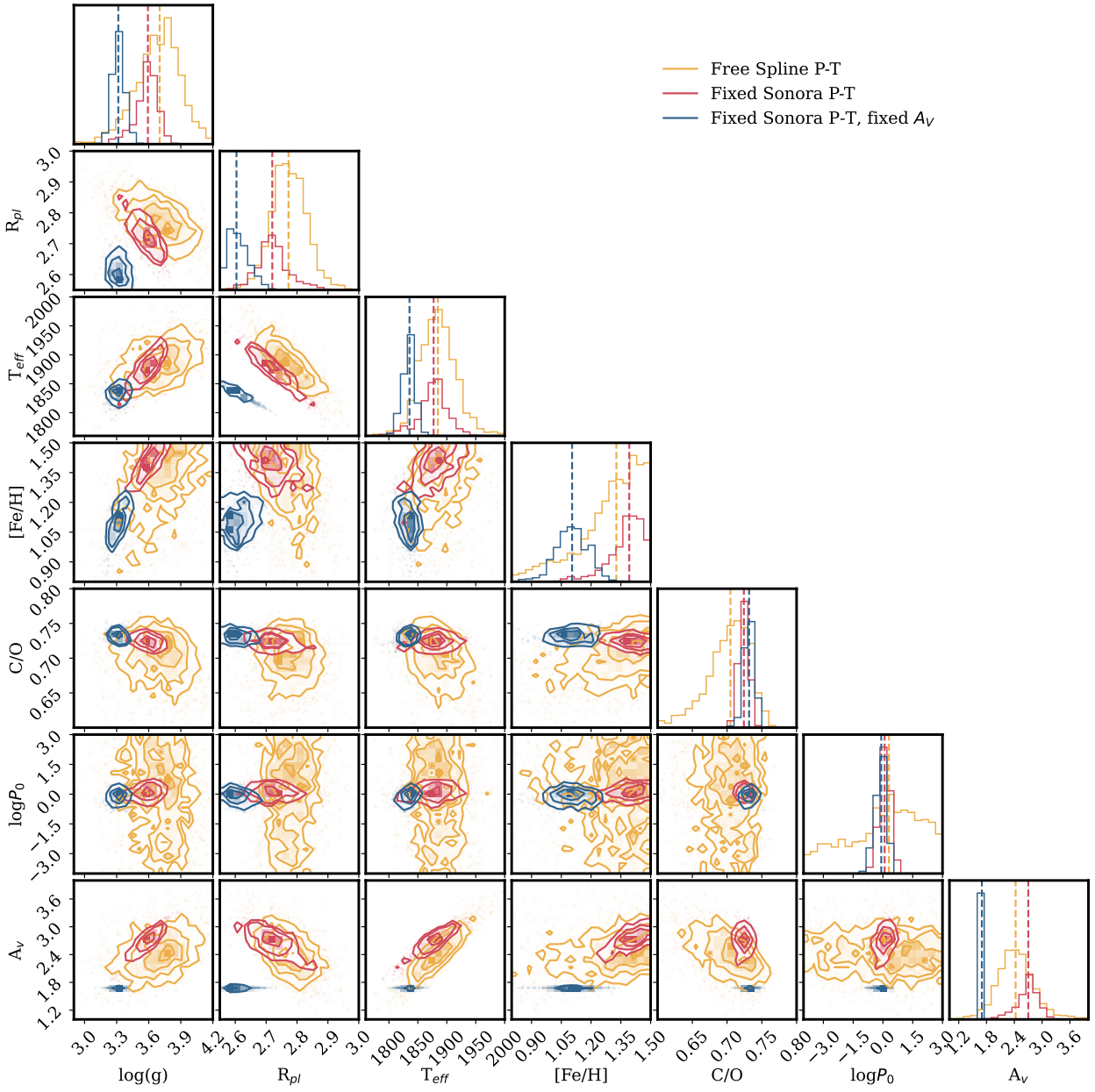

Figure 2.5 Corner plot comparing the posterior probability distributions of key parameters from our fixed and free P-T profile retrievals on our low-resolution spectrum using gray cloud model and a) unrestricted spline pressure-temperature (P-T) profile, b) the P-T profile fixed to a Sonora P-T profile (Marley et al., 2021a; Marley et al., 2021b), and c) a P-T profile fixed to a Sonora model P-T profile and the reddening coefficient fixed to the best fit stellar value from Bowler et al. (2014).

structure. It is most strongly observed to effect our retrieved metallicity. We find that our retrieved metallicity increases or decreases as the slope of our P-T profile changes from more isothermal to less. This makes it evident that the model is using the effects of the P-T profile to account for the effects of cloud on absorption depth, as a more isothermal atmospheres makes it harder to have deep absorption features. The metallicity as a result is driven up to account for the observed absorption features.

To confirm this, we perform similar tests restricting our metallicity to values lower than 0.5. In this case, the P-T structure is less isothermal. We observe the worst fit to occur in the H-band peak, suggesting this driving this degeneracy (Fig. 2.3). Since this feature is also a strong indicator of gravity, we therefore conclude that we cannot trust our retrieved gravity value either. We additionally observe a degeneracy between our optical extinction coefficient, A_V, and the cloud properties. For our free P-T profile retrievals, $A_V = 2.43 \pm 0.41$, and for our fixed P-T profile retrievals, it increases slightly to 2.67 ± 0.25. We find that the retrievals prefer to increase the A_V value rather than add clouds, likely because this involves toggling only a single parameter verses a combination of parameters, as the net effect of silicate clouds is to redden the observed spectrum.

In all versions of the fit, we consistently struggle to fit the J-band data with our models, particularly at the blue edge. This may be related to the extended wings of the Na and K lines. We compare retrievals using three different wing treatments described in §2.5, but are still unable to replicate the observed J-band shape. TiO also has absorption features around 1.2 microns, however we find that even when we include TiO with free abundance, it does not improve the quality of our fit.

Based on the observed degeneracies between various parameters in our low-resolution retrievals, we conclude that our retrieved abundances and other properties are likely unreliable.

High-resolution Retrievals

In this section, we present the results of our retrievals on the high-resolution data and compare with the results from our retrievals using the low-resolution data. We run the same suite of cloud models as we did on our low-resolution data and additionally fit for a projected rotational velocity ($v\sin i$) and a radial velocity (RV) offset. The best-fit values and uncertainties for key parameters including the C/O ratio, [Fe/H], $v\sin i$, $\log(g)$ and T_{eff} are listed in Table 2.3.

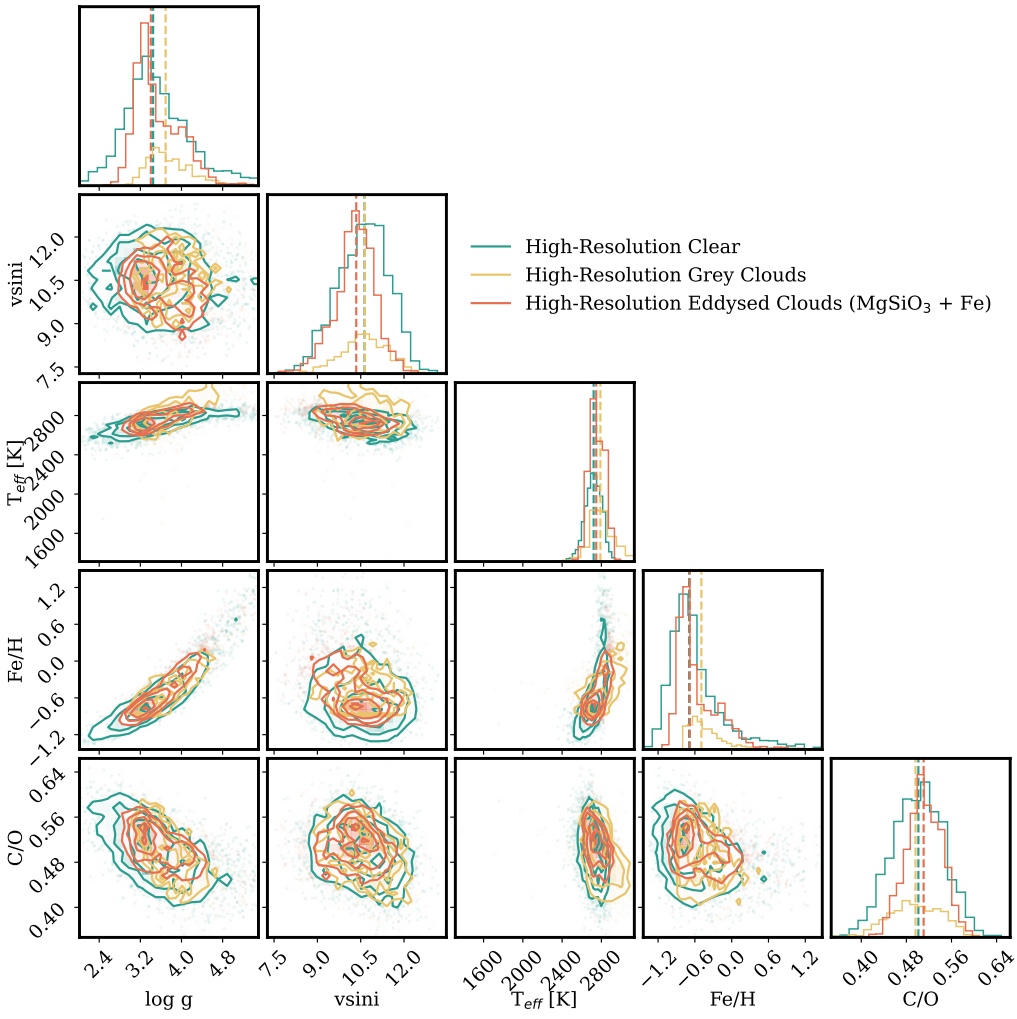

Figure 2.6 Corner plot comparing the posterior probability distributions of key parameters from retrievals on our high-resolution spectrum for three different cloud models: a clear sky, a simple gray cloud deck, and EddySed condensate clouds composed of Fe and $MgSiO_3$. We find identical posterior probability distributions regardless of the cloud model used.

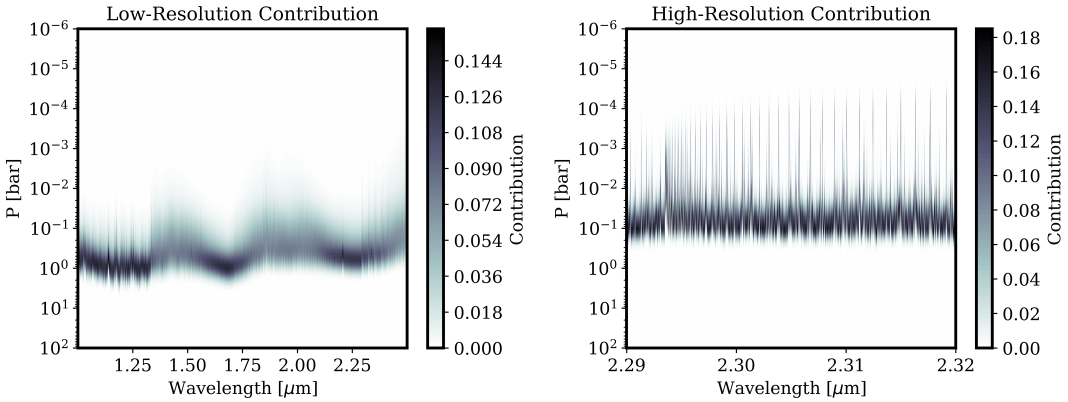

Figure 2.7 Contribution functions for the best-fit models for our low-resolution (left) and high-resolution (right) retrievals.

For our high-resolution data, we also find no difference in the quality of the fit between models with and without clouds. We compare the posteriors for the clear, grey cloud, and EddySed cloud models in Figure 2.6 and find that they all overlap. As a result, the Bayes factor prefers the simpler cloud-free model. Since our inferred parameters are not sensitive to our choice of cloud model, we use the parameters from the cloud-free model moving forward. We retrieve a moderately substellar metallicity of [Fe/H] = -0.67 ± 0.35, rather than the super-stellar metallicity preferred in our low-resolution retrievals. We find a C/O ratio of 0.505 ± 0.05, which is consistent with the solar C/O ratio of 0.59 ± 0.13 (Asplund et al., 2021). We find a radial velocity value $rv = 1.44 \pm 0.42$ kms^{-1}. We additionally constrain the projected spin rate $v\sin i$ to be 10.52 ± 0.92 km s^{-1}, which is in good agreement with the value of $9.5^{+2.1}_{-2.3}$ km s^{-1} found by Bryan et al. (2018) for these same data using a radiative equilibrium model and calculating the autocorrelation function. It is important to note that we utilized the instrumental broadening value reported by Bryan et al. (2018) in our fits rather than re-deriving our own estimate of this parameter; this means that our result is not a fully independent confirmation of the measurement reported in this study.

Unlike with the low-resolution data, the P-T profile in the cloud-free retrieval does not appear to be compensating for the effects of clouds by adopting an isothermal stratosphere. In Fig. 2.2 we show that the shape of our derived P-T profile for cloud free retrieval agrees with predictions from the cloudless Sonora Bobcat forward model grid for an object of the same effective temperature and $\log(g)$ (Marley et al., 2021a; Marley et al., 2021b), though it is possible that the presence of clouds would alter this profile. For models with clouds included, we find that the cloud parameters

are unconstrained. This indicates that our high-resolution data are not biased in the same way as the low-resolution retrievals by the presence of clouds, and are instead relatively unaffected by the presence of clouds.

In order to investigate why our high-resolution retrievals do not appear to be biased by the presence of clouds the same way our low-resolution retrievals are, we examine where the flux originates in our atmosphere relative to the expected positions of cloud layers. In Fig. 2.7 we plot the flux contribution functions for our best-fit models for our high-resolution and low-resolution retrievals. In the low-resolution retrievals, we see that the flux primarily originals at pressures greater than 10^{-1} bars, with some smearing out to lower pressures in the strong water features. For our high-resolution data, a substantial portion of the flux is emitted higher in the atmosphere, in the cores of individual lines. In Fig. 2.2, we show the contribution compared to our P-T profiles and condensation curves. We see that the intersection between the P-T profiles and condensation curves occurs deeper than where the flux contribution peaks in our high-resolution data. Based on this, it seems that the high-resolution data is less sensitive to clouds because the cores of the absorption lines probe higher in the atmosphere, above the clouds. In other words, the wavelength-averaged contribution function for our high-resolution data lies above the predicted cloud base for all three cloud species considered here (see Fig. 2.2). While the continuum is probably still affected by clouds, we lose continuum information in our data analysis. Larger wavelength coverage out to other bands, or flux calibrated high-resolution data should improve the sensitivity of high-resolution data to cloud properties.

Joint Retrievals

In addition to fitting both our high-resolution and low-resolution data sets for ROXs 42B b individually, we fit both together in a joint retrieval. As with the individual retrievals, we consider all three types of cloud model, and fit for all the parameters shown in Table 2.2. We show a subset of our retrieved values for these retrievals in Table 2.3 and the full posteriors are shown in Fig 2.8.

In this joint fit, we find a lower metallicity and better constrained cloud properties for both our gray clouds and EddySed models, which were unconstrained in the fits using only the low-resolution data. We additionally find that our retrieved parameters depend strongly on the cloud model used. Like in other retrievals, we observe a trade-off between retrieved radius and T_{eff}, which is expected as those

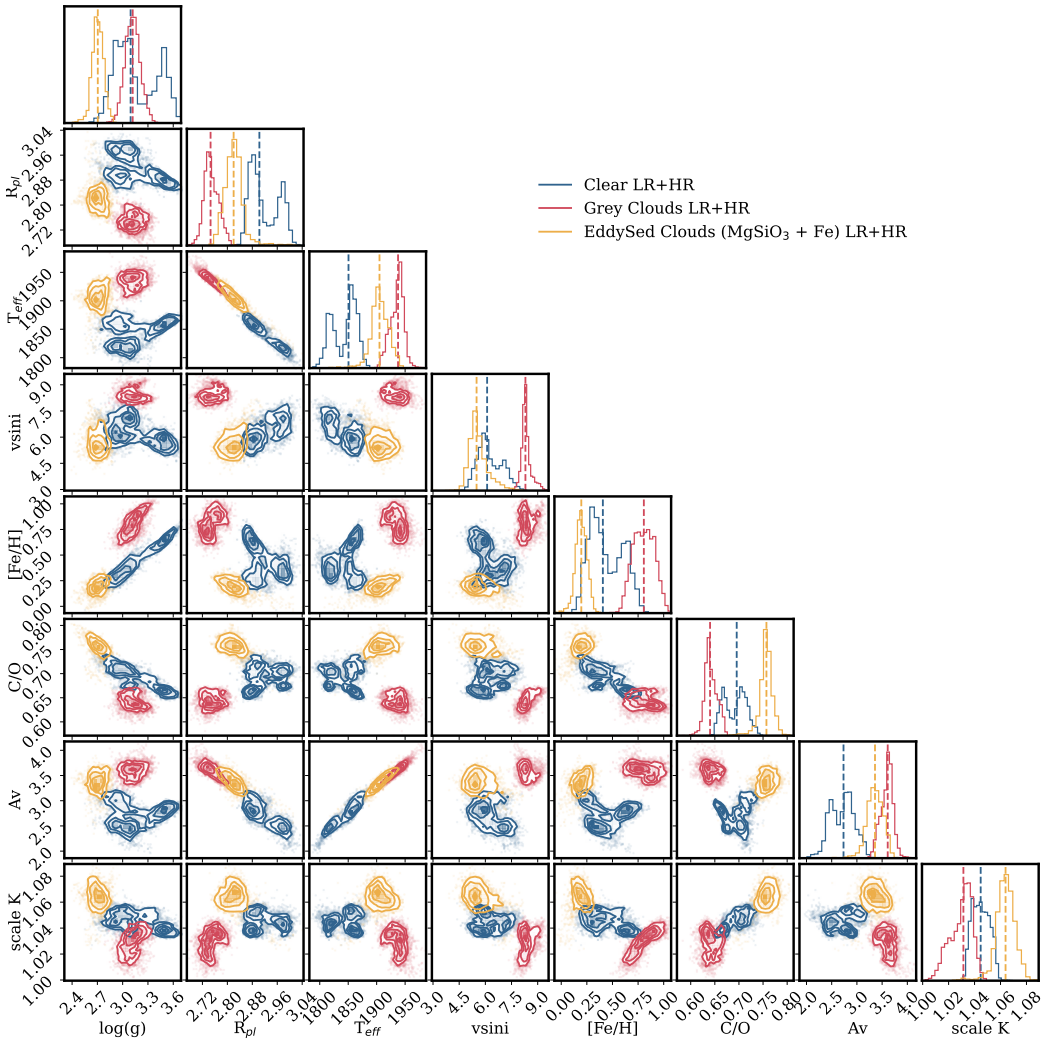

Figure 2.8 Corner plot comparing the posterior probability distributions of key parameters from joint retrievals on our low-resolution and high-resolution data sets for our three considered cloud models: a clear sky, a simple gray cloud deck, and EddySed condensate clouds composed of Fe and $MgSiO_3$.

parameters together determine the total luminosity of the planet. For our cloud-free case, we find a multi-modal posterior, and that it is disfavored over either of our cloudy models.

We find that the addition of the high-resolution data forces the model P-T profiles to be less isothermal than the low-resolution data alone. As discussed in §2.6, it is highly unlikely for clouds not to be present in the atmosphere of a young hot object like ROXs 42B b, and more likely degeneracies in our models that resulted in our low-resolution retrievals favoring cloud free models. As a result, the Bayes factor

strongly favors cloudy models, as cloud free models cannot provide a good match to both the shape of the low- and high-resolution spectra. Likely because it has fewer degrees of freedom and due to the lack of strong cloud features in the considered wavelength range, we find that our grey cloud model is preferred from the Bayes factor.

In the third panel of Fig. 2.2, we show our retrieved P-T profile for our preferred model. We find our P-T profile is consistent in the deep atmosphere with our high-resolution retrievals, but prefers a hotter upper atmosphere than the high-resolution retrievals alone. Our retrieved value for $v\sin i$ is also sensitive to our choice of cloud model in the joint fits. This is concerning, as the low resolution data do not contain any additional information about this parameter. For our EddySed cloud model, our retrieved value agrees with our high-resolution only retrievals and the value from Bryan et al. (2018), while the clear and grey cloud models find a lower value. This suggests that the need to match both data sets simultaneously alters the preferred solution in a way that biases our measurement of $v\sin i$ away from the true value.

In Fig. 2.9 we compared our retrieved cloud opacity for our retrievals on our low-resolution data only (dashed lines), and our joint retrievals (solid lines) for both our grey cloud models (green) and our EddySed cloud models (orange). We find that when we fit just the low-resolution data, the clouds are forced deep into the atmosphere where they do not affect the spectrum, while the P-T profile becomes isothermal to compensate for their effect (Fig. 2.2). When we jointly fit the low and high-resolution data, clouds are required to produce the observed absorption features of the high-resolution data and the shape of the low-resolution spectrum, forcing them into the visible region of the atmosphere.

Given the strong dependence of cloud model on our retrieved abundances and planet properties, we decide to adopt the parameters from our high-resolution-only retrieval for subsequent analysis.

2.7 Host Star Abundances

We fit for host star abundances by performing a 'grid-retrieval' where we interpolate the SPHINX model grid from Iyer et al. (2023). The SPHINX model grid spans the relevant parameter space for M-type stars in T_{eff} (2000 – 4000 K), gravity ($\log(g)$ between 4 – 5.5), C/O (0.3 – 0.9), and metallicity ($\log(Z)$ between -1.0 – 1.0). The SNIFS optical spectrum (see §2.4) contains the blended light from both binary components, so we model the spectrum as the sum of the flux contributions from

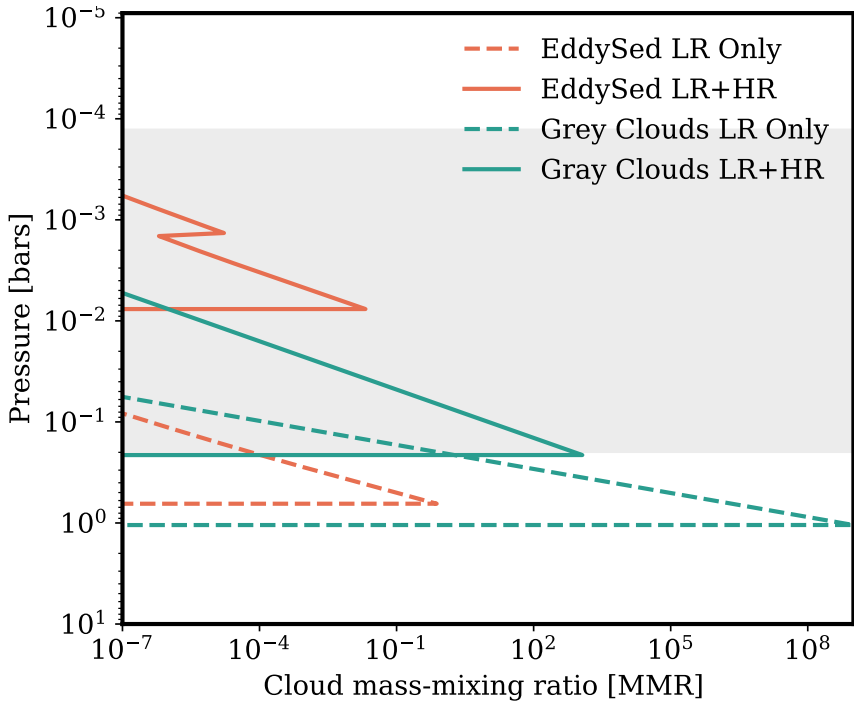

Figure 2.9 The retrieved cloud opacity for our EddySed cloud model (orange), compared with the retrieved cloud opacity for our grey slab cloud model (green) as a function of pressure, for our low-resolution only fits (dashed lines) and our joint high-resolution and low-resolution fits (solid lines). The grey shaded region represents the region of the atmosphere where the total contribution to flux is greater than 0.01%. For both cloud models we see that in the low-resolution only case, the clouds are placed deep in the atmosphere where they have minimal impact on the flux, and the inclusion of the high-resolution data requires the presence of clouds to explain the observed data.

each binary member. We then fit for the stellar radius, R_*, effective temperature, T_{eff}, and surface gravity, $\log(g)$ of each binary component. At each step in the fit, we scale our models to our flux calibrated spectrum using the Gaia measured distance of our system (146.447 Gaia Collaboration, 2022) and our stellar radii (see Table 2.1). We place a uniform prior of $0.5 - 3.5$ on the binary flux ratio based on the K-band ratio reported by Kraus et al. (2014).

We assume that both components of the binary share a single C/O ratio and bulk metallicity. Published studies have found that the metallicities of wide separation binaries can differ by up to $0.03 - 0.1$ dex, but this decreases with decreasing binary separation (e.g. Hawkins et al., 2020; Behmard et al., 2023). In this case, the binary components are only separated by $\sim$10 au (83 mas) (Kraus et al., 2014), and any differences in composition are therefore likely to be smaller than our measurement

errors. We additionally fit for an optical extinction coefficient, A_V, to account for extinction from dust and gas in the star forming complex. We also include an error inflation term as defined in Eq. 2.3 to allow for the possibility of data-model mismatches. Iyer et al. (2023) found that their models differed from the measured spectral shapes more at shorter wavelengths, suggesting that this region may be particularly challenging from a model fitting perspective. We use nested sampling with 1,000 initial live points.

We list the retrieved values for each component of the binary in Table 2.1. We obtain an optical extinction coefficient of $A_V = 1.4 \pm 0.1$, which is consistent with the value reported by Bowler et al. (2014). Our retrieved stellar radii are 1.42 ± 0.01 $R_\odot$ and 1.59 ± 0.02 $R_\odot$. Both of these values are consistent with predictions from the BHAC15 evolutionary model grids for low mass stars at the approximate age of these system (Baraffe et al., 2015) using the measured masses of the binary components from Kraus et al. (2014). However, when we invert our posteriors for our $\log(g)$ and radius, we find mass values of $M_1 = 1.12 \pm 0.13$ $M_\odot$ and $M_2 = 1.29 \pm 0.26$ $M_\odot$. While the mass of the more massive component is consistent within 2 σ, the less massive component is inconsistent at 3.5σ. This could be potentially due to flux calibration errors, a slightly incorrect distance, or slight issues with the models leading to an incorrect radius. Alternatively, since this is a very young system, activity of the stars could be contributing.

We note the disagreement between our models and data from 7000 - 9000 nm. This could be due to contamination from the strong telluric bands present at these wavelengths, missing opacity in the model, or interpolation errors from the limited grid resolution. Regardless, we overall find a decently good fit to our data, with values that match predictions for this system.

2.8 Discussion

Properties of the ROXs 42B System

We retrieve a C/O ratio of 0.50 ± 0.05 for ROXs 42B b from our high-resolution fits, in good agreement with the measured C/O ratio of 0.54 ± 0.01 for its host binary, ROXs 42B A+B. We find a similarly consistent sub-solar metallicity of -0.67 ± 0.35 for the planet and -0.30 ± 0.03 for the host binary, respectively, although we note that our value for the planet is poorly constrained in the high-resolution retrieval. Our retrieved metallicity for the host binary is in good agreement with the small number of published metallicity measurements for other stellar members of ρ-Ophuchius

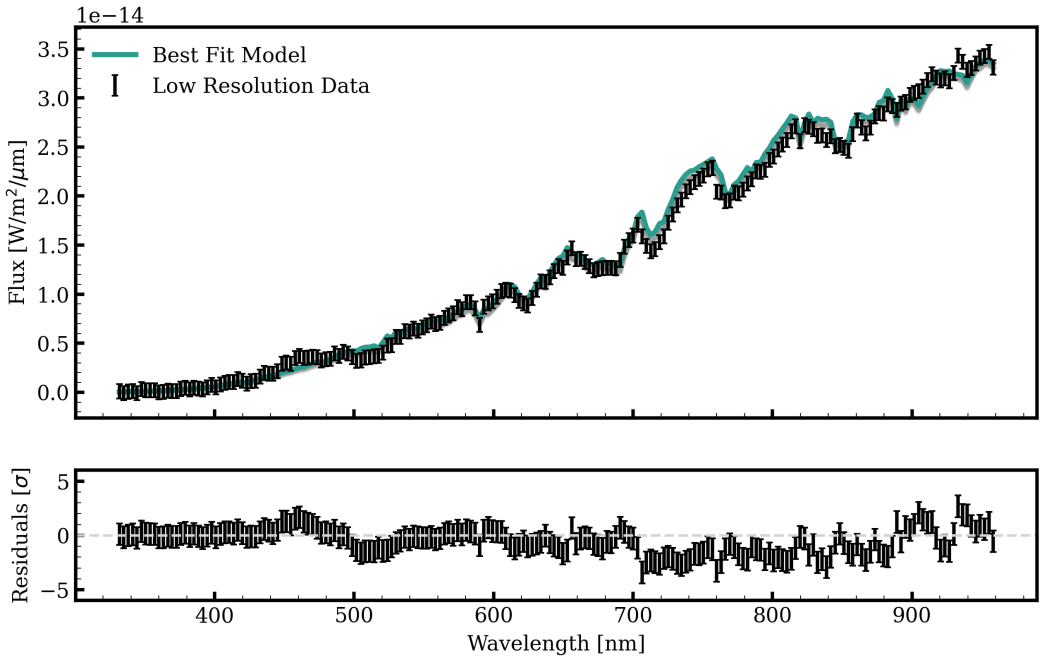

Figure 2.10 Best fit model to the SNIFS optical spectrum of the unresolved binary ROXs 42B (top panel) and error-weighted residuals (lower panel). The best fit model is shown in green, with random drawn samples shown in gray.

complex, which range from [Fe/H]= −0.3 to +0.05 (Spina et al., 2017). Other young star forming regions with more extensive metallicity measurements span a similar range of values (Spina et al., 2017). The fact that the primary in this system is a close binary is also consistent with a metallicity on the low end of this range. Both surveys and simulations of star formation have shown that the frequency of close binaries increases with decreasing stellar metallicity (Moe et al., 2019; Bate, 2019; Moe et al., 2021).

We next consider whether or not our inferred mass and radius for ROXs 42B b are consistent with the predictions of evolutionary models. Our high-resolution retrievals give a $\log(g)$ value of 3.49 ± 0.48 which is consistent with model predictions for an object of this age and mass, as well as previously published gravity values for ROXs 42B b, which were derived by matching its photometry with spectroscopic model grids sampling effective temperature and $\log(g)$. As discussed earlier, our high-resolution data are continuum normalized and therefore do not constrain the planet radius, which is derived from the overall luminosity. If we take the retrieved $\log(g)$ and radius from our low-resolution fits and use them to calculate a mass we find a value of $M_p = 16^{+11}_{-7}$ M_J for our free P-T profile retrievals, and $M_p = 6.5^{+1.6}_{-0.3}$

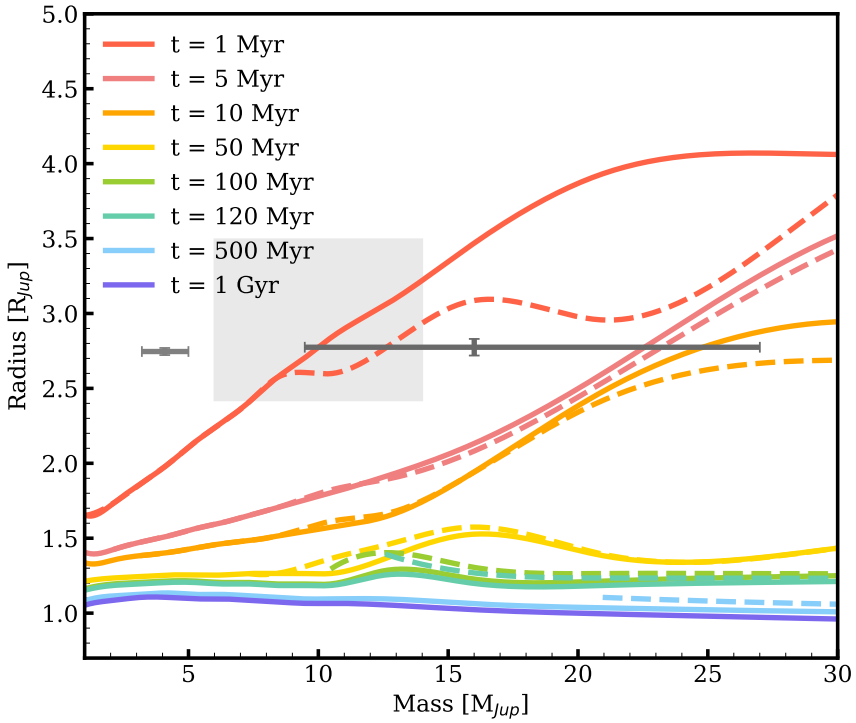

Figure 2.11 Radius as a function of mass at multiple epochs from multiple evolution model grids: the COND model grid (solid lines) and the DUSTY model grid from Allard et al. (2001) (dashed lines). The grey box represents the photometry-derived mass and radius from previous studies (Currie et al., 2014a; Daemgen et al., 2017). The grey point on the left is calculated using the radius and log(g) values from our joint retrieval. The dark grey point on the right is calculated using the radius and log(g) values from our low-resolution only retrieval.

M$_J$ for our fixed P-T and A_V retrievals. When we include our high-resolution data in the joint retrievals, this value becomes significantly smaller and more precise at $M_p = 4.1^{+0.9}_{-0.9}$ M$_J$. We compare this mass and radius to predictions from the COND and DUSTY evolutionary model grids in Figure 2.11. As a member of the ρ-Ophiucus complex, ROXs 42B has an estimated age between 1-5 Myr (Kraus et al., 2014). We therefore expect the radius of ROXs 42B b to be significantly larger than that of older objects with equivalent masses. We find our low-resolution retrievals give results consistent with previous studies and evolutionary model grids, while our joint retrievals give a mass and radius that imply a planet even younger than 1 Myr. It is possible that this object is younger than 1 Myr, as planet formation can take several Myr; thus the age of the companion may be younger than the isochronal age derived for stellar members of ρ-Ophiuchus. However, given the degeneracies and issues discussed above in both these retrievals, and their consequences on the retrieved radii, we cannot be sure either value reflects the true properties of this

system.

Constraints on Formation and Migration History

There have been multiple studies of directly-imaged companions that have attempted to leverage their atmospheric compositions to constrain their formation and migration histories. Whiteford et al. (2023) found a super-solar C/O ratio of $0.97^{+0.09}_{-0.2}$, and a poorly constrained, but broadly consistent with solar, metallicity of [Fe/H] = $-0.04^{+0.95}_{-0.49}$ for 51 Eri b (Macintosh et al., 2015), but note possible degeneracies with clouds in their models. Brown-Sevilla et al. (2023) reported a sub-solar C/O = 0.38 ± 0.09 and a metallicity [Fe/H] = 0.26 ± 0.30 for this same planet, which they argue is evidence in favor of formation via core accretion. However, their argument assumes that the host star has a solar C/O ratio.

The planets in the HR 8799 system are considered strong candidates for formation via gravitational instability, as it is difficult to produce four relatively massive planets around a low metallicity star via core accretion unless it hosted an unusually large protoplanetary disk (Mollière et al., 2020; Ruffio et al., 2021; Wang et al., 2020). Atmospheric retrievals of HR 8799 e by Mollière et al. (2020) and HR 8799 b,c,d (Ruffio et al., 2021) found that all of the planets in this system have C/O ratios consistent with the stellar value (Wang et al., 2020), in agreement with expectations for formation via disk instability. Ruffio et al. (2021) did not fit for metallicity for HR 8799 b,c,d, but found that solar metallicity templates were consistent with their data. HR 8799 is a λ Boötis type star, with a highly sub-solar iron abundance of [Fe/H] = $-0.65^{+0.02}_{-0.01}$ (Swastik et al., 2021), and C/H and O/H ratios consistent with solar values (Wang et al., 2020). Retrievals by Mollière et al. (2020) find a moderate metallicity enhancement of $0.48^{+0.25}_{-0.29}$ for HR 8799 e, the inner planet of this system, which has a similar orbital distance to 51 Eri b at 16 au. There is evidence that the recently discovered AF Lep b (Franson et al., 2023; De Rosa et al., 2023; Mesa et al., 2023), orbiting at around only 9 au, has a substantial metal enrichment ([Fe/H] > 1) relative to its host star ([Fe/H] = -0.27 ± 0.31), indicating substantial planetismal accretion, consistent with the observed debris disk around the star (Zhang et al., 2023).

Our results indicate that ROXs 42B b's C/O ratio and metallicity are also consistent with the stellar value, suggesting that it may share the same formation mechanism as the outer planets of the HR 8799 system. ROXs 42B b orbits at a distance much greater than any of the HR 8799 planets, which are all within 70 au. The CO ice

line for an A type star like HR 8799 could lie anywhere between ~50-hundreds of au depending on the disk properties (Oberg et al., 2011; Qi et al., 2015; Ruffio et al., 2021), so it is possible the planets in this system could have formed beyond it and then migrated inward afterward.

While it is often assumed that stellar C/O ratios are more likely when planets form via gravitational instability, there is one important caveat to this picture. At large separations where virtually all of the carbon- and oxygen-bearing species have condensed out into solids, the solid component of the gas will have a roughly solar C/O ratio. The gas in this region will be metal-poor, with a C/O ratio of ~1 due to a small amount of residual CO in the gas phase. As a result, planets formed in this region should have stellar C/O ratios as long as they accrete any amount of solids, whether they form from core accretion or disk instability (Turrini et al., 2021; Chachan et al., 2023). In Fig. 2.12 we show the expected atmospheric C/O ratio for ROXs 42B b as a function of final atmospheric metallicity, and the carbon abundance of the gas accreted, assuming formation beyond the C/O snowline. For our retrieved atmospheric metallicity constraints, we find that non-stellar C/O ratios are possible, but only for much larger than expected C abundances in the gas phase.

Our observations may also be consistent with a scenario in which the planet accreted most of its mass at smaller orbital separations before migrating outward and accreting its uppermost atmospheric layers beyond the CO ice line. If the planet's atmospheric envelope is not well mixed and instead has a layered structure similar to that of Jupiter (Debras et al., 2019; Stevenson, 2020), the observed C/O ratio would only reflect the material accreted towards the end of the planet formation process. It is possible that dynamical interactions with the primary binary during and after formation (e.g. Kozai-Lidov cycles) could have caused ROXs 42B b to migrate outward, akin to the dynamical evolution of a triple star system. In these three body systems, the orbit of the third body is unstable for orbital separations of less than ~3 times the orbital separation of the primary binary (Tokovinin et al., 2020). Using the present day projected binary separation, we find that the orbit of ROXs 42B b would have become unstable if it was located within ~ 30 au of the primary binary; this is well outside the predicted location of the CO ice line. While it is possible that ROXs 42B b formed in-situ at its currently observed location of 140 au (Bryan et al., 2018), the low expected disk surface densities at these large separations make it difficult to form such a massive planet through any formation channel. If it instead formed closer in (but still beyond 30 au) and then migrated outward, this would also be

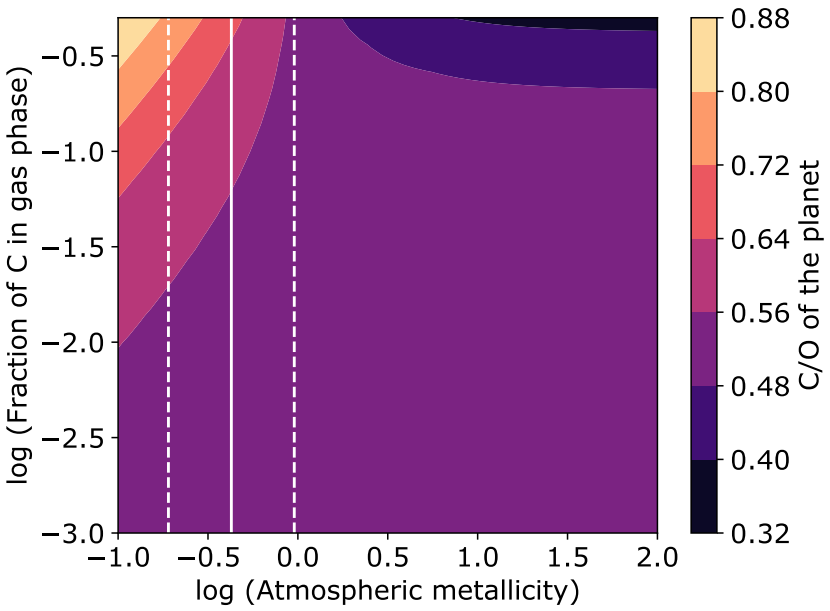

Figure 2.12 Predicted C/O ratio of ROXs 42B b as a function of final atmospheric metallicity and the carbon abundance of the gas accreted by the planet, assuming formation outside the CO snowline. Our derived metallicity constraints from our high-resolution fits are shown as white lines.

consistent with our observed C/O ratio.

The atmospheric metallicities of these objects provide us with complementary constraints on their formation and migration histories. Disk instability should produce planets with stellar compositions, although the presence of pressure bumps and spiral structures (e.g. Boley et al., 2011) can result in localized enhancements or reductions of metals compared to the surrounding nebula. Additionally, disk instabilities are most likely to occur early on, when the disk is more massive. If the protoplanet remains embedded in the disk after its formation, it could accrete additional solids and become enriched in metals. This may be more challenging for relatively massive gas giants like ROXs 42B b, which would need to accrete a significant fraction of the total solid budget of the disk in order to appreciably enhance its atmospheric metallicity (~ 2 M_J of solids for 10× metallicity predicted by our low-resolution retrievals). In the solar system, there is an ongoing debate over how to supply Jupiter with enough solids to produce its relatively modest metallicity of 3× solar (e.g. Shibata et al., 2022). Planets that migrate through the disk are predicted to end up with greater metal enhancements, as both pebble accretion (Humphries et al., 2018) and planetesimal accretion (Shibata et al., 2020; Turrini et al., 2021) become more efficient when the planet moves radially through the disk.

Morbidelli et al. (2023) show that giant planets forming in the inner regions of the disk can incorporate significant quantities of dust into their atmospheres, but this process becomes much less efficient in the outer disk where pressure bumps and gaps cut off the supply of pebbles to the giant planet.

Our retrieved metallicity for ROXs 42B b is both subsolar and slightly sub-stellar, consistent with expectations for in situ formation via gravitational instability. Low metallicity gas cools more quickly due to the lower gas opacity, and low metallicity disks are therefore more likely to fragment (Moe et al., 2019). Given the small (~10 au) orbital separation of the primary binary (Kraus et al., 2014), it is likely that the host stars formed via disk fragmentation. This would mean that either the original disk was fairly massive or that it had high stellar accretion rates in order to produce two separate fragmentation events that formed massive companions (Tokovinin et al., 2020). However, gas in the outer disk is also expected to be metal-poor due to the condensation of most carbon- and oxygen-bearing species, and our observations could therefore also be explained by accretion of metal-poor gas onto a solid core located in the outer disk. Because small solids tend to migrate inward over time, there might be relatively little solid mass left in the outer disk by the time the planet was accreting the outermost layers of its envelope.

It is also possible that rather than forming from within the circumstellar disk, ROXs 42B b could have form via turbulent fragmentation during the initial cloud collapse stage, making it analogous to wide binary stars. In this case, it is more surprising that it would have a composition similar to its host star, as wide binaries have been observed to have larger chemical variations (e.g. Hawkins et al., 2020; Behmard et al., 2023), but not inconsistent with this formation mechanism. However, given the very low mass of this companion, this is a less likely scenario as cloud collapse events occur when there is a significant gas reservoir, meaning that wide companions with extreme mass ratios are rare (Fisher, 2004).

Lastly, we consider whether our retrieved radius for ROXs 42B b might provide additional constraints on its formation mechanism. The amount of internal energy at formation is determined by the rate at which the planet forms. 'Hot start' models assume that the planets form quickly without sufficient time to cool; this is broadly consistent with a process like disk instability, which is expected to occur on relatively short timescales Burrows et al. (2003b) and Marley et al. (2007). On the other hand, 'cold start' models assume a relatively slow formation process, more analogous to core accretion, though core accretion planets could potentially fall in the hot

start regime, given that types of models depend on poorly constrained accretion processes. Both the COND and DUSTY models shown in Fig. 2.11 fall in the hot start regime. We compare our measured mass and radius for ROXs 42B b to the models presented in Spiegel et al. (2012) and find that we are unable to distinguish between these scenarios with the current large uncertainties in the planet mass and system age. For masses on the high end of our allowed range we can still match the planet's measured radius with cold start models, while masses on the lower end of our range are most consistent with hot start models.

2.9 Conclusions

In this paper we present the results of atmospheric retrievals on the young directly-imaged planet ROXs 42B b using low- and high-resolution spectroscopy. We find that our low-resolution spectra are sensitive to the presence of clouds, which are degenerate with the retrieved temperature structure, composition, and radius. We see no sign of this degeneracy in our high-resolution retrievals, which return consistent constraints regardless of our choice of cloud model. We retrieve a C/O ratio of 0.504 ± 0.048 and a subsolar metallicity of -0.67 ± 0.35 for ROXs 42B b using our high-resolution data. We additionally constrain the projected spin rate $v\sin i$ to be 10.52 ± 0.92 km s^{-1}, which is consistent with previous measurements. We conclude that high-resolution retrievals offer a promising avenue for obtaining robust abundance constraints for cloudy objects like ROXs 42B b. Future high-resolution studies of this planet would benefit from broader wavelength coverage, which should provide tighter constraints on cloud properties.

We also derive abundances for the unresolved binary host, ROXs 42B, using low-resolution SNIFS optical spectroscopy and the SPHINX M dwarf model grid from Iyer et al. (2023). We retrieve a C/O ratio of 0.54 ± 0.01 and metallicity of -0.30 ± 0.03 for the binary, which are consistent with our retrieved planetary values within 1σ. This result is consistent with expectations for both disk instability and core accretion models given ROXs 42B b's wide orbital separation, as it likely formed beyond the CO snow line where all major carbon- and oxygen-carrying species have condensed out of the gas phase. However, the low retrieved metallicity of both the host star and planet, as well as the retrieved C/O ratio, is most consistent with formation in the outer disk via gravitational instability. Measurements of the orbital eccentricity or obliquity of ROXs 42B b would provide another dimension that could help to better constrain its origins, as high eccentricities and misaligned obliquities are predicted to be common for planets that form via gravitational instability (Bowler

et al., 2020a; Bryan et al., 2021). While both an eccentricity (Bowler et al., 2020a) and variability measurement (Bowler et al., 2020b) for this system exist, they are both only upper limits. Mapping out the orbit of the primary binary would additionally provide extra information on the geometry of this system.

If we wish to obtain better constraints on the cloud properties of ROXs 42B b, mid infrared coverage with JWST/MIRI (5-16 μm) could provide access to features diagnostic of individual clouds species (Wakeford et al., 2015), including silicate features between 8-10 μm. A direct measurement of this silicate feature could help place tighter constraints on the location and scattering properties of cloud particles in ROXs 42B b's atmosphere, potentially mitigating the cloud-temperature degeneracy in the current near-infrared low-resolution data. Similar features were observed in 2M2224-0158 with Spitzer, which Burningham et al. (2021) were able to reproduce in their models using a combination of silicate and quartz clouds. Absorption features from silicate cloud have also be observed in the companion VHS 1256–1257 b with JWST (Miles et al., 2023). These observations demonstrate the power of mid-infrared observations in constraining clouds in young isolated objects.

Acknowledgements

This research was carried out at the Jet Propulsion Laboratory and the California Institute of Technology under a contract with the National Aeronautics and Space Administration and funded through the President's and Director's Research & Development Fund Program. The computations presented here were conducted in the Resnick High Performance Center, a facility supported by Resnick Sustainability Institute at the California Institute of Technology. Some of the data presented herein were obtained at the W. M. Keck Observatory, which is operated as a scientific partnership among the California Institute of Technology, the University of California and the National Aeronautics and Space Administration. The Observatory was made possible by the generous financial support of the W. M. Keck Foundation. The authors wish to recognize and acknowledge the very significant cultural role and reverence that the summit of Maunakea has always had within the indigenous Hawaiian community. We are most fortunate to have the opportunity to conduct observations from this mountain.

References

Ackerman, Andrew S. and Mark S. Marley (Aug. 2001). "Precipitating Condensation Clouds in Substellar Atmospheres". In: *The Astrophysical Journal* 556.2, p. 872. ISSN: 0004-637X. DOI: 10.1086/321540.

Alibert, Y. et al. (Apr. 2005). "Models of giant planet formation with migration and disc evolution". In: *Astronomy and Astrophysics* 434, pp. 343–353. ISSN: 0004-6361. DOI: 10.1051/0004-6361:20042032.

Allard, France et al. (July 2001). "The Limiting Effects of Dust in Brown Dwarf Model Atmospheres". In: *The Astrophysical Journal* 556.1, p. 357. ISSN: 0004-637X. DOI: 10.1086/321547.

Apai, Dániel et al. (Apr. 2013). "HST Spectral Mapping of L/T Transition Brown Dwarfs Reveals Cloud Thickness Variations". In: *The Astrophysical Journal* 768.2, p. 121. ISSN: 0004-637X. DOI: 10.1088/0004-637X/768/2/121.

Asplund, M., A. M. Amarsi, and N. Grevesse (Sept. 2021). "The chemical make-up of the Sun: A 2020 vision". In: *Astronomy and Astrophysics* 653, A141. ISSN: 0004-6361. DOI: 10.1051/0004-6361/202140445.

Bailer-Jones, C. A. L. and R. Mundt (Aug. 1999). "A search for variability in brown dwarfs and L dwarfs". In: *Astronomy and Astrophysics* 348, pp. 800–804. ISSN: 0004-6361. DOI: 10.48550/arXiv.astro-ph/9906439.

Baraffe, Isabelle et al. (May 2015). "New evolutionary models for pre-main sequence and main sequence low-mass stars down to the hydrogen-burning limit". In: *Astronomy & Astrophysics* 577, A42. ISSN: 0004-6361, 1432-0746. DOI: 10.1051/0004-6361/201425481.

Barman, Travis S. et al. (June 2011). "The Young Planet-Mass Object 2M1207b: a Cool, Cloudy, and Methane-Poor Atmosphere". In: *The Astrophysical Journal Letters* 735.2, p. L39. ISSN: 2041-8205. DOI: 10.1088/2041-8205/735/2/L39.

Bate, Matthew R (Apr. 2019). "The statistical properties of stars and their dependence on metallicity". In: *Monthly Notices of the Royal Astronomical Society* 484.2, pp. 2341–2361. ISSN: 0035-8711. DOI: 10.1093/mnras/stz103.

Behmard, Aida et al. (Mar. 2023). "Planet Engulfment Detections are Rare According to Observations and Stellar Modeling". In: *Monthly Notices of the Royal Astronomical Society* 521.2, pp. 2969–2987. ISSN: 0035-8711, 1365-2966. DOI: 10.1093/mnras/stad745.

Benneke, Björn and Sara Seager (Nov. 2013). "How to Distinguish between Cloudy Mini-Neptunes and Water/Volatile-Dominated Super-Earths". In: *The Astrophysical Journal* 778.2, p. 153. ISSN: 0004-637X, 1538-4357. DOI: 10.1088/0004-637X/778/2/153.

Boley, Aaron C. (Mar. 2009). "The Two Modes of Gas Giant Planet Formation". In: *The Astrophysical Journal* 695.1, p. L53. ISSN: 0004-637X. DOI: 10.1088/0004-637X/695/1/L53.

Boley, Aaron C. and Richard H. Durisen (Nov. 2010). "On the Possibility of Enrichment and Differentiation in Gas Giants During Birth by Disk Instability". In: *The Astrophysical Journal* 724.1, pp. 618–639. ISSN: 0004-637X, 1538-4357. DOI: 10.1088/0004-637X/724/1/618.

Boley, Aaron C., Ravit Helled, and Matthew J. Payne (July 2011). "The Heavy-Element Composition of Disk Instability Planets can Range From Sub- to Super-Nebular". In: *The Astrophysical Journal* 735.1, p. 30. ISSN: 0004-637X, 1538-4357. DOI: 10.1088/0004-637X/735/1/30.

Boss, Alan P. (June 1997). "Giant Planet Formation by Gravitational Instability". In: *Science* 276.5320, pp. 1836–1839. DOI: 10.1126/science.276.5320.1836.

Bouvier, J. and I. Appenzeller (Feb. 1992). "A magnitude-limited spectroscopic and photometric survey of rho OphiuchusX-ray sources." en. In: *Astronomy and Astrophysics Supplement Series* 92, pp. 481–516. ISSN: 0365-0138.

Bowler (Oct. 2016). "Imaging Extrasolar Giant Planets". In: *Publications of the Astronomical Society of the Pacific* 128, p. 102001. ISSN: 0004-6280. DOI: 10.1088/1538-3873/128/968/102001.

Bowler, Blunt, and Nielsen (Jan. 2020a). "Population-level Eccentricity Distributions of Imaged Exoplanets and Brown Dwarf Companions: Dynamical Evidence for Distinct Formation Channels*". In: *The Astronomical Journal* 159.2, p. 63. ISSN: 1538-3881. DOI: 10.3847/1538-3881/ab5b11.

Bowler, Brendan P. et al. (Apr. 2020b). "Strong Near-infrared Spectral Variability of the Young Cloudy L Dwarf Companion VHS J1256-1257 b". In: *The Astrophysical Journal* 893, p. L30. ISSN: 0004-637X. DOI: 10.3847/2041-8213/ab8197.

Bowler, Brendan P. et al. (Apr. 2023). "Rotation Periods, Inclinations, and Obliquities of Cool Stars Hosting Directly Imaged Substellar Companions: Spin-Orbit Misalignments Are Common". In: *The Astronomical Journal* 165, p. 164. ISSN: 0004-6256. DOI: 10.3847/1538-3881/acbd34.

Bowler et al. (Mar. 2014). "Spectroscopic Confirmation of Young Planetary-Mass Companions on Wide Orbits". In: *The Astrophysical Journal* 784.1, p. 65. ISSN: 0004-637X, 1538-4357. DOI: 10.1088/0004-637X/784/1/65.

Brown-Sevilla, S. B. et al. (May 2023). "Revisiting the atmosphere of the exoplanet 51 Eridani b with VLT/SPHERE". In: *Astronomy & Astrophysics* 673, A98. ISSN: 0004-6361, 1432-0746. DOI: 10.1051/0004-6361/202244826.

Bryan, Marta L. et al. (Aug. 2016). "Searching for Scatterers: High-Contrast Imaging of Young Stars Hosting Wide-Separation Planetary-Mass Companions". In: *The Astrophysical Journal* 827.2, p. 100. ISSN: 0004-637X. DOI: 10.3847/0004-637X/827/2/100.

Bryan, Marta L. et al. (Dec. 2018). "Constraints on the spin evolution of young planetary-mass companions". In: *Nature Astronomy* 2, pp. 138–144. ISSN: 2397-3366. DOI: 10.1038/s41550-017-0325-8.

Bryan, Marta L. et al. (Nov. 2021). "Obliquity Constraints on the Planetary-mass Companion HD 106906 b". In: *The Astronomical Journal* 162, p. 217. ISSN: 0004-6256. DOI: 10.3847/1538-3881/ac1bb1.

Burgasser, Adam J. et al. (Feb. 2008). "Clouds, Gravity, and Metallicity in Blue L Dwarfs: The Case of 2MASS J11263991–5003550*". In: *The Astrophysical Journal* 674.1, p. 451. ISSN: 0004-637X. DOI: 10.1086/524726.

Burningham, Ben et al. (Sept. 2017). "Retrieval of atmospheric properties of cloudy L dwarfs". In: *Monthly Notices of the Royal Astronomical Society* 470.1, pp. 1177–1197. ISSN: 0035-8711, 1365-2966. DOI: 10.1093/mnras/stx1246.

Burningham, Ben et al. (July 2021). "Cloud busting: enstatite and quartz clouds in the atmosphere of 2M2224-0158". In: *Monthly Notices of the Royal Astronomical Society* 506.2, pp. 1944–1961. ISSN: 0035-8711, 1365-2966. DOI: 10.1093/mnras/stab1361.

Burrows, Adam and Maxim Volobuyev (Feb. 2003a). "Calculations of the Far-Wing Line Profiles of Sodium and Potassium in the Atmospheres of Substellar-Mass Objects". In: *The Astrophysical Journal* 583, pp. 985–995. ISSN: 0004-637X. DOI: 10.1086/345412.

Burrows, Sudarsky, and Lunine (Oct. 2003b). "Beyond the T Dwarfs: Theoretical Spectra, Colors, and Detectability of the Coolest Brown Dwarfs". In: *The Astrophysical Journal* 596.1, p. 587. ISSN: 0004-637X. DOI: 10.1086/377709.

Calamari et al. (Dec. 2022). "An Atmospheric Retrieval of the Brown Dwarf Gliese 229B". In: *The Astrophysical Journal* 940.2, p. 164. ISSN: 0004-637X. DOI: 10.3847/1538-4357/ac9cc9.

Chabrier et al. (Oct. 2000). "Evolutionary Models for Very Low-Mass Stars and Brown Dwarfs with Dusty Atmospheres". In: *The Astrophysical Journal* 542, pp. 464–472. ISSN: 0004-637X. DOI: 10.1086/309513.

Chachan et al. (Jan. 2023). "Breaking Degeneracies in Formation Histories by Measuring Refractory Content in Gas Giants". en. In: *The Astrophysical Journal* 943.2, p. 112. ISSN: 0004-637X. DOI: 10.3847/1538-4357/aca614.

Cridland, Alex J., Ralph E. Pudritz, and Matthew Alessi (Sept. 2016). "Composition of Early Planetary Atmospheres I: Connecting Disk Astrochemistry to the Formation of Planetary Atmospheres". In: *Monthly Notices of the Royal Astronomical Society* 461.3, pp. 3274–3295. ISSN: 0035-8711, 1365-2966. DOI: 10.1093/mnras/stw1511.

Currie, Thayne, Adam Burrows, and Sebastian Daemgen (May 2014a). "A First-Look Atmospheric Modeling Study of the Young Directly-Imaged Planet-Mass Companion, ROXs 42Bb". In: *The Astrophysical Journal* 787.2, p. 104. ISSN: 0004-637X, 1538-4357. DOI: 10.1088/0004-637X/787/2/104.

Currie, Thayne et al. (Jan. 2014b). "Direct Imaging and Spectroscopy of a Candidate Companion Below/Near the Deuterium-Burning Limit In The Young Binary Star System, ROXs 42B". In: *The Astrophysical Journal* 780.2, p. L30. ISSN: 2041-8205, 2041-8213. DOI: 10.1088/2041-8205/780/2/L30.

Currie, Thayne et al. (Dec. 2022). *Direct Imaging and Spectroscopy of Extrasolar Planets*. arXiv:2205.05696 [astro-ph]. DOI: 10.48550/arXiv.2205.05696.

Currie et al. (Mar. 2011). "A Combined Subaru/VLT/MMT 1-5 m Study of Planets Orbiting HR 8799: Implications for Atmospheric Properties, Masses, and Formation". In: *The Astrophysical Journal* 729, p. 128. ISSN: 0004-637X. DOI: 10.1088/0004-637X/729/2/128.

Cushing, Michael C. et al. (Sept. 2006). "A Spitzer Infrared Spectrograph Spectral Sequence of M, L, and T Dwarfs". In: *The Astrophysical Journal* 648.1, p. 614. ISSN: 0004-637X. DOI: 10.1086/505637.

Daemgen, Sebastian et al. (May 2017). "Mid-infrared characterization of the planetary-mass companion ROXs 42B b". In: *Astronomy & Astrophysics* 601, A65. ISSN: 0004-6361, 1432-0746. DOI: 10.1051/0004-6361/201629949.

De Rosa, Robert J. et al. (Apr. 2023). "Direct imaging discovery of a super-Jovian around the young Sun-like star AF Leporis". In: *Astronomy and Astrophysics* 672, A94. ISSN: 0004-6361. DOI: 10.1051/0004-6361/202345877.

Debras, Florian and Gilles Chabrier (Feb. 2019). "New Models of Jupiter in the Context of Juno and Galileo". In: *The Astrophysical Journal* 872, p. 100. ISSN: 0004-637X. DOI: 10.3847/1538-4357/aaff65.

Feroz, F., M. P. Hobson, and M. Bridges (Oct. 2009). "MultiNest: an efficient and robust Bayesian inference tool for cosmology and particle physics". In: *Monthly Notices of the Royal Astronomical Society* 398.4, pp. 1601–1614. ISSN: 00358711, 13652966. DOI: 10.1111/j.1365-2966.2009.14548.x.

Fisher, Robert T. (Jan. 2004). "A Turbulent Interstellar Medium Origin of the Binary Period Distribution". In: *The Astrophysical Journal* 600.2, p. 769. ISSN: 0004-637X. DOI: 10.1086/380111.

Fortney, Jonathan J. et al. (Nov. 2020). "Beyond Equilibrium Temperature: How the Atmosphere/Interior Connection Affects the Onset of Methane, Ammonia, and Clouds in Warm Transiting Giant Planets". en. In: *The Astronomical Journal* 160.6, p. 288. ISSN: 1538-3881. DOI: 10.3847/1538-3881/abc5bd.

Franson, Kyle et al. (June 2023). "Astrometric Accelerations as Dynamical Beacons: A Giant Planet Imaged inside the Debris Disk of the Young Star AF Lep". In: *The Astrophysical Journal* 950, p. L19. ISSN: 0004-637X. DOI: 10.3847/2041-8213/acd6f6.

Gaia Collaboration (May 2022). "VizieR Online Data Catalog: Gaia DR3 Part 1. Main source (Gaia Collaboration, 2022)". In: *VizieR Online Data Catalog*, pp. I/355.

Galicher, Raphaël et al. (Sept. 2011). "M-Band Imaging of the HR 8799 Planetary System Using an Innovative Loci-Based Background Subtraction Technique". In: *The Astrophysical Journal Letters* 739.2, p. L41. ISSN: 2041-8205. DOI: 10.1088/2041-8205/739/2/L41.

Gandhi, Siddharth, Matteo Brogi, and Rebecca K Webb (Sept. 2020). "Seeing above the clouds with high-resolution spectroscopy". In: *Monthly Notices of the Royal Astronomical Society* 498.1, pp. 194–204. ISSN: 0035-8711. DOI: 10.1093/mnras/staa2424.

Gao, Peter et al. (Oct. 2020). "Aerosol composition of hot giant exoplanets dominated by silicates and hydrocarbon hazes". In: *Nature Astronomy* 4.10, pp. 951–956. ISSN: 2397-3366. DOI: 10.1038/s41550-020-1114-3.

Gelino, Christopher R. et al. (Sept. 2002). "L Dwarf Variability: I-Band Observations". In: *The Astrophysical Journal* 577.1, p. 433. ISSN: 0004-637X. DOI: 10.1086/342150.

Hawkins, Keith et al. (Feb. 2020). "Identical or fraternal twins? : The chemical homogeneity of wide binaries from Gaia DR2". In: *Monthly Notices of the Royal Astronomical Society* 492.1, pp. 1164–1179. ISSN: 0035-8711, 1365-2966. DOI: 10.1093/mnras/stz3132.

Hood, Callie E. et al. (Oct. 2020). "Prospects for Characterizing the Haziest Sub-Neptune Exoplanets with High-resolution Spectroscopy". In: *The Astronomical Journal* 160.5, p. 198. ISSN: 1538-3881. DOI: 10.3847/1538-3881/abb46b.

Hood, Callie E. et al. (Aug. 2023). "Brown Dwarf Retrievals on FIRE!: Atmospheric Constraints and Lessons Learned from High Signal-to-noise Medium-resolution Spectroscopy of a T9 Dwarf". en. In: *The Astrophysical Journal* 953.2, p. 170. ISSN: 0004-637X. DOI: 10.3847/1538-4357/ace32e.

Humphries, R. J. and S. Nayakshin (June 2018). "Changes in the metallicity of gas giant planets due to pebble accretion". In: *Monthly Notices of the Royal Astronomical Society* 477, pp. 593–615. ISSN: 0035-8711. DOI: 10.1093/mnras/sty569.

Iyer, Aishwarya R. et al. (Feb. 2023). "The SPHINX M-dwarf Spectral Grid. I. Benchmarking New Model Atmospheres to Derive Fundamental M-dwarf Properties". In: *The Astrophysical Journal* 944.1, p. 41. ISSN: 0004-637X. DOI: 10.3847/1538-4357/acabc2.

Kraus, Adam L. et al. (Jan. 2014). "Three Wide Planetary-Mass Companions to FW Tau, ROXs 12, and ROXs 42B". In: *The Astrophysical Journal* 781.1, p. 20. ISSN: 0004-637X, 1538-4357. DOI: 10.1088/0004-637X/781/1/20.

Lambrechts, M. and A. Johansen (Aug. 2012). "Rapid growth of gas-giant cores by pebble accretion". In: *Astronomy & Astrophysics* 544, A32. ISSN: 0004-6361, 1432-0746. DOI: 10.1051/0004-6361/201219127.

Larkin, James et al. (June 2006). "OSIRIS: a diffraction limited integral field spectrograph for Keck". In: 6269, 62691A. DOI: 10.1117/12.672061.

Line, Michael R. et al. (Oct. 2017). "Uniform Atmospheric Retrieval Analysis of Ultracool Dwarfs. II. Properties of 11 T dwarfs". In: *The Astrophysical Journal* 848.2, p. 83. ISSN: 0004-637X. DOI: 10.3847/1538-4357/aa7ff0.

Lueber, Anna et al. (May 2022). "Retrieval Study of Brown Dwarfs Across the L-T Sequence". In: *The Astrophysical Journal* 930.2, p. 136. ISSN: 0004-637X, 1538-4357. DOI: 10.3847/1538-4357/ac63b9.

Luna, Jessica L. and Caroline V. Morley (Oct. 2021). "Empirically Determining Substellar Cloud Compositions in the Era of the James Webb Space Telescope". In: *The Astrophysical Journal* 920.2, p. 146. ISSN: 0004-637X. DOI: 10.3847/1538-4357/ac1865.

Macintosh, B. et al. (Oct. 2015). "Discovery and spectroscopy of the young jovian planet 51 Eri b with the Gemini Planet Imager". In: *Science* 350, pp. 64–67. ISSN: 0036-8075. DOI: 10.1126/science.aac5891.

Madhusudhan, Nikku (Oct. 2012). "C/O Ratio as a Dimension for Characterizing Exoplanetary Atmospheres". In: *The Astrophysical Journal* 758.1, p. 36. ISSN: 0004-637X, 1538-4357. DOI: 10.1088/0004-637X/758/1/36.

Marley, M.S. and T.D. Robinson (2015). "On the Cool Side: Modeling the Atmospheres of Brown Dwarfs and Giant Planets". In: *Annual Review of Astronomy and Astrophysics* 53.1, pp. 279–323. DOI: 10.1146/annurev-astro-082214-122522.

Marley, Mark et al. (July 2021a). *Sonora Bobcat: cloud-free, substellar atmosphere models, spectra, photometry, evolution, and chemistry*. DOI: 10.5281/zenodo.5063476.

Marley, Mark S., Didier Saumon, and Colin Goldblatt (Oct. 2010). "A Patchy Cloud Model For the L to T Dwarf Transition". en. In: *The Astrophysical Journal Letters* 723.1, p. L117. ISSN: 2041-8205. DOI: 10.1088/2041-8205/723/1/L117.

Marley, Mark S. et al. (Jan. 2007). "On the Luminosity of Young Jupiters". In: *The Astrophysical Journal* 655.1, pp. 541–549. ISSN: 0004-637X, 1538-4357. DOI: 10.1086/509759.

Marley, Mark S. et al. (July 2012). "Masses, Radii, and Cloud Properties of the HR 8799 Planets". In: *The Astrophysical Journal* 754.2, p. 135. ISSN: 0004-637X. DOI: 10.1088/0004-637X/754/2/135.

Marley, Mark S. et al. (Oct. 2021b). "The Sonora Brown Dwarf Atmosphere and Evolution Models I. Model Description and Application to Cloudless Atmospheres in Rainout Chemical Equilibrium". In: *The Astrophysical Journal* 920.2, p. 85. ISSN: 0004-637X, 1538-4357. DOI: 10.3847/1538-4357/ac141d.

Martinez, Raquel A. and Adam L. Kraus (Dec. 2021). "A Mid-infrared Study of Directly Imaged Planetary-mass Companions Using Archival Spitzer/IRAC Images". In: *The Astronomical Journal* 163.1, p. 36. ISSN: 1538-3881. DOI: 10.3847/1538-3881/ac3745.

McGregor, Peter J. et al. (Mar. 2003). "Gemini near-infrared integral field spectrograph (NIFS)". In: 4841, pp. 1581–1591. DOI: 10.1117/12.459448.

Mesa, D. et al. (Apr. 2023). "AF Lep b: The lowest-mass planet detected by coupling astrometric and direct imaging data". In: *Astronomy and Astrophysics* 672, A93. ISSN: 0004-6361. DOI: 10.1051/0004-6361/202345865.

Miles, Brittany E. et al. (Mar. 2023). "The JWST Early-release Science Program for Direct Observations of Exoplanetary Systems II: A 1 to 20 m Spectrum of the Planetary-mass Companion VHS 1256–1257 b". In: *The Astrophysical Journal Letters* 946.1, p. L6. ISSN: 2041-8205. DOI: 10.3847/2041-8213/acb04a.

Moe, Maxwell and Kaitlin M. Kratter (Sept. 2021). "Impact of Binary Stars on Planet Statistics – I. Planet Occurrence Rates, Trends with Stellar Mass, and Wide Companions to Hot Jupiter Hosts". In: *Monthly Notices of the Royal Astronomical Society* 507.3, pp. 3593–3611. ISSN: 0035-8711, 1365-2966. DOI: 10.1093/mnras/stab2328.

Moe, Maxwell, Kaitlin M. Kratter, and Carles Badenes (Apr. 2019). "The Close Binary Fraction of Solar-type Stars Is Strongly Anticorrelated with Metallicity". In: *The Astrophysical Journal* 875.1, p. 61. ISSN: 0004-637X. DOI: 10.3847/1538-4357/ab0d88.

Mollière, P. et al. (July 2019). "petitRADTRANS: a Python radiative transfer package for exoplanet characterization and retrieval". In: *Astronomy & Astrophysics* 627, A67. ISSN: 0004-6361, 1432-0746. DOI: 10.1051/0004-6361/201935470.

Mollière, P. et al. (Aug. 2020). "Retrieving scattering clouds and disequilibrium chemistry in the atmosphere of HR 8799e". In: *Astronomy & Astrophysics* 640, A131. ISSN: 0004-6361, 1432-0746. DOI: 10.1051/0004-6361/202038325.

Montmerle, Thierry et al. (1983). "Einstein observations of the Rho Ophiuchi dark cloud-an X-ray Christmas tree". In: *Astrophysical Journal, Part 1 (ISSN 0004-637X), vol. 269, June 1, 1983, p. 182-201. Research supported by the Ministere des Relations Exterieures of France.* 269, pp. 182–201.

Morbidelli, A., K. Batygin, and E. Lega (July 2023). "In situ enrichment in heavy elements of hot Jupiters". In: *Astronomy and Astrophysics* 675, A75. ISSN: 0004-6361. DOI: 10.1051/0004-6361/202346868.

Mordasini, Christoph et al. (Nov. 2016). "The imprint of exoplanet formation history on observable present-day spectra of hot Jupiters". In: *The Astrophysical Journal* 832.1, p. 41. ISSN: 1538-4357. DOI: 10.3847/0004-637X/832/1/41.

Nagpal, Vighnesh et al. (Feb. 2023). "The Impact of Bayesian Hyperpriors on the Population-level Eccentricity Distribution of Imaged Planets". In: *The Astronomical Journal* 165, p. 32. ISSN: 0004-6256. DOI: 10.3847/1538-3881/ac9fd2.

Nielsen, Eric L. et al. (July 2019). "The Gemini Planet Imager Exoplanet Survey: Giant Planet and Brown Dwarf Demographics from 10 to 100 au". In: *The Astronomical Journal* 158, p. 13. ISSN: 0004-6256. DOI: 10.3847/1538-3881/ab16e9.

Oberg, Karin I., Ruth Murray-Clay, and Edwin A. Bergin (Dec. 2011). "The effects of snowlines on C/O in planetary atmospheres". In: *The Astrophysical Journal* 743.1, p. L16. ISSN: 2041-8205, 2041-8213. DOI: 10.1088/2041-8205/743/1/L16.

Phillips, Mark W. et al. (May 2020). "A new set of atmosphere and evolution models for cool T-Y brown dwarfs and giant exoplanets". In: *Astronomy & Astrophysics* 637, A38. ISSN: 0004-6361, 1432-0746. DOI: 10.1051/0004-6361/201937381.

Pickles, A. J. (July 1998). "A Stellar Spectral Flux Library: 1150-25000 Å". In: *Publications of the Astronomical Society of the Pacific* 110, pp. 863–878. ISSN: 0004-6280. DOI: 10.1086/316197.

Piette, Anjali A. A. and Nikku Madhusudhan (Oct. 2020). "Considerations for Atmospheric Retrieval of High-Precision Brown Dwarf Spectra". In: *Monthly Notices of the Royal Astronomical Society* 497.4, pp. 5136–5154. ISSN: 0035-8711, 1365-2966. DOI: 10.1093/mnras/staa2289.

Piskunov, N. E. et al. (Sept. 1995). "VALD: The Vienna Atomic Line Data Base." In: *Astronomy and Astrophysics Supplement Series* 112, p. 525. ISSN: 0365-0138.

Pollack, James B. et al. (Nov. 1996). "Formation of the Giant Planets by Concurrent Accretion of Solids and Gas". In: *Icarus* 124, pp. 62–85. ISSN: 0019-1035. DOI: 10.1006/icar.1996.0190.

Qi, Chunhua et al. (Nov. 2015). "Chemical Imaging of the CO Snow Line in the HD 163296 Disk". en. In: *The Astrophysical Journal* 813.2, p. 128. ISSN: 0004-637X. DOI: 10.1088/0004-637X/813/2/128.

Radigan, Jacqueline et al. (Oct. 2014). "Strong Brightness Variations Signal Cloudy-to-clear Transition of Brown Dwarfs". In: *The Astrophysical Journal* 793, p. 75. ISSN: 0004-637X. DOI: 10.1088/0004-637X/793/2/75.

Ratzka, Thorsten, Rainer Koehler, and Christoph Leinert (July 2005). "A Multiplicity Survey of the Rho Ophiuchi Molecular Clouds". In: *Astronomy & Astrophysics* 437.2, pp. 611–626. ISSN: 0004-6361, 1432-0746. DOI: 10.1051/0004-6361:20042107.

Ruffio, Jean-Baptiste et al. (Dec. 2021). "Deep exploration of the planets HR 8799 b, c, and d with moderate resolution spectroscopy". In: *The Astronomical Journal* 162.6, p. 290. ISSN: 0004-6256, 1538-3881. DOI: 10.3847/1538-3881/ac273a.

Scharf, Caleb and Kristen Menou (Mar. 2009). "Long-Period Exoplanets From Dynamical Relaxation". In: *The Astrophysical Journal* 693, pp. L113–L117. ISSN: 0004-637X. DOI: 10.1088/0004-637X/693/2/L113.

Schweitzer, A. et al. (Dec. 1996). "Analysis of Keck high-resolution spectra of VB 10". en. In: *Monthly Notices of the Royal Astronomical Society* 283.3, pp. 821–829. ISSN: 0035-8711, 1365-2966. DOI: 10.1093/mnras/283.3.821.

Shibata, Sho and Ravit Helled (Feb. 2022). "Enrichment of Jupiter's atmosphere by late planetesimal bombardment". In: *The Astrophysical Journal Letters* 926.2, p. L37. ISSN: 2041-8205, 2041-8213. DOI: 10.3847/2041-8213/ac54b1.

Shibata, Sho, Ravit Helled, and Masahiro Ikoma (Jan. 2020). "The origin of the high metallicity of close-in giant exoplanets - Combined effects of resonant and aerodynamic shepherding". en. In: *Astronomy & Astrophysics* 633. Publisher: EDP Sciences, A33. ISSN: 0004-6361, 1432-0746. DOI: 10.1051/0004-6361/201936700.

Spiegel, David S. and Adam Burrows (Jan. 2012). "Spectral and Photometric Diagnostics of Giant Planet Formation Scenarios". en. In: *The Astrophysical Journal* 745.2, p. 174. ISSN: 0004-637X. DOI: 10.1088/0004-637X/745/2/174.

Spina, L. et al. (May 2017). "The Gaia-ESO Survey: the present-day radial metallicity distribution of the Galactic disc probed by pre-main-sequence clusters". In: *Astronomy & Astrophysics* 601, A70. ISSN: 0004-6361, 1432-0746. DOI: 10.1051/0004-6361/201630078.

Stevenson, David J. (2020). "Jupiter's Interior as Revealed by Juno". In: *Annual Review of Earth and Planetary Sciences* 48.1, pp. 465–489. DOI: 10.1146/annurev-earth-081619-052855.

Suárez, Genaro and Stanimir Metchev (Aug. 2023). "Ultracool dwarfs observed with the Spitzer Infrared Spectrograph – III. Dust grains in young L dwarf atmospheres are heavier". In: *Monthly Notices of the Royal Astronomical Society* 523.3, pp. 4739–4747. ISSN: 0035-8711. DOI: 10.1093/mnras/stad1711.

Swastik, C. et al. (Feb. 2021). "Host Star Metallicity of Directly Imaged Wide-orbit Planets: Implications for Planet Formation". en. In: *The Astronomical Journal* 161.3, p. 114. ISSN: 1538-3881. DOI: 10.3847/1538-3881/abd802.

Tokovinin, Andrei and Maxwell Moe (Feb. 2020). "Formation of close binaries by disc fragmentation and migration, and its statistical modelling". In: *Monthly Notices of the Royal Astronomical Society* 491.4, pp. 5158–5171. ISSN: 0035-8711. DOI: 10.1093/mnras/stz3299.

Tremblin, P. et al. (Nov. 2017). "Cloudless Atmospheres for Young Low-gravity Substellar Objects". en. In: *The Astrophysical Journal* 850.1, p. 46. ISSN: 0004-637X. DOI: 10.3847/1538-4357/aa9214.

Turrini, D. et al. (Mar. 2021). “Tracing the Formation History of Giant Planets in Protoplanetary Disks with Carbon, Oxygen, Nitrogen, and Sulfur”. en. In: *The Astrophysical Journal* 909.1, p. 40. ISSN: 0004-637X. DOI: 10.3847/1538-4357/abd6e5.

Visscher, Channon, Katharina Lodders, and Bruce Fegley (May 2010). “Atmospheric Chemistry in Giant Planets, Brown Dwarfs, and Low-Mass Dwarf Stars. III. Iron, Magnesium, and Silicon”. en. In: *The Astrophysical Journal* 716.2, p. 1060. ISSN: 0004-637X. DOI: 10.1088/0004-637X/716/2/1060.

Vos, Johanna M. et al. (Feb. 2019). “A search for variability in exoplanet analogues and low-gravity brown dwarfs”. In: *Monthly Notices of the Royal Astronomical Society* 483, pp. 480–502. ISSN: 0035-8711. DOI: 10.1093/mnras/sty3123.

Wagner, Kevin, Dániel Apai, and Kaitlin M. Kratter (May 2019). “On the Mass Function, Multiplicity, and Origins of Wide-orbit Giant Planets”. In: *The Astrophysical Journal* 877, p. 46. ISSN: 0004-637X. DOI: 10.3847/1538-4357/ab1904.

Wakeford, H. R. and D. K. Sing (Jan. 2015). “Transmission spectral properties of clouds for hot Jupiter exoplanets”. en. In: *Astronomy & Astrophysics* 573, A122. ISSN: 0004-6361, 1432-0746. DOI: 10.1051/0004-6361/201424207.

Wang, Ji et al. (Sept. 2020). “On the Chemical Abundance of HR 8799 and the Planet c”. en. In: *The Astronomical Journal* 160.3, p. 150. ISSN: 1538-3881. DOI: 10.3847/1538-3881/ababa7.

Wang, Ji et al. (Dec. 2022). “Retrieving C and O Abundance of HR 8799 c by Combining High- and Low-resolution Data”. en. In: *The Astronomical Journal* 165.1, p. 4. ISSN: 1538-3881. DOI: 10.3847/1538-3881/ac9f19.

Whiteford, Niall et al. (Oct. 2023). “Retrieval study of cool directly imaged exoplanet 51 Eri b”. In: *Monthly Notices of the Royal Astronomical Society* 525, pp. 1375–1400. ISSN: 0035-8711. DOI: 10.1093/mnras/stad670.

Xuan, Jerry W. et al. (Oct. 2022). “A Clear View of a Cloudy Brown Dwarf Companion from High-resolution Spectroscopy”. In: *The Astrophysical Journal* 937, p. 54. ISSN: 0004-637X. DOI: 10.3847/1538-4357/ac8673.

Zhang, Zhoujian et al. (Oct. 2023). “ELemental abundances of Planets and brown dwarfs Imaged around Stars (ELPIS). I. Potential Metal Enrichment of the Exoplanet AF Lep b and a Novel Retrieval Approach for Cloudy Self-luminous Atmospheres”. en. In: *The Astronomical Journal* 166.5, p. 198. ISSN: 1538-3881. DOI: 10.3847/1538-3881/acf768.

Chapter 3

THE ORBITAL ARCHITECTURE AND ORIGINS OF THE YOUNG, PLANETARY MASS COMPANION HOST SYSTEM, ROXS 42B

3.1 Introduction

Direct imaging has enabled the discovery of a few dozen planetary mass companions ($2 - 13$ M_{Jup}, or stellar mass ratios $q \ll 0.1$) orbiting their host stars at wide separations ($10 -$ 100s au), but there is still an ongoing debate over the origin of these objects (Currie et al., 2023). These companions appear to have lower orbital eccentricities (Bowler et al., 2020; Do Ó et al., 2023), distinct stellar spin-orbit orientations (Bowler et al., 2023) and mass functions (Wagner et al., 2019), and a higher occurrence rate when compared to brown dwarf companions on similarly wide orbits (Nielsen et al., 2019). This implies that the two populations have distinct formation mechanisms. There are multiple proposed explanations for the origin of planetary mass companions (Currie et al., 2023), including formation in a disk via core accretion or disk instability (e.g. Durisen et al., 2007), and isolated core fragmentation (e.g. Bate, 2012) followed by dynamical capture (e.g. Perets et al., 2012).

Previous studies of these companions have sought to use their atmospheric compositions to distinguish between formation mechanisms (e.g. Mollière et al., 2020; Wang et al., 2022; Nasedkin et al., 2024; Zhang et al., 2023; Palma-Bifani et al., 2024; Inglis et al., 2024; Xuan et al., 2024). Most of these studies parameterized the atmospheric composition as a metallicity and C/O ratio, and some obtained additional constraints on the abundances of isotopologues of carbon and oxygen (Zhang et al., 2021; Zhang et al., 2024; Xuan et al., 2024). However, subsequent modeling studies have demonstrated that these quantities can be degenerate between multiple formation scenarios, especially for objects formed outside the CO snowline where many of these companions are observed (Chachan et al., 2023; Cridland et al., 2020).

A subset of planetary mass companions have been found to orbit binary hosts rather than single stars (Kuzuhara et al., 2011; Kraus et al., 2013; Bailey et al., 2014; Gauza et al., 2015). For these systems, we can leverage the binary properties to obtain

additional constraints on formation scenarios for the planetary mass companions. Binary stars are known to dramatically alter the properties of the protoplanetary disk, which in turn can have profound implications for planet formation. Binary stars can truncate, warp, and dispel disks on short timescales (Barenfeld et al., 2019), making it difficult to form giant planets (Artymowicz et al., 1994). The effect of the binary on the disk is strongly dependent on the orbital separation, eccentricity, and mass ratio of the central binary, making these key parameters for understanding the formation history of any given system (Artymowicz et al., 1994; Harris et al., 2012).

Both models and observations find that the lifetimes of circumbinary disks are significantly shorter for binaries with intermediate separations (∼tens of au, e.g. Kraus et al., 2011; Elsender et al., 2023), making this arguably the single most important binary property for planet formation. The discovery of more than a dozen planets orbiting eclipsing binaries with small orbital semi-major axes, most of which were discovered using the transit technique, confirms that close binaries readily form planetary companions. Transiting circumbinary planets have significantly lower masses than most directly-imaged companions, and typically have orbital periods just outside the unstable region (e.g. Holman et al., 1999; Sutherland et al., 2019). Observational studies find low mutual inclinations between the binary and planetary orbits (Pierens et al., 2018; Dupuy et al., 2022), favoring formation in a well-aligned circumbinary disk. This same trend appears to extend to non-transiting companions detected using the radial velocity and transit timing techniques (e.g. Goldberg et al., 2023), although there have been relatively few such systems discovered to date. The low mutual inclinations of these systems are in good agreement with both models and observations of circumbinary disks, which indicate that close binaries ($\lesssim$ 20 days) possess small (< 5) mutual inclinations with their disk (Czekala et al., 2019).

For moderate binary separations (orbital periods greater than ∼30 days) this distribution widens (Czekala et al., 2019), and observations indicate that many disks are inclined and/or warped (e.g. Guilloteau et al., 1999; Chiang et al., 2004; Brinch et al., 2016; Kraus et al., 2020), with some disks found in near polar orientations (Kennedy et al., 2019; Czekala et al., 2019). Moderate separation binary orbits also tend to have larger eccentricities, which can drive the disk to librate around an inclination of 90 (Verrier et al., 2009; Farago et al., 2010; Naoz et al., 2017). Long period, eccentric binaries are the most likely to host highly-inclined disks (Czekala et al., 2019).

It is clear that the orbital properties of the host binary have strong implications for the formation and subsequent evolution of planetary mass companions. This makes measuring qualities such as the orbit to constrain the formation and subsequent dynamical evolution of these systems. However, the only planetary mass companions currently known to orbit longer period ($P > 30$ days) binaries are non-transiting, and have long orbital timescales requiring many years of baseline to obtain an orbital solution. As discussed above, there are also multiple competing formation mechanisms that have been proposed for these companions, whereas the lower mass transiting circumbinary planets likely formed via core accretion (e.g. Coleman et al., 2023). This mutual inclination has been measured several times for the VHS 1256-1257 system, which consists of a sub-stellar binary with a planetary mass companion at 170 au (Gauza et al., 2015). Dupuy et al. (2023) recently found a mutual inclination of 115 ± 14 between the binary and companion orbit. In this paper, we aim to repeat this measurement for a second system, ROXs 42B.

ROXs 42B is a young triple system located in the Rho Ophiuchus star forming region. Isochronal fitting gives an approximate stellar age of $6.8^{+3.4}_{-2.3}$ Myr (Kraus et al., 2013). Photometric fits have suggested individual masses of 0.89 ± 0.08 $M_{\odot}$ and 0.36 ± 0.04 $M_{\odot}$ for the two components of the primary binary (Kraus et al., 2013), which has a combined spectral type of M0 (Bowler et al., 2014). The third component of the system is a planetary mass companion initially identified by Ratzka et al. (2005) and later confirmed by Kraus et al. (2013) and Currie et al. (2014), with a photometrically derived mass of 10 ± 4 M_J for an assumed age between $1 - 5$ Myr (Kraus et al., 2013). In Inglis et al. (2024) and Xuan et al. (2024), we performed atmospheric retrievals on the planetary mass companion, ROXs 42B b, and showed that it has a composition consistent with both of its host stars. However, the measured atmospheric composition constraints did not allow us to strongly rule out core-accretion scenarios, as this companion is located beyond the CO snow line.

In this paper we use long-term, ground-based monitoring of the ROXs 42B[1] system from 2001 to 2022 to map the orbit of the host binary (Section 3.3) and the planetary mass companion ROXs 42B b (Section 3.3). We additionally place constraints on the mutual inclination between the binary and companion orbit in Section 3.3. In Section 3.4, we use numerical modeling to study the short and long-term evolution of this system. Finally, in Section 3.5, we discuss the possible origins of this system

[1]ROXs 42A and ROXs 42C are two unrelated nearby stars (Bouvier et al., 1992) that were found within the error circle of the Einstein Observatory, which first identified the Rho Ophiuchus X-ray source, ROXs 42 (Montmerle et al., 1983).

in combination with our numerical models and derived orbits.

3.2 Observations and Data Analysis

SPHERE Observations and Astrometry

ROXs 42B was observed with SPHERE (Beuzit et al., 2008) on UT-3 at the Very Large Telescope on 2017 March 16 (Program ID: 098.C-0864(A) Jensen-Clem et al., 2020). The observations were obtained using the IRDIS instrument (Dohlen et al., 2008) in dual-channel differential polarization mode Langlois et al. (2014) using the J-band filter, with the goal of detecting polarization in ROXs 42 **b**. The header reported a seeing of 0.64" and a windspeed of 5.18 m/s.

The full observing sequence consisted of an off-axis PSF image (typically used for flux calibration), a centering image with AO-induced waffle-spots, followed by a set of coronagraphic images using orthogonally polarized filters in each beam. A half-wave plate was present in the beam and was rotate at intervals of 225 between each exposure. In this study we make use only of the off-axis PSF image and the first image from the coronagraphic dataset. The exposure times for the PSF image and the polarimetry image were 2-s and 32-s, respectively. The results of the polarimetric study of ROXs 42 *b* have been previously published by Jensen-Clem et al. (2020). The raw frames were corrected for bad pixels, flat-field effects and then each channel in each image was centered using the waffle-spot image. We then separately combined both channels in the off-axis PSF image and the one coronagraphic science image to obtain total intensity images. Figure 3.1 displays the 2-s off-axis PSF image where the host binary, the planet, and a known background object (Bryan et al., 2016) can all be seen.

In order to obtain relative astrometric measurements of the stars we chose to perform PSF-fitting, where a PSF model is scaled in flux, and shifted in position for each object. Often in high-contrast measurements of planets a stellar PSF is used (e.g. obtained using an off-axis PSF, or satellite spots induced by a wire grid placed in a pupil plane; Sivaramakrishnan et al., 2006; Marois et al., 2006). However, in our case the stellar PSF is a binary whose positions we wish to measure. Instead we use the PSF of the *planet* from the first coronagraphic polarimetry image (where due to a longer exposure time the S/N of the PSF is higher than in Figure 3.1) to model the *stellar* PSFs (Figure 3.2).

We fit the relative positions of the two host stars using the Parallel-Tempered sampler from the `emcee` Markov Chain Monte Carlo python package (Foreman-Mackey et

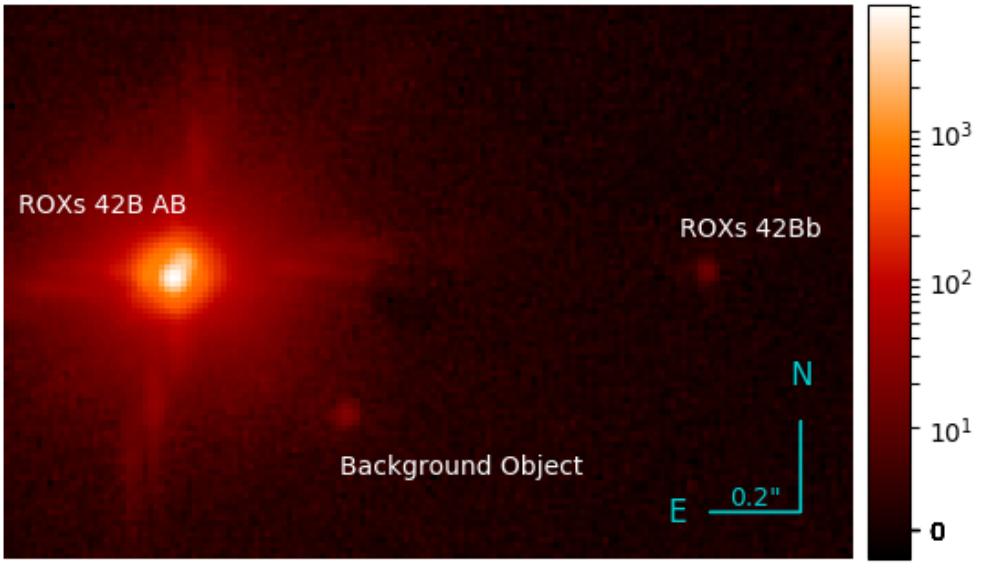

Figure 3.1 The off-axis PSF image of ROXs 42B obtained with SPHERE/IRDIS. The secondary host star component can be seen at ~0.08" to the North-West of the brighter primary host star. The image has been rotated from its original state to place North up and East to the left. The colormap is shown on a logarithmic scale to highlight all components at once.

al., 2013a). Preliminary fitting of the stellar positions revealed a slight mismatch between the shape of the planet PSF and those of the two stars. To compensate for this mismatch we included as part of the fitting a Gaussian mixture model (e.g. Hogg et al., 2010). The Gaussian mixture model allowed us to introduce the probability that each pixel is drawn from a Gaussian distribution rather than the PSF model (consisting of one PSF for each star), by only including three additional nuisance parameters: P_b, the prior probability that any individual data point is bad; Y_b, the mean of the distribution of the bad points; and, V_b, the variance of the distribution of the bad points. In doing so, we were able to give lesser weight in the fitting to pixels where the model PSF was poorly matched to the stellar PSFs, while giving full weight where the PSF was well matched (typically in the core of the PSFs). Several analytical 2D PSF models were also tried (e.g. Gaussian, Moffat, Airy, etc.) as well as different combinations of the planet's PSF from multiple polarimetry images, but in the end we found that the planet PSF from first polarimetry image—the closest in time to the off-axis PSF image—combined with the mixture model resulted in the smallest residuals.

Each iteration of the MCMC chain fits for nine parameters: a ΔX, ΔY (between the and flux scaling factor for each of the two stars, as well as the three Gaussian Mixture parameters (P_b, Y_b, V_b), where ΔX and ΔY represent the offsets of each star relative to the initial position of the model PSF. For each step, two copies of the model PSF are shifted and scaled, and the model *log-likelihood* is calculated from a cropped section of the full image (a 20 by 20 pixel box) roughly centered on the stellar PSF. The box excludes the outer regions of the PSF that contain the residual diffraction spikes from the telescope spider-structure (not seen in the lower S/N planet PSF) and focuses on the brighter core of the PSF. The errors were assumed to be Poisson noise, using a gain of $1.75e^{-}$/ADU, based on the value read from the FITS headers. The final log-likelihood is the combination of the model log-likelihood and the Gaussian mixture likelihood.

The stellar positions were fit with the parallel-tempered sampler using 256 MCMC chains and 20 temperatures, with a burn-in of 500 steps. The full fitting run consisted of 6,000 MCMC steps. The best-fit separation and position angle can be seen in Figure 3.2.

Keck NIRC Speckle Data

Following the initial identification of the binarity of ROXs 42B by lunar occultation observations (Simon et al., 1995), the target was monitored by speckle interferometry before the wide-spread availability of facility adaptive optics systems. In particular, we use observations from the Keck I 10 m telescope with the facility's Near Infrared Camera (NIRC, Matthews et al. 1996) taken between 2001-2005 to derive astrometry for the tight binary component of the system. The specific observation epochs are given in Table 3.2 The observations were taken in the K-band ($\lambda_o = 2.2\mu m, \Delta\lambda = 0.4\mu m$) using the high angular resolution mode of NIRC coupled with rapid detector readout, enabling speckle interferometry. In all epochs, four stacks of 190 target exposures of 0.137 s each were taken in stationary mode. Analagous stacks of known single calibration stars (Haro 1-16 or HD 115127) were also taken in each epoch, as well as dark, sky, and flat exposures.

The object frames were corrected using dark and sky subtraction, bad pixel repair, and flatfield correction. They were then corrected for known optical distortion in the NIRC camera and re-imaging optics for high-resolution mode (Lu et al., 2009). The data are then processed using both a shift-and-add technique to generate near-diffraction limited image (Ghez et al., 1998) and a Fourier transform technique

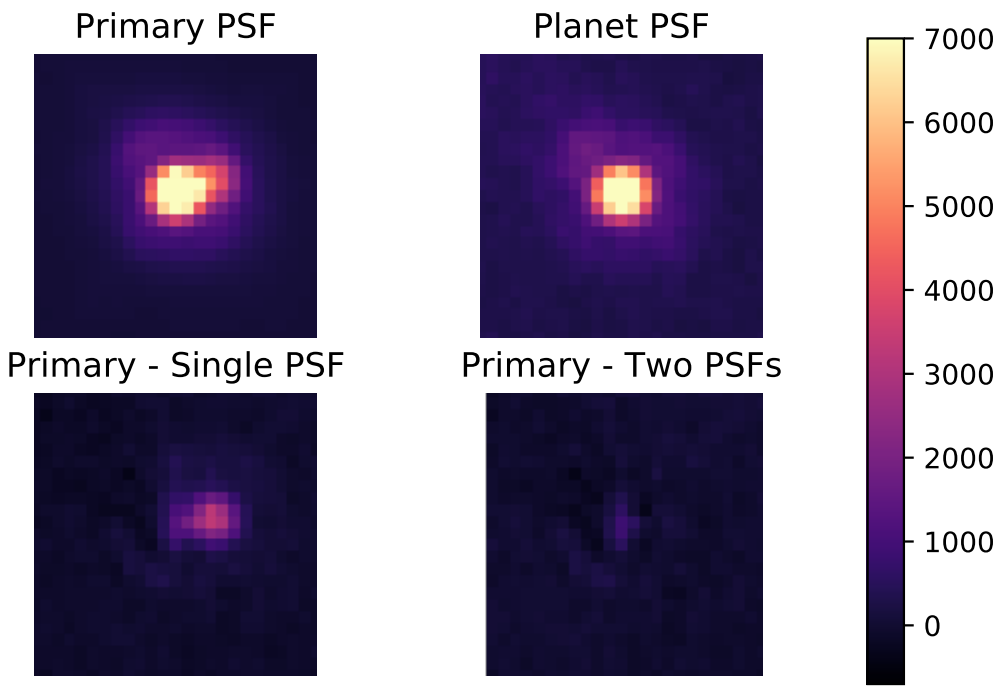

Figure 3.2 Top-Left: A zoom in on the the binary host stars in the off-axis PSF image frmo the IRDIS total intensity image. Top-Right: A zoom in on the PSF of the planet, ROXs 42 *b* in the first coronagraphic image (collapsed to total intensity from the two orthogonal polarization images). Bottom Left: The host star image after subtracting a model of the primary PSF (composed of a shifted and scaled planet PSF). Bottom Right: The host star image after subtracting a model for both the primary and secondary host star.

to generate a power spectrum. The latter are used for fitting for the separation, position angle, and flux ratio of the binary. The shift-and-add images are then visually inspected to resolve the 180° degeneracy in the position angle computed from power spectra. Additional details of power spectrum generation and fitting are described in detail in Ghez et al. (1995) and Konopacky et al. (2007). Uncertainties are derived by performing the same fitting procedure on individual image stacks and computing the RMS of each derived property.

Figure 3.3 shows an example of the speckle data from the 2005 epoch, including combined power spectra for each speckle epoch, a one-dimensional cut-through showing a portion of the sinusoidal fit to the data, which is appropriate when there are two sources in the field of view, and the shift-and-add image. Derived astrometry and flux ratio information is given in Table 3.2.

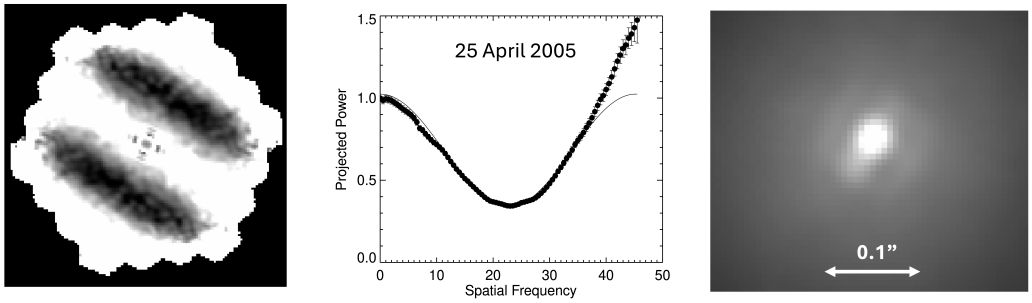

Figure 3.3 Example of speckle data products from one of the four epochs presented in this paper (25 April 20-05). *Left*: Two-dimensional power spectrum for the ROX 42B, demonstrating the sinusoidal pattern consistent with binarity. The frequency of the sinusoid is proportional to the binary separation, while the amplitude is proportional to the flux ratio. *Middle*: One-dimensional projection of the two-D spectrum shown on the left. The points show the actual data, while the line shows the sinusoidal fit to the data. The data and fit diverge at high spatial frequencies due to noise. *Right*: Shift-and-add reconstructed image of the binary from the speckle cubes. These images are not used for astrometry, but for defining the true position angle of the binary, which is not definable from the power spectra alone. The secondary is clearly seen to the southeast of the primary in these images.

NIRC2 AO Data

Finally, we utilize archival engineering observations of ROXs 42B with NIRC2 from UT 2022-07-15 taken as part of the KPIC Phase 2 PyWFS recovery and engineering program (PI Marin). The data was retrieved from the Keck Observatory Archives. We utilize functions from the Vortex Image Processing (`VIP`) (Gomez Gonzalez et al., 2017), as well as some of the custom routines from Xuan et al. (2018) to process the images, including the removal of bad and dead pixels. We replace bad pixels replaced with the median of the neighboring pixels, excluding the area around either the companion or binary PSFs. We perform background substraction using a median of the full frame.

As there are no available reference star images for this archival observation and the PSFs of the binary stars are blended, we utilize two different techniques to get the relative astrometry of the binary component. Firstly, as above, we construct a reference PSF using the companion, visible in all images. We compare this method to modeling the blended psf of the two stars simply using multi-parameter Gaussian PSFs, and found consistent results for both methods. The derived astrometry values are displayed in Table 3.2

Table 3.1. Measured and literature-sourced values for the relative astrometry of ROXs 42B B and ROXs 42B b used in this paper, along with their corresponding instruments. All astrometry points are measured relative to ROXs 42B A.

Target	Epoch	Instrument	Band	Sep [mas]	PA [°]	Flux ratio	Reference
ROXs 42B B	2001.345	NIRC	K	81 ± 3	147.5 ± 3	0.243 ± 0.009	This work
ROXs 42B B	2002.545	NIRC	K	73 ± 1	147.91 ± 0.95	0.30 ± 0.03	This work
ROXs 42B B	2003.301	NIRC	K	68.7 ± 0.7	149.05 ± 0.58	0.32 ± 0.01	This work
ROXs 42B B	2005.29	NIRC2	K	54 ± 8	146 ± 10	0.8 ± 0.2	This work
ROXs 42B B	2005.315	NIRC	K	57 ± 1	147.93 ± 0.74	0.27 ± 0.01	This work
ROXs 42B B	2017.287	SPHERE	J	39.23 ± 0.4	331.2 ± 1	0.285 ± 0.009	This work
ROXs 42B B	2022.	NIRC2	K	51 ± 2	148 ± 3	0.24 ± 0.1	This work
ROXs 42B b	2001.	SHARP1	K	1137±	268 ± 0.3	0.002 ± 0.001	Ratzka et al. (2005)
ROXs 42B b	2017.287	SPHERE	J	1175.5 ± 2	271.4 ± 0.2	0.003 ± 0.001	this work
ROXs 42B b	2022.	NIRC2	K	1178 ± 6	271 ± 1	0.002 ± 0.001	this work

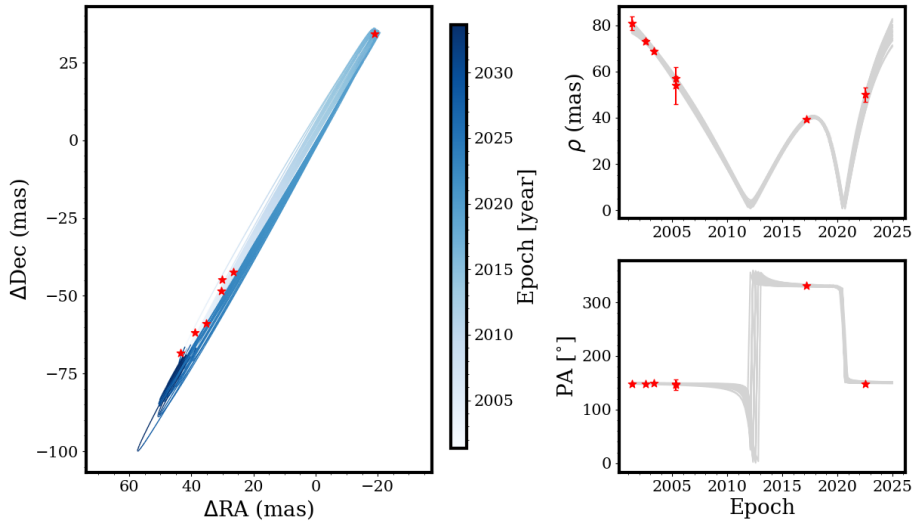

Figure 3.4 LEFT 50 randomly drawn orbits of the lower mass component of the binary, ROXs 42B B, color coded by epoch. The individual astrometry points, with their error bars, are represented by red stars. RIGHT The corresponding separation and position angle of ROXs 42B B as a function of epoch. The individual astrometry points are represented by red stars. The corresponding astrometry points are located in Table 3.2.

3.3 Orbital Fits

Although the ROXs 42B system is a three-body system, we initially consider just the inner binary orbit and neglect the outer companion. Dynamical interactions between the outer companion, ROXs 42B b, and the inner binary are negligible given the wide separation (~180 au) and small mass ratio of the companion to its host binary ($M_{comp}/M_{host} \sim 0.01$). Our solution for the outer companion's orbit does depend on our retrieved orbital fit for the inner binary, because we measure the motion of the companion relative to the barycenter of the system. We therefore carry out that fit after we derive the orbital solution for the inner binary.

Inner Binary Orbit

We fit the orbit of the host binary, which we refer to hereafter as ROXs 42B AB, using the Bayesian parameter inference tool implemented in the open-sourced package `orbitize!` (Blunt et al., 2020). We use the default orbital priors from `orbitize!` for the semi-major axis, a, inclination, i, eccentricity, e, argument of periastron, ω, position angle of the ascending node, Ω, and the phase of periastron, τ. For the total mass, we adopt a wide Gaussian prior based on the total photometrically

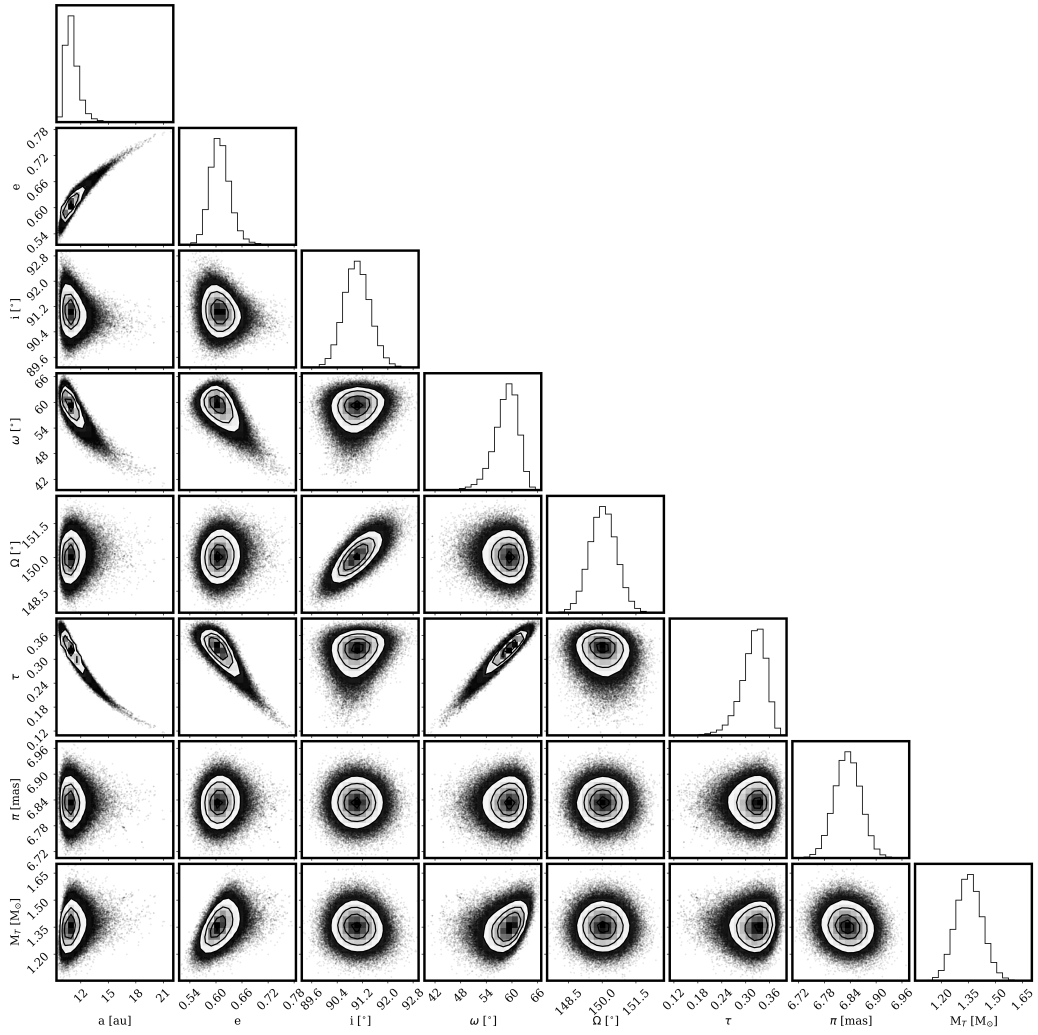

Figure 3.5 Posterior distribution of orbital parameters of the lower mass component of the binary, ROXs 42B B from our `orbitize!` fit using the astrometry relative to ROXs 42B A.

derived mass from Kraus et al. (2013), $M_T = 1.3 \pm 0.2$ $M_\odot$. For the parallax we use a Gaussian prior based on the measured value of 6.83 ± 0.03 mas from Gaia Collaboration (2020). We change the reference epoch to 55197 MJD (2010.0) as the default reference period of 2020.0 coincidentally occurs close to the time of periastron in our orbital fits.

`orbitize!` uses `ptemcee` (Vousden et al., 2021), the parallel-tempered version of the affine-invariant ensemble sampler implemented in `emcee` (Foreman-Mackey et al., 2013b), in order to prevent walkers from being trapped in local minima. We use 1000 walkers and 20 temperatures with 10^6 steps in order to ensure convergence of

our posterior. The parameters in our fit along with their priors are shown in Table. 3.2, along with the median and 1σ uncertainties of their posteriors. The posteriors are shown in Fig. 3.5. A sample of binary orbits drawn from our posteriors is shown in Fig. 3.4.

Relative astrometry only allows us to constrain the total mass of the ROXs 42B AB system. We obtain a total mass of 1.34 ± 0.07 $M_\odot$, which is consistent at the 1σ level with the photometrically-derived masses of the individual components published in Kraus et al. (2013), 0.89 ± 0.08 $M_\odot$ and 0.36 ± 0.04 $M_\odot$. Our orbital fit finds a semi-major axis of $10.9^{+0.8}_{-0.5}$ au, corresponding to an orbital period of 31^{+3}_{-2} years. This is significantly longer than any of the planet-hosting binary systems detected using transits or radial velocity measurements, and also longer than the 7 year orbital period of the central binary in the VHS J1256-1257 system (Dupuy et al., 2023). We find a moderately high eccentricity of 0.61 ± 0.02 for the binary. This is consistent with the observed eccentricity distribution of field binaries with similar binary mass ratios and orbital periods (Moe et al., 2017), and comparable to the eccentricity of the VHS J1256-1257 binary ($e = 0.883 \pm 0.003$; Dupuy et al., 2023).

We find a near edge-on orbit, with a retrieved inclination of $91.0 \pm 0.4°$. We calculate an impact parameter based on our orbital fits and find that 1% of solutions result in at least a grazing eclipsing binary, assuming stellar radii based on evolutionary models and the photometric masses.

Companion Orbit

The mutual inclination between the binary and companion orbits encodes information about the formation and evolution of this system. In order to measure the mutual inclination, we first need the relative astrometry of the companion, ROXs 42B b, with respect to the barycenter of the ROXs 42B system. We use epochs of data where all three components of the system are visible in order to compute the relative astrometry of the companion to the most massive component of the binary, ROXs 42B A. We then use the relative astrometry of the inner binary derived in §3.3 and the published constraint on the mass ratio of 0.40 ± 0.06 from Kraus et al. (2013) to solve for the astrometry of the companion relative to the barycenter of the system.

After calculating the astrometry of the companion relative to the system's barycenter, we then use the Orbits-For-The-Impatient (`OFTI`) rejection sampling method from Blunt et al. (2017) implemented in the `orbitize!` package in order to derive a

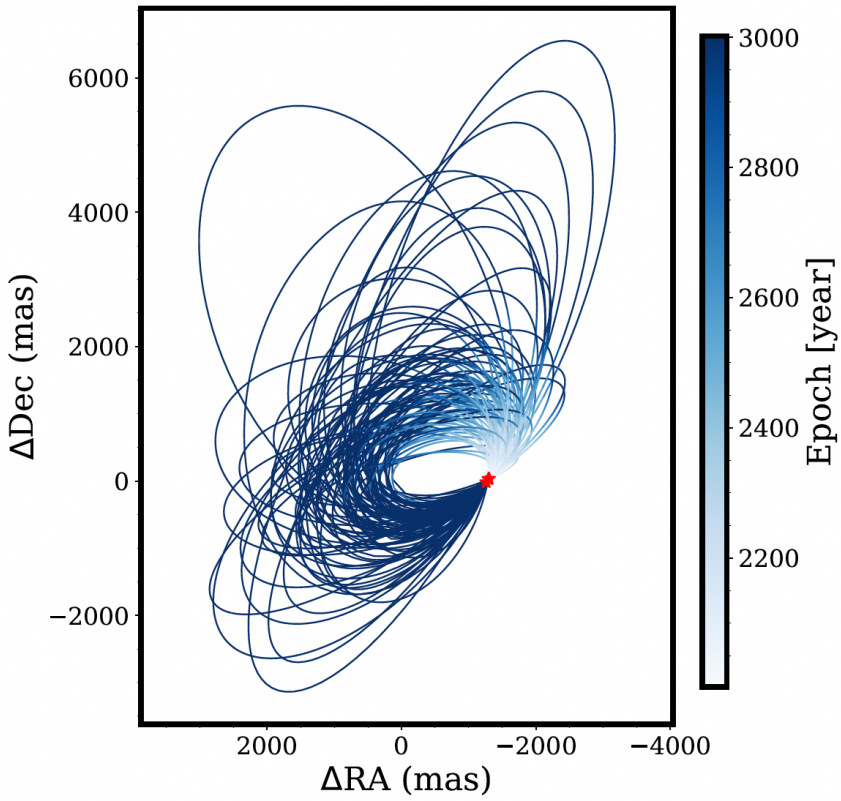

Figure 3.6 Randomly drawn sample of 50 orbits of the companion ROXs 42B b around the system barycenter, color coded by epoch, from our OFTI fits. The individual astrometry points are represented by red stars.

range of possible orbits for the companion. `OFTI` is a Bayesian rejection-sampling algorithm that estimates the posterior distributions of orbital elements for widely-separated companions, which commonly only have observations covering a small fraction of their total orbit. `OFTI` generates a random orbit from within the prior distribution and then rejects or accepts that orbit with a probability equal to the ratio of the computed likelihood to the maximum likelihood for the model (Blunt et al., 2017). The result is a sample of points where density is proportional to probability, equivalent to a MCMC chain. Unlike traditional Bayesian rejection-sampling algorithms, `OFTI` also includes a unique 'scale-and-rotate' step, which rescales the first orbits drawn in order to sharply restrict the volume of the prior space to the relevant parameters for the dataset. This approach has been shown to converge significantly faster than MCMC for these data sets (Blunt et al., 2017). We generate orbits until we have a sample of 10^7 accepted orbits. A sample of 50 randomly selected orbits is shown in Fig. 3.6. The parameters and initial priors used

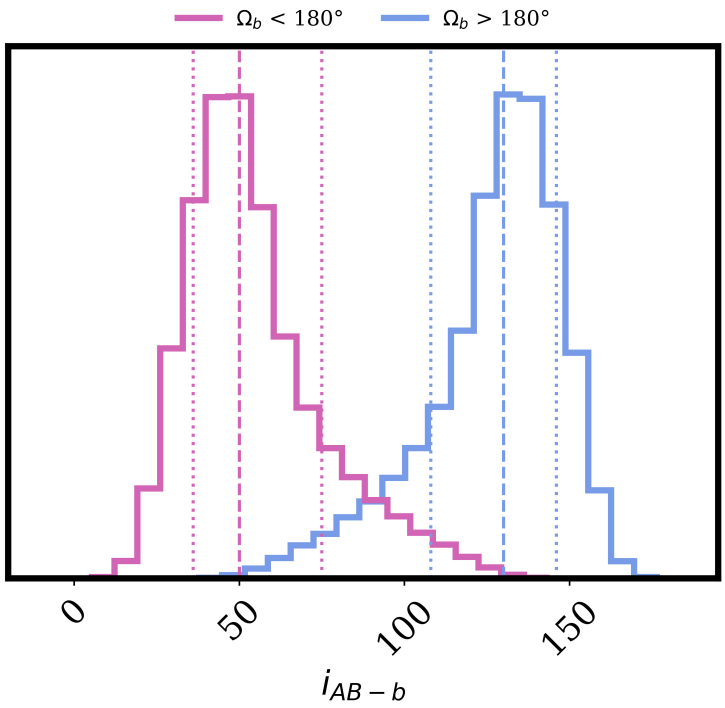

Figure 3.7 Derived posterior distribution mutual inclination, i_{AB-b} between the binary and companion orbits for the two possible solutions of Ω_b. The median and 1σ uncertainties are shown for each value of Ω_b.

for our `OFTI` fit are shown in Table 3.3, along with the median and 1σ uncertainties.

We find a median orbital semi-major axis of 222^{+134}_{-62} au for the companion, ROXs 42B b, which corresponds to an orbital period of approximately 3,000 years. Unlike the inner binary orbit, which is near edge on, we find a median inclination of $49^{+15}_{-20}{}^{\circ}$. Although our constraint on the orbital eccentricity is relatively weak, we can nonetheless rule out eccentricities greater than 0.89 at 99% confidence.

Due to the 180° degeneracy between ω and Ω for short orbits with relative astrometry, we only report the solutions less than 180° for these parameters, as is the common practice. However, there is a separate solution found by adding 180° to ω_b and Ω_b.

Mutual Inclination

After obtaining solutions to both the binary and companion orbit from their relative astrometry, we utilize our posteriors to calculate the mutual inclination between the binary and companion orbit using the formula:

$$\cos i_{AB-b} = \cos i_{AB} \cos i_b + \sin i_{AB} \sin i_b \cos(\Omega_{AB} - \Omega_b). \tag{3.1}$$

Table 3.2. Summary table of parameters and their median and 1σ uncertainties from our `orbitize!` fit to the relative astrometry of the inner binary, ROXs 42B AB. t_{ref} = 55197 MJD (2010.0)

Parameter	Prior	Value
Total mass, M_T [$M_\odot$]	$\mathcal{N}$(1.25,0.1)	1.35 ± 0.07
Semi-major axis, a [au]	log-$\mathcal{U}$(0.001,10^4)	$10.9^{+0.8}_{-0.5}$
Orbital Period, P [yr]	Derived	31^{+3}_{-2}
Eccentricity, e	$\mathcal{U}$(0,1)	0.61 ± 0.02
Inclination, i [°]	sin(0,180)	91.0 ± 0.4
Argument of periastron, ω	$\mathcal{U}$(0,360)	58^{+2}_{-3}
PA of Ascending node, Ω [°]	$\mathcal{U}$(0,360)	150.0 ± 0.6
$\tau = \frac{t_p - t_{\rm ref}}{P}$	$\mathcal{U}$(0,1)	0.32 ± 0.03
Time of periastron, t_p [MJD]	Derived	55207 ± 0.08

We utilize random draws from both posteriors in order to create a posterior distribution of mutual inclinations. Due to the 180° degeneracy between ω and Ω in the orbital fit of our companion, we find two distinct solutions for the mutual inclination dependent on whether $\Omega_b > 180°$ or $\Omega_b < 180°$. Our derived posterior for is plotted in Fig. 3.7. For the case where $\Omega_b < 180°$, we find a median mutual inclination of $51^{\circ+24}_{-14}$. In this case, the companion orbit is most likely prograde, but could be retrograde (2σ). For the case where $\Omega_b > 180°$, we find that the companion is likely on a retrograde orbit, 130^{+16}_{-22}. The latter scenario is similar to that of the $115 \pm 14°$ mutual inclination of the binary and planetary mass companion in the VHS J1256-1257 system (Dupuy et al., 2023). Importantly, our 99% confidence interval for the mutual inclination, including both distinct solutions, ($24° < i_{AB-b} < 158°$) excludes scenarios where the mutual inclination is consistent with zero with high statistical significance.

3.4 Orbital Evolution and Stability

In a three-body system, angular momentum exchange between the inner and outer orbits can result in eccentricity-inclination oscillations. In cases where the eccentricity is sufficiently large these oscillations can result in transitions from prograde to retrograde motions for the outer, less massive body (Naoz et al., 2017). They can also lead to changes in orbital semi-major axis (Ford et al., 2000; Lithwick et al., 2011), collisions, or even ejection (Toonen et al., 2020; Toonen et al., 2022). The ultimate fate of a triple system depends strongly on the relative masses and orbital parameters of the three components. It is therefore important to consider the dynam-

ical evolution and long-term stability of the ROXs 42B system when interpreting the measured mutual inclination.

Mardling (2001) derived a conservative stability criterion for triple systems:

$$\frac{a_{out}}{a_{in}}|_{crit} = \frac{2.8}{1-e_{out}}\left(1-\frac{0.3i}{\pi}\right)\left(\frac{(1+q_{out})(1+e_{out})}{(1-e_{out})^{1/2}}\right)^{3/2} \tag{3.2}$$

where $q_{out} = M_3/(M_1 + M_2)$, i is the inclination in radians, and e_{out} is in the eccentricity of the outer body. A triple system is stable in this case if:

$$\frac{a_{out}}{a_{in}} > \frac{a_{out}}{a_{in}}|_{crit}. \tag{3.3}$$

This criterion was initially derived for an equal mass, zero-inclination triple and later corrected to account for non-zero inclinations. It has since been validated using multiple methods for a wide range of systems (e.g. He et al., 2018; Mylläri et al., 2018). We evaluate this criterion using random draws from the companion and binary orbit posteriors. We find that with very few exceptions ($< 0.1\%$ of all draws considered), $\frac{a_{out}}{a_{in}} >> \frac{a_{out}}{a_{in}}|_{crit}$. We conclude that the observed architecture of the ROXs 42B system is very likely to be long-term stable.

We further investigate the short- and long-term dynamics of the ROXs 42B system utilizing the open-source software package `REBOUND` (Rein et al., 2012). `REBOUND` is an N-body integrator that models the motion of multiple particles under the influence of gravity. We model the three bodies in the ROXs 42B system using the median orbital distances from our posteriors and the derived photometric masses from Kraus et al. (2013). For completeness, we test the effect of tides and general relativity, implemented in `REBOUNDx` (Lu et al., 2023), but find that these effects are insignificant given the large present-day orbital distances between all three components of the system, as even at periastron, the present-day separation of the components of the binary is 4.4 au.

First, we consider how much the mutual inclination could have evolved over the relatively short lifetime of this system, assuming a maximum lifetime of 10 Myr. For the median values from both orbital fits we find octopole-driven oscillations with a secular timescale of ~4 Myr, comparable to the age of the system. In this case the mutual inclination oscillates between $\sim 40° - 90°$. However, both the oscillation amplitude and timescale can vary significantly between parameter draws. If the companion initially formed in a circumbinary disk that was misaligned with the binary orbit, this suggests that its present-day inclination has likely evolved away

from the original disk orientation. For cases where the disk and binary have low initial mutual inclinations ($\lesssim$ a few degrees), the mutual inclination of the system will remain low. We can therefore exclude the scenario where the planet formed in-situ in an aligned disk based on the observed misalignment between the binary and companion. Notably, this allows us to exclude the kinds of aligned disk geometries that are required to explain the transiting circumbinary planets observed by Kepler (Pierens et al., 2018; Dupuy et al., 2022).

One proposed theory for the origin of widely separated directly-imaged companions is scattering with other massive companions, planet-planet scattering (Perets et al., 2012). In order to understand if this is mechanism would reproduce the observed properties of the ROXs 42B system, we set up an experiment as follows: We initialize two companions with masses drawn randomly from 5-15 Jupiter masses, values consistent with the range of photometrically derived masses for ROXs 42B b. The semi-major axis of the two companions is drawn from 36 - 80 au. The lower bound is set by the approximate size of the inner cavity of the disk that would be carved by the binary (Artymowicz et al., 1994). The outer bound is based on the upper limit of predicted circumbinary disk radii from the hydrodynamic models in Elsender et al. (2023) for our retrieved binary separation. The eccentricity is drawn from 0 to 0.1, and the rest of the orbital parameters from within the range of possible values. We then evolve the simulation forward by 10^5 years. We consider a companion ejected when its semi major axis increases beyond 10^4 au. We repeat this experiment 1000 times.

We find that in the majority of runs, at least one companion is either ejected or collides with the binary. The surviving companion's orbital distance, eccentricity, and mutual inclination with the binary orbit are all increased. For example, in one run, the system starts with two companions: 15 M_J mass at 45 au, and 10 M_J mass as 60 au. Within the first 10^4 years, the inner companion's orbital eccentricity increases from 0.01 to 0.4 where it crosses the orbit of the binary and has a close encounter with one of the stars. The surviving companion is scattered out onto a 170 au orbit with an eccentricity of 0.75, and the mutual inclination of the system increases from 5° to 60°, both consistent with our observations of ROXs 42B b. While companion with a mass below 8 M_J can be initially scattered onto wide orbits, subsequent interactions with the binary result in a final orbital distance less than 100 au. We find that more massive companions better reproduce the observed configuration of this system. If the eccentricity of the surviving companion is above 0.9, we find

Table 3.3. Summary table of parameters and their median and 1σ uncertainties from our `OFTI` fit to the relative astrometry of the companion, ROXs 42B b. t_{ref} = 58849 MJD (2020.).

Parameter	Prior	Value
Semi-major axis, a [au]	log-$\mathcal{U}(0.01,10^4)$	223^{+150}_{-69}
Orbital Period, P [yr]	Derived	2873^{+3317}_{-1219}
Eccentricity, e	$\mathcal{U}(0,1)$	$0.4^{+0.2}_{-0.3}$
Inclination, i [°]	$\sin(0, 180)$	58^{+15}_{-20}
Argument of periastron, ω [°]	$\mathcal{U}(0,360)$	96^{+60}_{-66}
PA of Ascending node, Ω [°]	$\mathcal{U}(0,360)$	112^{+22}_{-23}
$\tau = \frac{t_p - t_{\rm ref}}{P}$	$\mathcal{U}(0,1)$	$0.77^{+0.13}_{-0.2}$
Time of periastron, t_p [MJD]	Derived	57069^{+878}_{-2434}

that the second companion is eventually ejected from the system. Fortunately, we are able to rule out this region of parameter space with our companion orbital fits, suggesting the system is likely stable.

3.5 Discussion

We consider four scenarios for the origin of the massive, wide companion, ROXs 42B b:

1. Capture: The companion formed separately and was later captured by the host binary, either as a free-floating planet, or part of another system, a process throught to form triple systems.

2. Binary Scattering + Stellar Flyby: The companion formed in a circumbinary disk at an orbital radius much smaller than its present-day separation. It then migrated inward until it encountered the binary's chaotic zone (Holman et al., 1999; Sutherland et al., 2019). Interactions with the chaotic zone resulted in stochastic gravitational kicks that scattered the companion onto a highly eccentric orbit. The companion was then stabilized onto its present-day orbit by an interaction with another massive object, such as another star in the cluster.

3. Planet-Planet Scattering: There were initially multiple planetary mass companions that formed at moderate separations from the ROXs 42B host binary. Scattering between the planetary mass companions resulted in the outward

migration of ROXs 42B b. The additional companion(s) either collided with the binary or were ejected from the system.

4. In-situ Formation: The companion formed in situ within a massive circumbinary disk. This would favor formation through gravitational instability over core accretion as a result of the large semi-major axis.

Scenarios One and Two require encounters with at least one other object within the cluster. In order to investigate the likelihood of these scenarios, we compute the rate of stellar encounters as:

$$\Gamma = \eta_* \sigma \langle v \rangle \tag{3.4}$$

where η_* is the stellar number density of the cluster, σ is the cross section of the interaction, and $\langle v \rangle$ is the velocity dispersion. The stellar number density of the clusters in ρ-Ophiuchus range from 29 (Ophiuchus center) to 337 stars/pc^3 (L1688; Schmeja et al., 2008). The velocity dispersion is approximately 1 km s^{-1} (Wilking et al., 2015). Depending on how early the capture or formation of ROXs 42B b occurred, these number densities may not be reflective of the true density during the encounter. During the early embedded phase of the cluster, the stellar density even in low mass clusters is expected to be sufficiently high that stellar encounters are common (Proszkow et al., 2009). To check that this wouldn't significantly influence our inferences about the origins of this system, we compare our values from addition to Equation 3.4 to the encounter rates derived in Proszkow et al. (2009) and find a similarly low probability of capture.

Numerical models of triple star system formation show that in order for an encounter to result in capture, the distance of closest approach with the inner binary must be much smaller than the binary separation (Hut et al., 1983; Hut, 1983). Using the present-day separation of the binary, 11 au, the probability of an encounter between the binary and the planetary mass companion, either free-floating or bound to another star, that results in a bound system, ranges from $1/10^6 - 1/10^4$, making this scenario unlikely.

In Scenario 2, the companion initially formed at a smaller orbital distance before being scattered out to its current orbital distance. The large semi-major axis (220 au) of the companion significantly increases the cross section for interactions with another body in the cluster and therefore the probability of a stabilizing encounter. Over the measured age range of this system, the probability of such an encounter ranges from $1/10^4$ to 1/100 for the most dense cluster and the highest end of the age

range for this system. 1% is on the order of the occurrence rate of circumbinary companions between 2-15 M_{Jup} detected in direct imaging surveys (Asensio-Torres et al., 2018), making this a plausible formation scenario for this system as well as other similar systems. This mechanism is also consistent with the companion's non-zero mutual inclination relative to the binary.

However, there is one important caveat. In order for a stellar flyby to stabilize the planet's orbit, the flyby needs to occur within the relatively narrow window of time before the planet is ejected from the system. Rodet et al. (2017) consider this scenario to explain the origin of the wide, circumbinary companion HD 106906 b and find that this significantly reduces the probability of such an event occurring. However, they assume a short timescale of 10^3 years where this encounter may occur. While simulating the evolution of triple systems, Toonen et al. (2022) found that this unstable phase could instead last thousands to millions of crossing times, and is dependent on the unknown original orbital parameters. We therefore still consider this to be a viable explanation for the ROXs 42B system. Alternatively, if the scattering event occurs while there is still some disk gas present, the disk itself could act to circularize the companion onto a stable orbit (Kikuchi et al., 2014; Heath et al., 2020).

The challenge of having a coincidentally-timed stellar flyby stabilize the companion orbit as it is being ejected is avoided in Scenario Three where the scattering occurs between multiple planetary mass companions. However, this scenario requires multiple super-Jupiter mass companions to form. While a handful of such systems have been observed, e.g. HR 8799 (1.47 $M_\odot$; Marois et al., 2008), PDS 70 (0.76 $M_\odot$; Keppler et al., 2018; Haffert et al., 2019), β pic (Lagrange et al., 2009; Lagrange et al., 2019), and YSES 1 (1.00 $M_\odot$; Bohn et al., 2020b; Bohn et al., 2020a), it is thought to be challenging to form multiple super Jupiter mass companions in a typical disk. In Section 3.4, we discuss results from numerical models of this scenario. We find that this scenario accounts for the present-day configuration of this system as the surviving companion can be moved out to orbital distances consistent with our retrieved values. Importantly, even in scenarios where the initial mutual inclination and eccentricities of the companions are low ($e \lesssim 0.1$), planet-planet scattering can increase the mutual inclination of the surviving companion with the binary orbit to above 60°. The orbital eccentricity of the surviving companion is similarly enhanced from less than 0.1 to moderate values ranging from $e = 0.3-0.85$, which is consistent with our observations. This scenario is also compatible with

observations suggesting a sizeable population of free floating planets, which could be generated by planet-planet scattering and ejection by a binary system (Miret-Roig et al., 2022).

If the companion formed in the inner disk before being scattered to its current orbital distance, we can place a lower bound on its initial semi-major axis based on the present-day separation of the binary. Studies of the formation of circumbinary planets find that the orbits of these planets become unstable after inward migration causes the planet to encounter mean-motion resonances with the host binary, (e.g. the 4:1 or 6:1 resonances; Pierens et al., 2008; Rodet et al., 2017). Resonant interactions then rapidly increase the planet's orbital eccentricity, which often results in ejection without a stabilizing interaction with a fourth body. For the present-day binary separation, the 4:1 resonance would occur at 28 au. Separately, studies of the stability of a third body around a massive binary predict a minimum stable radius of approximately three times the binary separation, or 33 au (Dvorak, 1986). Hydrodynamic models of circumbinary disk similarly predict the formation of an inner disk cavity of size approximately three times the binary separation for an orbital eccentricity of 0.6 (Artymowicz et al., 1994; Hirsh et al., 2020). For our purposes, these predictions provide an approximate inner bound on the formation location of the companion in this scenario. This carries important implications for interpreting the atmosphere of these objects. Formation outside the CO ice line can make it challenging to differentiate between core accretion and disk instability formation mechanisms for massive objects, as most major carbon and oxygen species have condensed out onto the solids. The expected location of the CO ice line varies greatly from theoretical predictions, $\sim$ 30 au, and observations, $\sim$ 30 to $\gtrsim$ 100 au (see Öberg et al., 2021). Accounting for multiple sources of radiation and heat generated by tidal interactions between binary stars can also push this value outwards by a few au, for 10 au binary stars (Shadmehri et al., 2015). It is still likely that objects like ROXs 42B b formed beyond the CO ice line of their disk, which is important context for interpretations of their atmospheres.

Our observations can also be explained by formation in situ in a large circumbinary disk (Scenario Three). The median orbital radius of the companion from our OFTI fit is 222 au. While this is larger than the average protoplanetary disk, there are circumbinary disks that extend out to these distances, such as the well-studied GG Tau A system. This system consists of an inclined, circumtriple disk that extends out to ~850 au (Guilloteau et al., 1999; Di Folco et al., 2014). Our fits find a median

total mass of the inner binary, ROXs 42B AB, of 1.35 $M_{\odot}$, which is similar to the estimated stellar mass of the GG Tau A system (1.37 ± 0.08 $M_{\odot}$; Guilloteau et al., 1999). The circumtriple disk around GG Tau A also has an estimated inclination of 37 ± 1° relative to the binary orbit (Guilloteau et al., 1999; Keppler et al., 2020). This misalignment can be explained by dynamical interactions with a moderately eccentric binary (Keppler et al., 2020; Toci et al., 2024). This suggests that the ROXs 42B system could have had a similarly misaligned disk, consistent with the moderately eccentric orbit of the inner binary.

Based on the above scenarios, it is likely that ROXs 42B formed within a circumbinary disk. Observational surveys (Kraus et al., 2011) show that 2/3 of binaries with a similar separation lose their disks within $\lesssim$ 1 Myr, and nearly all within 2 Myr. Given the long timescales involved with assembling a massive companion with core or pebble accretion, it would be extremely challenging to assemble a 6 − 14 M_{Jup} companion before the disk was dispersed. Disk instability is expected to occur on much shorter timescales and is most efficient at larger orbital distances, which is where the companion is most likely to have formed; therefore is the formation mechanism most consistent with the architecture of the ROXs 42B b system.

3.6 Conclusions

In this chapter, we use astrometric monitoring of the ROXs 42B triple system in order to investigate the origins of the wide, planetary-mass companion, ROXs 42B b. We find a moderately eccentric and edge-on orbit for the inner body. We find a mutual inclination of (insert final number) between the companion and binary orbits. We consider the possibility that ROXs 42B b was captured and bound as part of a dynamical interaction with a fourth body, but find that the probability of such an event is too low to be plausible. We conclude that this object most likely formed in a misaligned circumplanetary disk, but are unable differentiate between scenarios where it formed at moderate separations (30-80 au) and was later scattered out to its current location, either through interactions interactions with its host binary or another massive companion, or where it instead formed in situ near 220 au in an unusually massive circumbinary disk. In the future, additional high precision astrometric observations of ROXs 42B b could provide improved current constraints on its orbital inclination, semi-major axis, and eccentricity. If it has a relatively high orbital eccentricity (> 0.3) this would favor the scattering scenario, whereas if its orbit is instead close to circular this would favor in situ formation. Formation within the circumbinary disk beyond $\approx$ 30 au suggests disk

instability as the formation mechanism for ROXs 42B b, given the expected disk surface density, and shortened lifetime around moderately separated binaries, as it would be challenging to assemble a massive planet through core accretion.

ACKNOWLEDGMENTS

3.7 Acknowledgments

Some of the data presented herein were obtained at Keck Observatory, which is a private 501(c)3 non-profit organization operated as a scientific partnership among the California Institute of Technology, the University of California, and the National Aeronautics and Space Administration. The Observatory was made possible by the generous financial support of the W. M. Keck Foundation.

The authors wish to recognize and acknowledge the very significant cultural role and reverence that the summit of Maunakea has always had within the Native Hawaiian community. We are most fortunate to have the opportunity to conduct observations from this mountain. This research has made use of the Keck Observatory Archive (KOA), which is operated by the W. M. Keck Observatory and the NASA Exoplanet Science Institute (NExScI), under contract with the National Aeronautics and Space Administration.

References

Artymowicz, Pawel and Stephen H. Lubow (Feb. 1994). "Dynamics of Binary-Disk Interaction. I. Resonances and Disk Gap Sizes". In: *The Astrophysical Journal* 421, p. 651. ISSN: 0004-637X. DOI: 10.1086/173679.

Asensio-Torres, R. et al. (Nov. 2018). "SPOTS: The Search for Planets Orbiting Two Stars - III. Complete sample and statistical analysis". en. In: *Astronomy & Astrophysics* 619, A43. ISSN: 0004-6361, 1432-0746. DOI: 10.1051/0004-6361/201833349.

Bailey, Vanessa et al. (Jan. 2014). "HD 106906 b: A Planetary-mass Companion Outside a Massive Debris Disk". In: *The Astrophysical Journal* 780, p. L4. ISSN: 0004-637X. DOI: 10.1088/2041-8205/780/1/L4.

Barenfeld, Scott A. et al. (June 2019). "The Effect of Binarity on Circumstellar Disk Evolution". en. In: *The Astrophysical Journal* 878.1, p. 45. ISSN: 0004-637X. DOI: 10.3847/1538-4357/ab1e50.

Bate, Matthew R. (Feb. 2012). "Stellar, brown dwarf and multiple star properties from a radiation hydrodynamical simulation of star cluster formation". In: *Monthly Notices of the Royal Astronomical Society* 419.4, pp. 3115–3146. ISSN: 0035-8711. DOI: 10.1111/j.1365-2966.2011.19955.x.

Beuzit, J.-L. et al. (July 2008). "SPHERE: a 'Planet Finder' instrument for the VLT". In: *Ground-based and Airborne Instrumentation for Astronomy II*. Vol. 7014. 701418, p. 701418. DOI: 10.1117/12.790120.

Blunt, Sarah et al. (May 2017). "Orbits for the Impatient: A Bayesian Rejection-sampling Method for Quickly Fitting the Orbits of Long-period Exoplanets". In: *The Astronomical Journal* 153, p. 229. ISSN: 0004-6256. DOI: 10.3847/1538-3881/aa6930.

Blunt, Sarah et al. (Mar. 2020). "orbitize!: A Comprehensive Orbit-fitting Software Package for the High-contrast Imaging Community". In: *The Astronomical Journal* 159, p. 89. ISSN: 0004-6256. DOI: 10.3847/1538-3881/ab6663.

Bohn, A. J. et al. (Feb. 2020a). "The Young Suns Exoplanet Survey: Detection of a wide-orbit planetary-mass companion to a solar-type Sco-Cen member". In: *Monthly Notices of the Royal Astronomical Society* 492, pp. 431–443. ISSN: 0035-8711. DOI: 10.1093/mnras/stz3462.

Bohn, Alexander J. et al. (July 2020b). "Two Directly Imaged, Wide-orbit Giant Planets around the Young, Solar Analog TYC 8998-760-1". In: *The Astrophysical Journal* 898, p. L16. ISSN: 0004-637X. DOI: 10.3847/2041-8213/aba27e.

Bouvier, J. and I. Appenzeller (Feb. 1992). "A magnitude-limited spectroscopic and photometric survey of rho OphiuchusX-ray sources." en. In: *Astronomy and Astrophysics Supplement Series* 92, pp. 481–516. ISSN: 0365-0138.

Bowler, Blunt, and Nielsen (Jan. 2020). "Population-level Eccentricity Distributions of Imaged Exoplanets and Brown Dwarf Companions: Dynamical Evidence for Distinct Formation Channels*". In: *The Astronomical Journal* 159.2, p. 63. ISSN: 1538-3881. DOI: 10.3847/1538-3881/ab5b11.

Bowler, Brendan P. et al. (Apr. 2023). "Rotation Periods, Inclinations, and Obliquities of Cool Stars Hosting Directly Imaged Substellar Companions: Spin-Orbit Misalignments Are Common". In: *The Astronomical Journal* 165, p. 164. ISSN: 0004-6256. DOI: 10.3847/1538-3881/acbd34.

Bowler et al. (Mar. 2014). "Spectroscopic Confirmation of Young Planetary-Mass Companions on Wide Orbits". In: *The Astrophysical Journal* 784.1, p. 65. ISSN: 0004-637X, 1538-4357. DOI: 10.1088/0004-637X/784/1/65. (Visited on 06/30/2022).

Brinch, Christian et al. (Oct. 2016). "Misaligned Disks in the Binary Protostar IRS 43". In: *The Astrophysical Journal* 830, p. L16. ISSN: 0004-637X. DOI: 10.3847/2041-8205/830/1/L16.

Bryan, M. L. et al. (Aug. 2016). "Searching for Scatterers: High-Contrast Imaging of Young Stars Hosting Wide-Separation Planetary-Mass Companions". In: 827, 100, p. 100. DOI: 10.3847/0004-637X/827/2/100. arXiv: 1606.06744 [astro-ph.EP].

Chachan et al. (Jan. 2023). "Breaking Degeneracies in Formation Histories by Measuring Refractory Content in Gas Giants". en. In: *The Astrophysical Journal* 943.2, p. 112. ISSN: 0004-637X. DOI: 10.3847/1538-4357/aca614.

Chiang, Eugene I. and Ruth A. Murray-Clay (June 2004). "The Circumbinary Ring of KH 15D". In: *The Astrophysical Journal* 607, pp. 913–920. ISSN: 0004-637X. DOI: 10.1086/383522.

Coleman, Gavin A L, Richard P Nelson, and Amaury H M J Triaud (July 2023). "Global N-body simulations of circumbinary planet formation around Kepler-16 and -34 analogues I: Exploring the pebble accretion scenario". In: *Monthly Notices of the Royal Astronomical Society* 522.3, pp. 4352–4373. ISSN: 0035-8711. DOI: 10.1093/mnras/stad833.

Cridland et al. (Oct. 2020). "Connecting planet formation and astrochemistry - C/Os and N/Os of warm giant planets and Jupiter analogues". en. In: *Astronomy & Astrophysics* 642, A229. ISSN: 0004-6361, 1432-0746. DOI: 10.1051/0004-6361/202038767.

Currie, Thayne et al. (Jan. 2014). "Direct Imaging and Spectroscopy of a Candidate Companion Below/Near the Deuterium-Burning Limit In The Young Binary Star System, ROXs 42B". In: *The Astrophysical Journal* 780.2, p. L30. ISSN: 2041-8205, 2041-8213. DOI: 10.1088/2041-8205/780/2/L30.

Currie et al. (July 2023). "Direct Imaging and Spectroscopy of Extrasolar Planets". In: 534, p. 799. DOI: 10.48550/arXiv.2205.05696.

Czekala, Ian et al. (Sept. 2019). “The Degree of Alignment between Circumbinary Disks and Their Binary Hosts”. en. In: *The Astrophysical Journal* 883.1, p. 22. ISSN: 0004-637X. DOI: 10.3847/1538-4357/ab287b.

Di Folco, E. et al. (May 2014). “GG Tauri: the fifth element”. In: *Astronomy and Astrophysics* 565, p. L2. ISSN: 0004-6361. DOI: 10.1051/0004-6361/201423675.

Do Ó, Clarissa R. et al. (July 2023). “The Orbital Eccentricities of Directly Imaged Companions Using Observable-based Priors: Implications for Population-level Distributions”. en. In: *The Astronomical Journal* 166.2, p. 48. ISSN: 1538-3881. DOI: 10.3847/1538-3881/acdc9a.

Dohlen, K. et al. (July 2008). “The infra-red dual imaging and spectrograph for SPHERE: design and performance”. In: *Ground-based and Airborne Instrumentation for Astronomy II*. Vol. 7014. 70143L, p. 70143L. DOI: 10.1117/12.789786.

Dupuy, Trent J. et al. (Feb. 2023). “On the masses, age, and architecture of the VHSJ12561257AB b system”. In: *Monthly Notices of the Royal Astronomical Society* 519.2, pp. 1688–1694. ISSN: 0035-8711. DOI: 10.1093/mnras/stac3557.

Dupuy et al. (Mar. 2022). “Orbital Architectures of Planet-Hosting Binaries II. Low Mutual Inclinations Between Planetary and Stellar Orbits”. In: *Monthly Notices of the Royal Astronomical Society* 512.1, pp. 648–660. ISSN: 0035-8711, 1365-2966. DOI: 10.1093/mnras/stac306.

Durisen, R. H. et al. (Jan. 2007). *Gravitational Instabilities in Gaseous Protoplanetary Disks and Implications for Giant Planet Formation*. eprint: arXiv:astro-ph/0603179: University of Arizona Press. DOI: 10.48550/arXiv.astro-ph/0603179.

Dvorak, R. (Oct. 1986). “Critical orbits in the elliptic restricted three-body problem.” In: *Astronomy and Astrophysics* 167, pp. 379–386. ISSN: 0004-6361.

Elsender, Daniel et al. (Aug. 2023). “On the frequencies of circumbinary discs in protostellar systems”. In: *Monthly Notices of the Royal Astronomical Society* 523.3, pp. 4353–4364. ISSN: 0035-8711. DOI: 10.1093/mnras/stad1695.

Farago, F. and J. Laskar (Jan. 2010). “High-inclination orbits in the secular quadrupolar three-body problem”. In: *Monthly Notices of the Royal Astronomical Society* 401.2, pp. 1189–1198. ISSN: 0035-8711. DOI: 10.1111/j.1365-2966.2009.15711.x.

Ford, Eric B., Boris Kozinsky, and Frederic A. Rasio (May 2000). “Secular Evolution of Hierarchical Triple Star Systems”. In: *The Astrophysical Journal* 535, pp. 385–401. ISSN: 0004-637X. DOI: 10.1086/308815.

Foreman-Mackey, D. et al. (Mar. 2013a). “emcee: The MCMC Hammer”. In: 125, pp. 306–312. DOI: 10.1086/670067. arXiv: 1202.3665 [astro-ph.IM].

Foreman-Mackey, Daniel et al. (Feb. 2013b). “emcee: The MCMC Hammer”. en. In: *Publications of the Astronomical Society of the Pacific* 125.925, p. 306. ISSN: 1538-3873. DOI: 10.1086/670067.

Gaia Collaboration (Nov. 2020). "VizieR Online Data Catalog: Gaia EDR3 (Gaia Collaboration, 2020)". In: *VizieR Online Data Catalog* 1350, pp. I/350. DOI: 10.26093/cds/vizier.1350.

Gauza, Bartosz et al. (May 2015). "Discovery of a Young Planetary Mass Companion to the Nearby M Dwarf VHS J125601.92-125723.9*". en. In: *The Astrophysical Journal* 804.2, p. 96. ISSN: 0004-637X. DOI: 10.1088/0004-637X/804/2/96.

Ghez, A. M. et al. (Aug. 1995). "Speckle Imaging Measurements of the Relative Tangential Velocities of the Components of T Tauri Binary Stars". In: 110, p. 753. DOI: 10.1086/117560.

Ghez, A. M. et al. (Dec. 1998). "High Proper-Motion Stars in the Vicinity of Sagittarius A*: Evidence for a Supermassive Black Hole at the Center of Our Galaxy". In: 509.2, pp. 678–686. DOI: 10.1086/306528. arXiv: astro-ph/9807210 [astro-ph].

Goldberg, Max et al. (Nov. 2023). "A 5MJup non-transiting coplanar circumbinary planet around Kepler-1660AB". In: *Monthly Notices of the Royal Astronomical Society* 525, pp. 4628–4641. ISSN: 0035-8711. DOI: 10.1093/mnras/stad2568.

Gomez Gonzalez, Carlos Alberto et al. (July 2017). "VIP: Vortex Image Processing Package for High-contrast Direct Imaging". In: *The Astronomical Journal* 154, p. 7. ISSN: 0004-6256. DOI: 10.3847/1538-3881/aa73d7.

Guilloteau, Dutrey, and Simon (Aug. 1999). "GG Tauri: the ring world". In: *Astronomy and Astrophysics* 348, pp. 570–578. ISSN: 0004-6361.

Haffert, S. Y. et al. (June 2019). "Two accreting protoplanets around the young star PDS 70". In: *Nature Astronomy* 3, pp. 749–754. ISSN: 2397-3366. DOI: 10.1038/s41550-019-0780-5.

Harris, Robert J. et al. (June 2012). "A Resolved Census of Millimeter Emission from Taurus Multiple Star Systems". In: *The Astrophysical Journal* 751, p. 115. ISSN: 0004-637X. DOI: 10.1088/0004-637X/751/2/115.

He, Matthias Y. and Cristobal Petrovich (Feb. 2018). "On the stability and collisions in triple stellar systems". In: *Monthly Notices of the Royal Astronomical Society* 474.1, pp. 20–31. ISSN: 0035-8711. (Visited on 02/13/2025).

Heath, R. M. and C. J. Nixon (Sept. 2020). "On the orbital evolution of binaries with circumbinary discs". en. In: *Astronomy & Astrophysics* 641, A64. ISSN: 0004-6361, 1432-0746. DOI: 10.1051/0004-6361/202038548.

Hirsh, Kieran et al. (Sept. 2020). "On the cavity size in circumbinary discs". In: *Monthly Notices of the Royal Astronomical Society* 498.2, pp. 2936–2947. ISSN: 0035-8711. DOI: 10.1093/mnras/staa2536.

Hogg, D. W., J. Bovy, and D. Lang (Aug. 2010). "Data analysis recipes: Fitting a model to data". In: *ArXiv e-prints*. arXiv: 1008.4686 [astro-ph.IM].

Holman, Matthew J. and Paul A. Wiegert (Jan. 1999). "Long-Term Stability of Planets in Binary Systems". In: *The Astronomical Journal* 117, pp. 621–628. ISSN: 0004-6256. DOI: 10.1086/300695.

Hut, P. (May 1983). "Binary-single star scattering. II - Analytic approximations for high velocity". In: *The Astrophysical Journal* 268, pp. 342–355. ISSN: 0004-637X. DOI: 10.1086/160957.

Hut, P. and J. N. Bahcall (May 1983). "Binary-single star scattering. I - Numerical experiments for equal masses". In: *The Astrophysical Journal* 268, pp. 319–341. ISSN: 0004-637X. DOI: 10.1086/160956.

Inglis, Julie et al. (May 2024). "Atmospheric Retrievals of the Young Giant Planet ROXs 42B b from Low- and High-resolution Spectroscopy". In: *The Astronomical Journal* 167, p. 218. ISSN: 0004-6256. DOI: 10.3847/1538-3881/ad2771.

Jensen-Clem, Rebecca et al. (Dec. 2020). "A Search for Polarized Thermal Emission from Directly Imaged Exoplanets and Brown Dwarf Companions to Nearby Stars". In: 160.6, 286, p. 286. DOI: 10.3847/1538-3881/abc33d.

Kennedy, Grant M. et al. (Jan. 2019). "A circumbinary protoplanetary disk in a polar configuration". In: *Nature Astronomy* 3, pp. 230–235. ISSN: 2397-3366. DOI: 10.1038/s41550-018-0667-x.

Keppler, M. et al. (Sept. 2018). "Discovery of a planetary-mass companion within the gap of the transition disk around PDS 70". In: *Astronomy and Astrophysics* 617, A44. ISSN: 0004-6361. DOI: 10.1051/0004-6361/201832957.

Keppler et al. (July 2020). "Gap, shadows, spirals, and streamers: SPHERE observations of binary-disk interactions in GG Tauri A". en. In: *Astronomy & Astrophysics* 639, A62. ISSN: 0004-6361, 1432-0746. DOI: 10.1051/0004-6361/202038032.

Kikuchi, Akihiro, Arika Higuchi, and Shigeru Ida (Dec. 2014). "Orbital Circularization of a Planet Accreting Disk Gas: The Formation of Distant Jupiters in Circular Orbits Based on a Core Accretion Model". In: *The Astrophysical Journal* 797, p. 1. ISSN: 0004-637X. DOI: 10.1088/0004-637X/797/1/1.

Konopacky, Q. M. et al. (May 2007). "Measuring the Mass of a Pre-Main-Sequence Binary Star through the Orbit of TWA 5A". In: 133.5, pp. 2008–2014. DOI: 10.1086/513010. arXiv: astro-ph/0701551 [astro-ph].

Kraus, Adam L. et al. (Dec. 2011). "The Role of Multiplicity in Disk Evolution and Planet Formation". en. In: *The Astrophysical Journal* 745.1, p. 19. ISSN: 0004-637X. DOI: 10.1088/0004-637X/745/1/19.

Kraus, Stefan et al. (Sept. 2020). "A triple-star system with a misaligned and warped circumstellar disk shaped by disk tearing". In: *Science* 369, pp. 1233–1238. ISSN: 0036-8075. DOI: 10.1126/science.aba4633.

Kraus et al. (Dec. 2013). "Three Wide Planetary-Mass Companions to FW Tau, ROXs 12, and ROXs 42B". In: *The Astrophysical Journal* 781.1, p. 20. ISSN: 0004-637X, 1538-4357. DOI: 10.1088/0004-637X/781/1/20.

Kuzuhara, M. et al. (Apr. 2011). “The Widest-separation Substellar Companion Candidate to a Binary T Tauri Star”. In: *The Astronomical Journal* 141, p. 119. ISSN: 0004-6256. DOI: 10.1088/0004-6256/141/4/119.

Lagrange, A. -M. et al. (Jan. 2009). “A probable giant planet imaged in the Pictoris disk. VLT/NaCo deep L’-band imaging”. In: *Astronomy and Astrophysics* 493, pp. L21–L25. ISSN: 0004-6361. DOI: 10.1051/0004-6361:200811325.

Lagrange, A. -M. et al. (Aug. 2019). “Evidence for an additional planet in the Pictoris system”. In: *Nature Astronomy* 3, pp. 1135–1142. ISSN: 2397-3366. DOI: 10.1038/s41550-019-0857-1.

Langlois, M. et al. (July 2014). “High contrast polarimetry in the infrared with SPHERE on the VLT”. In: *Ground-based and Airborne Instrumentation for Astronomy V*. Vol. 9147. 91471R, 91471R. DOI: 10.1117/12.2055549.

Lithwick, Yoram and Smadar Naoz (Dec. 2011). “The Eccentric Kozai Mechanism for a Test Particle”. In: *The Astrophysical Journal* 742, p. 94. ISSN: 0004-637X. DOI: 10.1088/0004-637X/742/2/94.

Lu, J. R. et al. (Jan. 2009). “A Disk of Young Stars at the Galactic Center as Determined by Individual Stellar Orbits”. In: 690.2, pp. 1463–1487. DOI: 10.1088/0004-637X/690/2/1463. arXiv: 0808.3818 [astro-ph].

Lu, Tiger et al. (May 2023). “Self-consistent Spin, Tidal, and Dynamical Equations of Motion in the REBOUNDx Framework”. en. In: *The Astrophysical Journal* 948.1, p. 41. ISSN: 0004-637X. DOI: 10.3847/1538-4357/acc06d.

Mardling, Rosemary A. (Jan. 2001). “Stability in the General Three-Body Problem”. In: 229. Conference Name: Evolution of Binary and Multiple Star Systems ADS Bibcode: 2001ASPC..229..101M, p. 101.

Marois, C. et al. (Aug. 2006). “Accurate Astrometry and Photometry of Saturated and Coronagraphic Point Spread Functions”. In: 647, pp. 612–619. DOI: 10.1086/505191. eprint: astro-ph/0604256.

Marois, C. et al. (Nov. 2008). “Direct Imaging of Multiple Planets Orbiting the Star HR 8799”. In: *Science* 322.5906, pp. 1348–1352. ISSN: 0036-8075, 1095-9203. DOI: 10.1126/science.1166585.

Matthews, K. et al. (July 1996). “The First Diffraction-Limited Images from the W. M. Keck Telescope”. In: 108, p. 615. DOI: 10.1086/133773.

Miret-Roig, Núria et al. (Feb. 2022). “A rich population of free-floating planets in the Upper Scorpius young stellar association”. In: *Nature Astronomy* 6, pp. 89–97. ISSN: 2397-3366. DOI: 10.1038/s41550-021-01513-x.

Moe, Maxwell and Rosanne Di Stefano (June 2017). “Mind Your Ps and Qs: The Interrelation between Period (P) and Mass-ratio (Q) Distributions of Binary Stars”. en. In: *The Astrophysical Journal Supplement Series* 230.2, p. 15. ISSN: 0067-0049. DOI: 10.3847/1538-4365/aa6fb6.

Mollière et al. (Aug. 2020). "Retrieving scattering clouds and disequilibrium chemistry in the atmosphere of HR 8799e". en. In: *Astronomy & Astrophysics* 640, A131. ISSN: 0004-6361, 1432-0746. DOI: 10.1051/0004-6361/202038325. (Visited on 01/24/2025).

Montmerle, Thierry et al. (1983). "Einstein observations of the Rho Ophiuchi dark cloud-an X-ray Christmas tree". In: *Astrophysical Journal, Part 1 (ISSN 0004-637X), vol. 269, June 1, 1983, p. 182-201. Research supported by the Ministere des Relations Exterieures of France.* 269, pp. 182–201.

Mylläri, A. et al. (May 2018). "Stability of hierarchical triples - I. Dependence on inner eccentricity and inclination". In: *Monthly Notices of the Royal Astronomical Society* 476, pp. 830–841. ISSN: 0035-8711. DOI: 10.1093/mnras/sty237.

Naoz, Smadar et al. (June 2017). "The Eccentric Kozai–Lidov Mechanism for Outer Test Particle". en. In: *The Astronomical Journal* 154.1, p. 18. ISSN: 1538-3881. DOI: 10.3847/1538-3881/aa6fb0.

Nasedkin et al. (July 2024). "Four-of-a-kind? Comprehensive atmospheric characterisation of the HR 8799 planets with VLTI/GRAVITY". In: *Astronomy and Astrophysics* 687, A298. ISSN: 0004-6361. DOI: 10.1051/0004-6361/202449328.

Nielsen, Eric L. et al. (July 2019). "The Gemini Planet Imager Exoplanet Survey: Giant Planet and Brown Dwarf Demographics from 10 to 100 au". In: *The Astronomical Journal* 158, p. 13. ISSN: 0004-6256. DOI: 10.3847/1538-3881/ab16e9.

Öberg, Karin I. and Edwin A. Bergin (Jan. 2021). "Astrochemistry and compositions of planetary systems". In: *Physics Reports* 893, pp. 1–48. ISSN: 0370-1573. DOI: 10.1016/j.physrep.2020.09.004.

Palma-Bifani, P. et al. (Mar. 2024). "Atmospheric properties of AF Lep b with forward modeling". en. In: *Astronomy & Astrophysics* 683, A214. ISSN: 0004-6361, 1432-0746. DOI: 10.1051/0004-6361/202347653.

Perets, Hagai B. and M. B. N. Kouwenhoven (Apr. 2012). "On the Origin of Planets at Very Wide Orbits From the Recapture of Free Floating Planets". en. In: *The Astrophysical Journal* 750.1, p. 83. ISSN: 0004-637X. DOI: 10.1088/0004-637X/750/1/83.

Pierens, A and R P Nelson (June 2018). "Orbital alignment of circumbinary planets that form in misaligned circumbinary discs: the case of Kepler-413b". In: *Monthly Notices of the Royal Astronomical Society* 477.2, pp. 2547–2559. ISSN: 0035-8711. DOI: 10.1093/mnras/sty780.

– (May 2008). "On the formation and migration of giant planets in circumbinary discs". In: *Astronomy and Astrophysics* 483, pp. 633–642. ISSN: 0004-6361. DOI: 10.1051/0004-6361:200809453.

Proszkow, Eva-Marie and Fred C. Adams (Dec. 2009). "Dynamical Evolution of Young Embedded Clusters: A Parameter Space Survey". In: *The Astrophysical Journal Supplement Series* 185, pp. 486–510. ISSN: 0067-0049. DOI: 10.1088/0067-0049/185/2/486.

Ratzka, Thorsten, Rainer Koehler, and Christoph Leinert (July 2005). "A Multiplicity Survey of the Rho Ophiuchi Molecular Clouds". In: *Astronomy & Astrophysics* 437.2, pp. 611–626. ISSN: 0004-6361, 1432-0746. DOI: 10.1051/0004-6361:20042107.

Rein, H. and S. F. Liu (Jan. 2012). "REBOUND: an open-source multi-purpose N-body code for collisional dynamics". In: *Astronomy and Astrophysics* 537, A128. ISSN: 0004-6361. DOI: 10.1051/0004-6361/201118085.

Rodet, L. et al. (June 2017). "Origin of the wide-orbit circumbinary giant planet HD 106906. A dynamical scenario and its impact on the disk". In: *Astronomy and Astrophysics* 602, A12. ISSN: 0004-6361. DOI: 10.1051/0004-6361/201630269.

Schmeja, Kumar, and Ferreira (Sept. 2008). "The structures of embedded clusters in the Perseus, Serpens and Ophiuchus molecular clouds". In: *Monthly Notices of the Royal Astronomical Society* 389.3, pp. 1209–1217. ISSN: 0035-8711. DOI: 10.1111/j.1365-2966.2008.13442.x.

Shadmehri, Mohsen and Fazeleh Khajenabi (Feb. 2015). "On the location of the ice line in circumbinary discs". In: *Monthly Notices of the Royal Astronomical Society* 447.2, pp. 1439–1443. ISSN: 0035-8711. DOI: 10.1093/mnras/stu2522.

Simon, M. et al. (Apr. 1995). "A Lunar Occultation and Direct Imaging Survey of Multiplicity in the Ophiuchus and Taurus Star-forming Regions". In: 443, p. 625. DOI: 10.1086/175554.

Sivaramakrishnan, A. and B. R. Oppenheimer (Aug. 2006). "Astrometry and Photometry with Coronagraphs". In: 647, pp. 620–629. DOI: 10.1086/505192. eprint: astro-ph/0606136.

Sutherland, Adam P and Kaitlin M Kratter (Aug. 2019). "Instabilities in multiplanet circumbinary systems". In: *Monthly Notices of the Royal Astronomical Society* 487.3, pp. 3288–3304. ISSN: 0035-8711. DOI: 10.1093/mnras/stz1503.

Toci, Claudia et al. (Aug. 2024). "Orbital dynamics in the GG Tau A system: Investigating its enigmatic disc". en. In: *Astronomy & Astrophysics* 688, A102. ISSN: 0004-6361, 1432-0746. DOI: 10.1051/0004-6361/202348470.

Toonen, S., T. C. N. Boekholt, and S. Portegies Zwart (May 2022). "Stellar triples on the edge - Comprehensive overview of the evolution of destabilised triples leading to stellar and binary exotica". en. In: *Astronomy & Astrophysics* 661, A61. ISSN: 0004-6361, 1432-0746. DOI: 10.1051/0004-6361/202141991.

Toonen, S. et al. (Aug. 2020). “The evolution of stellar triples - The most common evolutionary pathways”. en. In: *Astronomy & Astrophysics* 640, A16. ISSN: 0004-6361, 1432-0746. DOI: 10.1051/0004-6361/201936835.

Verrier, P. E. and N. W. Evans (Apr. 2009). “High-inclination planets and asteroids in multistellar systems”. In: *Monthly Notices of the Royal Astronomical Society* 394.4, pp. 1721–1726. ISSN: 0035-8711. DOI: 10.1111/j.1365-2966.2009.14446.x.

Vousden, Will, Will M. Farr, and Ilya Mandel (Jan. 2021). “ptemcee: A parallel-tempered version of emcee”. In: *Astrophysics Source Code Library*, ascl:2101.006.

Wagner, Kevin, Dániel Apai, and Kaitlin M. Kratter (May 2019). “On the Mass Function, Multiplicity, and Origins of Wide-orbit Giant Planets”. In: *The Astrophysical Journal* 877, p. 46. ISSN: 0004-637X. DOI: 10.3847/1538-4357/ab1904.

Wang, Ji et al. (Dec. 2022). “Retrieving C and O Abundance of HR 8799 c by Combining High- and Low-resolution Data”. en. In: *The Astronomical Journal* 165.1, p. 4. ISSN: 1538-3881. DOI: 10.3847/1538-3881/ac9f19.

Wilking, Vrba, and Sullivan (Dec. 2015). “Relative Proper Motions in the Rho Ophiuchi Cluster”. en. In: *The Astrophysical Journal* 815.1, p. 2. ISSN: 0004-637X. DOI: 10.1088/0004-637X/815/1/2.

Xuan, W. Jerry et al. (Sept. 2018). “Characterizing the Performance of the NIRC2 Vortex Coronagraph at W. M. Keck Observatory”. en. In: *The Astronomical Journal* 156.4, p. 156. ISSN: 1538-3881. DOI: 10.3847/1538-3881/aadae6.

Xuan et al. (July 2024). “Are These Planets or Brown Dwarfs? Broadly Solar Compositions from High-resolution Atmospheric Retrievals of 10–30 MJup Companions”. en. In: *The Astrophysical Journal* 970.1, p. 71. ISSN: 0004-637X. DOI: 10.3847/1538-4357/ad4796.

Zhang, Yapeng et al. (July 2021). “The 13CO-rich atmosphere of a young accreting super-Jupiter”. In: *Nature* 595, pp. 370–372. ISSN: 0028-0836. DOI: 10.1038/s41586-021-03616-x.

Zhang, Zhoujian et al. (Oct. 2023). “ELemental abundances of Planets and brown dwarfs Imaged around Stars (ELPIS). I. Potential Metal Enrichment of the Exoplanet AF Lep b and a Novel Retrieval Approach for Cloudy Self-luminous Atmospheres”. en. In: *The Astronomical Journal* 166.5, p. 198. ISSN: 1538-3881. DOI: 10.3847/1538-3881/acf768.

Zhang et al. (Nov. 2024). “The ESO SupJup Survey. III. Confirmation of 13CO in YSES 1 b and Atmospheric Detection of YSES 1 c with CRIRES+”. en. In: *The Astronomical Journal* 168.6, p. 246. ISSN: 1538-3881. DOI: 10.3847/1538-3881/ad7ea9.

Chapter 4

QUARTZ CLOUDS IN THE DAYSIDE ATMOSPHERE OF THE QUINTESSENTIAL HOT JUPITER HD 189733 B

Inglis, Julie et al. (Oct. 2024). "Quartz Clouds in the Dayside Atmosphere of the Quintessential Hot Jupiter HD 189733 b". In: *The Astrophysical Journal* 973, p. L41. ISSN: 0004-637X. DOI: 10.3847/2041-8213/ad725e.

4.1 Abstract

Recent mid-infrared observations with JWST/MIRI have resulted in the first direct detections of absorption features from silicate clouds in the transmission spectra of two transiting exoplanets, WASP-17 b and WASP-107 b. In this paper, we measure the mid-infrared ($5 - 12$ μm) dayside emission spectrum of the benchmark hot Jupiter HD 189733 b with MIRI LRS by combining data from two secondary eclipse observations. We confirm the previous detection of H_2O absorption at 6.5 μm from Spitzer/IRS and additionally detect H_2S as well as an absorption feature at 8.7 μm in both secondary eclipse observations. The excess absorption at 8.7 μm can be explained by the presence of small (~0.01 μm) grains of SiO_2[s] in the uppermost layers of HD 189733 b's dayside atmosphere. This is the first direct detection of silicate clouds in HD 189733 b's atmosphere, and the first detection of a distinct absorption feature from silicate clouds on the day side of any hot Jupiter. We find that models including SiO_2[s] are preferred by $6 - 7\sigma$ over clear models and those with other potential cloud species. The high altitude location of these silicate particles is best explained by formation in the hottest regions of HD 189733 b's dayside atmosphere near the substellar point. We additionally find that HD 189733 b's emission spectrum longward of 9 μm displays residual features not well captured by our current atmospheric models. When combined with other JWST observations of HD 189733 b's transmission and emission spectrum at shorter wavelengths, these observations will provide us with the most detailed picture to date of the atmospheric composition and cloud properties of this benchmark hot Jupiter.

4.2 Introduction

HD 189733 b is unique amongst the population of hot Jupiter planets detected in the last few decades. At a distance of 19 pc, it is one of the closest of these planets,

orbiting a bright (V=7.7) K star with an orbital period of only 2.219 days (Bouchy et al., 2005). This makes HD 189733 b one of the most favorable hot Jupiter targets for detailed characterization studies. It was also one of the earliest transiting hot Jupiters discovered, and as a result it has accumulated a long list of historic firsts in the field of exoplanet atmospheric characterization.

Spitzer observations of HD 189733 b provided one of the earliest direct measurements of thermal emission from a transiting exoplanet, with a detection of its 16 μm secondary eclipse by Deming et al. (2006) using the Infrared Spectrograph (IRS). This planet was also one of the only hot Jupiters to have its mid-infrared emission spectrum measured with IRS (Grillmair et al., 2007; Grillmair et al., 2008; Todorov et al., 2014). HD 189733 b was the first planet to have its surface brightness mapped using a partial 8 μm Spitzer phase curve (Knutson et al., 2007), and the first to have a complementary dayside brightness map constructed from an ensemble of 8 μm secondary eclipses (Majeau et al., 2012; Wit et al., 2012). Both the phase curve measurements and eclipse map revealed that the hottest region in HD 189733 b's atmosphere is offset from the substellar point, indicating the presence of strong eastward jets that also warm the planet's permanently shadowed night side. HD 189733 b has been extensively studied both in transmission (e.g. Pont et al., 2007; Sing et al., 2009; Morello et al., 2014; McCullough et al., 2014) and emission (e.g. Deming et al., 2006; Knutson et al., 2007; Charbonneau et al., 2008; Agol et al., 2010; Crouzet et al., 2014), from both spaced-based observatories and ground-based telescopes. This extensive body of observations has made HD 189733 b into a benchmark system for studies of other hot Jupiters.

HD 189733 b has been the subject of many atmospheric retrieval studies over the years, both in transmission and emission (e.g. Madhusudhan et al., 2014; Welbanks et al., 2019; Zhang et al., 2020; Finnerty et al., 2023). These retrievals generally relied on a combination of spectroscopic detections of water absorption at near-infrared wavelengths and photometric constraints on the abundances of methane, carbon monoxide, and carbon dioxide at longer wavelengths. Very early on, water absorption was detected in HD 189733 b's mid-infrared dayside emission spectrum using Spitzer IRS observations (Charbonneau et al., 2008; Grillmair et al., 2008; Todorov et al., 2014). Although early transmission spectroscopy with HST/NICMOS found a near featureless spectrum at near-infrared wavelengths (Sing et al., 2009), more precise observations with HST/WFC3 later revealed a water absorption feature at 1.4 μm (McCullough et al., 2014). A comprehensive

joint retrieval on HD 189733 b's HST and Spitzer transmission and emission spectra found a modestly enhanced atmospheric metallicity of 12^{+8}_{-5} times solar and an atmospheric C/O ratio of $0.66^{+0.05}_{-0.09}$ (Zhang et al., 2020). Most recently, Finnerty et al. (2023) performed retrievals on high-resolution ground-based emission observations and found a lower C/O ratio of 0.3 ± 0.1 (2.7σ difference) and a consistent atmospheric metallicity [C/H] of $1 - 8\times$ solar. They also measure a log water abundance of -2.0 ± 0.4 (mass-mixing ratio). HD 189733 b has also been observed in both transmission and emission by four separate programs during JWST's Cycle 1; these observations will significantly improve our knowledge of its atmospheric composition.

Early transmission spectroscopy of HD 189733 b with HST also provided some of the earliest evidence for the presence of clouds or hazes in a planetary atmosphere. This planet's transmission spectrum exhibits a large optical scattering slope and muted near-infrared water absorption feature, indicating the presence of small scattering particles in the day-night terminator region (Pont et al., 2008; Lecavelier Des Etangs et al., 2008; Sing et al., 2009; Sing et al., 2011; Madhusudhan et al., 2014). Wakeford et al. (2015) identify scattering from small, sub-micron grains of enstatite ($MgSiO_3$[s]) as a potential source. Although HD 189733 is a relatively active K star, the super-Rayleigh scattering slope observed at optical wavelengths cannot be explained by the presence of unocculted star spots alone and is best reproduced by high altitude sub-μm scattering particles (Sing et al., 2011).

The presence of clouds in HD 189733 b's dayside atmosphere has also been more controversially inferred through measurements of its optical albedo. Evans et al. (2013) published a geometric albedo measurement using HST STIS that showed a sharp increase in reflected light at bluer wavelengths, suggesting the presence of sub-μm scattering aerosols. Although measurements of HD 189733 b's albedo from ground-based polarimetry initially found evidence for a significantly higher albedo (Berdyugina et al., 2011), subsequent observations by Wiktorowicz et al. (2015) resulted in a limit consistent with the lower albedo value from Evans et al. (2013). More recently, CHEOPS measured a smaller geometric albedo than found by Evans et al. (2013) using optical broadband photometry, consistent with predictions from dayside atmosphere models without significant scattering from clouds (Krenn et al., 2023). A $\sim 3\times$ solar Na abundance is required to explain both the CHEOPS and Evans et al. (2013) observations.

The current ensemble of evidence therefore suggests that HD 189733 b likely hosts

aerosols in its day-night terminator region, and these aerosols may also be abundant enough in the uppermost layers of the dayside atmosphere to significantly alter its optical albedo. Although we do not currently have any direct constraints on the composition of these aerosols, we can nonetheless make an educated guess based on HD 189733 b's measured atmospheric temperature distribution. Silicate clouds are expected to be the dominant source of cloud opacity at the temperatures and pressures relevant for most hot Jupiter atmospheres and to settle out of the visible atmosphere at temperatures just below the expected dayside temperature of HD 189733 b (Gao et al., 2020). However, general circulation models incorporating cloud formation and transport processes indicate that these particles can be carried far from their initial formation locations (Woitke et al., 2003; Parmentier et al., 2013).

Although photochemical hazes provide a plausible alternative to silicate clouds at lower temperatures, these hazes are unlikely to be present in significant quantities in HD 189733 b's dayside or terminator regions. Gao et al. (2020) predict that photochemically produced hazes should become the dominant aerosol for planetary atmospheres cooler than 950 K. This is confirmed by lab experiments which suggest hazes should be commonplace in atmospheres $\lesssim$800 K (Hörst et al., 2018; He et al., 2018). At the higher temperatures typical of HD 189733 b's day side and terminator, these hazes should be destroyed faster than they can accumulate. This suggests that silicate clouds remain the most plausible candidate for the aerosols observed in HD 189733 b's atmosphere.

Mid-infrared observations with Spitzer have confirmed the presence of silicate clouds in the atmospheres of isolated brown dwarfs at similar temperatures to hot Jupiters (e.g. Cushing et al., 2006; Burgasser et al., 2008; Burningham et al., 2021; Suárez et al., 2022). With JWST, we now have the ability to detect silicate absorption features in the atmospheres of transiting planets. Indeed, silicate cloud features have been recently confirmed with JWST/MIRI LRS in the atmospheres of both WASP-17 b (Grant et al., 2023) and WASP-107 b (Dyrek et al., 2023). JWST observations with MIRI LRS provide a means to confirm the presence of aerosols in the atmosphere of HD 189733 b and determine their composition for the first time by directly detecting their mid-infrared absorption features.

In this paper, we present an emission spectrum of the benchmark hot Jupiter HD 189733 b derived from two secondary eclipse measurements with JWST's MIRI instrument. We first discuss our observations and data reduction process (Sec. 4.4). We then compare our dayside emission spectrum to models and find an

additional absorption feature at 8.7 μm, as well as a region around 9.6 μm that is poorly matched by our models. We discuss the robustness of these features between two different data reduction pipelines, `Eureka!` and `SPARTA`, and two secondary eclipse observations (Sec. 4.5). We present possible explanations for both wavelength regions (Sec. 4.5 and 4.5), and discuss their implications for the atmosphere of HD 189733 b in context with other JWST MIRI LRS observations of transiting giant planets (Sec. 4.6).

4.3 Observations

We observe two full secondary eclipses of HD 189733 b with the JWST MIRI LRS instrument (Rieke et al., 2015) operating in slitless (SL) mode during separate visits as part of GO program 2021 (PI Brian Kilpatrick). The first visit began on October 18, 2022 16:38:42 UT and ended on Oct 18, 2022 22:29:04 UT. The second visit began on Jun 30, 2023 19:49:47 UT and ended on July 1, 2023 01:41:22 UT. We utilized the SLITLESSPRISM subarray for our observations and performed target acquisition using the FND filter. We observed with MIRI in FAST read mode with NGroups = 5, corresponding to a total integration time of 0.95 s per integration. Each secondary eclipse observation included a total of 17,035 integrations, corresponding to a total length of approximately six hours not including overheads. Due to the brightness of our target, the 26 shortest-wavelength pixels reach 80% of full-well within 5 groups, corresponding to wavelengths shorter than 5.43 μm.

4.4 Data Reduction

Following the precedent set by other JWST time series observations, (e.g. JWST Transiting Exoplanet Community Early Release Science Team et al., 2023; Kempton et al., 2023; Grant et al., 2023), we performed two independent reductions of our data using the `Eureka!` (Bell et al., 2022) and `SPARTA` (Kempton et al., 2023) pipelines in order to compare how different reduction choices affect the final spectrum. In the sections below we describe our general data reduction process and highlight key distinctions between the two pipelines.

`Eureka!` reduction

We began by using the open-source `Eureka!` (Bell et al., 2022) pipeline to reduce the MIRI observations. We used version 1.8.2 of the `JWST` pipeline (Bushouse et al., 2022), `CRDS` (Calibration Data Reference System) version 11.16.20, and version 0.9 of `Eureka!`. We followed all the default steps of `Eureka!` as described in

Table 4.1. Fitted and fixed parameters for our `Eureka!` white light curve ($5 - 12\ \mu$m) fits and retrieved values for each secondary eclipse fit both separately and jointly. Uniform priors and their bounds are denoted $\mathcal{U}$(a,b), and Guassian priors are denoted $\mathcal{N}(\mu,\sigma)$, where μ is the peak of the distribution, and σ is the width.

Parameter	Fixed/Free	Prior	Eclipse 1	Eclipse 2	Joint
		Astrophysical Model			
Orbital period, P[a]	Fixed	–	2.218575	2.218575	2.218575
Orbital eccentricity, e	Fixed	–	0	0	0
Planetary radius, R_p/R_*	Free	$\mathcal{N}(0.155,0.0001)$[b]	0.14 ± 0.02	0.17 ± 0.03	0.16 ± 0.02
Semi-major axis, a/R_*	Free	$\mathcal{N}(8.89,0.01)$[b]	8.4 ± 0.8	9.4 ± 0.9	9.1 ± 0.5
Inclination, i [degrees]	Free	$\mathcal{N}(85.72,0.02)$[b]	85 ± 1	86 ± 1	85.9 ± 0.6
Eclipse depth, F_p/F_*	Free	$\mathcal{U}(0.001,0.006)$	0.003156 ± 0.000009	0.003132 ± 0.000009	0.003143 ± 0.000006
Eclipse mid-time, T_c [BMJD_TDB]	Free	$t_0 + \mathcal{U}(0.07,0.15)$	59870.85625 ± 0.00004	60125.99235 ± 0.00004	
		Systematics Model			
y-offset, c_1	Free	$\mathcal{U}$(-1,1)	0.025 ± 0.001	0.028 ± 0.001	
x-offset, c_2	Free	$\mathcal{U}$(-1,1)	0.001 ± 0.001	0.002 ± 0.001	
PSF-width, c_3	Free	$\mathcal{U}$(-1,1)	-0.04 ± 0.001	-0.04 ± 0.01	
Linear time coefficient, c_4	Free	$\mathcal{U}$(-1,1)	-0.0032 ± 0.0001	-0.0010 ± 0.0001	
Exponential amplitude, c_5	Free	$\mathcal{U}$(-0.01,0.01)	0.00115 ± 0.00004	0.00042 ± 0.00006	
Exponential decay constant, c_6	Free	$\mathcal{U}$(0,0.2)	0.014 ± 0.001	0.010 ± 0.001	
error scale	Free	log-$\mathcal{U}$(-8,-9)	-8.2 ± 0.03	-8.2 ± 0.03	

Note. — Our retrieved systematic model and eclipse center times from our joint fit are consistent with our individual eclipse fits, so we only show the individual fits.

a - from Ivshina et al. (2022)

b - The Gaussian priors used for these values come from the best-fit values to Spitzer 8 μm transits of HD 189733 b from Table 4 in Agol et al. (2010).

Bell et al. (2022). By default, Eureka! utilizes the JWST pipeline Stage 1 steps of ramp fitting, non-linearity, gain scaling, saturation, and data quality flagging. For the jump detection step, we increased the detection threshold to 16σ to avoid introducing additional noise into our 1D spectra for this bright target, particularly at our shortest wavelengths where we had only 2-3 groups before saturation.

We also followed the default Stage 2 steps of the Eureka! pipeline, including the flat fielding and srctype steps of the JWST Science Calibration Pipeline. This meant that we skipped the background subtraction and flux calibration steps of the JWST Stage 2 pipeline in favour of the custom background subtraction and extraction of Eureka! Stage 3. This absolute flux calibration is unnecessary for our analysis, and has been shown to increase noise in the final light curves. We then passed the Stage 2 outputs through the Eureka! Stage 3 spectral extraction, which performs background subtraction and outputs 1D spectra from the 2D calibrated images.

Due to the brightness of our target, we compared both optimal and standard box extraction. For both extraction methods, we masked pixels marked as "DO NOT USE" in the data quality array as well as any other unflagged pixels with "NaN" or "inf" values for the spectral extraction. We manually set the gain value to 3.1 as per Bell et al. (2022). We performed background subtraction at each wavelength element by fitting a linear function in the cross-dispersion direction, considering only pixels outside an aperture with a half-width of 12 pixels centered on the trace. Similar to other MIRI LRS studies, we found this was sufficient to remove the observed periodic background noise (Bouwman et al., 2023; Kempton et al., 2023). For the spectral extraction step, we used an aperture with a half-width of 5 pixels centered on the fitted central pixel of the trace. We removed outliers using a double-iteration rejection scheme, flagging pixels deviating more than 5σ from the median frame. We found that our choice of extraction method had a negligible effect on our final dayside emission spectrum, and therefore elected to use optimal extraction for our final analysis.

SPARTA reduction

To validate our Eureka! reduction, we also extracted spectra using the fully independent SPARTA pipeline, first referenced in Kempton et al. (2023). Unlike Eureka!, which uses the default JWST pipeline for Stage 1 and Stage 2 of the reduction, SPARTA uses a custom routine for fitting a slope to the ramp, described in Kempton et al. (2023), that accounts for the non-linear response of groups.

This routine calculates custom weights for individual groups to straighten out non-linearity consistent across integrations resulting from sources such as the reset switch charge decay or last-frame effect. It additionally removes significant outliers that can result from cosmic rays. The non-linearity correction ignores the first group, leaving a total of four groups for this observation.

After the custom non-linearity correction in Stage 1, we used `SPARTA` to perform similar steps to those of the `JWST` pipeline Stage 2 reduction including flat fielding, gain correction, bad pixel mask and dark subtraction. For consistency we used the same reference files as for our `Eureka!` analysis to minimize potential sources of discrepancies between the two reductions. As in the `Eureka!` reduction, we use the constant gain value of 3.1 (Bell et al., 2022). Background subtraction is done by subtracting a row-wise median calculated using windows located above and below the trace, each with a width of 15 pixels and located 12 pixels from the center of the trace. We performed both optimal and standard extraction using a window with a half-width of 5 pixels centered on the trace. As with our `Eureka!` reduction, we compare both types of spectral extraction and find that they perform equivalently well, so we adopt the optimal extraction to compare with our `Eureka!` reduction.

Light Curve Fitting

We took the extracted 1D spectra from both reduction pipelines and produced spectroscopic light curves by binning into 32 bins with wavelengths between 5 and 12 μm. We used a custom binning scheme with bin widths of either 0.125, 0.25, and 0.5 μm depending on wavelength. We used 0.5 μm bins longwards of 10 μm, where the noise substantially increases due to the partially illuminated detector. We used 0.25 μm bins elsewhere except from $8.4 - 10$ μm, where we used 0.125 μm bins to better resolve that region of the spectrum. We removed outliers in our photometric time series for each bin by masking points greater than 5σ above the median value of a moving boxcar filter with a width of 10 points. For each frame we fit for an x- and y-offset by cross correlating with a median spectrum, and fitting for the peak position of the point spread function of the trace respectively. We included these values as detrending parameters in our light curve fits.

In order to fit our light curves we used the secondary eclipse model function implemented in the light curve fitting package `batman` (Kreidberg, 2015). We assumed a circular orbit, and fit for a planet/star flux ratio, F_p/F_* and secondary eclipse mid-time. For our spectroscopic light curve fits, we fixed the orbital separation, a/R_*,

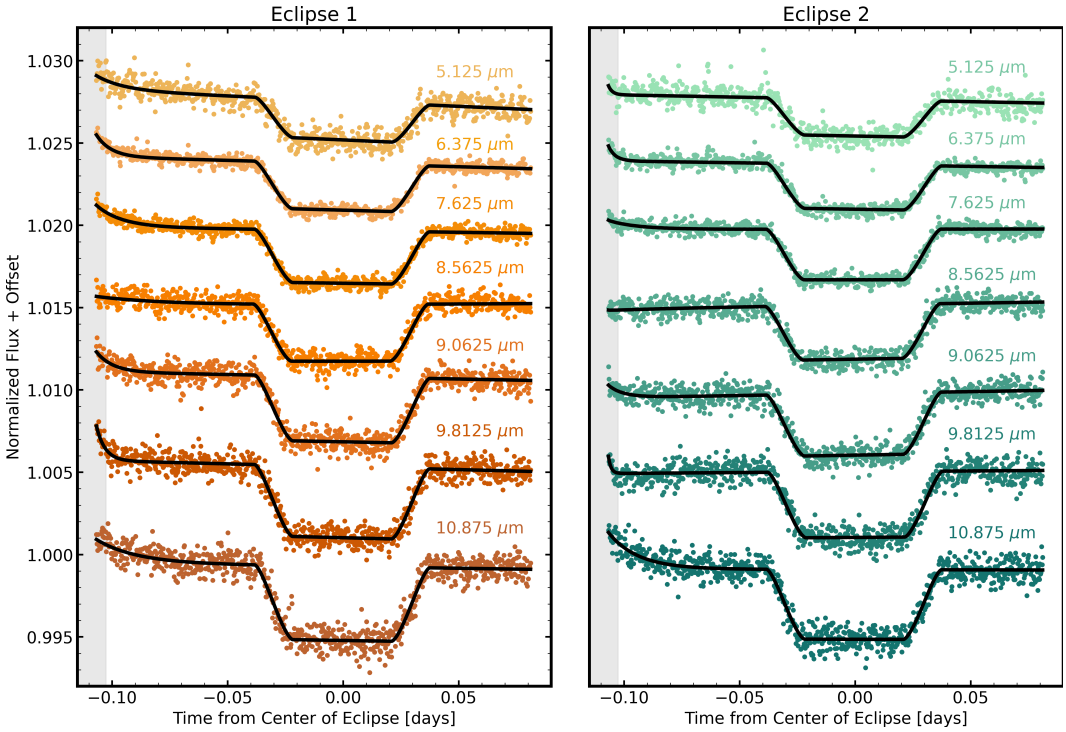

Figure 4.1 A sample of spectroscopic light curves from our `Eureka!` reduction for each of our two secondary eclipse observations. For our fits, we trim 100 integrations at the beginning of each observation to remove the sharp "hook" which cannot quite be captured by an exponential, shown in the grey shaded region. The best-fit combined instrumental and eclipse models are overplotted in black.

planetary radius R_p/R_* and inclination to the values from the white light curve fit, shown in Table 4.1.

As in other MIRI LRS time series observations (Kempton et al., 2023; Grant et al., 2023), we find that our light curves exhibit a large, wavelength dependent ramp with a structure that changes from short to long wavelengths. In Fig. 4.1 we plot a subset of representative spectroscopic light curves from this reduction with the best fit model overplotted in black. Similarly to these studies, we observed a turnover in this ramp at longer wavelengths in our second secondary eclipse observation where the ramp switches from negative to positive slope. This effect is thought to be dependent on the illumination history of the detector and its idle-recovery behaviour (Bouwman et al., 2023).

To detrend the ramp structure, we fit a combination of a linear slope and exponential ramp in time. We additionally discarded the first 350 integrations (~6 minutes) to remove the steepest part of the ramp at the start of each observation, which

is poorly fit by a single exponential. We also detrended against the x-position (dispersion direction), y-position (cross-dispersion), and the width of the PSF (δy). We subtracted the median y and x position from our position arrays, as well as the median PSF width. Our final systematics model took the form:

$$S = 1 + c_1 y + c_2 x + c_3 \delta y + c_4 t + c_5 exp(-(t - t_0)/c_6), \tag{4.1}$$

where each of the c_is represent the coefficients for each of our detrending parameters. The prior and best fit values for each parameter are summarized in Table 4.1.

Our combined model for fitting our light curves is as follows:

$$F_{rel} = M_{pl}(t) \times S(t), \tag{4.2}$$

where M_{pl} is the `batman` secondary eclipse model.

In Fig. 4.2 we plot the raw spectroscopic light curves and residuals for our `Eureka!` reduction for both secondary eclipses. Our wavelength-dependent secondary eclipse depth spectrum for our `Eureka!` reduction is shown in Fig. 4.3. A subset of our wavelength-dependent detrending parameters are shown in Fig. 4.4. In order to increase the visibility of absorption features, we convert our secondary eclipse depths to the corresponding brightness temperature using a BT-Settl model (Allard, 2014) corresponding to the best fit stellar parameters of HD 189733. We adopt the parameters from Rosenthal et al. (2021): T_{eff} = 5012 K, log(g)= 4.5, and metallicity, [Fe/H] = 0.04. We adopt the value of R_p/R_*= 0.155 from the best-fit value of 7 Spitzer 8 μm transits published in Agol et al. (2010). The BT-Settl model is consistent with the shape of our flux-calibrated in-eclipse stellar spectrum at the level of $1-2$ percent difference, using the most recent flux calibration reference file available. The larger difference occurs in the saturated region of the detector. We therefore use a stellar model in order to ensure that our estimate of the stellar flux in the saturated regions does not bias our calculated brightness temperatures. The stellar spectra from both visits show $\lesssim 0.3\%$ difference, so we use the same model for both visits. This is confirmed by ground-based monitoring of HD 189733 A, which confirms that stellar brightness variations are minimal during the time period these data was taken (Henry, G., private communication). Our secondary eclipse depths and corresponding brightness temperatures for our `Eureka!` reduction are shown in Table 4.2.

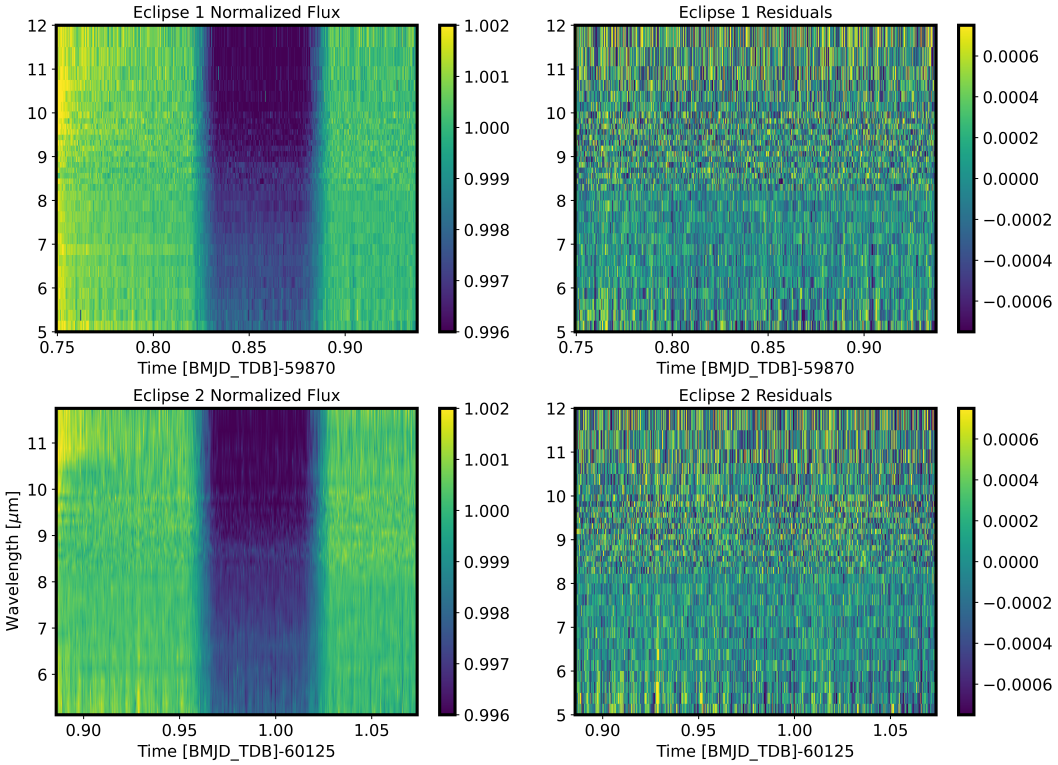

Figure 4.2 (left) Raw spectroscopic light curves from the `Eureka!` reduction for each of our MIRI LRS secondary eclipses and (right) residuals after subtracting the best-fit eclipse and instrumental ramp model. The strong wavelength-dependent instrumental ramp is visible at the beginning of the raw light curves for both observations.

`Eureka!` and `SPARTA` intercomparison

In Fig. 4.6 we plot our spectroscopic secondary eclipse depths as a function of wavelength for each eclipse and data reduction pipeline. We find the largest deviation shortwards of 5.5 μm. This occurs because most pixels are at least partially saturated in less than five groups short-wards of 5.4 μm, with the brightest pixels saturated in less than 3 groups. The small number of unsaturated groups results in a poor fit in the Stage 1 "ramps-to-slopes" step, which will bias the final eclipse depth. This effect seems to be worse for the `SPARTA` reduction, which does not remove saturated groups. Reducing the number of groups used for extracting slopes in our `SPARTA` reduction to 3 does not improve the difference between reductions. We therefore used the `Eureka!` reduction for subsequent analyses. The difference in non-linearity treatment between the `SPARTA` and `Eureka!` pipelines results in the systematic offset between reductions. The shape of the spectrum is consistent between reductions beyond 5.5 μm within 3σ therefore does not significantly impact

any of our subsequent interpretation of spectroscopic features in HD 189733b's dayside spectrum.

We find that both of our secondary eclipse observations and reductions are consistent within 3σ. However, we do see a high number of spectral channels with differences at the 2σ level than expected from just random noise. Since this also occurs for both eclipse observations between our two reductions, this suggests that our uncertainties are underestimated by a factor of $\sim 2-3$ due to unknown systematics or other noise sources. One possible source is the additional correlation between the ramp shape and eclipse depth that we do not account for in our uncertainties.

In Fig. 4.4, we examine potential trends in the best-fit parameters from our systematics model as a function of wavelength. The shape of the time-dependent ramp, particularly the linear slope with time, is the most significant change in systematics between Eclipse 1 and Eclipse 2. The largest change occurs at the region between $10-11$ μm. We observe a transition in the ramp structure from an increasing linear slope in time shortwards of 10 μm to a downwards trend from $10-11$ μm in the light curves for Eclipse 2 that is not seen in Eclipse 1 (Fig. 4.1). Comparing the difference between our `Eureka!` reductions for Eclipse 1 and Eclipse 2 to the best fit ramp parameters for each visit reveals that the largest differences in secondary eclipse depth correspond well with the largest differences in the linear slope component of the ramp. This suggests that the divergence in the ramp amplitude and linear slope results in offsets in our retrieved secondary eclipse depth. This is further supported by observed covariances between the linear slope, exponential amplitude and eclipse depth within the posteriors for our spectroscopic light curve fits. The largest differences in linear slope appear to result in changes at the $\sim 3\sigma$ level, which can be accounted for through inflation of our retrieved error bars. We see smaller differences in the ramp shape from $8.3-9$ μm between eclipses, where once again the ramp has a positive slope in Eclipse 2, and negative or zero slope in Eclipse 1. However that portion of the spectrum agrees well between visits, suggesting that only significant changes in ramp shapes as seen from $10-11$ μm bias the retrieved eclipse depth.

Comparison with Spitzer Eclipses

HD 1897333 b has been extensively studied in the mid-infrared with Spitzer. In Fig. 4.3 we compare our JWST emission spectrum to the combined Spitzer IRS spectrum from Todorov et al. (2014). We allow for an offset, but other than that find

Table 4.2. Spectroscopic eclipse depths and brightness temperatures of HD 1897333 b from our `Eureka!` reduction for Eclipse 1 and Eclipse 2.

Wavelength (μm)	Eclipse 1 depth (ppm)	Eclipse 1 T_{bright} (K)	Eclipse 2 depth (ppm)	Eclipse 2 T_{bright} (K)
5.125	2356 ± 40	1231 ± 4	2305 ± 35	1221 ± 4
5.375	2467 ± 36	1236 ± 4	2464 ± 27	1235 ± 3
5.625	2556 ± 21	1229 ± 2	2509 ± 31	1219 ± 3
5.875	2673 ± 19	1230 ± 2	2641 ± 24	1224 ± 2
6.125	2796 ± 26	1233 ± 3	2682 ± 23	1211 ± 2
6.375	2845 ± 19	1222 ± 2	2807 ± 20	1215 ± 2
6.625	2710 ± 23	1175 ± 2	2667 ± 19	1166 ± 2
6.875	2913 ± 23	1194 ± 2	2853 ± 24	1183 ± 2
7.125	2970 ± 20	1185 ± 2	3016 ± 22	1193 ± 2
7.375	3051 ± 20	1181 ± 2	3096 ± 19	1190 ± 2
7.625	3209 ± 23	1193 ± 2	3188 ± 25	1190 ± 2
7.875	3328 ± 21	1198 ± 2	3305 ± 20	1194 ± 2
8.125	3321 ± 28	1180 ± 3	3383 ± 22	1191 ± 2
8.3125	3370 ± 31	1177 ± 3	3432 ± 30	1189 ± 3
8.4375	3455 ± 29	1185 ± 3	3521 ± 28	1197 ± 3
8.5625	3461 ± 41	1179 ± 4	3414 ± 38	1171 ± 3
8.6875	3471 ± 33	1174 ± 3	3399 ± 32	1180 ± 3
8.8125	3544 ± 36	1179 ± 3	3546 ± 33	1161 ± 3
8.9375	3782 ± 38	1215 ± 3	3734 ± 31	1206 ± 3
9.0625	3970 ± 38	1242 ± 3	3880 ± 42	1226 ± 4
9.1875	3913 ± 39	1225 ± 3	4050 ± 44	1250 ± 4
9.3125	4150 ± 40	1260 ± 3	4075 ± 38	1245 ± 3
9.4375	4177 ± 35	1258 ± 3	4078 ± 36	1241 ± 3
9.5625	4119 ± 44	1242 ± 4	4062 ± 36	1232 ± 3
9.6875	4216 ± 8	1252 ± 3	4365 ± 36	1252 ± 5
9.8125	4328 ± 43	1266 ± 4	4249 ± 54	1278 ± 3
9.9375	4322 ± 43	1259 ± 4	4191 ± 40	1236 ± 4
10.125	4444 ± 30	1271 ± 4	4365 ± 35	1257 ± 3
10.375	4417 ± 38	1253 ± 4	4260 ± 33	1229 ± 3
10.625	4461 ± 42	1251 ± 5	4360 ± 37	1235 ± 3
10.875	4512 ± 60	1256 ± 3	4392 ± 50	1231 ± 4
11.25	4636 ± 56	1258 ± 5	4672 ± 58	1234 ± 5
11.75	4676 ± 73	1246 ± 6	4604 ± 59	1264 ± 5

good agreement between the slopes of the two spectra. The magnitude of the secondary eclipse depths in the Spitzer IRS data has been observed to shift depending on the correction used for the systematics and can vary significantly between individual reductions as a result (Grillmair et al., 2007; Grillmair et al., 2008; Todorov et al., 2014). In order to be consistent with the broadband observations, Zhang et al. (2020) found that a 30% relative shift upwards was required in their retrievals. Therefore while we trust the slope of the overall spectrum, we consider the overall magnitude of the Spitzer IRS emission spectrum to be unreliable.

The Spitzer IRS spectrum does not show a significant absorption feature at 8.7 μm, but this is expected given its relatively large measurement uncertainties. Like the Spitzer spectrum, our JWST spectrum shows an absorption feature from water at 6.5 μm. There is no obvious methane absorption in our spectrum, consistent with previous Spitzer observations. Both the IRS spectrum and our JWST spectrum show a dip from $10 - 11$ μm, though the magnitude of this feature varies with reduction method, and is smaller in our `Eureka!` Eclipse 1 spectrum. This is consistent with the location of absorption features from several silicate cloud features. It is also the location on the MIRI LRS detector where we observe changes in our systematics which may bias measurements of the eclipse depth (see the slopes of spectroscopic light curves shown in Fig. 4.1).

In order to facilitate comparisons between our new measurements and the previous Spitzer 8 μm photometry, we bin our data to create eclipse light curves with the same wavelength coverage as the Spitzer 8 μm bandpass (See Fig 4.3). We account for the relative throughput between Spitzer and MIRI LRS and and fit for the corresponding secondary eclipse depths. In Fig. 4.5a we plot our 8 μm eclipse depths for both Eclipse 1 and 2 using our `Eureka!` reduction. Our two 8 μm JWST secondary eclipse depths are consistent within 1σ. We compare these two secondary eclipse depths to the seven 8 μm eclipse depths published in Agol et al. (2010). We find that our two 8 μm JWST secondary eclipse depths are both smaller than any of the seven eclipses from (Agol et al., 2010), and differ from the average 8 μm eclipse depth reported in Agol et al. (2010) by 280 ppm (3σ). HD 189733 A is an active star, with observed variations in brightness across a 17 year baseline of around 5-7% based on ground-based photometric monitoring (Henry, G., private communication; Sing et al., 2011; Knutson et al., 2012). Using Eq. 7 in Zellem et al. (2017), we find that this corresponds to a change in the secondary eclipse depth of as much as 220 ppm. We conclude that the offset between the Spitzer 8 μm secondary eclipse depths and

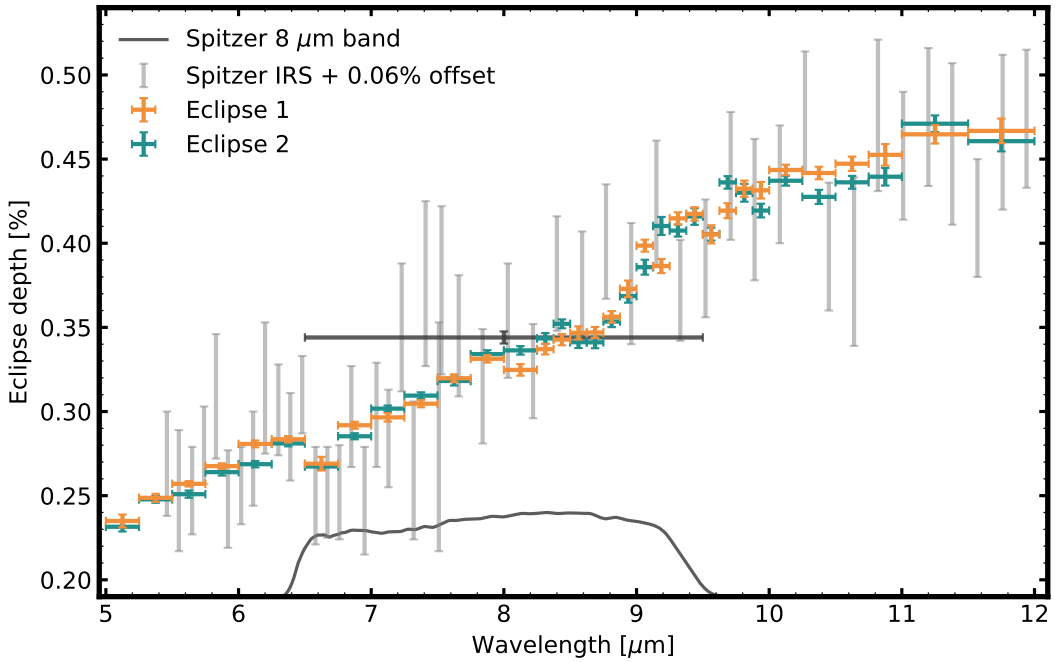

Figure 4.3 Our fitted spectroscopic secondary eclipse depths from 5 – 12 μm are plotted for both visits from our `Eureka!` reductions. The Spitzer 8 μm band response curve is shown in black. We compare our MIRI LRS emission spectrum to the Spitzer IRS spectrum from Todorov et al. (2014) (grey), with an applied offset of 0.06%. The misfit between eclipses at 10 – 11 μm matches the area of the detector where the ramp behaviour differs the most significantly between visits (see Sec 4.4).

our MIRI 8 μm secondary eclipse depths could potentially be explained by stellar variability.

We also note that the 8 μm photometry from Spitzer's IRAC instrument exhibited a ramp-like behavior similar to the one we see in our MIRI data. Agol et al. (2010) found that their measured eclipse depths were sensitive to their choice of ramp model. They ultimately selected a double exponential model for their final eclipse depth measurements, as they found that this model resulted in the best agreement in eclipse depths across their sample of seven measurements. In Fig. 4.5b we plot the best-fit ramp model for each of the seven eclipses from Agol et al. (2010), colored by increasing depth. We find that all but one of their secondary eclipses observations show strong negative time dependent ramps. Within this ensemble, we see that increasing negative ramp strength correlates with a deeper measured eclipse depth. This suggests that the ramp shape may be systematically biasing the measured eclipse depths for all visits to values that are slightly higher than the true

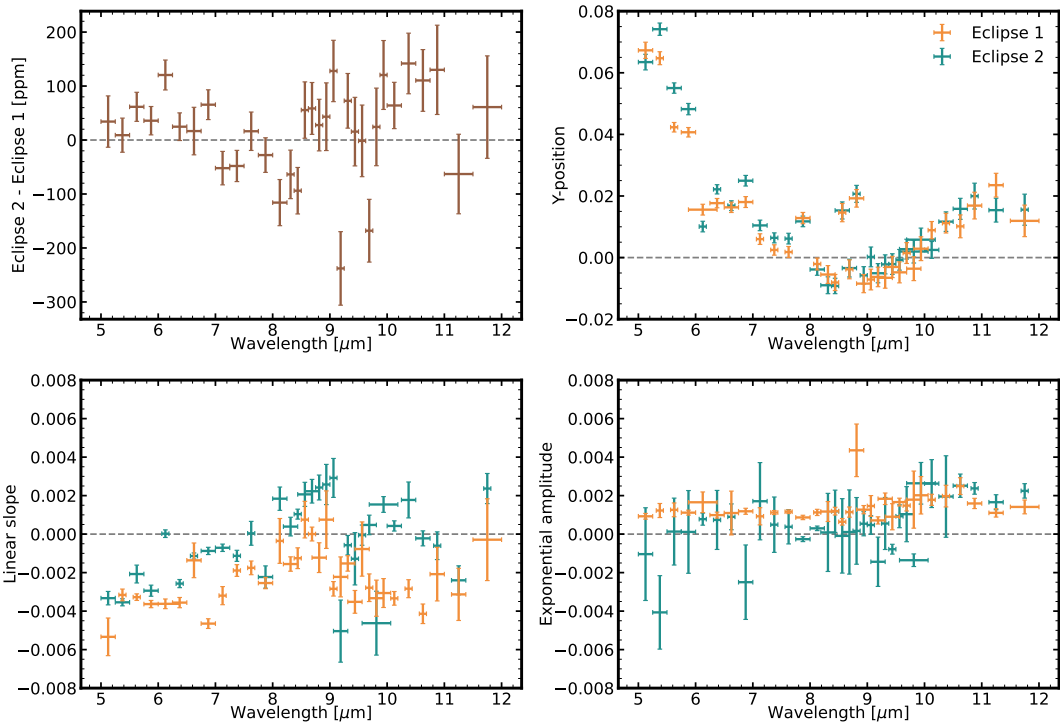

Figure 4.4 The fitted spectroscopic coefficients for three of our detrending parameters, PSF width, linear slope with time, and ramp amplitude, for each of our two secondary eclipse observations from our `Eureka!` reduction. While the best fit systematics differ between our two secondary eclipse observations, the shape of the emission spectrum is mostly consistent between the two visits at the 2σ level. The largest differences between visits occur where the linear component of the ramp varies most. The linear component of the ramp also switches sign between visits from $10-11$ μm. This suggests that this could lead to small offsets in eclipse depth (see Sec. 4.4).

value in the sample from Agol et al. (2010). In our JWST data, we see a positive ramp at these wavelengths, which could in turn bias our measured eclipse depths to slightly lower values. The offset between these two ensembles of observations is therefore also possibly explained by instrumental systematics. This slight offset from either the ramp or stellar variability would manifest in a small shift in retrieved dayside temperature.

4.5 Comparison to Models

We used two levels of model complexity and flexibility to interpret our measured mid-infrared dayside emission spectrum for HD 189733 b. First, we conducted a fully free chemistry, climate and cloud retrieval utilizing the retrieval code `petitRADTRANs`. The free retrieval framework allowed us to test different pos-

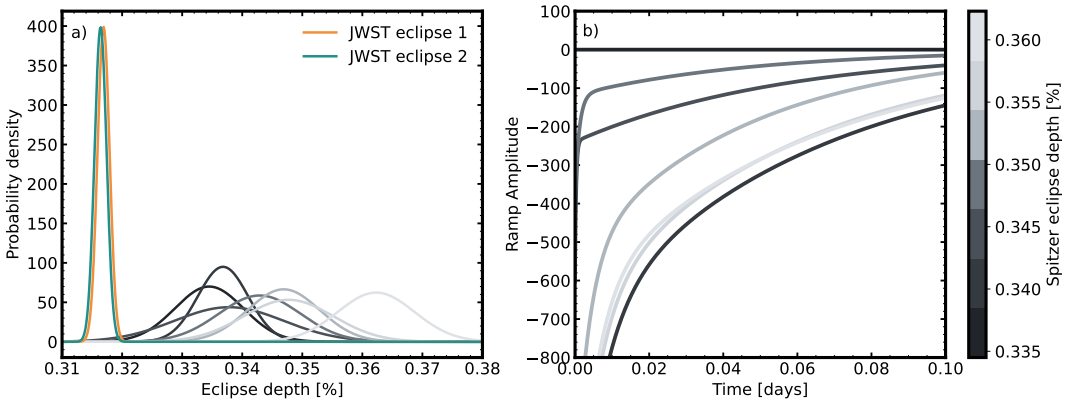

Figure 4.5 a) Measured 8 μm eclipse depths colored by eclipse depth for the seven Spitzer eclipses from Agol et al. (2010) as compared to our two JWST 8 μm eclipse depths (orange,blue). b) The ramps for the corresponding Spitzer eclipses from a) are plotted, and colored according to their depths.

sible condensate species in order to limit the species included in our forward models to reduce computational time. Second, we used `picaso` to compute a grid of radiative-convective models that were self-consistent in climate and chemistry. This imposed the strongest physical constraint on the fitting process. We leveraged the forward model grid but additionally fit for aerosol parameters that were not physically self-consistent with the climate model grid. In this case, the cloud was able to form at any pressure and was not bound by the condensation curve of the condensate species.

For both the free retrieval and grid we used a Bayesian framework to map our posterior space and determine our best fit parameters and errors. We fit both secondary eclipse measurements individually and jointly. The priors used for both fits are shown in Table 4.3, as well as our median retrieved values and 1σ uncertainties. For both our free retrievals and grid fits, we included an error inflation term, given the evidence that our uncertainties may be underestimated, as discussed in 4.4. We added a free error term added quadrature with the per point uncertainties obtained from our data reduction to obtain our combined error for our lileklihood function, σ_i so our final per point error, s_i took the form:

$$s_i^2 = \sigma_i^2 + 10^b, \tag{4.3}$$

where b is the free error scale parameter.

Table 4.3. Retrieved parameters for HD 189733 b from free retrievals with `petitRADTRANS` and `Picaso` forward grid models on our `Eureka!` reduction. For our `petitRADTRANS` retrievals, molecules with firm upper limits are reported as 99% upper limits.

Parameter	Fixed/Free	Prior	Eclipse 1	Eclipse 2	Joint
`petitRADTRANS` Free Retrievals					
T_{eq} [K]	Free	$\mathcal{U}(1000, 1400)$	1150 ± 40	1170 ± 60	1110 ± 50
T_{int} [K]	Free	$\mathcal{U}(100, 300)$	210 ± 60	210 ± 60	200 ± 60
γ	Free	$\mathcal{U}(0, 1)$	0.38 ± 0.05	0.44 ± 0.09	0.33 ± 0.06
log κ_{IR} [K]	Free	$\mathcal{U}(-6, 2)$	-1.0 ± 0.6	-1.2 ± 0.7	-0.76 ± 0.5
log (g [cgs])	Free	$\mathcal{U}(2.8, 3.8)$	3.4 ± 0.3	3.4 ± 0.3	3.7 ± 0.3
log X_{H_2O} [MMR]	Free	$\mathcal{U}(-10, 0)$	-3.0 ± 0.8	-3.0 ± 1.0	-3.7 ± 0.6
log X_{H_2S} [MMR]	Free	$\mathcal{U}(-10, 0)$	-2.2 ± 0.6	< -0.9	-2.4 ± 0.5
log X_{SO_2} [MMR]	Free	$\mathcal{U}(-10, 0)$	< -4.2	< 4.3	< -4.5
log X_{CO_2} [MMR]	Free	$\mathcal{U}(-10, 0)$	< -2.8	< 3.3	< -3.1
log $X_{SiO_2[s]}$ [MMR]	Free	$\mathcal{U}(-10, 0)$	-3.6 ± 0.6	-3.9 ± 0.8	-3.6 ± 0.7
log $r_{SiO_2[s]}$ [cm]	Free	$\mathcal{U}(-8, -3)$	-6.5 ± 0.7	-6.6 ± 0.8	-6.5 ± 0.7
log $P_{SiO_2[s]}$ [bars]	Free	$\mathcal{U}(-6, 2)$	-3.1 ± 0.6	-3.0 ± 0.8	-3.0 ± 0.6
σ_{norm}	Free	$\mathcal{U}(1.0, 3.0)$	1.9 ± 0.6	2.0 ± 0.6	1.9 ± 0.5
`PICASO` Grid Fit W/O Clouds					
heat redis.	Grid	[0.5,0.85]	$0.81^{+0.03}_{-0.06}$	$0.79^{+0.04}_{-0.04}$	$0.81^{+0.03}_{-0.04}$
M/H [dex]	Grid	[-1,1]	$-0.85^{+0.32}_{-0.1}$	$-0.72^{+0.16}_{-0.16}$	$-0.85^{+0.23}_{-0.1}$
C/O [rel. Sol=0.458]	Grid	[0.25,2]	$0.38^{+0.27}_{-0.09}$	$0.34^{+0.13}_{-0.06}$	$0.36^{+0.15}_{-0.07}$
b [log K]]	Free	$\mathcal{U}(-2.5, 2.5)$	$1.41^{+0.06}_{-0.05}$	$1.42^{+0.06}_{-0.05}$	$1.41^{+0.06}_{-0.05}$
logZ	-	-	-152	-154	-152
`PICASO` Grid Fit W/ Retrieved Clouds					
heat redis.	Grid	[0.5,0.85]	$0.83^{+0.01}_{-0.02}$	$0.82^{+0.02}_{-0.03}$	$0.82^{+0.02}_{-0.02}$
M/H [dex]	Grid	[-1,1]	$-0.88^{+0.79}_{-0.09}$	$-0.05^{+0.29}_{-0.19}$	$-0.12^{+0.19}_{-0.16}$
C/O [rel. Sol=0.458]	Grid	[0.25,2]	$0.74^{+0.77}_{-0.15}$	$1.32^{+0.14}_{-0.44}$	$1.43^{+0.06}_{-0.36}$
f_{sed} [dex]	Free	$\mathcal{U}(-1, 1)$	$-0.24^{+0.55}_{-0.51}$	$-0.46^{+0.62}_{-0.37}$	$-0.52^{+0.73}_{-0.37}$
log $\delta_{SiO_2[s]}$ [cm^{-2}]	Free	$\mathcal{U}(1, 10)$	$4.43^{+1.27}_{-1.49}$	$5.1^{+0.98}_{-1.16}$	$5.33^{+0.79}_{-1.21}$
log $r_{SiO_2[s]}$ [cm]	Free	$\mathcal{U}(-7, -3)$	$-5.21^{+1.0}_{-1.26}$	$-5.69^{+1.01}_{-0.91}$	$-5.96^{+1.17}_{-0.75}$
log $P_{SiO_2[s]}$ [bar]	Free	$\mathcal{U}(1, -4)$	$-2.85^{+1.97}_{-0.87}$	$-2.54^{+2.28}_{-1.1}$	$-3.45^{+1.0}_{-0.41}$
$\sigma_{\rm norm}$ -	Free	$\mathcal{U}(0.5, 2.5)$	$0.77^{+0.17}_{-0.18}$	$0.76^{+0.14}_{-0.17}$	$0.8^{+0.11}_{-0.18}$
b [log K]]	Free	$\mathcal{U}(-2.5, 2.5)$	$1.13^{+0.06}_{-0.06}$	$1.21^{+0.06}_{-0.06}$	$1.16^{+0.07}_{-0.06}$
logZ	-	-	-128	-135	-131

Note. — `PICASO` params: heat redis.= heat redistribution (full=0.5), M/H=log metallicity relative to solar, C/O=carbon-to-oxygen ratio relative to solar (solar=0.458), b=error inflation, fsed=cloud sedimentation efficiency, log $\delta_{SiO_2[s]}$=scaled cloud number density, log $r_{SiO_2[s]}$=mean cloud particle radius, log $P_{SiO_2[s]}$=cloud base pressure, $\sigma_{\rm norm}$=log normal radius distribution width for cloud particles, logZ=log likelihood from fitting results.

Free Bayesian Retrievals

We perform free chemistry retrievals using the retrieval framework implemented in the open-sourced `petitRADTRANS` (Mollière et al., 2019). Our retrievals included the free pressure temperature (P-T) profile parameterization from Guillot (2010), the surface gravity $\log(g)$, and the planetary radius R_P as free parameters, as well as gas phase species that might potentially be abundant enough to be detectable in the mid-infrared spectra of hot Jupiters, including H_2O, CO, CO_2, H_2S, FeH, SO_2, CH_4, C_2H_2, PH_3, HCN, NH_3, and SiO. We also include continuum opacity sources from H_2/H_2 and H_2/He collision-induced absorption. The sampling was performed using nested sampling implemented in `PyMultiNest`, the Python wrapper for MultiNest (Feroz et al., 2009), using 1000 live points. We evaluated the evidence with the sampling efficiency set to 0.3. We find an additional 95 ± 10 ppm error term added in quadrature is preferred in our free retrievals. This effectively increases our errors by a factor of $2 - 4$ depending on the channel.

We find a feature at 8.7 μm that we are unable to reproduce with the equilibrium gas phase absorbers predicted in the atmospheres of giant planets. We tested all of the gas-phase opacities available within `petitRADTRANS` and `ExoMol`, but were unable to fit these features. Next, we used Mie scattering coefficients, adapted from Kitzmann et al. (2018), to explore possible cloud species that might plausibly be present in the atmosphere of HD 1897333 b. We set up our cloud retrievals with the cloud base pressure, a power law scaling with pressure above the cloud base, cloud particle radius, and cloud abundance as free parameters. We tested scattering coefficients for MnS[s], ZnS[s], KCl[s], Fe[s], $MgSiO_3$[s], Mg_2SiO_4[s], and SiO_2[s] (where [s] refers to the solid phase). $MgSiO_3$[s] and Mg_2SiO_4[s] are thought to be the dominant silicate species in the atmospheres of hot Jupiters, but these species have strong features centered on 10 μm, not 8.7 μm (Wakeford et al., 2015). We considered both crystalline and amorphous particles when available in `petitRADTRANS`. We also fit a clear model and a simple grey cloud model with a cloud base and power-law opacity with pressure to compare with our cloudy models.

In Fig. 4.7c, we plot our best-fit joint free retrieval against our secondary eclipse brightness temperature spectrum. Our best-fit P-T profile and 1σ uncertainties are shown in Fig. 4.7d. We found that H_2O is the only gas phase molecule with a statistically significant detection in all of our fits, with a log-abundance of -3.7 ± 0.3 (MMR), irrespective of the cloud model used in the fit. This value was consistent between eclipses, and is smaller than the measurement reported in Finnerty et al.

(2023) using ground-based high-resolution spectroscopy with Keck/KPIC. We additionally detect H_2S in our first eclipse and our joint eclipse retrieval at a significance of 3.5σ. Our second eclipse retrieval only has a firm 99% upper limit of -0.9. H_2S has a broad, weak feature in the mid-infrared centered around 7 μm, which overlaps partially with the H_2O feature. As a result, it primarily affects the shape of the continuum and could be degenerate with clouds. However, the retrieved abundance of -2.2 ± 0.6 (MMR) is consistent with equilibrium chemistry predictions based on the previously derived parameters for HD 1897333 b's atmospheric composition from Finnerty et al. (2023). H_2S has also been detected in HD 189733 b's transmission spectrum (Fu et al., 2024), at an abundance of $-4.5^{+0.6}_{-0.4}$ (VMR), which is consistent at the 1.5σ level with our retrieved value. Its presence in the dayside atmosphere of HD 189733 b can be confirmed by observations at shorter wavelengths with JWST. As in Fu et al. (2024), we do not detect the photochemical product SO_2, retrieving only a strict upper limit of -4.7 (MMR). This is consistent with photochemical models for previously retrieved metallicity values for this atmosphere of $3-5\times$ solar (Fu et al., 2024).

We found that both amorphous and crystalline SiO_2[s] clouds were able to reproduce the absorption feature at 8.7 μm. Amorphous SiO_2[s] clouds were preferred only slightly to crystalline at $\lesssim 1\sigma$. We used the Bayes factor to compare to both grey cloud and clear atmosphere models and found that SiO_2[s] clouds are preferred over the clear atmosphere model at 6.0σ, and over the grey cloud model at 6.1σ for our joint eclipse retrievals. When compared to other condensate clouds, SiO_2[s] clouds are preferred to Mg_2SiO_4[s] at 6.1σ, $MgiO_3$[s] at 6.3σ, KCl[s] at 6.5σ and ZnS[s] at 6.2σ. All condensate cloud species tested but SiO_2 produce a comparably good fit to the retrieval with Mg_2SiO_4[s] shown in Fig. 4.7c as they fail to reproduce the 8.7 μm feature. We were unable to reproduce the spectral shape at 9.6 μm with any gas phase or scattering condensate opacity available in `petitRADTRANs` despite the flexibility of the free retrieval framework.

The largest difference between our `Eureka!` and `SPARTA` reductions occurs in the saturated wavelength range from $5-5.5$ μm. In order to make sure that this region is not biasing our fits, we perform additional retrievals excluding wavelengths shorter than 5.5 μm. We find no significant changes to our retrieved abundances or our retrieved cloud parameters. We also test the sensitivity of our retrieval results to our chosen binning scheme by re-binning our emission spectrum to uniform bin widths of 0.5, 0.25 and 0.125 μm. We then ran retrievals on each of these binning

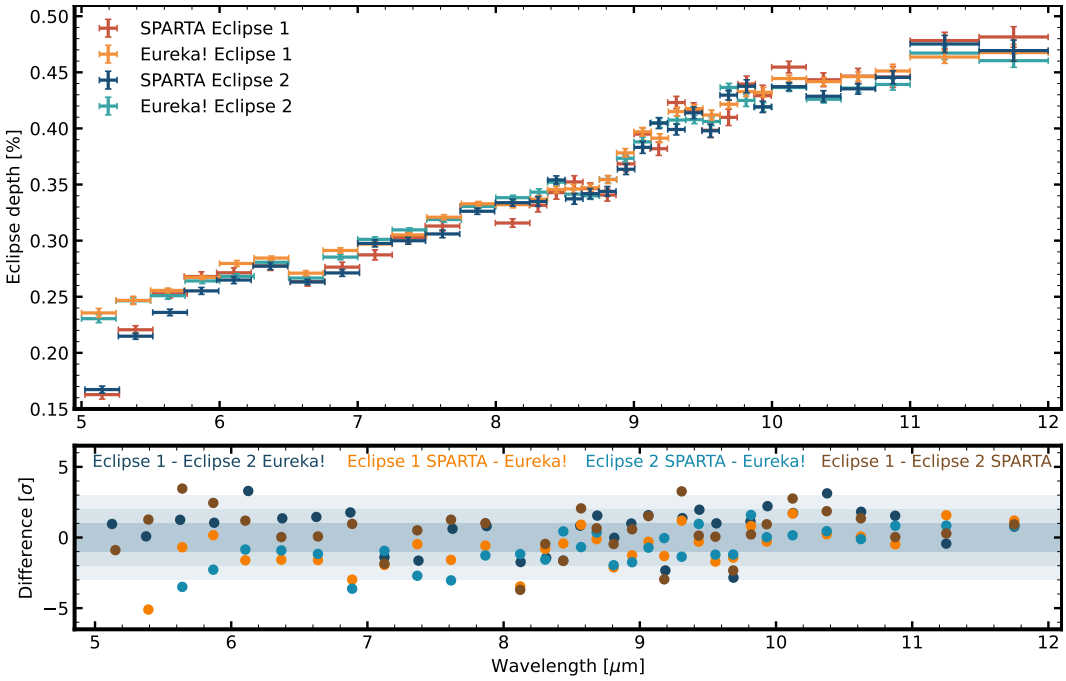

Figure 4.6 Comparison of our `Eureka!` and `SPARTA` reductions for each of our two secondary eclipse observations. The systematic differences between reductions are due to the different linearity corrections. Shortwards of 5.5 μm, the difference is increased by the partially saturated detector.

schemes and recovered consistent solutions. The only exception was our fit using 0.5 μm bins, where we found that the statistical significance of our water detection decreased due to our inability to fully resolve the water absorption feature at 6.5 microns.

Self-Consistent Radiative Convective Model Grid

The radiative-convective thermochemical equilibrium (RCTE) grid was computed using `PICASO v3.0` (Batalha et al., 2019). The climate modeling functionality in `PICASO` is based on the legacy code developed to study Titan (McKay et al., 1989) and Uranus (Marley et al., 1999). The new open source code is fully described in Mukherjee et al. (2023). Of note are the correlated-k opacities used in `PICASO`, which are described in Marley et al. (2021) and available for download in Lupu et al. (2021). The correlated-k table is precomputed using a grid of chemical equilibrium abundances for different metallicity and C/O values at 1460 pressure-temperature points. The chemistry grid contains 29 species and is detailed in Marley et al. (2021) using NASA's CEA code (Gordon et al., 1994) and the modeling work detailed in Fegley et al. (1994), Lodders (1999), Lodders (2002), Lodders et al. (2002), Visscher

et al. (2006), and Visscher et al. (2010). Lastly, our chemical equilibrium grid relies on the elemental abundances of Lodders (2010) where solar C/O=0.458.

The grid made for this analysis consisted of a total of 150 models of varying atmospheric properties at an interior temperature of 200 K and without radiatively active clouds. The properties varied were the atmospheric metallicity with six values from 0.1 to 10× solar, the C/O ratio with five values from 0.25 to 2× solar, and the heat redistribution factor with five values from 0.5 to 0.85. The heat redistribution factors specifically cluster around the higher values, with models generated at 0.5, 0.65, 0.75, 0.8, and 0.85 (a redistribution factor of 0.5 corresponds to full heat redistribution to the night side).

Our grid fitting procedure is based on the post-processing procedures utilized in studies of WASP-39 b (e.g. Rustamkulov et al., 2023) and WASP-17 b (Grant et al., 2023), among others. In this framework, the pressure-temperature profile is physically constrained by the RCTE grid, as well as the chemistry, which is constrained by chemical-equilibrium abundances at each pressure layer. We leverage the open source sampling code `Ultranest` (Buchner, 2021), which uses the MLFriends algorithm (Buchner, 2019) to fit for the best-fit parameters. This simply corresponds to our three grid parameters (M/H, C/O, and heat redistribution) for the cloud-free case. In doing so, we linearly interpolate the spectra computed for each grid point using `PICASO`'s rapid `custom_interp` function. For our cloud-free grid fit, we obtain a single best-fit model that corresponds to M/H=1.5×Solar, C/O=1.5×Solar (=0.687 absolute), and heat redistribution=0.7 (see the full table of retrieved parameters in Table 4.3).

In order to incorporate clouds we add five new free parameters to our fit: 1) the base pressure level of the cloud deck, 2) the sedimentation efficiency (f_{sed}), 3) the cloud particle density, 4) the mean particle radius, and 5) the particle size distribution width assuming a log normal distribution. For our cloud fit we assume a cloud species of SiO_2[s] and use the α-crystal optical constants computed at 928 K by Zeidler et al. (2013) (T_{eq} of HD 189733 b is ~1191 K). Note that in the free retrieval section above, we test out several different cloud species. These five free parameters allow us to represent a cloud deck with particles that are log-normally distributed, similar to that of the parameterized cloud model of Ackerman et al. (2001). In this model, the sedimentation efficiency, f_{sed}, describes the vertical extent of the cloud deck. Low f_{sed} (<1) represents a cloud with a large vertical extent, and high f_{sed} (>1) represents a cloud that quickly becomes optically thin toward decreasing pressures.

Our cloud routine is available via the `Virga` (Batalha et al., 2020; Rooney et al., 2022) open source tool function `calc_optics_user_r_dist` [1]. Unlike using the `Virga` cloud model directly, this cloud fitting routine provides more physical flexibility by allowing the cloud to form away from the computed saturation vapor pressure curve for SiO_2 derived in Grant et al. (2023). It also removes the physical relation between the particle radius, vertical mixing velocity (K_{zz}), and f_{sed}.

The parameters derived from our grid fit are also available in Table 4.3. Overall the cloudy model is strongly preferred to the cloud-free model with a difference in the ln Bayes Factor>19 for both individual eclipse visits as well as the joint fit. This translates to preference for the cloudy models at $6-7\sigma$ (as defined in Eqn. 21 from Trotta, 2008). We find that the metallicity and C/O ratio are not well-constrained in our fits. This is not surprising, as we were only able to detect two gas phase molecules, H_2O and H_2S, in our free retrievals. As a result, there is a degeneracy between our retrieved M/H and C/O. We find that the H_2O volume mixing ratio (VMR) is well-constrained with a value of $\log H_2O = -3.8^{+0.2}_{-0.1}$ for the cloudy model fits. This is consistent with the value found in our free retrievals, of -4.1 ± 0.4 (VMR).

The inferred cloud parameters are consistent within 1σ regardless of eclipse visit or joint fit. The cloud parameters are consistent with a vertically extended cloud deck starting at $\log P \sim -3$ [bar] with a mean particle radius of $< \log r = -4$ [cm]. For example, for the joint visit the retrieved cloud deck was $-3.45^{+1.0}_{-0.41}$ compared to $-2.54^{+2.28}_{-1.1}$, for eclipse 2. This level of agreement is also true for the cloud number density, particle radius, sedimentation efficiency, and particle distribution width. Therefore, the eclipse visit did not affect the inferred cloud parameters.

We additionally considered whether the presence of SiO_2[s] grains in the atmosphere of HD 189733 b should affect the thermal structure of the atmosphere through radiative feedback. We calculated the total optical depth from the clouds as a function of wavelength and found that the optical depth is always less than 0.05 between $1-8$ μm. Therefore, the radiative feedback from these clouds should have a minimal effect on the planet's vertical temperature profile.

Spectral Region Beyond 9.0 μm

In Fig. 4.7, we compare our best fit forward model and free retrieval models to our joint eclipse spectrum. We find that even after the inclusion of SiO_2 clouds, we

[1] See `Virga` tutorial.

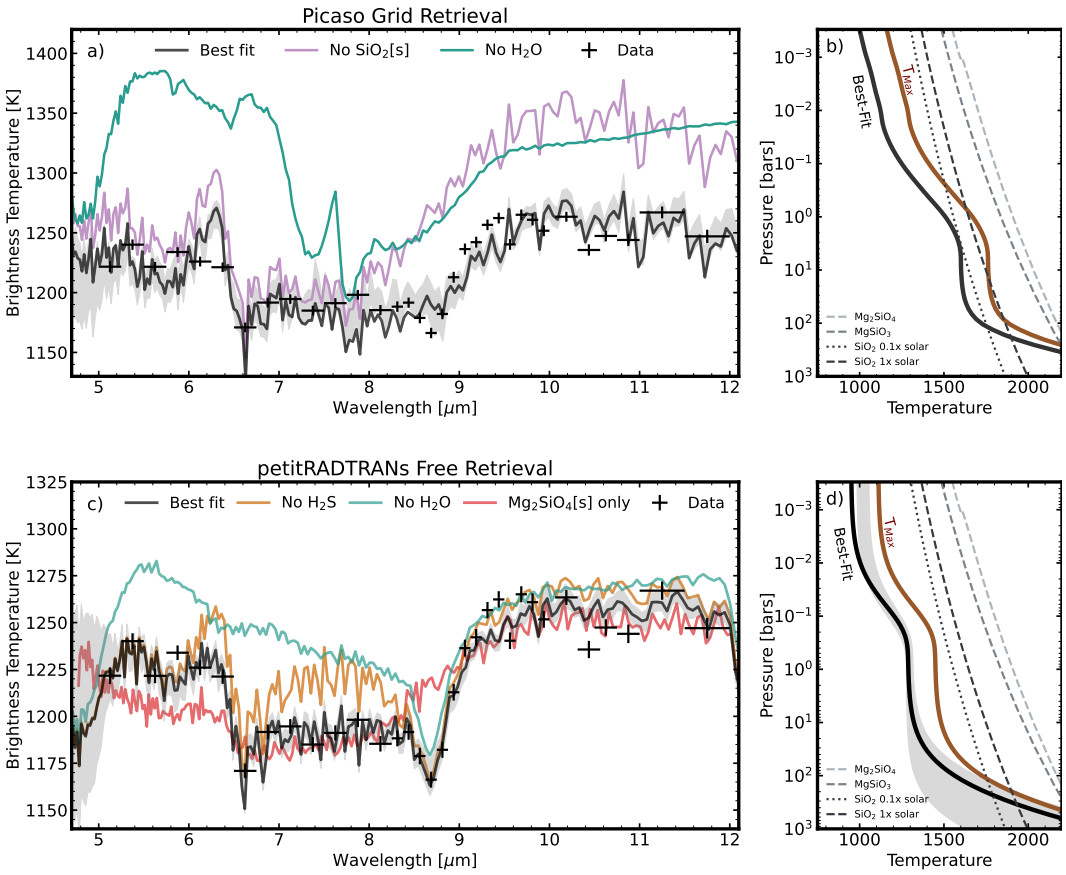

Figure 4.7 a) Our joint eclipse spectrum, converted to brightness temperature, plotted against the best fit `Picaso` forward model and 3σ upper limits. We show the same model with the contribution from the quartz (SiO_2[s]) grains (purple) and H_2O (blue) opacities removed. b) The best fit temperature-pressure profile predicted by forward models and maximum dayside temperature compared to condensation curves of major silicate cloud species. c) Our joint eclipse spectrum plotted against the best fit `petitRADNTRANs` free retrieval. We additionally compare to our best-fit model from a retrieval with fosterite (Mg_2SiO_4[s]) as the condensate species instead of SiO_2 (pink). We show the same model with opacities from the gas phase molecules detected in our retrievals, including H_2S (brown) and H_2O (blue), removed. d) The best fit retrieved P-T profile from the free retrievals and 1-sigma limits compared to condensation curves.

still obtain a relatively poor fit to the measured spectral shape beyond 9 μm. In the `PICASO` grid retrieval, the best fit cloud model does not capture the steep gradient in brightness temperature from $8.6 - 9.5$ μm. In the `petitRADTRANS` free retrieval, the gradient is fit better (residuals $< 1\sigma$), until 9.4 μm where the model begins to deviate from the data. This occurs for retrievals on both the `Eureka!` and `Sparta` data reductions. These sequence of points differ at more than 2σ from the best-fit models, even allowing for error inflation. Additionally, in both eclipses and both data reductions, we observe a potential feature at 9.6 μm, shown in Fig 4.6. While this feature is narrow, it appears consistently in all data reductions and in both visits. It vanishes for bin width larger than 0.3 μm, where the feature is no longer resolved. The other region with multiple consecutive points differing by more than 2σ from the best-fit models is between $10 - 11$ μm, where the ramp behavior changes on the detector and the differences between our two secondary eclipse observations are large.

The mismatch in the gradient from $8.6 - 9.5$ μm would likely benefit from more complex cloud modeling (e.g. patchy clouds, non-log-normal particle distributions, or improved optical properties). Additionally, if the 9.6 μm feature is real, the included species in our models could also be affecting this region. We briefly considered what absorbers could affect these wavelengths. Using the high-throughput quantum chemistry framework presented in Zapata Trujillo et al. (2023), we explored possible molecular species that could affect the spectral shape in this region. Methanol (CH_3OH) is observed in many astrophysical contexts including solar system bodies and planet-hosting disks around other stars (e.g. Drabek-Maunder et al., 2017; Booth et al., 2021). Although methanol is expected to be important in shaping HD 189733b's overall chemistry, its steady-state abundance is predicted to be many orders of magnitude lower than species such as H_2O, CO_2, and CH_4 (Moses et al., 2011). The available high-temperature line lists for methanol currently focus on near-infrared wavelengths (e.g. Majed et al., 2014) and do not allow for a robust determination of plausible CH_3OH abundances in HD 189733b's atmosphere from our JWST MIRI data. At this current time, no sufficient mid-infrared opacities for this molecule exist in any spectroscopy database, (e.g. HITEMP (Rothman et al., 2010), ExoMol (Tennyson et al., 2016), suitable for modeling existing exoplanet spectra. Future work focused on the expansion of current high-temperature line list for methanol, such as those from Ding et al. (2019), combined with additional observations of HD 189733 b's atmosphere at near-infrared wavelengths will be needed in order.

4.6 Discussion

In the previous section, we identified sub-micron grains of SiO_2[s] as the likely source of the excess absorption observed at 8.7 μm in HD 189733 b's dayside emission spectrum. Here, we examine the implications of this detection for the atmosphere of HD 189733 b, and place our detection in a broader context by comparing it to published detections of silicate grains with MIRI LRS for other hot Jupiters.

Silicate Grains in the Atmosphere of HD 189733 b

While silicate absorption features have been directly observed in the emission spectra of brown dwarfs and planetary mass companions between 5 – 14 μm using Spitzer IRS (Burgasser et al., 2008; Burningham et al., 2021; Suárez et al., 2022), they were only recently detected in the atmospheres of transiting planets using JWST (Grant et al., 2023; Dyrek et al., 2023). As illustrated in Fig. 4.3, MIRI LRS covers an equivalent 5 – 12 μm spectral region with a significantly higher spectral precision than Spitzer IRS, making it an ideal instrument to search for spectroscopic features from silicate clouds. Our detection of absorption from SiO_2[s] grains in HD 189733 b's dayside emission spectrum provides the first direct confirmation of silicate particles in the atmosphere of HD 189733 b. This provides evidence that the scattering particles invoked in previous studies to explain this planet's optical scattering slope in transmission (e.g. Pont et al., 2008; Wakeford et al., 2015) may indeed be composed of silicate materials, though the composition of particles in the terminator region may differ in composition from those detected on the hotter dayside.

In Fig. 4.7, we plot the best-fit spatially-averaged dayside temperature profile inferred from fits to our MIRI emission spectrum and compare it to the condensation curves of various silicate species. This temperature profile predicts that equilibrium condensation of all of these species should occur at relatively high pressures, where their effect on the emission spectrum should be minimal. Our retrievals, on the other hand, require cloud particles present at 10^{-2} – 10^{-3} bars. However, we know from both general circulation models (Showman et al., 2009; Kataria et al., 2015) and previously published phase curve observations of HD 189733 b that the dayside temperatures vary by hundreds of K across the dayside hemisphere (Knutson et al., 2007; Knutson et al., 2012; Majeau et al., 2012; Wit et al., 2012). This means that silicates could reasonably condense at the pressures retrieved in our models in the hottest regions of the dayside atmosphere near the substellar point (see panel b in

Fig. 4.7). At our best fit cloud base pressures, we find that a reasonable temperature-pressure profile for the hottest regions of HD 189733 b's dayside atmosphere could cross the condensation curve for SiO_2 only if the abundance is moderately sub-solar. Condensation curves for abundances closer to solar place the cloud base deeper in the atmosphere around 0.1-1 bars. Sub-micron-sized particles also have relatively long settling times, and we would therefore expect vertical mixing to transport these small particles to even lower pressures than the predicted cloud base (Parmentier et al., 2013; Lee et al., 2016). Alternatively, the retrieved cloud parameters are also consistent with homogeneous or heterogeneous nucleation in the upper atmosphere, rather than equilibrium cloud condensation (e.g. Helling et al., 2001; Lee et al., 2016; Powell et al., 2018).

It is worth considering why we see SiO_2[s] in HD 189733 b's dayside atmosphere, and not any of the other commonly predicted silicate cloud species. Equilibrium chemistry condensation models predict the formation of enstatite ($MgSiO_3$) and fosterite (Mg_2SiO_4) clouds (Burrows et al., 1999; Visscher et al., 2010). Microphysical cloud formation models from Gao et al. (2020) similarly predict that forsterite should be the dominant form of silicate clouds based on the relative nucleation potentials between the various silicate species. These predictions appear to be in good agreement with Spitzer observations of silicate absorption features in brown dwarf atmospheres, which are best-matched by models with enstatite and forsterite compositions (Cushing et al., 2006; Luna et al., 2021). On the other hand, kinetic cloud models from Helling et al. (2006) predict that $SiO2_2$ grains should dominate in the atmospheres of brown dwarfs. This has since been supported by Burningham et al. (2021), who find SiO_2[s] in addition to enstatite clouds in the atmosphere of an isolated brown dwarf. Dynamic cloud formation models for HD 189733 b from Lee et al. (2016) predict that SiO_2 will condense on top of TiO_2 seed particles to form small grains (< 0.1 μm), and that these small grains will dominate the aerosol distribution at low dayside latitudes and low pressures. In these models, Lee et al. (2016) find that in the hottest regions of HD 189733 b's day side, the growth of other silicate particles is suppressed. However, their models also predict that $MgSiO_3$ and Mg_2SiO_4 should dominate in the terminator regions probed by transmission spectroscopy. This prediction is testable with the upcoming MIRI transmission spectroscopy of HD 189733 b (Program IDs GTO 1185, PI Thomas P. Greene, and GO 1633, PI Drake Deming), which will be sensitive to the composition of cloud species closer to the terminator.

Comparison to other JWST MIRI Silicate Cloud Detections

Two recent studies of exoplanet transmission spectroscopy with JWST MIRI LRS have also produced detections of silicate clouds in the atmospheres of WASP-17 b (Grant et al., 2023) and WASP-107 b (Dyrek et al., 2023). Emission spectroscopy with MIRI LRS and JWST NIRCam has also provided evidence that aerosols are potentially present in the dayside atmosphere of WASP-69 b (Schlawin et al., 2024), with silicates being one of the models explored to reproduce their data. In terms of atmospheric equilibrium temperatures, HD 189733 b (T_{eq} ~1191 K) sits in between WASP-17 b (T_{eq} ~1771 K) and WASP-107 b (T_{eq} ~736 K) (Southworth, 2011), which provides an opportunity to explore the formation of silicate clouds across this important phase space.

Grant et al. (2023) detected absorption from small particles (0.01 μm) of SiO_2 in their JWST MIRI LRS transmission spectrum of hot Jupiter WASP-17 b with a sharp spectral peak near 8.6 μm. The predicted peak dayside temperatures of HD 189733 b at the pressures probed in emission (~100 mbar) are very similar to the predicted temperatures along WASP-17 b's terminator at the pressures probed in transmission (~1 − 10 mbar) (e.g. Kataria et al., 2016). However, their cloud properties in these regions might still differ if they have different atmospheric compositions; Grant et al. (2023) highlight the dependence of the condensation curve for SiO_2 on atmospheric metallicity. WASP-17 b appears to have a super-solar atmospheric metallicity (up to 100× solar; Alderson et al., 2022; Grant et al., 2023). Although we cannot place strong constraints on HD 189733 b's atmospheric metallicity from our JWST MIRI emission observations alone, previous studies of HD 189733 b's transmission and emission spectrum indicate that it is best-matched by an atmospheric metallicity that is 3-10× solar values (e.g. Zhang et al., 2020). Potentially, HD 189733 b's lower atmospheric metallicity could cause SiO_2 to condense at lower temperatures as compared with WASP-17 b (see Figure 4.7).

Dyrek et al. (2023) also recently detected evidence for sub-micron size silicate grains in their JWST MIRI LRS transmission spectrum of WASP-107 b. The 5 − 12 μm transmission spectrum of WASP-107 b does not exhibit a strong 8.6 − 8.7 μm feature explained best by SiO_2 alone. Instead Dyrek et al. (2023) find that the broad absorption due to clouds in WASP-107 b's mid-infrared transmission spectrum is best explained by composite clouds that include amorphous $MgSiO_3$, SiO_2, and SiO, with strong evidence for SiO[s] as the dominant silicate species. SiO[s] is likely thermally unstable on the substantially hotter dayside of HD 189733 b compared to

WASP-107 b's terminator region (Lee et al., 2016), which could account for their different cloud compositions.

Although the exact properties of the silicate cloud species identified in the atmospheres of WASP-17 b, WASP-107 b and now HD 189733 b may differ, they all challenge extrasolar giant planet cloud formation and evolution theories. Thermochemical equilibrium cloud formation (e.g. Marley et al., 2015) would predict that magnesium silicate clouds ($MgSiO_3$[s] or Mg_2SiO_4[s]) would be the primary cloud species to form in hot Jupiter atmospheres and that these clouds would subside to below the photosphere for cooler planets such as WASP-107 b. Non-equilibrium cloud formation models (e.g. Helling et al., 2006) do predict that SiO_2[s] should form a substantial fraction of the material composition of clouds in extrasolar giant planets and brown dwarfs, but not necessarily at the atmospheric temperatures and pressures where we are now observing them. As highlighted in works such as Lee et al. (2016), Parmentier et al. (2016), Kataria et al. (2016), Komacek et al. (2017), and Lines et al. (2018), cloud formation and evolution in hot Jupiters is strongly shaped by large day-night temperature gradients that also give rise to strong vertical and horizontal mixing. This strong atmospheric mixing is likely able to sustain the population of sub-micron size silicate cloud particles observed in WASP-17 b, HD 189733 b, and WASP-107 b. Further observations of giant exoplanet atmospheres spanning a broad range of temperatures, compositions, and gravities with JWST MIRI will hopefully provide additional detections of specific cloud species and constraints on their average particle sizes that will prove valuable to further refine cloud formation and evolution theories and models.

4.7 Conclusions

We have presented an updated mid-infrared dayside emission spectrum of the hot Jupiter HD 189733 b spanning 5 – 12 μm from two secondary eclipses observed with JWST/MIRI LRS. We find that our emission spectra from each of our two secondary eclipse observations are consistent within expectations of random noise from both our `Eureka!` and `SPARTA` data reduction pipelines. These results showcase the ability of JWST/MIRI LRS emission spectroscopy to identify new gas-phase absorption and cloud features in the atmospheres of transiting exoplanets at mid-infrared wavelengths. Our two secondary eclipse observations of HD 189733 b also demonstrate the repeatability of observations for relatively bright targets with JWST, while greatly improving upon previous Spitzer/IRS observations of this planet. We find that our new secondary eclipse observations are consistent with

the shape of previous Spitzer/IRS mid-infrared spectroscopy of this planet when we apply a fixed offset to the IRS data. When we bin our spectra to match the 8 μm Spitzer bandpass, we find that our new eclipse depths are slightly smaller than the ensemble of seven published Spitzer 8 μm eclipse observations, likely also as a result of instrumental systematics related to the steep time-dependent ramps in the Spitzer data. Overall, we find good consistency between the Spitzer and JWST observations for this planet.

Our dayside emission spectrum confirms the previous detections of H_2O in the dayside of HD 189733 b by Spitzer, HST, and ground-based observations, and is consistent with expectations for a moderately super-solar metallicity hydrogen-dominated atmosphere. We find that the absorption feature observed at 8.7 μm is well-matched by models with high altitude, sub-micron, $1.09^{+0.14}_{-0.06} \times 10^{-3}$ μm SiO_2 grains, confirming previous indirect inferences of scattering aerosols in this planet's atmosphere. Even after accounting for the effect of clouds on the spectrum, we find that the measured spectral shape at wavelengths beyond 9 μm is not well-matched by our models. However, we were unable to identify any candidate cloud or gas phases absorbers that could improve the fit in this region using currently available line lists. CH_3OH could potentially produce absorption in this region, but does not have a complete line list at relevant temperatures and pressures. Future improvements in mid-infrared opacities and additional JWST secondary eclipse measurements from NIRCAM at shorter wavelengths should be able to confirm or disprove the presence of trace species such as CH_3OH.

These same observations can be used to produce 2D eclipse maps of HD 189733 b's dayside atmosphere; we will present these maps in a future study and compare them to previously published 8 μm Spitzer eclipse maps for this planet. These new spectroscopic eclipse maps will also allow us to probe variations in the dayside atmospheric temperature structure over a wide range of pressures, and potentially to determine the spatial extent of the SiO_2 clouds in HD 189733 b's dayside atmosphere. HD 189733 b will soon be observed with multiple JWST instrument modes in both transmission and emission (Programs GTO 1185, PI Greene, GO 1633, PI Deming). By combining these data sets with the mid-infrared observations presented here, we will be able to fully quantify the molecular inventory of the dayside and terminator regions of HD 189733 b's atmosphere. Transmission observations with MIRI LRS will allow us to see if the clouds on the dayside extend into the terminator, and if these clouds have the same composition as those on the day side, or if they transition

to enstatite and forsterite as predicted by Lee et al. (2016). These observations can also be used to search for trace molecules produced by photochemistry (e.g. Moses et al., 2011), including their spatially varying abundances, and to quantify the effect of upward mixing on the observed methane abundance in HD 189733 b's upper atmosphere (e.g. Fortney et al., 2021). This extensive suite of JWST observations will make HD 189733 b a key touchstone for studies of silicate cloud formation and disequilibrium chemistry in hot Jupiter atmospheres, building on its legacy as one of the best-studied hot Jupiters with Spitzer and HST.

Acknowledgements

This work is based on observations made with the NASA/ESA/CSA James Webb Space Telescope. The data were obtained from the Mikulski Archive for Space Telescopes at the Space Telescope Science Institute, which is operated by the Association of Universities for Research in Astronomy, Inc., under NASA contract NAS 5-03127 for JWST. These observations are associated with the program JWST-GO-2021. Support for program JWST-GO-2021 was provided by NASA through a grant from the Space Telescope Science Institute, which is operated by the Association of Universities for Research in Astronomy, Inc., under NASA contract NAS 5-03127. Resources supporting this work were provided by the NASA High-End Computing (HEC) Program through the NASA Advanced Supercomputing (NAS) Division at Ames Research Center. N.E.B. acknowledges support from NASA'S Interdisciplinary Consortia for Astrobiology Research (NNH19ZDA001N-ICAR) under award number 19-ICAR19_2-0041. Part of the research was carried out at the Jet Propulsion Laboratory, California Institute of Technology, under contract with the National Aeronautics and Space Administration. The JWST data used in this observation were obtained from the Mikulski Archive for Space Telescopes (MAST) at the Space Telescope Science Institute. The specific observations can be accessed from DOI 10.17909/87p2-td95. Data products from this paper will be available in this Zenodo repository: http://10.5281/zenodo.11238250.

References

Ackerman, Andrew S. and Mark S. Marley (Aug. 2001). "Precipitating Condensation Clouds in Substellar Atmospheres". In: 556.2, pp. 872–884. DOI: 10.1086/321540. arXiv: astro-ph/0103423 [astro-ph].

Agol, E. et al. (Oct. 2010). "The climate of HD 189733b from fourteen transits and eclipses measured by Spitzer". In: *The Astrophysical Journal* 721.2, pp. 1861–1877. ISSN: 0004-637X, 1538-4357. DOI: 10.1088/0004-637X/721/2/1861.

Alderson, L. et al. (May 2022). "A comprehensive analysis of WASP-17b's transmission spectrum from space-based observations". In: 512.3, pp. 4185–4209. DOI: 10.1093/mnras/stac661. arXiv: 2203.02434 [astro-ph.EP].

Allard, F. (Jan. 2014). "The BT-Settl Model Atmospheres for Stars, Brown Dwarfs and Planets". In: 299, pp. 271–272. DOI: 10.1017/S1743921313008545.

Batalha, Natasha, Caoimhe Rooney, and Sagnick Mukherjee (Apr. 2020). *natasha-batalha/virga: Initial Release*. Zenodo. Version v0.0. DOI: 10.5281/zenodo.3759888.

Batalha, Natasha E. et al. (June 2019). "Exoplanet Reflected-light Spectroscopy with PICASO". In: 878.1, 70, p. 70. DOI: 10.3847/1538-4357/ab1b51. arXiv: 1904.09355 [astro-ph.EP].

Bell, Taylor J. et al. (2022). "Eureka!: An End-to-End Pipeline for JWST Time-Series Observations". In: *Journal of Open Source Software* 7.79, p. 4503. DOI: 10.21105/joss.04503.

Berdyugina, S. V. et al. (Feb. 2011). "Polarized reflected light from the exoplanet HD189733b: First multicolor observations and confirmation of detection". In: *The Astrophysical Journal* 728.1, p. L6. ISSN: 2041-8205, 2041-8213. DOI: 10.1088/2041-8205/728/1/L6.

Booth, Alice S. et al. (Jan. 2021). "An inherited complex organic molecule reservoir in a warm planet-hosting disk". In: *Nature Astronomy* 5, pp. 684–690. DOI: 10.1038/s41550-021-01352-w. arXiv: 2104.08348 [astro-ph.EP].

Bouchy, Francois et al. (Dec. 2005). "ELODIE metallicity-biased search for transiting Hot Jupiters II. A very hot Jupiter transiting the bright K star HD189733". In: *Astronomy & Astrophysics* 444.1, pp. L15–L19. ISSN: 0004-6361, 1432-0746. DOI: 10.1051/0004-6361:200500201.

Bouwman, Jeroen et al. (Mar. 2023). "Spectroscopic Time Series Performance of the Mid-infrared Instrument on the JWST". In: *Publications of the Astronomical Society of the Pacific* 135, p. 038002. ISSN: 0004-6280. DOI: 10.1088/1538-3873/acbc49.

Buchner, Johannes (Oct. 2019). "Collaborative Nested Sampling: Big Data versus Complex Physical Models". In: 131.1004, p. 108005. DOI: 10.1088/1538-3873/aae7fc. arXiv: 1707.04476 [stat.CO].

– (Apr. 2021). "UltraNest - a robust, general purpose Bayesian inference engine". In: *The Journal of Open Source Software* 6.60, 3001, p. 3001. DOI: 10.21105/joss.03001. arXiv: 2101.09604 [stat.CO].

Burgasser, Adam J. et al. (Feb. 2008). "Clouds, Gravity, and Metallicity in Blue L Dwarfs: The Case of 2MASS J11263991–5003550*". In: *The Astrophysical Journal* 674.1, p. 451. ISSN: 0004-637X. DOI: 10.1086/524726.

Burningham, Ben et al. (July 2021). "Cloud busting: enstatite and quartz clouds in the atmosphere of 2M2224-0158". In: *Monthly Notices of the Royal Astronomical Society* 506.2, pp. 1944–1961. ISSN: 0035-8711, 1365-2966. DOI: 10.1093/mnras/stab1361.

Burrows, Adam and C. M. Sharp (Feb. 1999). "Chemical Equilibrium Abundances in Brown Dwarf and Extrasolar Giant Planet Atmospheres". In: *The Astrophysical Journal* 512.2, p. 843. ISSN: 0004-637X. DOI: 10.1086/306811.

Bushouse, Howard et al. (Oct. 2022). *JWST Calibration Pipeline*. Version 1.8.2. DOI: 10.5281/zenodo.7229890.

Charbonneau, David et al. (Oct. 2008). "The Broadband Infrared Emission Spectrum of the Exoplanet HD 189733b". en. In: *The Astrophysical Journal* 686.2, p. 1341. ISSN: 0004-637X. DOI: 10.1086/591635.

Crouzet, Nicolas et al. (Nov. 2014). "Water Vapor in the Spectrum of the Extrasolar Planet HD 189733b. II. The Eclipse". In: *The Astrophysical Journal* 795, p. 166. ISSN: 0004-637X. DOI: 10.1088/0004-637X/795/2/166.

Cushing, Michael C. et al. (Sept. 2006). "A Spitzer Infrared Spectrograph Spectral Sequence of M, L, and T Dwarfs". In: *The Astrophysical Journal* 648.1, p. 614. ISSN: 0004-637X. DOI: 10.1086/505637.

Deming, Drake et al. (June 2006). "Strong Infrared Emission from the Extrasolar Planet HD 189733b". In: *The Astrophysical Journal* 644, pp. 560–564. ISSN: 0004-637X. DOI: 10.1086/503358.

Ding, Y., C. L. Strand, and R. K. Hanson (Feb. 2019). "High-temperature mid-infrared absorption spectra of methanol (CH3OH) and ethanol (C2H5OH) between 930 and 1170 cm-1". In: *Journal of Quantitative Spectroscopy and Radiative Transfer* 224, pp. 396–402. ISSN: 0022-4073. DOI: 10.1016/j.jqsrt.2018.11.034.

Drabek-Maunder, E. et al. (Sept. 2017). "Ground-based detection of a cloud of methanol from Enceladus: When is a biomarker not a biomarker?" In: *arXiv e-prints*, arXiv:1709.09638, arXiv:1709.09638. DOI: 10.48550/arXiv.1709.09638. arXiv: 1709.09638 [astro-ph.EP].

Dyrek, Achrène et al. (Nov. 2023). "SO2, silicate clouds, but no CH4 detected in a warm Neptune". en. In: *Nature*, pp. 1–3. ISSN: 1476-4687. DOI: 10.1038/s41586-023-06849-0.

Evans, Thomas M. et al. (July 2013). "The Deep Blue Color of HD189733b: Albedo Measurements with Hubble Space Telescope/Space Telescope Imaging Spectrograph at Visible Wavelengths". In: *The Astrophysical Journal* 772.2, p. L16. ISSN: 2041-8205, 2041-8213.

Fegley Bruce, Jr. and Katharina Lodders (July 1994). "Chemical Models of the Deep Atmospheres of Jupiter and Saturn". In: 110.1, pp. 117–154. DOI: 10.1006/icar.1994.1111.

Feroz, F., M. P. Hobson, and M. Bridges (Oct. 2009). "MultiNest: an efficient and robust Bayesian inference tool for cosmology and particle physics". In: *Monthly Notices of the Royal Astronomical Society* 398.4, pp. 1601–1614. ISSN: 00358711, 13652966. DOI: 10.1111/j.1365-2966.2009.14548.x.

Finnerty, Luke et al. (Nov. 2023). *Atmospheric metallicity and C/O of HD 189733 b from high-resolution spectroscopy*. DOI: 10.48550/arXiv.2312.00141.

Fortney, Jonathan J., Rebekah I. Dawson, and Thaddeus D. Komacek (2021). "Hot Jupiters: Origins, Structure, Atmospheres". en. In: *Journal of Geophysical Research: Planets* 126.3, e2020JE006629. ISSN: 2169-9100. DOI: 10.1029/2020JE006629.

Fu, Guangwei et al. (Oct. 2024). *Hydrogen sulfide detection and strong methane depletion in the super-stellar metallicity atmosphere of hot Jupiter HD 189733b*. DOI: 10.21203/rs.3.rs-3403333/v1.

Gao, Peter et al. (Oct. 2020). "Aerosol composition of hot giant exoplanets dominated by silicates and hydrocarbon hazes". In: *Nature Astronomy* 4.10, pp. 951–956. ISSN: 2397-3366. DOI: 10.1038/s41550-020-1114-3.

Gordon, Sanford and Bonnie J McBride (1994). *Computer program for calculation of complex chemical equilibrium compositions and applications. Part 1: Analysis*. Tech. rep.

Grant, David et al. (Oct. 2023). "JWST-TST DREAMS: Quartz Clouds in the Atmosphere of WASP-17b". In: 956.2, L29, p. L29. DOI: 10.3847/2041-8213/acfc3b. arXiv: 2310.08637 [astro-ph.EP].

Grillmair, C. J. et al. (Apr. 2007). "A Spitzer Spectrum of the Exoplanet HD 189733b". In: *The Astrophysical Journal* 658, pp. L115–L118. ISSN: 0004-637X. DOI: 10.1086/513741.

Grillmair, Carl J. et al. (Dec. 2008). "Strong water absorption in the dayside emission spectrum of the planet HD189733b". In: *Nature* 456, pp. 767–769. ISSN: 0028-0836. DOI: 10.1038/nature07574.

Guillot, T. (Sept. 2010). "On the radiative equilibrium of irradiated planetary atmospheres". In: *Astronomy and Astrophysics* 520, A27. ISSN: 0004-6361. DOI: 10.1051/0004-6361/200913396.

He, Chao et al. (Mar. 2018). "Laboratory Simulations of Haze Formation in the Atmospheres of Super-Earths and Mini-Neptunes: Particle Color and Size Distribution". In: *The Astrophysical Journal* 856, p. L3. ISSN: 0004-637X. DOI: 10.3847/2041-8213/aab42b.

Helling, Ch. et al. (Sept. 2001). "Dust in brown dwarfs. I. Dust formation under turbulent conditions on microscopic scales". In: *Astronomy and Astrophysics* 376, pp. 194–212. ISSN: 0004-6361. DOI: 10.1051/0004-6361:20010937.

Helling, Ch. et al. (May 2006). "Detectability of dirty dust grains in brown dwarf atmospheres". In: *Astronomy and Astrophysics* 451, pp. L9–L12. ISSN: 0004-6361. DOI: 10.1051/0004-6361:20064944.

Hörst, Sarah M. et al. (Mar. 2018). "Haze production rates in super-Earth and mini-Neptune atmosphere experiments". In: *Nature Astronomy* 2, pp. 303–306. ISSN: 2397-3366. DOI: 10.1038/s41550-018-0397-0.

Ivshina, Ekaterina S. and Joshua N. Winn (Apr. 2022). "TESS Transit Timing of Hundreds of Hot Jupiters". en. In: *The Astrophysical Journal Supplement Series* 259.2, p. 62. ISSN: 0067-0049. DOI: 10.3847/1538-4365/ac545b.

JWST Transiting Exoplanet Community Early Release Science Team et al. (Feb. 2023). "Identification of carbon dioxide in an exoplanet atmosphere". In: 614.7949, pp. 649–652. DOI: 10.1038/s41586-022-05269-w. arXiv: 2208.11692 [astro-ph.EP].

Kataria, Tiffany et al. (Mar. 2015). "The Atmospheric Circulation of the Hot Jupiter WASP-43b: Comparing Three-dimensional Models to Spectrophotometric Data". In: *The Astrophysical Journal* 801, p. 86. ISSN: 0004-637X. DOI: 10.1088/0004-637X/801/2/86.

Kataria, Tiffany et al. (Apr. 2016). "The atmospheric circulation of a nine-hot Jupiter sample: Probing circulation and chemistry over a wide phase space". In: *The Astrophysical Journal* 821.1, p. 9. ISSN: 1538-4357. DOI: 10.3847/0004-637X/821/1/9.

Kempton, Eliza M.-R. et al. (May 2023). "A reflective, metal-rich atmosphere for GJ 1214b from its JWST phase curve". In: pp. 1476–4687. DOI: 10.1038/s41586-023-06159-5. arXiv: 2305.06240 [astro-ph.EP].

Kitzmann, Daniel and Kevin Heng (Mar. 2018). "Optical properties of potential condensates in exoplanetary atmospheres". en. In: *Monthly Notices of the Royal Astronomical Society* 475.1, pp. 94–107. ISSN: 0035-8711, 1365-2966. DOI: 10.1093/mnras/stx3141.

Knutson, Heather A. et al. (May 2007). "A map of the day-night contrast of the extrasolar planet HD 189733b". In: *Nature* 447, pp. 183–186. ISSN: 0028-0836. DOI: 10.1038/nature05782.

Knutson, Heather A. et al. (July 2012). "3.6 and 4.5 m Phase Curves and Evidence for Non-equilibrium Chemistry in the Atmosphere of Extrasolar Planet HD 189733b". In: *The Astrophysical Journal* 754, p. 22. ISSN: 0004-637X. DOI: 10.1088/0004-637X/754/1/22.

Komacek, Thaddeus D., Adam P. Showman, and Xianyu Tan (Feb. 2017). "Atmospheric Circulation of Hot Jupiters: Dayside-Nightside Temperature Differences. II. Comparison with Observations". In: 835.2, 198, p. 198. DOI: 10.3847/1538-4357/835/2/198. arXiv: 1610.03893 [astro-ph.EP].

Kreidberg, Laura (Nov. 2015). "batman: BAsic Transit Model cAlculatioN in Python". en. In: *Publications of the Astronomical Society of the Pacific* 127.957, p. 1161. ISSN: 1538-3873. DOI: 10.1086/683602.

Krenn, A. F. et al. (Apr. 2023). "The geometric albedo of the hot Jupiter HD 189733b measured with CHEOPS". In: *Astronomy & Astrophysics* 672, A24. ISSN: 0004-6361, 1432-0746. DOI: 10.1051/0004-6361/202245016.

Lecavelier Des Etangs, A. et al. (Apr. 2008). "Rayleigh scattering in the transit spectrum of HD 189733b". In: *Astronomy and Astrophysics* 481, pp. L83–L86. ISSN: 0004-6361. DOI: 10.1051/0004-6361:200809388.

Lee, E. et al. (Oct. 2016). "Dynamic mineral clouds on HD 189733b - I. 3D RHD with kinetic, non-equilibrium cloud formation". In: *Astronomy & Astrophysics* 594, A48. ISSN: 0004-6361, 1432-0746. DOI: 10.1051/0004-6361/201628606.

Lines, S. et al. (July 2018). "Simulating the cloudy atmospheres of HD 209458 b and HD 189733 b with the 3D Met Office Unified Model". In: 615, A97, A97. DOI: 10.1051/0004-6361/201732278. arXiv: 1803.00226 [astro-ph.EP].

Lodders, Katharina (July 1999). "Alkali Element Chemistry in Cool Dwarf Atmospheres". In: 519.2, pp. 793–801. DOI: 10.1086/307387.

– (Oct. 2002). "Titanium and Vanadium Chemistry in Low-Mass Dwarf Stars". In: *The Astrophysical Journal* 577.2, pp. 974–985. DOI: 10.1086/342241.

– (Jan. 2010). "Solar System Abundances of the Elements". In: *Principles and Perspectives in Cosmochemistry*. Vol. 16. Astrophysics and Space Science Proceedings, p. 379. DOI: 10.1007/978-3-642-10352-0_8. arXiv: 1010.2746 [astro-ph.SR].

Lodders, Katharina and Bruce Fegley (Feb. 2002). "Atmospheric Chemistry in Giant Planets, Brown Dwarfs, and Low-Mass Dwarf Stars. I. Carbon, Nitrogen, and Oxygen". In: 155.2, pp. 393–424. DOI: 10.1006/icar.2001.6740.

Luna, Jessica L. and Caroline V. Morley (Oct. 2021). "Empirically Determining Substellar Cloud Compositions in the Era of the James Webb Space Telescope". In: *The Astrophysical Journal* 920.2, p. 146. ISSN: 0004-637X. DOI: 10.3847/1538-4357/ac1865.

Lupu, Roxana et al. (Oct. 2021). *Correlated k coefficients for H2-He atmospheres; 196 spectral windows and 1460 pressure-temperature points*. Zenodo. DOI: 10.5281/zenodo.5590989.

Madhusudhan, Nikku et al. (July 2014). "H2O Abundances in the Atmospheres of Three Hot Jupiters". In: *The Astrophysical Journal Letters* 791.1, p. L9. ISSN: 2041-8205. DOI: 10.1088/2041-8205/791/1/L9.

Majeau, C., E. Agol, and N. Cowan (Mar. 2012). "A Two-Dimensional Infrared Map of the Extrasolar Planet HD 189733b". In: *The Astrophysical Journal* 747.2, p. L20. ISSN: 2041-8205, 2041-8213. DOI: 10.1088/2041-8205/747/2/L20.

Majed, Alrefae, Es-sebbar Et-touhami, and Farooq Aamir (2014). "Absorption cross-section measurements of methane, ethane, ethylene and methanol at high temperatures". In: *Journal of Molecular Spectroscopy* 303, pp. 8–14. ISSN: 0022-2852. DOI: https://doi.org/10.1016/j.jms.2014.06.007.

Marley, M. S. and T. D. Robinson (Aug. 2015). "On the Cool Side: Modeling the Atmospheres of Brown Dwarfs and Giant Planets". In: 53, pp. 279–323. DOI: 10.1146/annurev-astro-082214-122522. arXiv: 1410.6512 [astro-ph.EP].

Marley, Mark S. and Christopher P. McKay (Apr. 1999). "Thermal Structure of Uranus' Atmosphere". In: 138.2, pp. 268–286. DOI: 10.1006/icar.1998.6071.

Marley, Mark S. et al. (Oct. 2021). "The Sonora Brown Dwarf Atmosphere and Evolution Models. I. Model Description and Application to Cloudless Atmospheres in Rainout Chemical Equilibrium". In: 920.2, 85, p. 85. DOI: 10.3847/1538-4357/ac141d. arXiv: 2107.07434 [astro-ph.SR].

McCullough, P. R. et al. (July 2014). "Water Vapor in the Spectrum of the Extrasolar Planet HD 189733b. I. The Transit". In: *The Astrophysical Journal* 791.1, p. 55. ISSN: 0004-637X. DOI: 10.1088/0004-637X/791/1/55.

McKay, C. P., J. B. Pollack, and R. Courtin (July 1989). "The thermal structure of Titan's atmosphere". In: 80.1, pp. 23–53. DOI: 10.1016/0019-1035(89)90160-7.

Mollière, P. et al. (July 2019). "petitRADTRANS: a Python radiative transfer package for exoplanet characterization and retrieval". In: *Astronomy & Astrophysics* 627, A67. ISSN: 0004-6361, 1432-0746. DOI: 10.1051/0004-6361/201935470.

Morello, G. et al. (May 2014). "A New Look at Spitzer Primary Transit Observations of the Exoplanet HD 189733b". In: *The Astrophysical Journal* 786, p. 22. ISSN: 0004-637X. DOI: 10.1088/0004-637X/786/1/22.

Moses, Julianne I. et al. (Aug. 2011). "Disequilibrium Carbon, Oxygen, and Nitrogen Chemistry in the Atmospheres of HD 189733b and HD 209458b". In: 737.1, 15, p. 15. DOI: 10.1088/0004-637X/737/1/15. arXiv: 1102.0063 [astro-ph.EP].

Mukherjee, Sagnick et al. (2023). "PICASO 3.0: a one-dimensional climate model for giant planets and brown dwarfs". In: *The Astrophysical Journal* 942.2, p. 71.

Parmentier, Vivien, Adam P. Showman, and Yuan Lian (Oct. 2013). "3D mixing in hot Jupiters atmospheres. I. Application to the day/night cold trap in HD 209458b". In: *Astronomy and Astrophysics* 558, A91. ISSN: 0004-6361. DOI: 10.1051/0004-6361/201321132.

Parmentier, Vivien et al. (Sept. 2016). "Transitions in the Cloud Composition of Hot Jupiters". In: 828.1, 22, p. 22. DOI: 10.3847/0004-637X/828/1/22. arXiv: 1602.03088 [astro-ph.EP].

Pont, F. et al. (Dec. 2007). "Hubble Space Telescope time-series photometry of the planetary transit of HD 189733: no moon, no rings, starspots". In: *Astronomy and Astrophysics* 476, pp. 1347–1355. ISSN: 0004-6361. DOI: 10.1051/0004-6361:20078269.

Pont, F. et al. (Mar. 2008). "Detection of atmospheric haze on an extrasolar planet: the 0.55-1.05 μm transmission spectrum of HD 189733b with the HubbleSpaceTelescope". In: 385.1, pp. 109–118. DOI: 10.1111/j.1365-2966.2008.12852.x. arXiv: 0712.1374 [astro-ph].

Powell, Diana et al. (June 2018). "Formation of Silicate and Titanium Clouds on Hot Jupiters". en. In: *The Astrophysical Journal* 860.1, p. 18. ISSN: 0004-637X. DOI: 10.3847/1538-4357/aac215.

Rieke, G. H. et al. (July 2015). "The Mid-Infrared Instrument for the James Webb Space Telescope, I: Introduction". In: *Publications of the Astronomical Society of the Pacific* 127, p. 584. ISSN: 0004-6280. DOI: 10.1086/682252.

Rooney, Caoimhe M. et al. (Jan. 2022). "A New Sedimentation Model for Greater Cloud Diversity in Giant Exoplanets and Brown Dwarfs". In: 925.1, 33, p. 33. DOI: 10.3847/1538-4357/ac307a. arXiv: 2110.05903 [astro-ph.EP].

Rosenthal, Lee J. et al. (July 2021). "The California Legacy Survey. I. A Catalog of 178 Planets from Precision Radial Velocity Monitoring of 719 Nearby Stars over Three Decades". In: *The Astrophysical Journal Supplement Series* 255, p. 8. ISSN: 0067-0049. DOI: 10.3847/1538-4365/abe23c.

Rothman, L. S. et al. (Oct. 2010). "HITEMP, the high-temperature molecular spectroscopic database". In: *Journal of Quantitative Spectroscopy and Radiative Transfer*. XVIth Symposium on High Resolution Molecular Spectroscopy (HighRus-2009) 111.15, pp. 2139–2150. ISSN: 0022-4073. DOI: 10.1016/j.jqsrt.2010.05.001.

Rustamkulov, Z. et al. (Feb. 2023). "Early Release Science of the exoplanet WASP-39b with JWST NIRSpec PRISM". In: 614.7949, pp. 659–663. DOI: 10.1038/s41586-022-05677-y. arXiv: 2211.10487 [astro-ph.EP].

Schlawin, Everett et al. (June 2024). *Multiple Clues for Dayside Aerosols and Temperature Gradients in WASP-69 b from a Panchromatic JWST Emission Spectrum*. DOI: 10.3847/1538-3881/ad58e0.

Showman, Adam P. et al. (June 2009). "Atmospheric Circulation of Hot Jupiters: Coupled Radiative-Dynamical General Circulation Model Simulations of HD 189733b and HD 209458b". In: *The Astrophysical Journal* 699.1, p. 564. ISSN: 0004-637X. DOI: 10.1088/0004-637X/699/1/564.

Sing, D. K. et al. (Oct. 2009). "Transit spectrophotometry of the exoplanet HD 189733b - I. Searching for water but finding haze with HST NICMOS". In: *Astronomy & Astrophysics* 505.2, pp. 891–899. ISSN: 0004-6361, 1432-0746. DOI: 10.1051/0004-6361/200912776.

Sing, D. K. et al. (2011). "Hubble Space Telescope transmission spectroscopy of the exoplanet HD 189733b: high-altitude atmospheric haze in the optical and near-ultraviolet with STIS". In: *Monthly Notices of the Royal Astronomical Society* 416.2, pp. 1443–1455. ISSN: 1365-2966. DOI: 10.1111/j.1365-2966.2011.19142.x.

Southworth, John (Nov. 2011). "Homogeneous studies of transiting extrasolar planets - IV. Thirty systems with space-based light curves". In: 417.3, pp. 2166–2196. DOI: 10.1111/j.1365-2966.2011.19399.x. eprint: 1107.1235 (astro-ph.EP).

Suárez, Genaro and Stanimir Metchev (May 2022). "Ultracool dwarfs observed with the *Spitzer* infrared spectrograph – II. Emergence and sedimentation of silicate clouds in L dwarfs, and analysis of the full M5–T9 field dwarf spectroscopic sample". In: *Monthly Notices of the Royal Astronomical Society* 513.4, pp. 5701–5726. ISSN: 0035-8711, 1365-2966. DOI: 10.1093/mnras/stac1205.

Tennyson, Jonathan et al. (Sept. 2016). "The ExoMol database: Molecular line lists for exoplanet and other hot atmospheres". In: *Journal of Molecular Spectroscopy*. New Visions of Spectroscopic Databases, Volume II 327, pp. 73–94. ISSN: 0022-2852. DOI: 10.1016/j.jms.2016.05.002.

Todorov, Kamen O. et al. (Nov. 2014). "Updated Spitzer Emission Spectroscopy of Bright Transiting Hot Jupiter HD 189733b". In: *The Astrophysical Journal* 796.2, p. 100. ISSN: 0004-637X. DOI: 10.1088/0004-637X/796/2/100.

Trotta, Roberto (Mar. 2008). "Bayes in the sky: Bayesian inference and model selection in cosmology". In: *Contemporary Physics* 49.2, pp. 71–104. DOI: 10.1080/00107510802066753. arXiv: 0803.4089 [astro-ph].

Visscher, Channon, Katharina Lodders, and Bruce Fegley (May 2010). "Atmospheric Chemistry in Giant Planets, Brown Dwarfs, and Low-Mass Dwarf Stars. III. Iron, Magnesium, and Silicon". en. In: *The Astrophysical Journal* 716.2, p. 1060. ISSN: 0004-637X. DOI: 10.1088/0004-637X/716/2/1060.

Visscher, Channon, Katharina Lodders, and Jr. Fegley Bruce (Sept. 2006). "Atmospheric Chemistry in Giant Planets, Brown Dwarfs, and Low-Mass Dwarf Stars. II. Sulfur and Phosphorus". In: 648.2, pp. 1181–1195. DOI: 10.1086/506245. arXiv: astro-ph/0511136 [astro-ph].

Wakeford, H. R. and D. K. Sing (Jan. 2015). "Transmission spectral properties of clouds for hot Jupiter exoplanets". In: *Astronomy and Astrophysics* 573, A122. ISSN: 0004-6361. DOI: 10.1051/0004-6361/201424207.

Welbanks, Luis et al. (Dec. 2019). "Mass–Metallicity Trends in Transiting Exoplanets from Atmospheric Abundances of H2O, Na, and K". In: *The Astrophysical Journal Letters* 887.1, p. L20. ISSN: 2041-8205. DOI: 10.3847/2041-8213/ab5a89.

Wiktorowicz, Sloane J. et al. (Oct. 2015). "A Ground-Based Albedo Upper Limit for HD 189733b from Polarimetry". In: *The Astrophysical Journal* 813.1, p. 48. ISSN: 1538-4357. DOI: 10.1088/0004-637X/813/1/48.

Wit, J. de et al. (Dec. 2012). "Towards consistent mapping of distant worlds: secondary-eclipse scanning of the exoplanet HD 189733b". In: *Astronomy and Astrophysics* 548, A128. ISSN: 0004-6361. DOI: 10.1051/0004-6361/201219060.

Woitke, P. and Ch. Helling (Feb. 2003). "Dust in brown dwarfs: II. The coupled problem of dust formation and sedimentation". In: *Astronomy & Astrophysics* 399.1, pp. 297–313. ISSN: 0004-6361, 1432-0746. DOI: 10.1051/0004-6361:20021734.

Zapata Trujillo, Juan C., Maria M. Pettyjohn, and Laura K. McKemmish (Sept. 2023). "High-throughput quantum chemistry: empowering the search for molecular candidates behind unknown spectral signatures in exoplanetary atmospheres". In: 524.1, pp. 361–376. DOI: 10.1093/mnras/stad1717. arXiv: 2306.11988 [astro-ph.EP].

Zeidler, Simon, Th Posch, and Harald Mutschke (2013). "Optical constants of refractory oxides at high temperatures-Mid-infrared properties of corundum, spinel, and α-quartz, potential carriers of the 13 μm feature". In: *Astronomy & Astrophysics* 553, A81.

Zellem, Robert T. et al. (July 2017). "Forecasting the Impact of Stellar Activity on Transiting Exoplanet Spectra". In: *The Astrophysical Journal* 844.1, p. 27. ISSN: 0004-637X. DOI: 10.3847/1538-4357/aa79f5.

Zhang, Michael et al. (Aug. 2020). "PLATON II: New Capabilities and a Comprehensive Retrieval on HD 189733b Transit and Eclipse Data". In: *The Astrophysical Journal* 899.1, p. 27. ISSN: 0004-637X. DOI: 10.3847/1538-4357/aba1e6.

Chapter 5

KPF OBSERVATIONS OF THE ULTRA-HOT JUPITER TOI-2109 B

5.1 Introduction

Ultra-hot Jupiters (UHJs) are a rare and extreme class of gas giant exoplanets. Characterized by equilibrium temperatures exceeding ~2200 K, these planets host dayside atmospheres that contain primarily atomic and ionic species, with only a few molecular species (e.g. CO) present at an observable abundance Parmentier et al., 2018; Tan et al., 2019, e.g. Their unique chemistry and the presence of strong optical and UV absorption due to a combination of atomic species such as Fe and Mg drives the formation of large thermal inversions in their dayside atmospheres without the need for molecules such as TiO or VO (Hubeny et al., 2003; Lothringer et al., 2018; Gandhi et al., 2019), creating strong emission features that are readily observable in transmission and emission spectroscopy. Ultra-hot Jupiters therefore offer a unique laboratory to explore the physics and chemistry of planetary atmospheres in extreme temperature regimes.

These close-in planets are expected to be tidally locked with their host stars, resulting in large day-night temperature gradients that drive fast winds that redistribute heat from the day to night side (Miller-Ricci Kempton et al., 2012; Showman et al., 2012; Parmentier et al., 2013). General circulation models (Komacek et al., 2017; Parmentier et al., 2018; Tan et al., 2019) predict that the efficiency of this day-night heat redistribution should decrease as the incident flux increases, in good agreement with published dayside emission and phase curve observations of hot Jupiters. At the high temperatures reached in ultra-hot Jupiter atmospheres, there are additional effects that can alter the efficiency of day-night transport. As the temperature rises, the atmosphere becomes increasingly ionized; if the planet possesses a strong magnetic field, this can result in a frictional drag force that reduces the speed of zonal winds carrying energy to the planet's night side (Beltz et al., 2021; Beltz et al., 2024). However, at temperatures above $\sim$ 3000 K dissociation of H_2 on the day side followed by recombination on the cooler night side can also increase the efficiency of day-night energy transport (Bell et al., 2018; Tan et al., 2019). This means that although it is generally expected that UHJs will have large day-

night temperature gradients, their observed atmospheric circulation patterns and longitudinal temperature profiles can vary from planet to planet.

The high atmospheric temperatures of UHJs mean that they contain measurable amounts of gas-phase refractory species. By measuring the abundances of these species, we can directly constrain the gas-to-solid ratio of the materials incorporated into the atmosphere, breaking degeneracies in the interpretation of C/O ratio measurements from CO and H_2O abundances measured at infrared wavelengths (Chachan et al., 2023). We can measure the abundances of both refractory and volatile species in UHJ atmospheres using high-resolution spectrographs on large ground-based telescopes. This technique exploits the large radial velocity shift over the course of an observation due to the planet's orbital motion to separate the atmospheric signal of the planet from that of its host star. These observations have revealed that the dayside atmospheres of UHJs are dominated by Fe I and CO features, while water is largely dissociated. Many additional atomic species have been detected, including Na, Mg, Ca, Sr, Ti, V, Cr, Fe, and Ni, (see review by Snellen (2025) and references within). The progressive disappearance of these species with decreasing stellar irradiation can be used to constrain the condensation of these species into cold traps on the planets' night sides (Gandhi et al., 2023). At the same time, the measured broadening and velocity shifts of lines probing different pressures can also be used to characterize their global atmospheric circulation patterns (e.g. Showman et al., 2012; Kesseli et al., 2024).

Here, we utilize high-resolution emission spectroscopy at optical wavelengths to characterize the atmosphere of the recently discovered UHJ TOI-2109 b (Wong et al., 2021). This planet orbits a main sequence F0 star with an effective temperature of 6530 K. With an orbital period of just 16 hours, TOI-2109 b is located closer to its host star than any other giant planet currently known (see Table 5.1 for a complete list of system parameters). With an equilibrium temperature of 3650 K, this makes TOI-210b b the second hottest transiting planet after Kelt-9 b (T_{eq} = 4050 K Gaudi et al., 2017). This planet therefore serves as a critical transition point between Kelt-9 b and the rest of the ultra-hot Jupiters, which all have $T_{eq} < 3000$ K. TOI-2109 b also has a relatively high mass of 5 ± 1 M_J, making it the second most massive UHJ after WASP-18 b (Hellier et al., 2009). Although its high surface gravity makes this planet challenging to observe using transmission spectroscopy, its high dayside temperature means that it is one of the most favorable UHJ targets for emission spectroscopy.

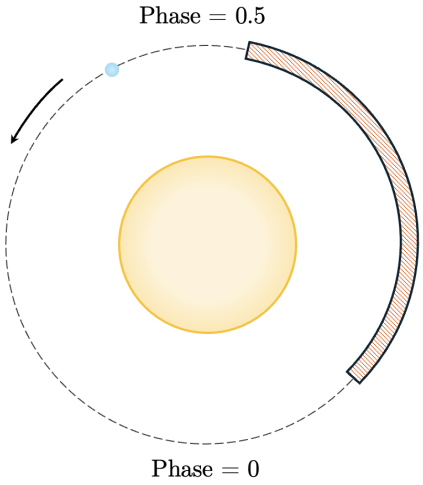

Figure 5.1 The TOI-2109 b system, to scale, showing the relative size of the planet and host star, as well as the orbital axis. The phase coverage of our KPF observation is shown.

We observed TOI-2109 b for slightly more than 1/4 of its orbit using the high-resolution optical spectrograph the Keck Planet Finder (KPF) on Keck I. In Section 5.2 we describe our observations and data reduction process. In Section 5.2 we show the results of our cross correlations analysis on the processed data, and in Section 5.3 we discuss the current status of our data and the next steps.

5.2 Observations and Data Reduction

We observed TOI-2109 b for one night using Keck/KPF (Gibson et al., 2016) on 2025-06-11 UT. Clouds were present throughout the observations, and as a result we used an exposure time of 6 minutes in order to achieve adequate SNR for each exposure. We also discarded several exposures with low SNRs at the beginning of our observations. We observed TOI-2109 b for a total of $\sim$ 5.3 hours, corresponding to 33% of its 16 hour orbital period. Our observations began at an orbital phase of 0.12 and continued until the start of secondary eclipse (orbital phase of approximately 0.45).

We extracted 1D spectra using version 2.7.1 of the KPF Data Reduction Pipeline (DRP). KPF features both a red and green channel spanning ~4450 – 6000 Å over 35 orders and ~6000 – 8700 Å over 32 orders, respectively. Additionally, KPF splits the light from its primary science fiber over three smaller fibers, resulting in three science spectra per exposure. We treated both the chips, individual science spectra, and orders as separate during the blaze function correction and continuum removal steps.

Table 5.1. Summary of the previously derived system parameters and data used in our analysis of TOI-2109 b.

Parameter	Value	Reference
Primary (TOI-2109 A)		
RA (J2000)	16 52 44.71	Gaia Collaboration (2022)
Dec (J2000)	+16 34 47.70	Gaia Collaboration (2022)
SpT	F	Wong et al. (2021)
m_v (mag)	10.217 ± 0.004	Høg et al. (2000)
distance (pc)	$262.041^{+2.753}_{-2.698}$	Gaia Collaboration (2022)
v_{sys} (km/s)	-19.2	(Gaia Collaboration, 2020)
Age (Myr)	$1.77^{+0.88}_{-0.68}$	Wong et al. (2021)
M_* ($M_\odot$)	$1.447^{+0.075}_{-0.078}$	Wong et al. (2021)
R_* ($R_\odot$)	$1.698^{+0.062}_{-0.057}$	Wong et al. (2021)
$T_{\rm eff}$ (K)	6530^{+160}_{-150}	Wong et al. (2021)
log g_* (cgs)	4.139 ± 0.1	Wong et al. (2021)
[Fe/H]	$0.068^{+0.070}_{-0.062}$	Wong et al. (2021)
Companion (TOI-2109 b)		
Period (days)	0.672469 ± 0.000015	Wong et al. (2021)
T_c ()	2459378.459370 ± 0.000059	Wong et al. (2021)
inc (°)	70.74 ± 0.37	Wong et al. (2021)
a/R_*	$2.60^{+0.30}_{-0.24}$	Wong et al. (2021)
a (au)	0.0179 ± 0.00065	Wong et al. (2021)
R (R_J)	1.347 ± 0.047	Wong et al. (2021)
M (M_J)	5 ± 1	Wong et al. (2021)
$T_{\rm eq}$ (K)	3646 ± 88	Wong et al. (2021)

In order to correct for the blaze function in each order, we used our 2D flat-field images to reconstruct a "smooth lamp pattern" for each order. First, we smoothed the smooth lamp pattern over 200 pixels in the dispersion direction and 1 pixel in the cross-dispersion direction. We removed outliers greater than 3σ and then extracted the 1D smooth lamp pattern using the KPF DRP. We then divided the 1D spectra of TOI-2109 by this function.

Next, we removed the continuum by utilizing an iterative spline fitting procedure to the median spectrum of each order. After continuum normalizing each other, we combined all the orders on the red and green chip into one spectrum for each of the 3 science fibers. At shorter wavelengths, there is a large amount of overlap between orders, but at the reddest wavelengths gaps appear between subsequent orders. Before combining the orders into one spectrum, we first performed a clip for low SNR utilizing the raw 1D spectra. Wavelength values within the gaps were assigned a flux value of zero. We then interpolated the orders onto a uniform

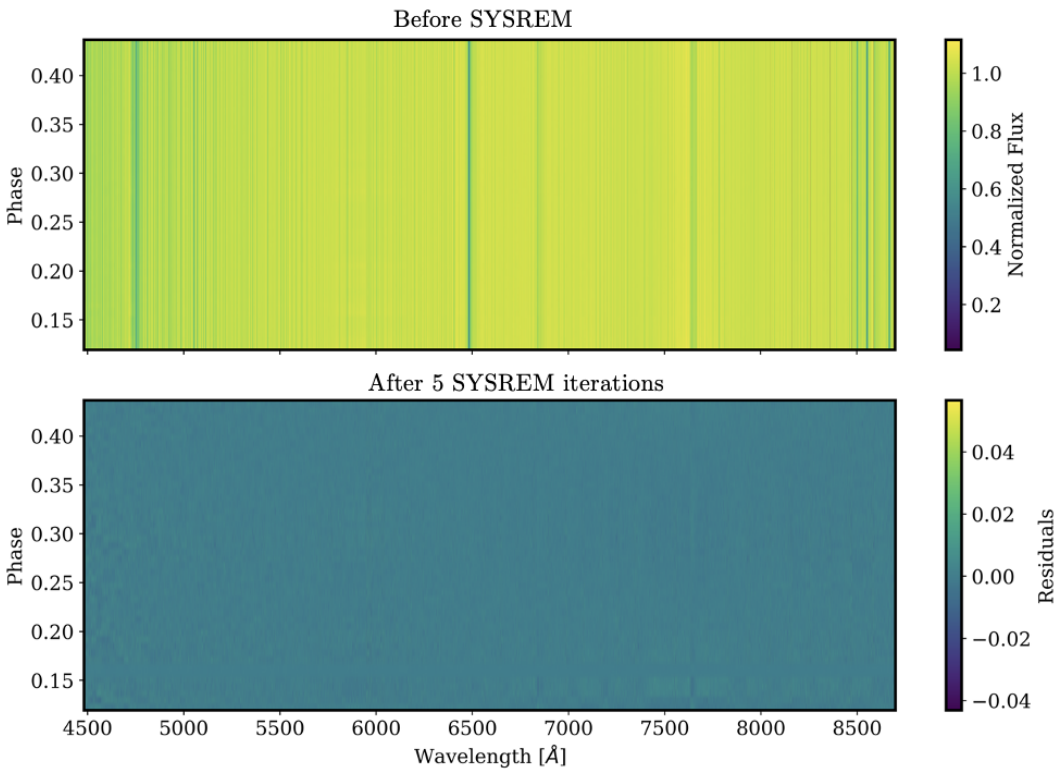

Figure 5.2 Upper panel: Processed 1D KPF spectra as a function of orbital face before applying SYSREM. Lower panel: The residuals as a function of orbital phase after applying 5 iterations of SYSREM to the data.

wavelength grid in log-space that closely matched the original wavelength spacing. The flux values in the overlapping regions were determined using a mean of the overlapping orders.

After continuum normalizing and combining individual order to produce a 1D spectrum for each of the three science fibers, we then interpolated the spectra onto a common wavelength grid and coadded them to produce one spectrum for each exposure. Householder et al. (in prep) considered how combining the three fibers with their varying LSF functions could introduce errors into the final atmospheric analysis, but found that had a negligible effect in their observations.

After creating a single combined spectrum for each exposure. We then removed the spectrum of the host star and tellurics from our observations by dividing by the median spectrum. We remove outliers deviating from the median spectrum at greater than 4σ. We removed residual time-varying telluric and stellar features using the SYSREM algorithm (Tamuz et al., 2005). We compare the significance of our detection of Fe using different numbers of SYSREM iterations and find that using

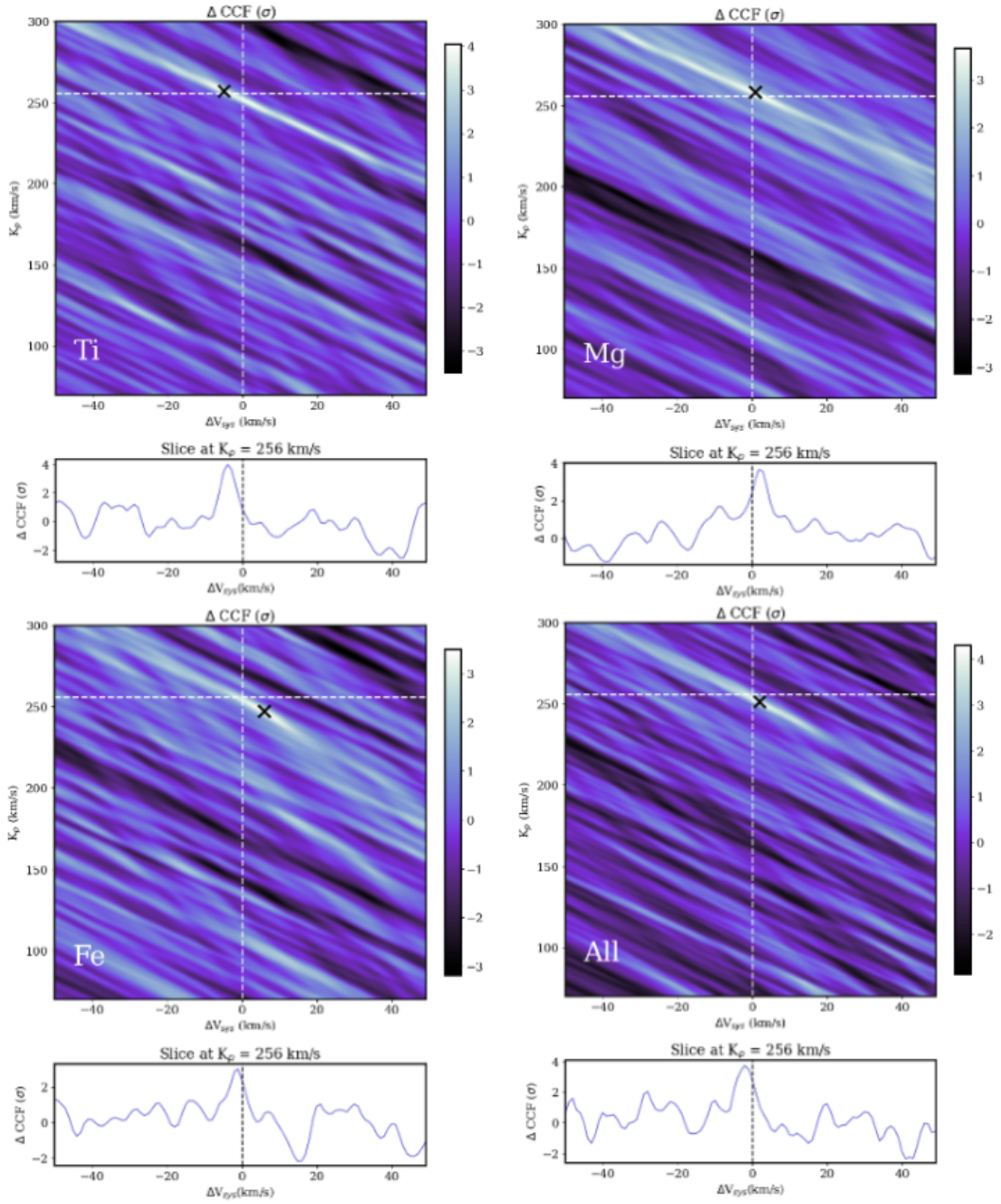

Figure 5.3 K_p - Δv_{sys} plots for our TOI-2109 b observations using individual templates for Fe, Mg, and Ti, as well as a full model template generated by `petitRADTRANS`. The expected K_p and Δv_{sys} are indicated by the white dashed lines.

four iterations leads to the strongest signal. We finally shift the spectra into the stellar rest frame by correcting for the reflex motion of the star due to the planet, which has a measured amplitude of 0.86 ± 0.13 km/s Wong et al. (2021).

Cross-Correlation Analysis

We used the cross correlation method to search for signals from different potential atmospheric constituents. First, we generated atmospheric model templates for individual atomic and ionic species including Fe I, Fe II, Mg I, Ti I, Cr I, V I, and Ca I. We then generated a template atmospheres containing all species with significant detections using the radiative transfer code `petitRADTRANS` (Mollière et al., 2019). We used an inverted P-T profile calculated with the parameters reported for TOI-2109b in Cont et al. (2025). Other planetary parameters, such as log g, are fixed to the values from Wong et al. (2021), and displayed in Table 5.1. We did not include the effect of the planetary rotation rate on the measured line shapes and velocity shifts in these initial models. The chemical abundances are computed assuming equilibrium chemistry at solar atmospheric abundances.

Next, we Doppler-shifted the template model onto an RV grid with a range of -400 km/s to 400 km/s in increments of 1 km/s. We then interpolated the shifted template onto the wavelength grid of the data and calculated the corresponding cross-correlation value for that RV shift. We arranged the cross correlation functions (CCFS) for each exposure in a two dimensional array to create a CCF map for this observation and aligned this map to the rest frame of TOI-2109b for a range of possible values of the system velocity, v_{sys} and planet radial velocity semi-amplitudes, K_p. The resulting $K_p - v_{sys}$ plot was divided by the standard deviation to convert to units of detection significance. In Fig. 5.3, we plot our resulting K_p-v_{sys} maps for the three atomic species with a detection significance $> 3\sigma$ at the expected K_p and v_{sys}.

When we plotted the CCF map as a function of orbital phase for Fe before applying the `SYSREM` algorithm, (Fig. 5.4), we found that there was a strong structure located at velocity shifts between -80 and 80 km/s, which is similar in magnitude to the measured rotational velocity of the host star. This structure is not present for any other atomic species aside from Fe I, which has many lines spanning the entire wavelength range of KPF and is present in both the planet and host star. This structure overlaps with the expected radial velocity of the planet just before secondary eclipse ingress (phases > 0.45). We tested the effect of this region on our Fe I detection significance by masking out the phases greater than 0.45 and found that the detection significance changed by less than 0.1σ. We found that applying `SYSREM` to the observations partially removed this structure, but likely removes some of the planetary signal as well. As this signal occurs near the rotational velocity of

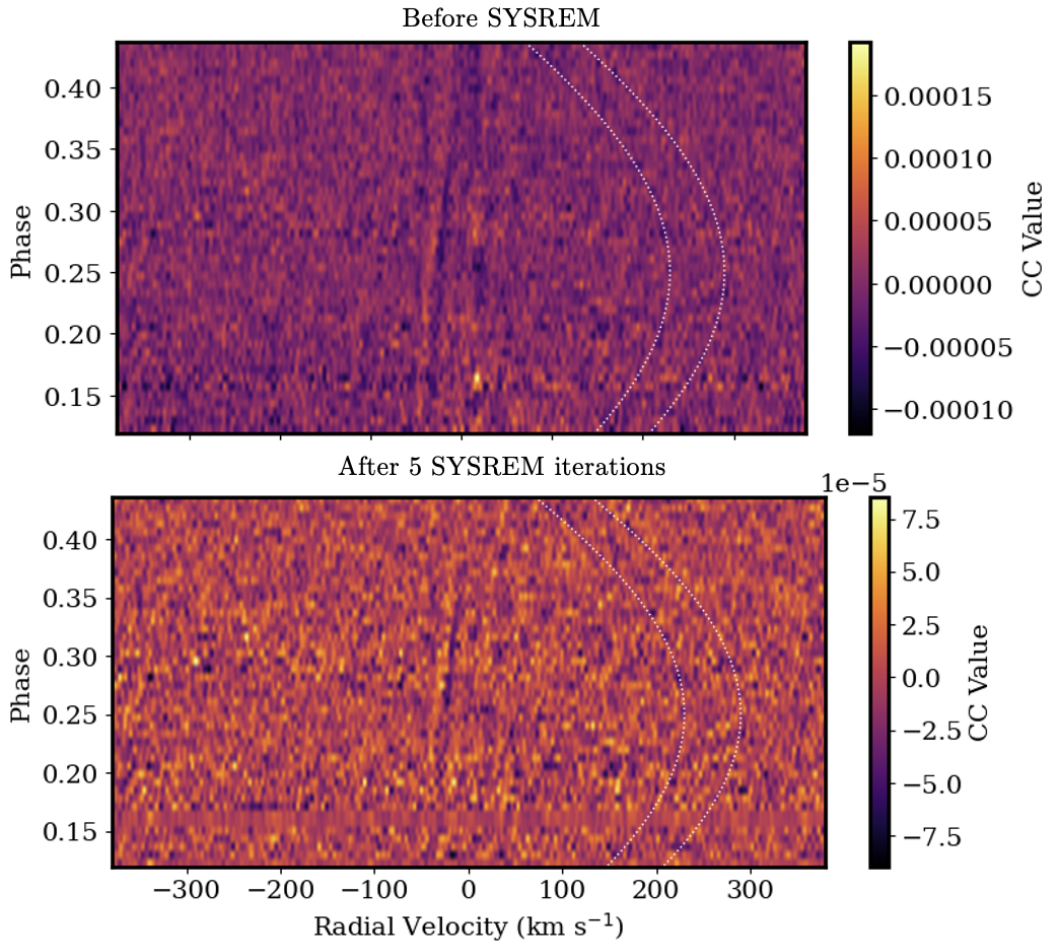

Figure 5.4 Upper panel: Cross correlation function map for Fe as a function of orbital phase and radial velocity shift calculated prior to applying `SYSREM`. Lower panel: Cross correlation function map for the same template as above calculated after five iterations of `SYSREM`.

the star, this is likely the result of imperfectly removed stellar lines. There is a known instrument drift over the course of the night on the order of 10s m/s, which has not been corrected in our current data reduction and may have resulted in residual stellar lines in the processed data. An imperfect correction for the stellar radial velocity shifts due to the orbiting planet, which has a semi-amplitude of ∼1 km/s, could also have contributed. Alternatively, this signal may be due to stellar pulsations, which have been observed in other high-resolution datasets, most significantly in observations WASP-33b, which have made detections of features in the planetary atmosphere challenging (Cont et al., 2022; Snellen, 2025).

5.3 Current Results and Next Steps

Our detection of Fe is consistent with the previously published observations of this system from Cont et al. (2025) utilizing CARMENES, who detected Fe at a SNR of 3σ. Our Fe detection is only slightly stronger with a detection significance of 3.5σ, despite the larger aperture size of Keck. This is likely due to a combination of factors, including the lower-than-expected SNR of the observations due to clouds, as well as the residual structure in the CCF phase map shown in Fig. 5.4.

As in Cont et al. (2025), we find that template models with a thermal inversion are preferred. In addition, we detect both Ti (4.2σ) and Mg (3.7σ), neither of which was detected in the CARMENES observations. We find that the velocity of the CCF peak differs slightly for each species detected, but this shift is sensitive to the number of `SYSREM` iterations used. This suggests that `SYSREM` may be subtracting off part of the planetary signal; this is something that we can explore in more depth using injection recovery tests if needed. The measured shift is also strongest for Fe I, which is affected by additional structure in the CCF map as noted in the previous section. Our detections of Fe I, Mg I and Ti I are consistent with previous studies of ultra-hot Jupiters. Currently, Ti I has only been detected in WASP-189 b (T_{eq} = 2640 K), WASP-33 b (T_{eq} = 2780 K) and KELT-9 b (T_{eq} = 4050 K), and now in TOI-2109 b, whereas Mg I and Fe I are detected in every ultra-hot Jupiter with T_{eq} greater than ~2000 K (see references in Snellen, 2025).

Moving forward, we intend to re-reduce these data with an updated version of the KPF pipeline, which should improve the SNR of the observation and better correct for the radial velocity drift over the course of the night. We will also correct for telluric absorption in individual exposures using the forward model `molecfit` rather than removing them using PCA with `SYSREM`, as this can remove part of the planetary signal. If we conclude that the residual structure in the CCF map is due to stellar pulsations, we will mask out that region of the CCF space.

After improving our data analysis process to maximize the retrieved signal, we will perform retrievals on these observations to convert our detected signals into abundances for Fe, Mg, and Ti. We will additionally measure other parameters, such as the line broadening, to constrain the properties of the atmospheric circulation. If we can separate out our detections into subsets of lines that probe different atmospheric pressures, we may also be able to measure the magnitude of the velocity shift as a function of depth in the planet's atmosphere (e.g. Kesseli et al., 2024).

We additionally have a JWST/NIRSpec cycle 4 program (GO 8877) that recently

observed a near infrared (3 – 5 μm) phase curve of TOI-2109 b, which will allow us to obtain robust constraints on vertical temperature profile of this planet as a function of longitude. We also have two complementary phase curves of TOI-2109 b observed with HST/WFC3 G141 (1.1 - 1.7 μm). These spectroscopically resolved phase curve observations can be used to map both the planet's longitudinally varying thermal structure and to measure the spatially resolved abundances of species such as SiO, H_2O, H-, CO_2 and CO. Using these data, we will be able to quantify changes in the extent of dissociation of molecules like H_2O and H_2 from the day to the night side, infer the direction and strength of atmospheric winds using the wavelength-dependent offset in the location of the hot spot near the substellar point, and potentially constrain the onset of cloud formation via the removal of SiO from the gas phase.

Fits to the low-resolution night-side emission spectrum can also be used to better constrain the abundances of volatile species such as water that are partially or fully dissociated on the day side. These complementary datasets will provide strong constraints on TOI-2109 b's atmospheric properties that will enhance our ability to robustly interpret the high-resolution data presented here and provide new insights into the atmospheric composition and corresponding accretion history of this massive planet.

References

Bell, Taylor J. and Nicolas B. Cowan (Apr. 2018). "Increased Heat Transport in Ultra-hot Jupiter Atmospheres through H2 Dissociation and Recombination". In: *The Astrophysical Journal* 857, p. L20. ISSN: 0004-637X. DOI: 10.3847/2041-8213/aabcc8.

Beltz, Hayley and Emily Rauscher (Nov. 2024). "Comparative Planetology of Magnetic Effects in Ultrahot Jupiters: Trends in High-resolution Spectroscopy". en. In: *The Astrophysical Journal* 976.1, p. 32. ISSN: 0004-637X. DOI: 10.3847/1538-4357/ad7ded.

Beltz, Hayley et al. (Dec. 2021). "Exploring the Effects of Active Magnetic Drag in a General Circulation Model of the Ultrahot Jupiter WASP-76b". en. In: *The Astronomical Journal* 163.1, p. 35. ISSN: 1538-3881. DOI: 10.3847/1538-3881/ac3746.

Chachan et al. (Jan. 2023). "Breaking Degeneracies in Formation Histories by Measuring Refractory Content in Gas Giants". en. In: *The Astrophysical Journal* 943.2, p. 112. ISSN: 0004-637X. DOI: 10.3847/1538-4357/aca614.

Cont, D. et al. (Dec. 2022). “Atmospheric characterization of the ultra-hot Jupiter WASP-33b. Detection of Ti and V emission lines and retrieval of a broadened line profile”. In: *Astronomy and Astrophysics* 668, A53. ISSN: 0004-6361. DOI: 10.1051/0004-6361/202244277. (Visited on 08/22/2025).

Cont, D. et al. (June 2025). “Retrieving day- and nightside atmospheric properties of the ultra-hot Jupiter TOI-2109b - Detection of Fe and CO emission lines and evidence for inefficient heat transport”. en. In: *Astronomy & Astrophysics* 698, A31. ISSN: 0004-6361, 1432-0746. DOI: 10.1051/0004-6361/202554572.

Gaia Collaboration (Nov. 2020). “VizieR Online Data Catalog: Gaia EDR3 (Gaia Collaboration, 2020)”. In: *VizieR Online Data Catalog* 1350, pp. I/350. DOI: 10.26093/cds/vizier.1350.

– (May 2022). “VizieR Online Data Catalog: Gaia DR3 Part 1. Main source (Gaia Collaboration, 2022)”. In: *VizieR Online Data Catalog*, pp. I/355.

Gandhi, Siddharth and Nikku Madhusudhan (June 2019). “New Avenues for Thermal Inversions in hot Jupiters”. In: *Monthly Notices of the Royal Astronomical Society* 485.4, pp. 5817–5830. ISSN: 0035-8711, 1365-2966. DOI: 10.1093/mnras/stz751.

Gandhi, Siddharth et al. (May 2023). “Retrieval Survey of Metals in Six Ultrahot Jupiters: Trends in Chemistry, Rain-out, Ionization, and Atmospheric Dynamics”. en. In: *The Astronomical Journal* 165.6, p. 242. ISSN: 1538-3881. DOI: 10.3847/1538-3881/accd65.

Gaudi, B. Scott et al. (June 2017). “A giant planet undergoing extreme-ultraviolet irradiation by its hot massive-star host”. In: *Nature* 546, pp. 514–518. ISSN: 0028-0836. DOI: 10.1038/nature22392.

Gibson, Steven R. et al. (Aug. 2016). “KPF: Keck Planet Finder”. In: vol. 9908, p. 990870. DOI: 10.1117/12.2233334.

Hellier, Coel et al. (Aug. 2009). “An orbital period of 0.94 days for the hot-Jupiter planet WASP-18b”. en. In: *Nature* 460.7259, pp. 1098–1100. ISSN: 1476-4687. DOI: 10.1038/nature08245.

Høg, E. et al. (Mar. 2000). “The Tycho-2 catalogue of the 2.5 million brightest stars”. In: *Astronomy and Astrophysics* 355, pp. L27–L30. ISSN: 0004-6361.

Hubeny, Ivan, Adam Burrows, and David Sudarsky (Sept. 2003). “A Possible Bifurcation in Atmospheres of Strongly Irradiated Stars and Planets”. en. In: *The Astrophysical Journal* 594.2, p. 1011. ISSN: 0004-637X. DOI: 10.1086/377080.

Kesseli, Aurora Y. et al. (Oct. 2024). “Up, Up, and Away: Winds and Dynamical Structure as a Function of Altitude in the Ultrahot Jupiter WASP-76b”. en. In: *The Astrophysical Journal* 975.1. Publisher: The American Astronomical Society, p. 9. ISSN: 0004-637X. DOI: 10.3847/1538-4357/ad772f.

Komacek, Thaddeus D., Adam P. Showman, and Xianyu Tan (Jan. 2017). "Atmospheric Circulation of Hot Jupiters: Dayside–Nightside Temperature Differences. II. Comparison with Observations". en. In: *The Astrophysical Journal* 835.2. Publisher: The American Astronomical Society, p. 198. ISSN: 0004-637X. DOI: 10.3847/1538-4357/835/2/198.

Lothringer, Joshua D., Travis Barman, and Tommi Koskinen (Oct. 2018). "Extremely Irradiated Hot Jupiters: Non-oxide Inversions, H- Opacity, and Thermal Dissociation of Molecules". In: *The Astrophysical Journal* 866, p. 27. ISSN: 0004-637X. DOI: 10.3847/1538-4357/aadd9e.

Miller-Ricci Kempton, Eliza and Emily Rauscher (June 2012). "Constraining High-speed Winds in Exoplanet Atmospheres through Observations of Anomalous Doppler Shifts during Transit". In: *The Astrophysical Journal* 751, p. 117. ISSN: 0004-637X. DOI: 10.1088/0004-637X/751/2/117.

Mollière, P. et al. (July 2019). "petitRADTRANS: a Python radiative transfer package for exoplanet characterization and retrieval". In: *Astronomy & Astrophysics* 627, A67. ISSN: 0004-6361, 1432-0746. DOI: 10.1051/0004-6361/201935470.

Parmentier, Vivien, Adam P. Showman, and Yuan Lian (Oct. 2013). "3D mixing in hot Jupiters atmospheres. I. Application to the day/night cold trap in HD 209458b". In: *Astronomy and Astrophysics* 558, A91. ISSN: 0004-6361. DOI: 10.1051/0004-6361/201321132.

Parmentier, Vivien et al. (Sept. 2018). "From thermal dissociation to condensation in the atmospheres of ultra hot Jupiters: WASP-121b in context". In: *Astronomy and Astrophysics* 617, A110. ISSN: 0004-6361. DOI: 10.1051/0004-6361/201833059.

Showman, Adam P. et al. (Dec. 2012). "Doppler Signatures of the Atmospheric Circulation on Hot Jupiters". en. In: *The Astrophysical Journal* 762.1, p. 24. ISSN: 0004-637X. DOI: 10.1088/0004-637X/762/1/24.

Snellen, Ignas (May 2025). *Exoplanet atmospheres at high spectral resolution*. DOI: 10.48550/arXiv.2505.08926.

Tamuz, O., T. Mazeh, and S. Zucker (Feb. 2005). "Correcting systematic effects in a large set of photometric light curves". In: *Monthly Notices of the Royal Astronomical Society* 356. Publisher: OUP ADS Bibcode: 2005MNRAS.356.1466T, pp. 1466–1470. ISSN: 0035-8711. DOI: 10.1111/j.1365-2966.2004.08585.x.

Tan, Xianyu and Thaddeus D. Komacek (Nov. 2019). "The Atmospheric Circulation of Ultra-hot Jupiters". en. In: *The Astrophysical Journal* 886.1, p. 26. ISSN: 0004-637X. DOI: 10.3847/1538-4357/ab4a76.

Wong, Ian et al. (Dec. 2021). "TOI-2109: An Ultrahot Gas Giant on a 16 hr Orbit". In: *The Astronomical Journal* 162, p. 256. ISSN: 0004-6256. DOI: 10.3847/1538-3881/ac26bd.

Chapter 6

CONCLUSIONS

6.1 Summary

In this thesis, I explored how the present day atmospheric properties and orbital configurations of giant planets can be used to constrain their origins. In Chapter 2, I measured the atmospheric composition of the directly-imaged companion ROXs 42B b and showed that it is consistent with that of its host binary. I demonstrated the challenges of using only a single atmospheric composition measurement, such as the C/O ratio, to distinguish between formation scenarios, especially for companions that likely formed outside the CO ice line. I also showed how the presence of clouds in the atmospheres of giant planets can result in strongly biased measurements of key parameters, such as the atmospheric composition and temperature-pressure profile, when fitting low-resolution near-infrared spectra. I showed that high-resolution data can overcome these biases because the cores of individual absorption lines are formed high in the atmosphere above the location of the clouds. high-resolution spectroscopy also provides tight constraints on the abundance ratios of different molecules using their relative line depths, which are relatively insensitive to the values of other model parameters, such as the temperature-pressure profile. These two facts combined allowed me to obtain better constraints on the C/O ratio of ROXs 42B b than with the low resolution observations.

In Chapter 3, I used two decades of astrometric observations to constrain the orbits of both the binary and the planetary mass companion in the ROXs 42 B system in order to place additional constraints on the origin of the planetary mass companion. When combined, these two orbital solutions revealed that the companion orbit is highly misaligned with respect to the plane of the binary orbit. I then considered a range of possible scenarios that could reproduce this configuration, and concluded that due to the density of the stellar environment the system formed in and the age of the system, the companion was unlikely to have been captured and most likely formed within the circumbinary disk. However, even with all of the available information it is still challenging to differentiate between formation via core accretion versus disk instability.

In Chapter 4, I showed how mid-infrared observations with JWST MIRI LRS can

be used to characterize the compositions of clouds in giant planet atmospheres, a common obstacle to obtaining robust inferences about other atmospheric properties. Our MIRI LRS spectrum of the transiting hot Jupiter HD 189733b revealed nm-sized quartz grains at millibar pressures in the dayside atmosphere, challenging our current understanding of cloud formation processes. These clouds may have formed through equilibrium condensation in the hottest region of the atmosphere, just east of the sub-stellar point. The small sizes of these particles suggest that they might act as seeds for condensate cloud formation, as they are similar to the expected sizes of seed particles in microphysical models (Lee et al., 2016). Models predict that nucleation of these seeds can only occur when the partial pressure of the condensible species significantly exceeds the saturation vapor pressure. (Lee et al., 2016; Powell et al., 2018). For HD 189733 b, this corresponds to relatively low atmospheric pressures, comparable to those where the particles are observed to reside.

In Chapter 5, I used high-resolution spectra obtained using Keck I/KPF to observe the dayside emission of the ultra-hot Jupiter TOI-2109 b, which is expected to contain multiple refractory species in the gas phase. I was able to obtain preliminary detections of Fe, Ti, and Mg. Moving forward, I will use these detections to constrain the abundances of these three species in TOI-2109 b's dayside atmosphere in order to infer the temperature of its night-side cold trap and constrain the solid-to-gas ratio of the materials incorporated into its atmosphere, providing us with new insights into its past accretion and migration history.

6.2 Lessons Learned and Future Work

One of the main goals of this thesis was to understand the origins of gas giant planets and explore how measurements of atmospheric composition can be used to trace formation history. It is clear that a single measurement, such as the C/O ratio or metallicity [Fe/H], of a given target is insufficient to differentiate between formation scenarios. Combining these measurements with additional information about the architecture of the system, such as the thousands of orbital solutions that will be provided in the upcoming Gaia DR4, can help to rule out more scenarios. Measurements of elemental abundances for additional species can similarly help to improve our understanding of the formation and migration histories of individual systems. If these measurements can constrain the ratio of volatile to refractory material, this can in turn be used to estimate the solid-to-gas ratio of the accreted material (e.g Chachan et al., 2023). This was recently demonstrated using sulfur abundances, in the form of SO_2 and H_2S, from JWST observations of the transiting

gas giant planets WASP-39b Rustamkulov et al. (2023) and HD 189733b (Fu et al., 2024; Inglis et al., 2024). Ultra-hot Jupiters like TOI-2109b provide a unique opportunity to make this measurement, because their dayside temperatures are so high (>2500 K) that we are able to obtain precise abundance measurements for a wide range of refractory species including Fe, Mg, and Ti (Snellen, 2025). On the other hand, due to tidal locking and poor heat redistribution, their night sides are cool enough for measurements of volatiles such as H_2O that are partially dissociated on the day side. These objects are also useful for understanding cloud formation, as we can directly measure the gas phase abundances of refractory cloud-forming materials and observe how these materials are progressively removed from the atmosphere with decreasing equilibrium temperature (e.g. Gandhi et al., 2023). Eventually, high-resolution spectrographs on 30 meter-class extremely large telescopes (ELTs) will be able to provide even stronger constraints on the chemistry and dynamics of giant planet atmospheres, as well as smaller and cooler planets that are currently not accessible from the ground.

Clouds appear to be present in most hot Jupiter and directly-imaged planet atmospheres. This means that in order to accurately retrieve the atmospheric compositions of these objects, it is critically important to understand the relevant cloud formation and transport processes, which in turn determine the 3D distribution and optical properties of the cloud particles. Observations with MIRI LRS have already provided valuable insights into cloud formation processes in hot Jupiter atmospheres, revealing the presence of very small SiO_2 grains rather than the $MgSiO_3$ and Mg_2SiO_4 particles that are typically used for atmospheric modeling of these objects. Moving forward, additional mid-infrared observations using JWST/MIRI LRS of planets spanning the entire range of relevant parameter space (temperature, log g, and composition) as well as more spatially resolved (day side versus evening and morning temperature, or phase curves) observations, will be vital in order to improve our understanding of cloud formation in hot Jupiter atmospheres.

More broadly, it should be an over-arching goal of the field to obtain a much larger sample of atmospheric composition measurements for both transiting and directly-imaged gas giants. Xuan et al. (2024) showed that many widely-separated directly-imaged companions like ROXs 42B b have atmospheric compositions similar to those of their host stars, suggesting that they share a common formation channel. In contrast, the hot Jupiter population appears to span a broader range of atmospheric compositions, although the published C/O ratios and metallicity mea-

surements from high-resolution and spaced-based measurements are sometimes mutually inconsistent (Kempton et al., 2024). Taken at face value, this could be inferred as evidence that most or all hot Jupiters formed via core accretion, which can produce a wide range of atmospheric compositions, while the population of widely-separated planetary-mass companions formed via disk instability. This hypothesis motivated me to begin a survey to measure the metallicities and C/O ratios of transiting super Jupiters, which have masses that are comparable to those of the widely-separated directly-imaged companions (approximately 4-13 M_J). If there is a shift in formation mechanism from core accretion to disk instability within this mass range, then we might be able to see this reflected in the measured atmospheric compositions as a function of planet mass. If such a transition were observed, this would allow us to empirically constrain the upper bound of the mass distribution for close-in gas giant planets formed via core accretion. We can then compare this value to the corresponding constraint from atmospheric composition studies of directly-imaged companions on wide orbits, and to predictions from core accretion and gravitational instability models.

We can also obtain complementary constraints on the formation mechanisms of gas giant exoplanets by measuring their fluid Love numbers, h_f, which directly constrain their core-mass fractions. This can be done through measurements of the ellipsoidal distortion of a handful of ultra-hot Jupiters orbiting within a few stellar radii of their host stars. Ultra-precise transit and phase curve observations with JWST can potentially constrain this value for $\sim$ 20 targets. This would greatly improve upon current estimates based on the observed radii and masses of transiting gas giant planets (e.g. the work by Thorngren et al., 2016; Thorngren et al., 2019). I am Co-PI of a Cycle 4 JWST program (GO 8877) that recently obtained a phase curve of the ultra-hot super Jupiter, TOI-2109 b, in order to measure its core-mass fraction. These observations will place additional constraints on the formation mechanism of this 5 M_{Jup} planet.

References

Chachan et al. (Jan. 2023). "Breaking Degeneracies in Formation Histories by Measuring Refractory Content in Gas Giants". en. In: *The Astrophysical Journal* 943.2, p. 112. ISSN: 0004-637X. DOI: 10.3847/1538-4357/aca614.

Fu, Guangwei et al. (Oct. 2024). *Hydrogen sulfide detection and strong methane depletion in the super-stellar metallicity atmosphere of hot Jupiter HD 189733b*. DOI: 10.21203/rs.3.rs-3403333/v1.

Gandhi, Siddharth et al. (May 2023). "Retrieval Survey of Metals in Six Ultrahot Jupiters: Trends in Chemistry, Rain-out, Ionization, and Atmospheric Dynamics". en. In: *The Astronomical Journal* 165.6, p. 242. ISSN: 1538-3881. DOI: 10.3847/1538-3881/accd65.

Inglis, Julie et al. (Oct. 2024). "Quartz Clouds in the Dayside Atmosphere of the Quintessential Hot Jupiter HD 189733 b". In: *The Astrophysical Journal* 973, p. L41. ISSN: 0004-637X. DOI: 10.3847/2041-8213/ad725e.

Kempton, Eliza M. -R. and Heather A. Knutson (July 2024). "Transiting Exoplanet Atmospheres in the Era of JWST". In: *Reviews in Mineralogy and Geochemistry* 90, pp. 411–464. DOI: 10.2138/rmg.2024.90.12.

Lee, E. et al. (Oct. 2016). "Dynamic mineral clouds on HD 189733b - I. 3D RHD with kinetic, non-equilibrium cloud formation". In: *Astronomy & Astrophysics* 594, A48. ISSN: 0004-6361, 1432-0746. DOI: 10.1051/0004-6361/201628606.

Powell, Diana et al. (June 2018). "Formation of Silicate and Titanium Clouds on Hot Jupiters". en. In: *The Astrophysical Journal* 860.1, p. 18. ISSN: 0004-637X. DOI: 10.3847/1538-4357/aac215.

Rustamkulov, Z. et al. (Feb. 2023). "Early Release Science of the exoplanet WASP-39b with JWST NIRSpec PRISM". In: 614.7949, pp. 659–663. DOI: 10.1038/s41586-022-05677-y. arXiv: 2211.10487 [astro-ph.EP].

Snellen, Ignas (May 2025). *Exoplanet atmospheres at high spectral resolution*. DOI: 10.48550/arXiv.2505.08926.

Thorngren, Daniel P. and Jonathan J. Fortney (Apr. 2019). "Connecting Giant Planet Atmosphere and Interior Modeling: Constraints on Atmospheric Metal Enrichment". In: *The Astrophysical Journal* 874.2, p. L31. ISSN: 2041-8213. DOI: 10.3847/2041-8213/ab1137.

Thorngren, Daniel P. et al. (Oct. 2016). "The Mass–Metallicity Relation for Giant Planets". en. In: *The Astrophysical Journal* 831.1, p. 64. ISSN: 0004-637X. DOI: 10.3847/0004-637X/831/1/64.

Xuan et al. (July 2024). "Are These Planets or Brown Dwarfs? Broadly Solar Compositions from High-resolution Atmospheric Retrievals of 10–30 MJup Companions". en. In: *The Astrophysical Journal* 970.1, p. 71. ISSN: 0004-637X. DOI: 10.3847/1538-4357/ad4796.